Real-Time Quantum Sensing in Rubidium

Few-Photon Probing of Ultracold Gases and Rydberg Microwave Polarimetry

Laurits Nikolaj Stokholm

PhD Thesis
Aarhus University

Laurits Stokholm, PhD Thesis, 2026
Real-Time Quantum Sensing in Rubidium: Few-Photon Probing of Ultracold Gases and Rydberg Microwave Polarimetry

PhD Dissertation submitted to
the Graduate School of Natural Sciences (GSNS),
Aarhus University, Denmark.

The PhD project is supervised by Jan Joachim Arlt at
Center for Complex Quantum System (CCQ),
Department of Physics and Astronomy,
Aarhus University, Denmark.

Typesetting done with LaTeX, BibLaTeX and the MEMOIR class.
Compiled using pdfLaTeX.
Figures are made with Matplotlib, TikZ/PGF and InkScape.
Printed at Aarhus University.

Abstract

Atomic systems, ranging from room-temperature vapours to ultracold quantum gases, form a cornerstone of modern physics. Their high degree of experimental control enables precise engineering and probing of quantum matter, establishing them as a powerful platform for quantum simulation and precision measurements. Applications in quantum technologies has driven advances in the field of neutral atoms in quantum metrology, sensing and computing.

Experimental access to ultracold gases relies on probing the atoms with light fields, and absorption imaging has long served as the workhorse technique for estimating atom numbers and temperatures. Employing resonant light at intensities above saturation and using time-of-flight expansion to reduce high in-situ optical density and improve spatial resolution is, however, inherently destructive and necessitates a new atomic cloud for each measurement. This introduces preparation noise and places strong demands on experimental cycle times. To overcome this limitation, alternative dispersive techniques have been developed, such as phase-contrast imaging and Faraday imaging. These approaches are generally restricted to far-detuned operation to suppress absorption. This thesis presents the development of a novel nondestructive probing technique that combines the far-detuned and resonant regimes. The method relies on three primary components: (1) a Raman laser system providing a versatile probe spanning a 9 GHz frequency range within 100 ms; (2) a single-photon detection setup enabling time-resolved measurements at the few-photon level; and (3) a dark-ground imaging configuration that enhances the signal-to-noise ratio and provides sensitivity to dispersive phase shifts. Using this approach, a new class of nondestructive in-situ measurements is demonstrated. Ultracold atomic clouds are spectroscopically probed across varying condensate fractions, with extracted atom numbers and temperatures in agreement with absorption imaging. The method offers enhanced sensitivity to weak thermal components at high condensate fractions. Time-resolved measurements performed on a single cloud accelerate experiments such that calibrations and optimisations are completed in minutes rather than hours.

In addition, this thesis presents the construction of a Rydberg-atom-based electromagnetically induced transparency sensor for characterising external microwave fields using a room-temperature Rb vapour cell. The Autler-Townes splitting of Rydberg states is shown to exhibit a substructure at strong microwave fields that had not been experimentally resolved in earlier studies. Finally, the setup demonstrates a complete microwave-polarimeter via distinct spectroscopic fingerprints.

Resumé

Neutrale atomsystemer, der spænder fra stuetemperaturdampe til ultrakolde kvantegasser, spiller en central rolle i moderne fysik. Deres høje grad af eksperimentel kontrol muliggør præcis manipulation og undersøgelse af kvantematerie, hvilket har etableret en unik platform for kvantesimulering og præcisionsmålinger. Kvanteteknologier driver fortsat forskning i ultrakolde atomer, særligt inden for kvantemetrologi, sensorteknologi og kvantecomputere.

Måling af ultrakolde gasser baseres på vekselvirkningen med lysfelter, hvor absorptionsafbildning længe har været standardmetoden til at bestemme atomantal og temperaturer. Denne metode er dog destruktiv, og kræver ofte en flyvetidsekspansion (*time-of-flight*) for at reducere den høje optiske tæthed *in-situ* og forøge den rumlige opløsning. Dette nødvendiggører forberedelsen af en ny atomsky for hver måling, hvilket introducerer forberedelsesstøj og øger eksperimentets varighed. Dette motiverer ikke-destruktive teknikker som fasekontrast- og Faraday-afbildning, som dog generelt er begrænset til lys af stor frekvensforskydning (*detuning*) for at undertrykke absorption. Denne afhandling præsenterer udviklingen af en ny ikke-destruktiv detektionsmetode til ultrakolde gasser af ^{87}Rb-atomer, som forbinder resonant- og frekvensforskudte lysregimer. Metoden bygger på tre hovedkomponenter: (1) et Raman-lasersystem, der leverer en fleksibel probe der kan spænde et frekvensinterval på 9 GHz inden for 100 ms; (2) et enkeltfotondetektionssystem, som muliggør tidsopløste målinger ved svage lysfelter; og (3) en mørk-baggrunds-afbildningskonfiguration, der forbedrer signal/støj-forholdet og kan måle frekvensafhængige faseforskydninger. Med denne opstilling demonstreres en række nye *in-situ* målinger. Spektroskopier af ultrakolde atomskyer måles ved varierende kondensationsbrøker, og de estimerede atomantal og temperaturer stemmer overens med absorptionsafbildning. Metoden supplerer afbildningsregimet, og viser forøget følsomhed for termiske atomer ved høje kondensatbrøker.Tidsopløste målinger på en enkelt sky reducerer eksperimenternes varighed, og muliggør kalibrering og parameteroptimering på minutter frem for timer.

Desuden omfatter afhandlingen konstruktionen af en Rydberg-atom-baseret elektromagnetisk induceret gennemsigtigheds sensor til karakterisering af eksterne mikrobølgefelter ved anvendelse af en stuetemperaturs Rb dampcelle. Autler–Townes opspaltningen af Rydberg-tilstande påvises en understruktur ved stærke mikrobølgefelter, som tidligere var forudsagt, men manglede eksperimentelt bevis. Endelig demonstrerer opstillingen et fuldstændigt mikrobølgepolarimeter baseret på unikke spektroskopiske fingeraftryk.

Publications

Peer-Reviewed Publications

[1] T. Vibel, M. B. Christensen, M. A. Kristensen, J. J. Thuesen, L. N. Stokholm, C. A. Weidner, and J. J. Arlt, "Spatial calibration of high-density absorption imaging", Journal of Physics B: Atomic, Molecular and Optical Physics **57**, 145301 (2024).

[2] T. Vibel, M. B. Christensen, R. M. F Andersen, L. N. Stokholm, K. Pawłowski, K. Rzążewski, M. A. Kristensen, and J. J. Arlt, "Atom number fluctuations in Bose gases—statistical analysis of parameter estimation", Journal of Physics B: Atomic, Molecular and Optical Physics **57**, 195301 (2024).

[3] R. M. F Andersen, S. Frederiksen, L. N. Stokholm, I. Zebergs, M. Kristensen, C. Weidner, and J. J. Arlt, "Cloud parameter estimation for interacting BEC after time-of-flight", (2026).

Non-First-Author Manuscripts in Preparation

[4] R. M. F Andersen, L. N. Stokholm, I. Zebergs, N. R. Neubert, A. S. Chatterly, and J. J. Arlt, "Few-photon spectroscopy of Bose-Einstein condensates", Manuscript in preparation (expected 2026).

First-Author Manuscripts in Preparation

[5] L. N. Stokholm, R. M. F Andersen, I. Zebergs, N. R. Neubert, A. S. Chatterly, and J. J. Arlt, "Observation of dynamics in ultracold gases using dark-ground detection", Manuscript in preparation (expected 2026).

[6] M. Chilcott, L. N. Stokholm, M. Cloutman, J. S. Otto, A. B. Deb, and N. Kjærgaard, "Quantum-enabled complete RF-polarimetry", Manuscript in preparation (expected 2026).

Abbreviations

BF/DG Bright-Field / Dark-ground (imaging configuration)

MB Maxwell-Boltzmann

BEC Bose-Einstein Condensate

TF Thomas-Fermi

EIT Electromagnetically Induced Transparency

AT Autler-Townes

MW/UV Microwave/ultraviolet (radiation)

DDS Direct Digital Synthesiser

TTL Transistor-transistor logic (standard digital binary signal)

PM-SM Polarisation maintaining single mode (optical fibre)

CCD Charge-Coupled Device

OD Optical density

LIA Lock-in amplifier

ILA Injection-Locked amplified

(P)BS cube (Polarising) Beam splitter cube

ECDL External Cavity Diode Laser

SPDM Single-photon detector module

MPS Mechanical positioning system

RWA Rotating Wave Approximation

Notation

All experiments are performed with ^{87}Rb-atoms. The quantum states are typically denoted by $|F, m_{\mathrm{F}}\rangle$, where F is the total hyperfine angular momentum and m_{F} is its projection onto the quantisation axis. Deviations will be specified in the text. When referring to the D2 transition, a distinction is made between the ground and excited hyperfine levels by writing F for the $5\mathrm{S}_{1/2}$ ground state and F' for the $5\mathrm{P}_{3/2}$ excited state.

Contents

CHAPTER 1

Introduction

Atoms and molecules may exist but this is irrelevant from the point of view of physics.

Quoted by Eugene Wigner, recalling his first physics book [7]

Eugene Wigner's remark reflects a time when the microscopic constituents of matter were largely inaccessible to direct experimental control. In modern atomic physics, however, atoms and molecules are not merely abstract constructs but tangible systems that can be isolated, manipulated and observed with extraordinary precision. Nowhere is this more evident than in the definition and realisation of the International System of Units, where atomic transitions form the basis of the unit of time. Atomic clocks and related metrological techniques exploit the intrinsic stability and reproducibility of quantum systems to achieve unprecedented accuracy, placing atomic physics at the foundation of modern precision measurement.

With the invention of laser cooling and trapping techniques it became possible to create atomic clouds and cool them down to a few millionths of a degree above absolute zero. These temperatures lie far below those found in naturally occurring environments, including interstellar space, which is characterised by a background temperature of a few Kelvin. Under such extreme conditions atoms can drastically change their behaviour and condense into a single common quantum state called the Bose-Einstein condensate (BEC). This was theoretically predicted

by Albert Einstein in 1924 [8, 9] based on work by Satyendra Nath Bose [10], but it would take 70 years for the first experimental realisation and observation [11–13]. Now, a century after their theoretical prediction and two decades after their first experimental realisation, BECs and related ultracold quantum gases are routinely created and observed in laboratory experiments. What began as proof-of-principle realisations of BEC has matured into a cornerstone of modern physics, underpinning advances in quantum simulation and related technologies. BECs provide an exceptional platform for quantum engineering, in which complex quantum systems can be studied in a coherent and highly controllable setting. Atoms can be loaded into optical lattices with precise control over lattice geometry and dimensionality, enabling quantum simulations of a wide range of condensed-matter models. Interatomic interactions may be tuned using magnetic Feshbach resonances, granting access to both weakly and strongly interacting limits within a single experimental system. Moreover, the high optical densities achievable in BECs enable strong light-matter interactions forming the basis for experiments utilising phenomena such as electromagnetically-induced transparency (EIT), where an otherwise opaque medium can be rendered transparent, allowing for striking demonstrations on slow and stopped light. Such experiments can in turn provide powerful tools for probing and controlling ultracold atomic systems.

Advancements in ultracold atomic physics critically depend on the ability to measure quantum systems with high accuracy and efficiency. Imaging and spectroscopy are central to this effort, forming the experimental interface between theory and observation. While absorption imaging has proven enormously successful in the study of ultracold atoms, the technique inherently perturbs the system and imposes limitations when probing high optical densities and strongly interacting regimes. Its destructive nature necessitates the preparation of a new atomic cloud for each measurement, and real-time dynamical processes can only be reconstructed from a collection of images. As experiments increasingly target subtle correlations, long coherence times, and real-time evolution, there is a growing need for measurement techniques that are both sensitive and minimally invasive. In this context, nondestructive probing enables repeated, in-situ measurements on a single quantum system, increasing the information obtainable per cloud while reducing the experimental cycle time required.

This thesis presents the development and application of a novel nondestructive measurement technique for ultracold gases, potentially offering an increase in bandwidth compared to camera-based imaging methods. Time-resolved absorption spectra are recorded using a highly sensitive single-photon detector module in

combination with a Raman-laser system, which provides a pair of optically phase-locked lasers as well as a versatile probe field capable of scanning up to 9 GHz within 100 ms. A dark-ground imaging configuration enhances the signal-to-noise ratio, enabling detection at weak probe intensities. In addition, it provides sensitivity to dispersive phase shifts. Analysis of the resulting spectra reveals intricate structures arising from spatial variations in optical density, which carry information about cloud parameters such as atom number and temperature. The detection technique is applied to ultracold ^{87}Rb clouds across a broad range of temperatures and optical densities, extending from the thermal regime to purely condensed samples. Comparison with conventional absorption imaging demonstrates quantitative agreement while extending measurement capabilities beyond the limits of standard imaging, particularly at low temperatures and high optical densities. Moreover, a spectral model enables sensitivity to deviations from the predicted spectra arising from light induced dipole-dipole interactions, which occur at high atomic densities. Additionally, time-resolved interrogation of atomic clouds provides access to dynamical behaviour. This thesis thus presents a series of experiments tracking the evolution of individual atomic samples in real time.

This work also explores coherent light–matter interactions enabled by the Raman-laser system, facilitating studies of three-level atomic systems in both the EIT and Autler–Townes (AT) regimes, as well as two-photon Raman transitions in ultracold atomic clouds. These techniques provide both sensitive probes of atomic structure and flexible tools for quantum state manipulation.

In addition, this thesis presents the construction of a Rydberg-atom-based EIT sensor for characterising external microwave fields using a room-temperature Rb vapour cell. The AT splitting of Rydberg states is shown to exhibit a substructure at strong microwave fields that, while previously predicted [14], had not been experimentally resolved in earlier studies. Finally, the setup demonstrates a complete microwave-polarimeter via distinct spectroscopic fingerprints [6].

Collectively, these experiments demonstrate the critical role of advanced measurement techniques and high-resolution spectroscopy in atomic gases, with significant implications for developing emerging quantum-sensing technologies.

Thesis outline

Chapter 2: Theoretical Framework In this chapter fundamental principles are presented, beginning with the description of light-matter interactions at the single-atom level. The interaction Hamiltonians are derived for two-, three- and four-level systems and their time-evolution is described via the Lindblad master equation. Using a single-atom model of quasi-hydrogenic systems, the tools required for calculating overlap integrals are derived from first principles. The discussion extends from single atoms to atomic ensembles, where ultracold gases are described using Bose-Einstein statistics to establish models for thermal and condensed regimes. In particular, the Gross-Pitaevskii equation is derived with emphasis on the Thomas-Fermi limit. Light-matter interactions are reformulated in the context of atomic gases, forming the basis of imaging and detection techniques used in experiments. Finally, theoretical descriptions of both the room-temperature- and the ultracold gas experiments are presented, supported by corresponding density matrix simulations.

Chapter 3: Production of Ultracold Atomic Gases The apparatus used to produce ultracold gases is described, with particular emphasis on the modifications and developments implemented during the course of this doctoral project.

Chapter 4: Few-Photon Probing of Ultracold Atoms Ultracold atomic clouds are spectroscopically probed, and theoretical models enable atom number and temperature estimations, which are shown to be in agreement with conventional time-of-flight absorption images. The nondestructive method offers an enhanced sensitivity to thermal components at high condensate fractions. Subsequently, a series of time-resolved experiments are performed via the novel detection technique that enables real-time measurements on a single atomic cloud probing both internal and external dynamics. This work led to two publications [4, 5] in preparation.

Chapter 5: Quantum Sensing using Rydberg Atoms This chapter presents the work carried out during my seven-week-long research stay abroad, focusing on the development of a Rydberg-atom-based EIT sensor for characterising external microwave (MW) fields using a room-temperature Rb vapour cell. At strong MW fields, the AT splitting of the Rydberg levels exhibits experimentally resolved substructure. Finally, the setup demonstrates MW polarimetry, where distinct spectral signatures enable reconstruction of the MW field polarisation. This ultimately led to a publication [6] in preparation.

CHAPTER 2

Theoretical Framework

This chapter provides the theoretical framework necessary to understand the two key experiments presented in this thesis: (1) measurements performed on ultracold bosonic gases near quantum degeneracy, and (2) spectroscopic studies of thermal Rydberg atoms. Although these two systems operate in very different temperature regimes, they share common foundational elements in light-matter interactions and atomic structure. The goal of this chapter is therefore to build and motivate the theoretical tools that are essential for analysing these highly engineered quantum experiments.

Central to both experiments is the subject of light-matter interactions, which will be discussed in Section 2.1. This is followed by the treatment of single-valence electron atoms, including both alkali and Rydberg atoms, in Section 2.2. This builds on the light-matter interactions by displaying useful formulas that later will be used for density matrix simulations of both experiments. Section 2.3 extends the discussion from single atoms to atomic ensembles, turning to the physics of trapped ultracold bosonic gases. The statistical and mean-field descriptions of thermal clouds and BECs are put to work to model the density profiles relevant for the experiments of type (1). Section 2.4 treats ultracold atom detection, which is based on probing atomic ensembles with light. The absorption imaging method is described and formula for both transmitted probe fields in bright- and dark-field configurations are presented, which is the groundwork for the nondestructive measurements presented in Chapter 4. Finally, Section 2.5 presents the dynamical

evolution of both the type (1) and (2) systems. For this purpose, the density-matrix formalism is presented through the von Neumann master equation, allowing for coherent driving with decoherences and dissipation in the entire ^{87}Rb D2 line used for controlling and probing the ultracold gases near quantum degeneracy, and the multi-level Rydberg excitation schemes used for MW polarimetry. These equations are solved in the steady-state regime, relevant for spectroscopic measurements, and through full time propagation which captures transient dynamics.

2.1 Light-Matter Interaction

2.1.1 Interaction Hamiltonian

The Atomic Two Level System

Consider the two-level system with energies given by $H_0 = \hbar\left(\omega_g|g\rangle\langle g| + \omega_e|e\rangle\langle e|\right)$. Suppose the atom has an electric dipole moment, $\boldsymbol{d} = -e\boldsymbol{r}$, which is introduced to a laser field $\boldsymbol{E} = E_0\cos(\omega t)\hat{\boldsymbol{\varepsilon}}$. characterised by its field strength, E_0, angular frequency ω and polarisation $\hat{\boldsymbol{\varepsilon}}$. This semi-classical picture is accurate for field strengths typically used in the laboratory, and the dynamics is described by the interaction $H_{\text{int}} = -\boldsymbol{d}\cdot\boldsymbol{E}$. The transition strength is conveniently characterised in terms of the Rabi frequency $\hbar\Omega = \boldsymbol{d}\cdot\hat{\boldsymbol{\varepsilon}}E_0$, which gives:

$$H_{\text{int}} = -\frac{\hbar\Omega}{2}\left(e^{-i\omega t} + e^{i\omega t}\right)|e\rangle\langle g| + \text{h.c.} \tag{2.1}$$

The dynamics of the system is properly described in the interaction picture (IP) [15], which relates to the Schrödinger picture (SP) used above by the unitary transformation $\mathcal{U} = e^{-iH_0t/\hbar}$. This operation acts as a coordinate transformation on a general state-vector $|x\rangle_{\text{IP}} = \mathcal{U}|x\rangle_{\text{SP}}$. This gives $|e\rangle\langle g| \mapsto e^{-i\omega_0 t}|e\rangle\langle g|$, where $\omega_0 = \omega_{\text{e}} - \omega_{\text{g}}$ is the resonance transition frequency. Together with the time dependency from the electric field, the interaction Hamiltonian reads:

$$H_{\text{int}} = -\frac{\hbar\Omega}{2}\left(e^{-i(\omega-\omega_0)t}|e\rangle\langle g| + e^{i(\omega+\omega_0)t}|e\rangle\langle g|\right) + \text{h.c.} \tag{2.2}$$

The condition $\omega - \omega_0 \ll \omega + \omega_0$ is true for all driven transitions in this thesis, even the far-detuned two-photon Raman-Rabi oscillations described in Chapter 4. Hence, the rotating-wave approximation (RWA) is applicable for further analysis.[1] The interaction Hamiltonian in the RWA is:

$$H_{\text{int}} = -\frac{\hbar\Omega}{2}e^{-i\Delta t}|e\rangle\langle g| + \text{h.c.} \tag{2.3}$$

[1] For reference, the RWA introduces an error of 15.4% for the dipole trap (see Section 3.1.3), which is detuned 1070 THz (i.e. 1064 nm from 780 nm). The greatest probe detuning in our experiment is ~ 5 GHz–well within RWA.

The Hamiltonian is explicitly time-dependent in the interaction picture. There is a standard approach to circumvent this [16]. If $|e\rangle \mapsto e^{i\Delta t/2}|e\rangle$ and $|g\rangle \mapsto e^{-i\Delta t/2}|g\rangle$, the phases cancel. This amounts to the unitary transformation $\mathcal{U} = e^{-i\Delta t\sigma_z/2}$, which is known as a co-rotating frame. The Hamiltonian transform according to $H \mapsto \mathcal{U}^\dagger H\mathcal{U} - i\hbar\mathcal{U}^\dagger \frac{d}{dt}\mathcal{U}$, which leads to,

$$H_{\text{2-level}} = \frac{\hbar}{2}\begin{pmatrix} 0 & \Omega \\ \Omega^* & -2\Delta \end{pmatrix}, \tag{2.4}$$

after absorbing a global phase for convenience. A lot of interesting physical insight is already given by Eq. (2.4). Coupling the "bare" atomic two level system with a laser field causes new eigenstates of the Hamiltonian with eigenvalues,

$$E_\pm = \frac{\hbar}{2}\left(-\Delta \pm \tilde{\Omega}\right), \tag{2.5}$$

where $\tilde{\Omega} = \sqrt{\Omega^2 + \Delta^2}$ is the generalised Rabi frequency. The new eigenstates are referred to as "*dressed-states*" and the spectral splitting of the two levels is given by $\tilde{\Omega}$, which is minimum at resonance. Solving the time-dependent Schrödinger equation with Eq. (2.4) yields the famous Rabi oscillations, where the electronic population periodically oscillates between the bare atomic states.

So far, decoherence mechanisms have been neglected in the description of coherent atomic excitation, although they play a central role for realistic systems. The density matrix formalism, specifically the Lindblad master equation, provides a natural framework for such processes, like spontaneous decay, open system effects and dephasing. This will be addressed in Section 2.5. For now, note that for Rabi oscillations to be observable, their characteristic timescale must be shorter than the relevant decoherence times.

While there is a large gap between the idealised two-level system and the realistic, complex multi-level systems considered in this thesis, a two-level model is often well justified, particularly for closed cycling transitions. However, multi-level systems exhibit additional features, including quantum interference phenomena relevant for precision experiments and coherent control. This motivates the study of a three-level system.

The Atomic Three-Level System

Three-level atoms play a central role for both experimental setups described in this thesis; and form the minimal models for coherent population trapping (CPT), electromagnetically induced transparency (EIT) and Raman transitions.

The energy levels can be structured in either a Λ- ("*lambda*"), V- ("*vee*") or Ξ- ("*ascending ladder*") scheme, where each label refers to the geometry when drawing the energy levels of the system. Both the Λ and Ξ configurations are experimentally realised in this thesis. The choice solely changes the connectivity in the fundamental Hamiltonian, and without loss of generality, this section describes the Ξ scheme, associated with the ordered basis, $(|g\rangle, |i\rangle, |e\rangle)$. As shown in Fig. 2.1 (a), a probe and coupling field address the transitions $|g\rangle \leftrightarrow |i\rangle$ and $|i\rangle \leftrightarrow |e\rangle$ respectively. The fields are characterised by their Rabi frequency Ω_{i}, and detuning Δ_{i}; and the two-photon detuning is δ. Using these parameters, the three-level Hamiltonian takes the same form as outlined in Section 2.1.1:

$$H_{\text{3-level}} = \frac{\hbar}{2}\begin{pmatrix} 0 & \Omega_{\mathrm{p}} & 0 \\ \Omega_{\mathrm{p}} & -2\Delta_{\mathrm{p}} & \Omega_{\mathrm{c}} \\ 0 & \Omega_{\mathrm{c}} & -2(\Delta_{\mathrm{p}} + \Delta_{\mathrm{c}}) \end{pmatrix}. \tag{2.6}$$

For now, each optical field is assumed to only connect the transitions shown in Fig. 2.1. Similarly, the Λ system in Fig. 2.1 (b) consists of two ground-states that are optically connected to a shared excited state, and where the transition $|g_1\rangle \leftrightarrow |g_2\rangle$ is dipole forbidden. Section 2.5 treats the Λ configuration in a more complex setting, where each optical field interact with both ground-states. This

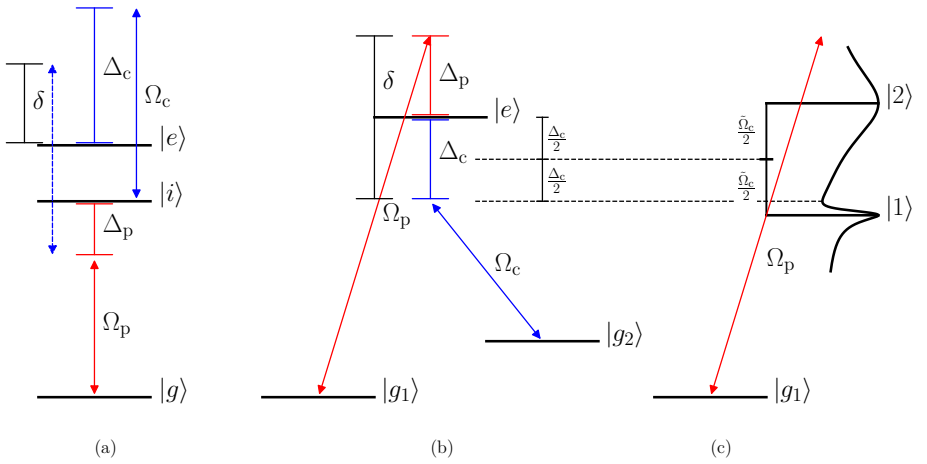

Figure 2.1: *The three-level configurations considered in this thesis. (a) Ladder scheme used for Rydberg-atom-based EIT sensing of external MW fields. (b) Λ-system investigated in the ^{87}Rb D2 line. The probe (red) and coupling (blue) light fields are characterised by their detuning, Δ_k, and Rabi frequency, Ω_k and the two-photon detuning is denoted by δ. (c) In the weak-probe limit ($\Omega_p \ll \Omega_c$), the probe addresses the dressed states due to the interaction with the strong coupling field. The spectroscopy is given by Eq.* (2.7)

mechanism adds multiple decoherence channels to the system. This is particularly relevant for the far-detuned two-photon Raman-Rabi measurements in Chapter 4, where both fields are detuned on the order of the groundstate hyperfine splitting.

Electromagnetically Induced Transparency

The perturbative regime in the probe field is considered in Fig. 2.1 (c), corresponding to a strong coupling field and a weak probe field, with $\Omega_\mathrm{p} \ll \Omega_\mathrm{c}$. In this regime, the probe field addresses the dressed states formed by the interaction of the atom with the strong coupling field. The atomic two-level system associated with the coupling field transition $|g_2\rangle \leftrightarrow |e\rangle$ gives rise to two dressed states denoted $|1\rangle$ and $|2\rangle$, shown in Fig. 2.1 (c). Their energies are obtained from the eigenenergies given in Eq. (2.5), relative to the bare excited state $|e\rangle$, and are split by the generalised Rabi frequency $\tilde{\Omega}_\mathrm{c}$, also known as the Autler-Townes (AT) splitting. The weak probe field couples to both states without significantly perturbing their structure. Since, the same photon polarisation addresses both transitions, interference effects between the two excitation pathways can occur. The linear electric susceptibility is given by [17, 18],

$$\chi = \frac{i\tilde{\Gamma}_2 + 2\tilde{\delta}}{\tilde{\Omega}_\mathrm{c}^2 + \left(\tilde{\Gamma}_2 - i2\tilde{\delta}\right)\left(1 - i2\left(\tilde{\Delta}_\mathrm{c} + \tilde{\delta}\right)\right)}, \tag{2.7}$$

where $\tilde{\Gamma}_2 = \Gamma_2/\Gamma$ is the normalised dephasing rate of $|g_2\rangle$, $\tilde{\delta} = \delta/\Gamma$ is the normalised two-photon detuning, and $\tilde{\Delta}_\mathrm{c} = \Delta_\mathrm{c}/\Gamma$ is the normalised coupling detuning. Here, Γ denotes the decay rate of $|e\rangle$, and all linewidths refer to the full widths at half maximum (FWHM) linewidth. For sufficiently strong coupling, $\Gamma \leq \tilde{\Omega}_\mathrm{c}$, Eq. (2.7) describes the AT regime, in which the dressed states are spectrally resolved. As shown in Section 2.4, the real part of χ is related to absorption. To illustrate the expected probe field spectrum for the dressed state system, $\mathrm{Re}(\chi)$ is plotted in Fig. 2.1 (c). The system reduces to an effective two-level system in two limiting cases: in the absence of the coupling field, or for an infinitely far-detuned coupling field. This follows directly from Eq. (2.7) by either setting $\Delta_\mathrm{c} = \Omega_\mathrm{c} = \Gamma_2 = 0$ and $\delta = \Delta_\mathrm{p}$, or taking the limit $\Delta_\mathrm{c} \to \infty$ with $\Delta_\mathrm{p} \ll \Delta_\mathrm{c}$. The far-detuned coupling limit can be understood intuitively from the dressed-state energies in Eq. (2.5). In this case, one dressed state remains at the energy of $|e\rangle$, while the other is shifted far out of resonance. A strongly detuned coupling field therefore no longer interacts with the system unless the probe field is equally detuned, in which case a narrow two-photon Raman transition occurs. On two-photon resonance, Eq. (2.7)

simplifies to

$$\chi_{\delta=0} = \frac{i\tilde{\Gamma}_2}{\tilde{\Omega}_c^2 + \tilde{\Gamma}_2\left(1 - i2\tilde{\Delta}_c\right)}. \tag{2.8}$$

The consequences are most clearly seen in the ideal case of vanishing dephasing, $\Gamma_2 = 0$. In this limit, $\chi = 0$, and the medium exhibits no interaction with the probe field in terms of absorption or phase shift at two-photon resonance. For $\Delta_c = 0$, the condition $\delta = \Delta_p$ holds, such that no interaction occurs even on the single-photon resonance, where absorption is usually strongest. This induced transparency gives rise to the term *electromagnetically induced transparency* (EIT).

The absence of absorption can be understood as a destructive interference between the excitation pathways involving the dressed states, which cancel exactly on two-photon resonance. Alternatively, the phenomenon can be interpreted as a Fano resonance, similar to the auto-ionisation of doubly excited states [19]. The probe absorption proceeds either directly via $|g_1\rangle \rightarrow |e\rangle$ or indirectly through the pathway $|g_1\rangle \rightarrow |e\rangle \rightarrow |g_2\rangle \rightarrow |e\rangle$. The Rabi cycling between $|g_2\rangle$ and $|e\rangle$ introduces a relative minus sign in the wavefunction. Of course, an infinite number of Rabi cycles between $|g_2\rangle$ and back to $|e\rangle$ will contribute to the interference process.

Importantly, the spectral features associated with EIT are extremely narrow compared to Γ. This leads to a very steep dispersion in $\mathrm{Re}(\chi)$ and, consequently, to strongly reduced group velocities for light propagating through the medium [17]. This effect was experimentally demonstrated in 1999 by Lene Hau and co-workers, who slowed light down to $17\,\mathrm{m\,s^{-1}}$ [20]. Other applications of EIT include stopped-light schemes for quantum memories [21–24], and as we will see in Chapter 5, Rydberg-atom-based EIT sensing [14].

The Atomic Four Level System

The ladder system is easily extended indefinitely by adding excited states, but particularly the four-level system is relevant for the Rydberg-atom-based EIT sensing of external MW fields. In this case, the two excited states are highly excited Rydberg levels, and to reflect the experiments, the basis will be denoted by $\{|g\rangle, |i\rangle, |r_1\rangle, |r_2\rangle\}$. The transition $|r_1\rangle \leftrightarrow |r_2\rangle$ is addressed by an additional coupling field, which experimentally is in the MW domain. The interaction

Hamiltonian is obtained similarly as in Section 2.1.1:

$$H_{\text{4-level}} = \frac{\hbar}{2}\begin{pmatrix} 0 & \Omega_{\text{p}} & 0 & 0 \\ \Omega_{\text{p}} & -2\Delta_{\text{p}} & \Omega_{\text{c}} & 0 \\ 0 & \Omega_{\text{c}} & -2(\Delta_{\text{p}}+\Delta_{\text{c}}) & \Omega_{\text{MW}} \\ 0 & 0 & \Omega_{\text{MW}} & -2(\Delta_{\text{p}}+\Delta_{\text{c}}+\Delta_{\text{MW}}) \end{pmatrix}. \tag{2.9}$$

The interaction Hamiltonian captures the coherent dynamics. However, decoherence processes, which are detrimental to experiments, have so far been neglected, and the next step toward a full simulation is to incorporate these effects.

2.1.2 Time Evolution of Atomic Systems

The temporal evolution is governed by the optical Bloch equations that can be derived from the density matrix formalism using the Lindblad master equation [25],

$$\dot{\rho} = \frac{1}{i\hbar}[H,\rho(t)] + \sum_k \gamma_k \left(L_k \rho(t) L_k^\dagger - \frac{1}{2}\{L_k^\dagger L_k, \rho(t)\} \right), \tag{2.10}$$

where ρ is the system's density operator and $\{L_k\}$ are a set of Lindblad operators that represent non-unitary operations such as decay and phase decoherence. The two superoperators, $[,]$, and $\{,\}$, are the commutator and anti-commutator. Eq. (2.10) builds on top of the von Neumann equation by including dissipation via the Lindblad operator, L. Unlike the Hamiltonian, the Lindblad operators are not required to be hermitian. In fact, they rarely are! For instance, the decay from a state $|i\rangle$ to $|g\rangle$, is the jumping operator $L = |g\rangle\langle i|$. When solving Eq. (2.10), it is convenient to vectorise the problem, so it has the form $\dot{\rho} = \mathcal{L}\rho$, where $\mathcal{L}$ is a superoperator of dimension $\dim(\mathcal{L}) = \dim(H)^2$, and ρ is reshaped into a vector. Rephrasing the problem via the language of linear algebra enables well known solving techniques for numerical analysis. Now, the problem is to systematically construct the superoperator, $\mathcal{L}$, given the Hamiltonian and total set of Lindblad operators. This can be achieved by using the general matrix algebra identity,

$$\text{vec}\,(A\rho B) = (B^T \otimes A)\text{vec}(\rho), \tag{2.11}$$

that relates the vectorisation of a matrix product of three matrices to the Kronecker product of two of them. Strategically inserting the identity operator in Eq. (2.10) to sandwich ρ, followed by the use of Eq. (2.11), yields the following expression for the superoperator:

$$\mathcal{L} = \frac{1}{i\hbar}\left(\mathbb{1}\otimes H - H^T \otimes \mathbb{1}\right) + \sum_k \gamma_k \left(L_k^* \otimes L_k - \frac{1}{2}\left(\mathbb{1}\otimes L_k^\dagger L_k + L_k^T L_k^* \otimes \mathbb{1}\right)\right). \tag{2.12}$$

Eq. (2.12) is central for the density matrix simulations presented in Section 2.5. However, many details are still missing. In particular, all interaction Hamiltonians include Rabi frequencies, Ω_i, in the off-diagonal elements, and this parameter is essential for describing the light-matter interaction. The Rabi frequency depends strongly on physical properties such as the quantum states involved and the polarisation of the light field. The goal of the next section is to describe how to incorporate this dependence into the physical model. Specifically, some of the experiments involve transitions between highly excited Rydberg states, and analysing these experiments requires calculations of the relevant overlap integrals.

2.2 Quasi-Hydrogenic Atoms

Ground state alkali atoms have a relatively simple electronic structure consisting of a single valence electron in an s-orbital outside a closed-shell core. The core electrons are much more tightly bound than the single valence electron[2]. As a result, the atomic response to the light field is captured by considering only the valence electron. Due to the spherical symmetry of the core, the valence electron moves in an effective central potential, where the nuclear charge Ze is screened by the $Z-1$ inner electrons. Looking at the potential at long range, the shielding leads to a Coulombic potential that scales as $-1/r$. This thesis focuses on alkali atoms excited to a Rydberg state, with a large principal quantum number n, compared to the ground state. In this limit, the valence electron experiences the Coulombic potential, which is why Rydberg atoms behaves spectroscopically similarly to a highly excited hydrogen atom. However, the electronic wave function for states with low angular momentum ($l < 3$), penetrates the core region, resulting in an effective core charge which is partially smeared out. For this reason, these states are referred to as core-penetrating, and their energies deviate from the simple hydrogenic scaling.

2.2.1 Quantum Defect

The model can be maintained for quasi-hydrogenic systems by introducing a quantum defect δ_{nlj} that modifies the binding energy of the weakly bound valence electron, and leads to the modified Rydberg-Ritz formula,

$$E_{\mathrm{nlj}} = \frac{-hcR_{\mathrm{y}}}{(n-\delta_{\mathrm{nlj}})^2}, \tag{2.13}$$

[2]The ionisation threshold of ^{87}Rb is 4.18 eV, and the weakest bound core electron in $4P_{3/2}$ is bound by 15.3 eV [19]

where $n - \delta_{\mathrm{nlj}}$ is the effective principal quantum number, and $R_{\mathrm{y}} = \mu R_{\infty}$ is the Rydberg constant scaled by the reduced mass of the atom. The quantum defect depends on the atomic species and the numerical value is found by spectroscopic methods. Data for rubidium [26, 27] is fitted to the empirical formula,

$$\delta_{\mathrm{nlj}} = \delta_0(l,j) + \frac{\delta_2(l,j)}{\|n-\delta_0(l,j)\|^2} + \frac{\delta_4(l,j)}{\|n-\delta_0(l,j)\|^4} + \frac{\delta_6(l,j)}{\|n-\delta_0(l,j)\|^6} + \dots \quad (2.14)$$

where δ_i are modified Rydberg-Ritz coefficients. Knowing the quantum defect is essential for calculating the binding energy, which serves as the eigenvalue of the Schrödinger equation and determines the electronic wave function. The wave function, in turn, governs the transition probability amplitudes between states.

2.2.2 Radial Wave Function

The motion of the valence electron in the atomic potential is described by the time-independent Schrödinger equation,

$$H\psi(r) = \left(-\frac{\hbar^2}{2m_{\mathrm{e}}}\nabla^2 + V(r)\right)\psi = E_{\mathrm{nlj}}\psi(r), \quad (2.15)$$

where r is the radial distance between the core and the electron and $V(r)$ is the electronic potential. For alkali Rydberg atoms, the potential can be modified to compensate for several effects via the so called model-potentials [28]. Firstly, depending on l, the valence electron penetrates the core and moves in a potential landscape from a smeared out radial charge. The interaction is then modelled by a modified Coulomb interaction of the form,

$$V_C(r) = -\frac{e^2}{4\pi\varepsilon_0}\frac{1+(Z-1)e^{\alpha_1 r} - r(\alpha_3+\alpha_4 r)e^{-\alpha_2 r}}{r}, \quad (2.16)$$

where coefficients α_i depend on the atomic species and orbital angular momentum, l [28]. Secondly, a correction term proportional to the core dipole polarisability is included, which has the form,

$$V_{\mathrm{p}} = -\frac{e^2}{(4\pi\varepsilon_0)^2}\frac{\alpha_{\mathrm{p}}}{2r^4}\left(1 - e^{-(r/r_{\mathrm{c}})^6}\right), \quad (2.17)$$

where α_{p} is the core dipole polarisability and r_{c} is the effective core size. Other effects such as the spin-orbit interaction that results in a fine-structure splitting can be included. The simulations shown in this thesis includes all interactions described in [29], but Eq. (2.16) and Eq. (2.17) are the most dominant effects. With these considerations, an expression for effective potential is obtained by

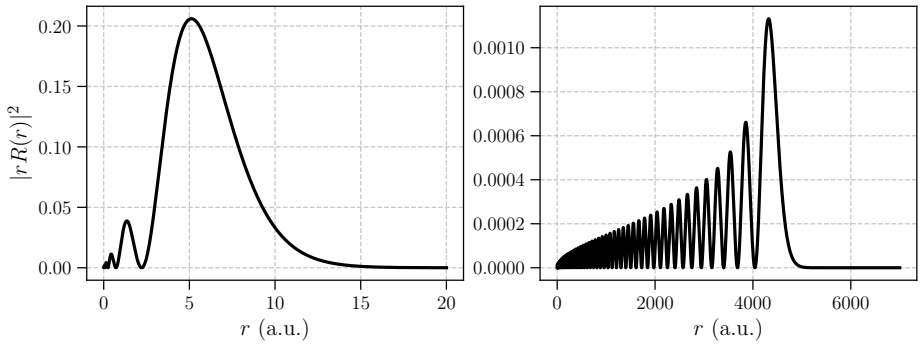

Figure 2.2: *Radial wave functions for* ^{87}Rb *of* $5S_{1/2}$ *(left) and* $50P_{3/2}$ *(right). Notice the difference in the expectation value* $\langle r \rangle$*. This is crucial for simulations, as different grids are used for calculating the wave functions, and interpolation onto a commond grid is required for determining the overlap integrals.*

summing all the contributions. Importantly, the potential retains the spherical symmetry of the hydrogen atom, and the well-known method of separation of variables can be used, which give solutions of the form $\psi(\boldsymbol{r}) = R_{\mathrm{nl}}(r)Y_l^m(\theta, \phi)$, where R is the radial wave function and Y denotes the spherical harmonics. The radial wave function is obtained from solving the second order differential equation,

$$\left[\frac{-\hbar^2}{2m_{\mathrm{e}}}\left(\frac{d^2}{dr^2} + \frac{2}{r}\frac{d}{dr} - \frac{l(l+1)}{r^2}\right) + V(r)\right] R_{\mathrm{nl}}(r) = E_{\mathrm{nlj}} R_{\mathrm{nl}}(r), \tag{2.18}$$

which can only be done analytically for the hydrogen atom. One therefore relies on numerical methods, such as Numerov's method. Figure 2.2 shows the radial wave functions for $5\mathrm{S}_{1/2}$ and $50\mathrm{P}_{3/2}$, which will be investigated in this thesis. Clearly, the electronic orbital radius, which scales as $(n - \delta_{\mathrm{nlj}})^2$, is greatly exaggerated for Rydberg states. This pronounced spatial extent, together with other properties that are strongly enhanced at large effective principal quantum number, is widely exploited in experiments involving Rydberg atoms. However, for this reason alone, the numerical computation of radial wave functions for low-lying and highly excited states must be computed on different spatial grids, making interpolation onto a common grid necessary when evaluating overlap integrals.

2.2.3 Dipole Matrix Elements

When atoms interact with an electromagnetic field, the valence electron can transition between electronic states characterised by certain quantum numbers.

With the radial wave function at hand, the probability amplitudes for each transition channel can be calculated and structured into the transition dipole matrix, which is given by,

$$\langle f|H_{\text{int}}|i\rangle = -eE_0 \exp(-i\omega t)\,\langle f|\hat{\boldsymbol{\varepsilon}}\cdot\boldsymbol{r}|i\rangle, \tag{2.19}$$

where the specific set of quantum numbers for the initial and final states are abstracted away. Eq. (2.19) can be simplified by the dipole approximation, since the optical wavelengths are $\lambda \sim 1000\,\text{a.u.}$, and all optical properties can be considered constant over the size of the electronic wave function. The main task is now to calculate the matrix element $\langle f|\boldsymbol{r}|i\rangle$. We continue in the basis of orbital angular momentum (n, L, m)[3], and extend to general angular momentum later. The unit vector can be reexpressed in the polarisation basis $\hat{\pi} = \hat{e}_{\text{z}}$, $\hat{\sigma^{\pm}} = (\mp\hat{e}_{\text{x}} + i\hat{e}_{\text{y}})/\sqrt{2}$. This leads to,

$$\boldsymbol{r} = r\sqrt{\frac{4\pi}{3}}\left(Y_1^{-1}\hat{\sigma^{+}} + Y_1^{0}\hat{\pi} + Y_1^{1}\hat{\sigma^{-}}\right), \tag{2.20}$$

where the angular dependencies are written into spherical harmonics. Now, with the separation of variables in mind, the dipole matrix elements naturally decomposes to,

$$\langle n'L'm'|rY_1^q|nLm\rangle = \langle n'L'|r|nL\rangle\langle L'm'|Y_1^q|Lm\rangle, \tag{2.21}$$

where the matrix elements simplifies to a product of radial and angular part. The radial part is determined by the radial wave functions:

$$\langle n'L'|r|nL\rangle = \int_0^\infty R_{\text{n'L'}}(r)\,r\,R_{\text{nL}}(r)\,r^2\,\text{d}r\,. \tag{2.22}$$

The angular part can be written in an analytical form using the Wigner-Eckart theorem,

$$\langle L'm'|Y_1^q|Lm\rangle = (-1)^{L'-m'}\begin{pmatrix} L' & 1 & L \\ -m' & q & m \end{pmatrix}\langle L'||Y_1||L\rangle, \tag{2.23}$$

which states that matrix elements of the spherical harmonic can be expressed as products of Wigner 3-j symbol (alternatively Clebsch-Gordan coefficients) and a reduced matrix element, indicated by the double bar notation $\langle\cdot||\_||\cdot\rangle$, which is independent of the angular momentum orientation. The Wigner 3-j symbols encompass the dipole selection rules and relate the relative scalings between states

[3] $l \mapsto L$ to prepare for general angular momentum in this section

of different orientations. The spherical harmonic has a reduced matrix element that is given by:

$$\langle L'||Y_1||L\rangle = (-1)^L \sqrt{\frac{3(2L+1)(2L'+1)}{4\pi}} \begin{pmatrix} L' & 1 & L \\ 0 & 0 & 0 \end{pmatrix}. \tag{2.24}$$

Eq. (2.23) has the same form for any generalised angular momentum. To extend Eq. (2.24) for coupled angular momentum, the reduced matrix element has to encode the geometry of coupling spin and orbital angular momentum,

$$\begin{aligned}\langle L'SJ'||Y_1||LSJ\rangle = (-1)^{1+L'+S+J}\sqrt{(2J+1)(2J'+1)} \\ \times \begin{Bmatrix} L' & J' & S \\ J & L & 1 \end{Bmatrix} \langle L'||Y_1||L\rangle.\end{aligned} \tag{2.25}$$

Wigner 6-j symbol takes care of the combinatorics of coupling angular momenta. Repeated use of the Wigner-Eckart theorem extends this for hyperfine structure:

$$\begin{aligned}\langle L'SJ'IF'||Y_1||LSJIF\rangle = (-1)^{1+J'+I+F}\sqrt{(2F+1)(2F'+1)} \\ \times \begin{Bmatrix} J' & F' & I \\ F & J & 1 \end{Bmatrix} \langle L'SJ'||Y_1||LSJ\rangle.\end{aligned} \tag{2.26}$$

Only transitions in the ^{87}Rb spectrum are considered in this thesis, and hence all electronic states share $S = 1/2$ and $I = 3/2$. This remark concludes the single-atom perspective on light-matter interactions, and the focus now shifts to ultracold gases, in which collective quantum effects arise and many-body phenomena can be explored under precise experimental control.

2.3 Ultracold Atoms

This section introduces the physics of ultracold bosonic gases with particular emphasis on Bose-Einstein condensation (BEC). The phenomenon of BEC was first predicted in the early 1920s by Satyendra Nath Bose in his statistical description of photons, and subsequently extended to massive particle by Albert Einstein. Despite this early theoretical insight, the experimental realisation of BECs remained elusive for several decades. It was only towards the end of the twentieth century, following the development of lasers and in particular, techniques for laser cooling, magnetic and optical trapping, and evaporative cooling, that the first experimental observation of a BEC was achieved in 1995 by three independent groups separated by only a few months [11–13]. In this section, the theoretical

description of atomic ensembles is briefly reviewed, with emphasis on the density distributions of thermal gases and BECs. This discussion also serves to motivate the approximations commonly employed in the analysis of experiments.

A unique property of quantum mechanical particles are their indistinguishability, which fundamentally distinguishes them from classically distinguishable particles and gives rise to quantum statistics [15]. The wave function for two identical particles must be invariant under $\hat{\Pi}^2$, where Π is the particle exchange operator. Hence, these wave functions belong to an eigenspace of Π with eigenvalues $\lambda = \pm 1$, resulting in the classification of identical particles by their exchange symmetry. Particles described by symmetric wave functions are known as bosons and obey Bose-Einstein (BE) statistics, which permit multiple particles to occupy the same quantum state. A familiar example is provided by lasers, where the bosonic nature of photons allow for macroscopic occupation of a single mode. In contrast, particles described by antisymmetric wave functions are fermions and obey Fermi-Dirac statistics. The antisymmetry of the wave function leads directly to the Pauli exclusion principle, which forbids multiple fermions from occupying the same quantum state, as this would result in a vanishing many-body wave function, $\Psi = 0$. A prominent consequence is the building up of electronic shell structures, where electrons are restricted to distinct quantum states, fundamental to the periodic table.

The focus of this thesis is on bosonic atoms which, despite being composed of fermionic constituents, behave as composite bosons and therefore obey BE statistics as a whole. Under appropriate conditions such systems can undergo BEC, forming a macroscopic quantum state which constitute the central subject of the work presented here.

2.3.1 Bose-Einstein Statistics

Consider a gas of non-interacting bosons in contact with a reservoir of heat and particles. Each single-particle state $|i\rangle$ with energy E_i can have N_i particles. The occupancy is governed by the grand canonical factor, $e^{(E_\mathrm{i}-\mu)/k_\mathrm{B}T}$, where T is the temperature and μ is the chemical potential. This leads to the Bose-Einstein (BE) distribution [30],

$$N^{\mathrm{BE}}(T, \mu; E_\mathrm{i}) = \frac{1}{e^{(E_\mathrm{i}-\mu)/k_\mathrm{B}T} - 1}, \tag{2.27}$$

that relates the average number of particles in state $|i\rangle$ with the energy of the state, the temperature and chemical potential. The restriction $\mu < E_0$ must be satisfied for physical occupation numbers. In the classical regime, the particles

are spread over a great number of states, and each quantum state has an average occupancy less than one, i.e. $N_\mathrm{i} \ll 1$. This means the denominator in Eq. (2.27) must be large, $e^{(E_\mathrm{i}-\mu)/k_\mathrm{B}T} - 1 \gg 1$ or equivalently only the exponential is of importance. This obtains the classical Maxwell-Boltzmann (MB) distribution,

$$N^{\mathrm{BE}}(T,\mu;E_\mathrm{i}) \xrightarrow{\text{classical limit}} \exp\left(-\frac{E_\mathrm{i}-\mu}{k_\mathrm{B}T}\right) = N^{\mathrm{MB}}(T,\mu;E_\mathrm{i}). \tag{2.28}$$

The BE distribution differs from MB only by the -1 term in the denominator, which, as we will see, is a reflection of quantum enhancement of low energy occupation. To understand what happens as temperature decreases, we must understand the chemical potential. One way is to consider the total number of atoms, which must agree with summing over all occupancies. For high temperatures, this involves a lot of states and the sum can be approximated by a quasi-continuous distribution function,

$$N_\mathrm{th}(T,\mu) = \int_0^\infty g(E)N(E)\ \mathrm{d}E\ = \int_0^\infty g(E)\frac{1}{e^{(E-\mu)/k_\mathrm{B}T}-1}\ \mathrm{d}E\,, \tag{2.29}$$

where the density of states $g(E)$ is introduced, which is the number of single particle states per unit of energy, and depends on the trapping potential of the system. Suppose the cloud is cooled at a fixed number of particles. Then, as the temperature decreases, the integral in Eq. (2.29) shrinks and the excited states hold fewer atoms. To keep $N_\mathrm{th} = N$ fixed, $\mu \to E_0$ from below. Eventually, μ reaches the limit and the excited states are saturated. This defines the critical temperature, T_c. For $T < T_\mathrm{c}$, μ is at its maximum and the thermally occupied excited states can no longer increase. Remaining particles must enter the ground state, which is suddenly getting a macroscopic occupancy. This phenomenon is known as Bose-Einstein condensation. This naturally motivates the binary distinction of "condensed" particles in the ground state and all other "thermal" particles. Notice, Eq. (2.29) is a fair approximation for the thermal atom number but completely fails to account for the sudden macroscopic occupation of the ground state.

Up until now, no conditions have been imposed on the trapping potential. All experiments are, however, conducted in a 3D harmonic trap characterised by the three trap frequencies, ω_i. The rest of the chapter will use this trapping potential to reflect the discussion onto the experiment.

2.3.2 Critical Temperature

The density of states for a 3D harmonic trap is $g(E) = \frac{E^2}{2(\hbar\bar{\omega})^3}$, where $\bar{\omega} = (\omega_1\omega_2\omega_3)^{1/3}$ is the geometric mean of the trap frequencies [30]. Now, Eq. (2.29) can be solved for the critical temperature, by taking the limit $\mu \to E_0 = 0$, where the ground state energy is chosen to set the zero point energy.

$$N = N_{\mathrm{th}}(T_{\mathrm{c}}, 0) = \int_0^\infty \left(\frac{E^2}{2(\hbar\bar{\omega})^3}\right) \frac{1}{e^{E/k_{\mathrm{B}}T_{\mathrm{c}}} - 1}\, \mathrm{d}E = \zeta(3) \left(\frac{k_{\mathrm{B}}T_{\mathrm{c}}}{\hbar\bar{\omega}}\right)^3, \quad (2.30)$$

where ζ is the Riemann-zeta function. Solving for the critical temperature gives

$$T_{\mathrm{c}} = \frac{\hbar\bar{\omega}}{k_{\mathrm{B}}\zeta(3)^{1/3}} N^{1/3}. \quad (2.31)$$

For $T < T_{\mathrm{c}}$, where $\mu = 0$ is fixed for the ideal gas, similar results to Eq. (2.30) are achieved by substituting $T_{\mathrm{c}} \mapsto T$. Subtracting the thermal component from the total number of atoms, leaves out the condensate, $N_0 = N - N_{\mathrm{th}}$, and by re-expressing the total number in terms of the critical temperature, and the thermal atom number by the temperature, gives a simple expression for the condensate fraction,

$$\frac{N_0}{N} = 1 - \left(\frac{T}{T_{\mathrm{c}}}\right)^3. \quad (2.32)$$

This result is extended for a more accurate model that includes interactions between the BEC and thermal components in Eq. (2.47) using the semi-ideal model.

2.3.3 Thermal Cloud

At $T > T_{\mathrm{c}}$, the gas is entirely thermal and since the thermal energy $k_{\mathrm{B}}T$ greatly exceeds the quantised level spacing $\hbar\bar{\omega}$ for experiments, the semiclassical approximation is valid, as thermal particles are smeared out over a great number of states and hence experiences a continuum of states. Then, the single particle energy is $E = \boldsymbol{p}^2/2m + V(\boldsymbol{r})$. To obtain expressions for the spatial- and momentum distribution, it is convenient to work directly in phase-space, where the density of states is $1/(2\pi\hbar)^3$. The phase-space distribution is obtained by Eq. (2.27),

$$\rho_{\mathrm{th}}(\boldsymbol{r}, \boldsymbol{p}) = \frac{1}{(2\pi\hbar)^3} \frac{1}{e^{\left(\frac{\boldsymbol{p}^2}{2m} + V(\boldsymbol{r}) - \mu\right)/k_{\mathrm{B}}T} - 1}, \quad (2.33)$$

where $\rho_{\mathrm{th}} \mathrm{d}\boldsymbol{r}\, \mathrm{d}\boldsymbol{p}$ gives the mean number of thermal particles in the phase-space volume element. Hence, integrating Eq. (2.33) over all momenta yields the spatial

distribution [30],

$$n_{\mathrm{th}}(\boldsymbol{r}) = \int \rho_{\mathrm{th}}(\boldsymbol{r},\boldsymbol{p})\ \mathrm{d}\boldsymbol{p} = \left(\frac{mk_{\mathrm{B}}T}{2\pi\hbar^2}\right)^{3/2} g_{3/2}\left(e^{-(V(\boldsymbol{r})-\mu)/k_{\mathrm{B}}T}\right), \tag{2.34}$$

where the polylogarithm function is used, which has the form,

$$g_\gamma = \sum_{i=1}^{\infty} \frac{x^i}{i^\gamma}. \tag{2.35}$$

Eq. (2.34) is known as the Bose-enhanced distribution. It resembles a Gaussian distribution but is more heavily concentrated at the centre. Taking the classical limit of Eq. (2.34), where the exponential is small either by high temperatures or small atom numbers, the polylogarithm function is linear to first order and gives,

$$n_{\mathrm{th}}(\boldsymbol{r}) \xrightarrow{\text{classical limit}} \left(\frac{mk_{\mathrm{B}}T}{2\pi\hbar^2}\right)^{3/2} e^{-(V(\boldsymbol{r})-\mu)/k_{\mathrm{B}}T}, \tag{2.36}$$

For the harmonic trap, this is the well-known Gaussian distribution. Hence, at high temperatures or at low atom numbers, the atoms will be spatially distributed according to a Gaussian, but as the temperature decreases, the particles are attracted towards the centre and follow the Bose-enhanced distribution. The attraction is purely a consequence of bosonic statistics, as the model has not included interparticle interactions yet.

2.3.4 Bose-Einstein Condensate

Up to this point, the description of the gas has relied on the semiclassical BE distribution. This accurately captures the thermal component and determines thermodynamic properties and the onset of condensation. Below T_{c}, the single-particle ground state of the trap becomes macroscopically occupied. The system acquires a long range coherence and the condensate is described by a macroscopic wave function obeying the Gross-Pitaevskii equation. This section shows the mean-field framework that establishes the condensate density, and in particular, the Thomas-Fermi profile relevant for experiments.

2.3.5 Gross-Pitaevskii Equation

All particles in the condensate occupy the same single-particle wave function $\phi(\boldsymbol{r}_i)$, with the usual normalisation,

$$\int |\phi(\boldsymbol{r})|^2\ \mathrm{d}\boldsymbol{r} = 1, \tag{2.37}$$

and the macroscopic wave function is a symmetrised product of the single particle wave functions,

$$\Psi(\boldsymbol{r}_1, \boldsymbol{r}_2, \ldots, \boldsymbol{r}_N) = \prod_{i=1}^{N} \phi(\boldsymbol{r}_i). \tag{2.38}$$

For an ultracold, dilute gas, the interatomic collisions are well within the s-wave approximation, where contributions to the partial wave expansion from components with $l > 0$ are neglected, encoding the entire interaction in a single parameter: the s-wave scattering length, a. This leads to a contact potential of the form $V_{\text{int}}(\boldsymbol{r}_i, \boldsymbol{r}_j) = U_0 \delta(\boldsymbol{r}_i - \boldsymbol{r}_j)$, where δ is the Dirac delta function, and $U_0 = 4\pi\hbar^2 a/m$ is the interaction strength. The Hamiltonian is given by [30]:

$$\hat{H} = \sum_{i=1}^{N} \left(\frac{-\hbar}{2m} \nabla_i^2 + V_{\text{trap}}(\boldsymbol{r}_i) \right) + U_0 \sum_{i<j} \delta(\boldsymbol{r}_i - \boldsymbol{r}_j). \tag{2.39}$$

The energy of the condensate is given by the expectation value $E = \langle \Psi | \hat{H} | \Psi \rangle$. This quantity can be written in terms of the condensate wave function, $\psi(\boldsymbol{r}) = N^{1/2}\phi(\boldsymbol{r})$, which is normalised to the number of atoms, $\int \mathrm{d}\boldsymbol{r}\, |\psi(\boldsymbol{r})|^2 = N$. The density of the condensate is therefore, $n(\boldsymbol{r}) = |\psi(\boldsymbol{r})|^2$. Neglecting terms of order $1/N$, the energy of the condensate can be expressed as:

$$E = \int \mathrm{d}\boldsymbol{r} \left(\frac{\hbar^2}{2m} |\nabla\psi|^2 + V_{\text{trap}}(\boldsymbol{r}) |\psi(\boldsymbol{r})|^2 + \frac{U_0}{2} |\psi(\boldsymbol{r})|^4 \right). \tag{2.40}$$

Eq. (2.40) is minimised under the constraint that the total number of particles is constant. This is done minimising $E - \mu N$, where μ enters as a Lagrange multiplier. Without this constraint, any minimisation routine finds the global minimum of zero bosons giving zero energy. The resulting equation is the time-independent Gross-Pitaevskii equation,

$$\left[\frac{-\hbar^2}{2m} \nabla^2 + V_{\text{trap}}(\boldsymbol{r}) + U_0 |\psi(\boldsymbol{r})|^2 \right] \psi(\boldsymbol{r}) = \mu \psi(\boldsymbol{r}), \tag{2.41}$$

which is in the form of a non-linear Schrödinger equation with a few modifications. The chemical potential substitutes the total energy and the potential energy function is the sum of an external potential and a non-linear term that accounts for the mean field produced by other bosons. This is an important result, but solving this equation exactly is only numerically possible for most traps. However, the Thomas-Fermi approximation captures the equilibrium condensate structure and provides simple analytic expressions for the density profile, chemical potential and radii of the cloud.

2.3.6 Thomas-Fermi Approximation

At low temperatures and large condensate atom numbers, the interactions are sufficiently strong that the mean-field interaction energy, which scales with $U_0|\psi(\boldsymbol{r},t)|^2$, dominates the kinetic term that scales in proportion with $\nabla^2\psi(\boldsymbol{r},t)$. In the harmonic trap, this regime is governed by the inequality $Na/a_{\rm ho} \gg 1$, where $a_{\rm ho} = \sqrt{\hbar/m\bar{\omega}}$ is the harmonic oscillator length. Then, the density varies slowly in space, so that the gradient is negligible in Eq. (2.41), giving a simple algebraic expression that can be solved for the density,

$$n_0(\boldsymbol{r}) = |\psi(\boldsymbol{r})|^2 = \frac{\mu - V_{\rm trap}(\boldsymbol{r})}{U_0}\Theta\left(\mu - V_{\rm trap}(\boldsymbol{r})\right), \tag{2.42}$$

where $\Theta(x)$ is the Heaviside step function, that ensures the boundary of the cloud given by $V_{\rm trap}(\boldsymbol{R}) = \mu$. Now, the density profile mirrors the trapping potential due to the repulsive interactions. For a harmonic potential, the density profile is in the shape of an inverted parabola. The Thomas-Fermi radii can be defined as the extensions along each semi-axes, which are calculated from the boundary condition:

$$R_i = \sqrt{\frac{2\mu}{m\omega_i^2}}. \tag{2.43}$$

An expression for the condensate density profile in a harmonic trap potential can be explicitly written as,

$$n_0(\boldsymbol{r}) = \frac{15}{8\pi}\frac{N_0}{R_1R_2R_3}\max\left(0, 1 - \left(\frac{x_1}{R_1}\right)^2 + \left(\frac{x_2}{R_2}\right)^2 + \left(\frac{x_3}{R_3}\right)^2\right), \tag{2.44}$$

and the chemical potential, which due to interactions is no longer pinned at $\mu = 0$, can be calculated by integrating over the cloud:

$$\mu = \frac{\hbar\bar{\omega}}{2}\left(\frac{15Na}{a_{\rm ho}}\right)^{2/5}. \tag{2.45}$$

2.3.7 Bimodal Clouds

When an ultracold bosonic gas is cooled below the critical temperature $T_{\rm c}$, the atomic ensemble consists of both thermal and condensate components. The two components occupy the same harmonic trap but exhibit different density distributions as was shown in Sections 2.3.3 and 2.3.6. The thermal cloud is governed by the Bose-enhanced distribution, Eq. (2.34), which resembles the Gaussian distribution in the classical limit. In contrast, the condensate was

described, in the Thomas-Fermi limit, by Eq. (2.44) which is an inverted parabola. However, this is not the full story, as the two components are not independent and each produces a mean-field potential that perturbs the density profile of the other. The semi-ideal model takes the condensate mean-field repulsive potential into account on the thermal cloud, but neglects the effect of the thermal cloud repulsion on the condensate, due to its significantly smaller cloud density, leaving the Thomas-Fermi distribution unperturbed. Therefore, the thermal cloud is treated as an ideal Bose gas moving in the effective potential $V_{\text{eff}}(\boldsymbol{r}) = V_{\text{trap}}(\boldsymbol{r}) + U_0 n_0(\boldsymbol{r})$, and Eq. (2.34) becomes:

$$n_{\text{th}}(\boldsymbol{r}) = \left(\frac{mk_{\text{B}}T}{2\pi\hbar^2}\right)^{3/2} g_{3/2}\left(e^{|V_{\text{eff}}(\boldsymbol{r})-\mu|/k_{\text{B}}T}\right). \tag{2.46}$$

Physically, the thermal component is pushed away from the centre by the condensate, so the thermal cloud profile has a dip in the middle. The semi-ideal model expands on the BEC fraction in Eq. (2.32) [31],

$$\frac{N_0}{N} = 1 - \left(\frac{T}{T_{\text{c}}}\right)^3 - \eta\frac{\zeta(2)}{\zeta(3)}\left(\frac{T}{T_{\text{c}}}\right)^2\left(\frac{N_0}{N}\right)^{2/5}, \tag{2.47}$$

where the scaling parameter is given by,

$$\eta = \frac{1}{2}\zeta(3)^{1/3}\left(\frac{15aN^{1/6}}{a_{\text{ho}}}\right)^{2/5}. \tag{2.48}$$

2.3.8 Freely Expanding Clouds

Suppose the harmonic trapping potential is abruptly turned off, and the ultracold gas is released for free expansion during a short time of flight. To extract accurate information from the cloud distribution, a model for cloud expansion is required.

Thermal Cloud Expansion

For thermal clouds, the in-trap spatial distribution is calculated from Eq. (2.34). To model the expansion during time of flight, it may be assumed that after abruptly turning off the trap, the atoms travel ballistically according to the in-trap initial momentum. Consequently, the probability of atoms arriving at a point $\boldsymbol{r}$ has contributions from all parts of the in-trap cloud after a time of flight,

and the contribution is calculated by substituting $\boldsymbol{r} - \boldsymbol{p}t/m$ into Eq. (2.34),

$$n_{\mathrm{th}}(\boldsymbol{r},t) = \frac{1}{(2\pi\hbar)^3}\int\left(e^{\frac{\frac{\boldsymbol{p}^2}{2m}+V\left(\boldsymbol{r}-\frac{\boldsymbol{p}t}{m}\right)-\mu}{k_{\mathrm{B}}T}}-1\right)^{-1}\mathrm{d}\boldsymbol{p}$$
$$= \left(\frac{mk_{\mathrm{B}}T}{2\pi\hbar^2}\right)^{3/2} g_{3/2}\left(\tilde{z}e^{-\left(\frac{x^2}{2w_{\mathrm{x}}^2}+\frac{y^2}{2w_{\mathrm{y}}^2}+\frac{z^2}{2w_{\mathrm{z}}^2}\right)}\right), \tag{2.49}$$

introducing the fugacity $\tilde{z} = \exp(\mu/k_{\mathrm{B}}T)$, the in-situ width, $\sigma_{\mathrm{i}} = \sqrt{\frac{k_{\mathrm{B}}T}{m\omega_{\mathrm{i}}^2}}$, from Eq. (2.34), and the width after time of flight, $w_{\mathrm{i}} = \sigma_{\mathrm{i}}\sqrt{1+\omega_{\mathrm{i}}^2t^2}$.

Eq. (2.49) is valid for purely thermal clouds, but fails in the semi-ideal model. For partially condensed clouds, numerical analysis is required to account for the mean-field potential from the BEC [3].

Condensed Cloud Expansion

During free expansion in time-of-flight, a condensed atomic cloud preserves its overall density profile, with the radii evolving in time according to $R_{\mathrm{i}}(t) = \lambda_{\mathrm{i}}(t)R_{\mathrm{i}}$. The time dependence of the scaling parameters, $\lambda_{\mathrm{i}}(t)$, is governed by the set of coupled differential equations [32]:

$$\ddot{\lambda_i} = \frac{\omega_{\mathrm{i}}^2}{\lambda_{\mathrm{i}}\lambda_1\lambda_2\lambda_3}. \tag{2.50}$$

Note that Eq. (2.50) is valid within the semi-ideal model, as the approximation also neglects the mean-field contribution from the thermal cloud. Unlike the ballistic expansion exhibited by a thermal cloud, Eq. (2.50) predicts an inversion of the aspect ratio of the BEC, a phenomenon that is intrinsically quantum mechanical. This beaviour is understood via the Heisenbergs uncertainty principle: tighter confinement in a given spatial direction corresponds to a broader momentum distribution along that axis. This feature is a clear signature of a BEC. Another defining feature of a BEC is the appearance of the bimodal density distribution, consisting of a narrow Thomas-Fermi profile superimposed on the broader Bose-enhanced Gaussian background.

Absorption images of ultracold clouds are shown in Fig. 2.3. Cross-sectional density profiles taken along the horizontal and vertical directions illustrate the spatial structure of each cloud. Such images are central to experimental investigations of ultracold gases, and a discussion of atom detection techniques naturally follows, before proceeding to the experimental chapters.

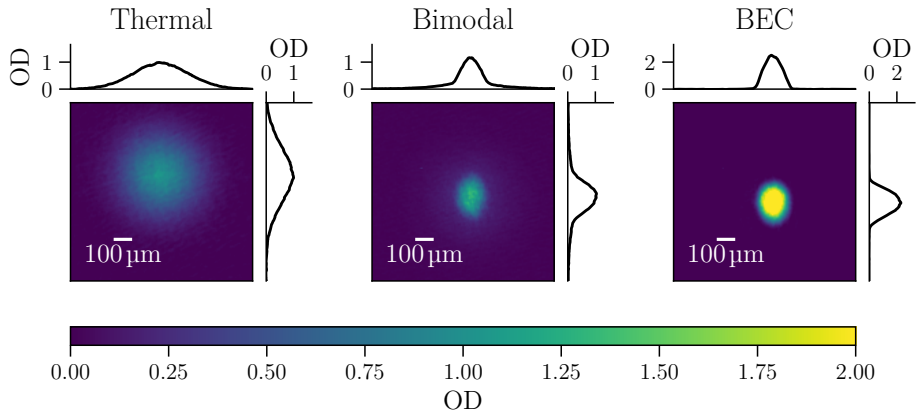

Figure 2.3: *Column densities extracted from absorption images providing cloud parameters such as atom number and temperature. These are obtained by fitting the density profiles with the corresponding models from Eqs.* (2.65) *to* (2.67)*. Three temperature regimes are displayed: a purely thermal cloud (left), a bimodal cloud (centre), and a pure BEC (right). Each image is supplied with cross-sectional optical densities averaged in a small window of* $\pm 20\,\mathrm{px}$ *around the cloud centre. The iconic time-of-flight feature of a BEC is evident from the fixed-range colourmap, which emphases the transition to a high-density, narrow central peak.*

2.4 Ultracold Atom Detection

Light-matter interactions were treated for single atoms in Section 2.1, and the single atom description was extended to gases in Section 2.3. This section will treat the description of light in high-density media, which is a central topic in this thesis work.

Detection schemes for ultracold atom experiments can typically be categorised in detection of light from fluorescence, absorption or phase-contrast imaging.

To extract thermodynamic quantities such as the temperature, atom number and condensed fraction, the technique of absorption imaging is the work horse of the field, and it has played a central role in the observation and characterisation of BEC. Extensive work in correcting absorption imaging for various effects was central for a number of previous theses [33–35] and this thesis will only briefly describe the technique, showcasing relevant theory without a thorough description. Absorption techniques rely on high intensity, resonant light, and the in-situ densities are typically too high to probe for accurate measurements. BECs typically have optical density on the order of 500 in-situ and the image is fully

saturated or blacked out, making it impossible to extract any meaningful column density from images. Hence, the method relies on the release of the cloud for a time of flight expansion to decrease the optical density. Besides the resonant interaction with high intensity, the cloud release is destructive, and experiments have to prepare new clouds for each atom image. Although optical densities in the order of 2 is achieved via time of flight, the expansion of a bimodal cloud is difficult to model. However, this thesis introduces another detection scheme relying on non-destructive spectroscopic methods, which can be used to probe clouds in-situ.

Previous detection schemes have been either far-detuned for phase contrasting or resonant for absorption imaging. This detection scheme fills the gap and scans the frequency over the full spectrum.

2.4.1 Complex Refractive Index

Consider a monochromatic, plane wave of angular frequency ω and wavenumber $k = \omega/c$ propagating along the $\hat{\boldsymbol{z}}$ direction in vacuum. The complex electric field can be written as,

$$E(t, x, y, z) = A(x, y, z)e^{i\phi(t,x,y,z)}, \tag{2.51}$$

where the phase is $\phi = (zk - \omega t)$, and A denotes the complex field amplitude. The dispersion of light propagating in a medium is conveniently described by the refractive index, n, and the phase change of the electric field is: $\mathrm{d}\phi = nk\mathrm{d}z - \omega\mathrm{d}t$. Moreover, the absorption caused by the medium decreases the field strength: $\mathrm{d}A = -\kappa A\mathrm{d}z$, where κ is an attenuation constant. This z-dependence, $e^{-\kappa \mathrm{d}z}$, can be moved to the phase in Eq. (2.51) by introducing the complex refractive index, $\tilde{n} = n + i\kappa$. Then,

$$\mathrm{d}\phi = \tilde{n}k\mathrm{d}z - \omega\mathrm{d}t. \tag{2.52}$$

The total dispersive phase shift of light propagating through a medium compared to vacuum is:

$$\Delta\phi(x, y) = k\int_{-\infty}^{\infty} (\tilde{n}(x, y, z) - 1)\,\mathrm{d}z, \tag{2.53}$$

where the spatial dependence enters through the density distribution of the medium. Knowing the spatial dependence of the complex refractive index, $\tilde{n}(x, y, z)$ for a small atomic cloud, achieves a model for how light propagates through the cloud. In a homogeneous medium consisting of two-level atoms, with resonance frequency ω_0 and FWHM linewidth Γ, the complex index of refraction is $\tilde{n} = \sqrt{1 + \chi}$, where the complex electric susceptibility obtained from the steady-state solution of the

optical Bloch equation is [36, eq. 6.3.28],

$$\chi = \frac{\rho\sigma_0}{k}\frac{-2\delta/\Gamma + i}{1 + (2\delta/\Gamma)^2 + I/I_{\text{sat}}}, \tag{2.54}$$

where δ is the detuning, $s_0 = I/I_{\text{sat}}$ is the saturation parameter, $\sigma_0 = 6\pi/k^2$ is the resonant-cross section and the atomic density is now denoted by ρ as n is already in use for the refractive index. The cloud is not a continuous medium, however, and Eq. (2.54) can be corrected for the discrete nature by treating each constituent particle as if they were in a spherical cavity carved out of a continuous polarised medium. This is the Lorentz-Lorenz model which captures local-field corrections and leads to:

$$\tilde{n} = \sqrt{1 + \frac{\chi}{1 - \chi/3}}. \tag{2.55}$$

It is common for experiments on ultracold gasses to work in the low density regime, $\frac{\sigma_0\rho}{k} \ll 1$, and the first order expansion of Eq. (2.55) leads to

$$\tilde{n} \approx 1 + \frac{1}{2}\chi. \tag{2.56}$$

Eq. (2.56) does not always hold for the high atomic densities present in our experiment, especially for atoms in-situ, but can typically be applied for time-of-flight images. For a quick calculation, suppose ρ is in units of atom numbers per optical wavelength cube, then $N \ll \frac{k\lambda^3}{\sigma_0} = 13$. Experimentally, our experiment can produce clouds of $N/\lambda^3 \sim 200$.

2.4.2 Absorption

In general, experiments measure the intensity, which is related to the electric field by the time-average over one period, $T = \frac{2\pi}{\omega}$:

$$I = \frac{c\varepsilon_0}{T}\int_0^T \text{Re}(E)^2 \text{d}t\,. \tag{2.57}$$

Suppose the light transmitted through a cloud has acquired a complex phase change, $\Delta\phi$, then, the transmitted intensity is:

$$\begin{aligned} I_{\text{out}} =& \frac{c\varepsilon_0}{T}|A|^2\int_0^T \text{Re}(e^{i(\Delta\phi-\omega t)})^2\text{d}t \\ =& \frac{2I_{\text{in}}}{T}\int_0^T e^{-2\,\text{Im}(\Delta\phi)}\cos^2(\text{Re}(\Delta\phi)-\omega t)\text{d}t\,. \end{aligned} \tag{2.58}$$

where $I_{\text{in}} = \frac{c\varepsilon_0}{2}|A|^2$ is obtained from Eq. (2.57). $\text{Im}(\Delta\phi)$ only depends on spatial coordinates, not time, and can be taken outside the integral. $\text{Re}(\Delta\phi)$ is time-independent and the integral of cosinus over one period, $\frac{1}{\tau}\int_0^\tau \cos^2(t)\mathrm{d}t = \frac{1}{2}$. This leads to:

$$I_{\text{out}} = I_{\text{in}} e^{-2\,\text{Im}(\Delta\phi)}. \tag{2.59}$$

which is the general expression for the absorption of light through the cloud.

2.4.3 Resonant Absorption in Dilute Clouds

Consider the low density regime, and suppose the light is tuned to resonance and propagating along $\hat{z}$ direction. Then Eq. (2.59) reads,

$$I(z) = I_{\text{in}} e^{-2\,\text{Im}(\Delta\phi(z))}. \tag{2.60}$$

Taking the imaginary part of Eq. (2.53) using Eq. (2.56):

$$2\,\text{Im}(\Delta\phi) = 2k\int_{-\infty}^{z} \text{Im}(\tilde{n})\mathrm{d}z \approx k\int_{-\infty}^{z} \text{Im}(\chi)\mathrm{d}z = \sigma_0 \int_{-\infty}^{z} \frac{\rho}{1+I/I_{\text{sat}}}\mathrm{d}z\,, \tag{2.61}$$

where the imaginary part of χ is attained from Eq. (2.54). Differentiating both sides of Eq. (2.60) with respect to z:

$$\frac{dI(z)}{dz} = I_{\text{in}} e^{-2\,\text{Im}(\Delta\phi(z))}\frac{d}{dz}(-2\,\text{Im}(\Delta\phi(z))) = -I(z)\frac{\sigma_0\rho}{1+I/I_{\text{sat}}}. \tag{2.62}$$

The differential equation can be solved by gathering all terms dependent on I on one side and integrating along the z-direction:

$$-\int_{I_{\text{in}}}^{I_{\text{out}}} \frac{1+I/I_{\text{sat}}}{I}\mathrm{d}I = \sigma_0 \int_{-\infty}^{\infty} \rho\mathrm{d}z\,. \tag{2.63}$$

The two integrals evaluate to,

$$\ln\left(\frac{I_{\text{in}}}{I_{\text{out}}}\right) + \frac{I_{\text{in}} - I_{\text{out}}}{I_{\text{sat}}} = \sigma_0\tilde{\rho}, \tag{2.64}$$

where $\tilde{\rho}$ is the column density of the atoms, and $\sigma_0\rho$ is known as the optical density, which is denoted by od. Eq. (2.64) is the famous Beer-Lambert's law modified for saturation effects for a resonant light field. In the limit $I \ll I_{\text{sat}}$ it reduces to a simple exponential decay, $I_{\text{out}} = I_{\text{in}}e^{-\text{od}}$. The column densities are calculated from the distributions described in Section 2.3, and for completion,

column-densities are noted for the most typical clouds in our experiments:

$$\tilde{\rho}_{\text{Bose-Enhanced}} = \frac{N_{\text{th}}}{2\pi w_{\text{x}} w_{\text{y}} g_3(\tilde{z})} g_2\left(\tilde{z} e^{-x^2/(2w_{\text{x}}^2) - y^2/(2w_{\text{y}}^2)}\right) \tag{2.65}$$

$$\tilde{\rho}_{\text{Gaussian}} = \frac{N_{\text{th}}}{2\pi w_{\text{x}} w_{\text{y}}} e^{-x^2/(2w_{\text{x}}^2) - y^2/(2w_{\text{y}}^2)} \tag{2.66}$$

$$\tilde{\rho}_{\text{Thomas-Fermi}} = \frac{5}{2\pi} \frac{N_0}{R_{\text{x}} R_{\text{y}}} \max\left(0, \left(1 - \frac{x^2}{R_{\text{x}}^2} - \frac{y^2}{R_{\text{y}}^2}\right)\right), \tag{2.67}$$

where the imaging direction is again taken along the $\hat{z}$ direction.

2.4.4 Absorption Imaging

Absorption imaging is a standard technique for inferring the density distribution of an ultracold atomic cloud. In this method, near-resonant light is shone onto the atoms, and the resulting shadow cast by the cloud is imaged onto a CCD camera. From the attenuation of the imaging light, the optical density of the cloud can be extracted, providing access to atom number, density profiles and temperature.

In our experiments, absorption imaging is performed using resonant light at intensities well above the saturation intensity. This approach give reliable absorption images for high optical densities on the order of 2 to 3, with the useful rule of thumb $I_{\text{in}} \sim \max(\text{od}) I_{\text{sat}}^{\text{eff}}$ [37]. The method is typically applied after a time-of-flight expansion, particularly for BECs where the in-situ optical density would otherwise be too large. Both the resonant light-matter interaction and the release of the cloud from the trap render this imaging method destructive.

To determine the od, four images are recorded: an image with atoms present I_{atom}, a reference image without atoms I_{beam} and corresponding background images $I_{\text{atom, bg}}$ and $I_{\text{beam, bg}}$, which account for camera offsets and stray light. The corrected intensities $I - I_{\text{bg}}$ are then combined using Eq. (2.64).

In practice, several experimental imperfections require a modification of Eq. (2.62). These include imperfect imaging polarisation, misalignment between the magnetic field and the imaging beam, and deviations from a closed two-level system due to the multilevel structure of the atom. To account for these effects, the resonant scattering cross-section and the saturation intensity are rescaled by a dimensionless correction factor, α^*, leading to the modified relation [37]:

$$\frac{dI}{dz} = -\rho \sigma_0^{\text{eff}} \frac{I}{1 + I/I_{\text{sat}}^{\text{eff}}}, \tag{2.68}$$

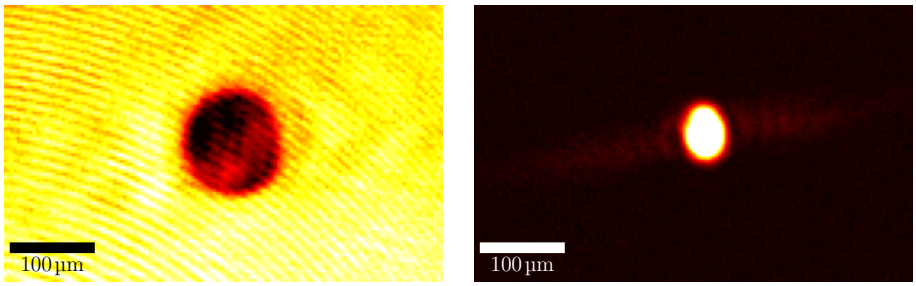

Figure 2.4: *Absorption images corresponding to the bright-field (left) and dark-ground (right) configurations. Notice the stripes on the dark-ground image, which is due to the finite size of the dark-ground target. The pattern resembles the Fourier transform of a rectangle.*

where $\sigma_0^{\text{eff}} = \sigma_0/\alpha^*$, and $I_{\text{sat}}^{\text{eff}} = \alpha^* I_{\text{sat}}$. The parameter α^* balances the logarithmic and linear terms in Eq. (2.64) such that the extracted optical density, which is an intrinsic property of the atomic cloud, remains independent of the probe intensity. A detailed calibration procedure is presented in previous work [1].

2.4.5 Bright-Field and Dark-Ground Configurations

The work presented in this thesis relies on two complementary detection schemes, known as the bright-field and dark-ground configuration. Both schemes will be described in this section.

Bright-field is conceptually the simplest of the two schemes, as it measures the transmitted probe light directly. It is also the most commonly used configuration for absorption imaging. Although absorption imaging is destructive, this is a consequence of the use of resonant light at high intensities, rather than an intrinsic property of the bright-field scheme itself. Bright-field can equally be operated in the far-detuned and low intensity regimes, both enabling conditions for nondestructive measurements. A non-exhaustive list of bright-field implementations includes: dual-port Faraday imaging [38], partial-transfer [39] and phase-contrast imaging [40]. The bright-field configuration has been used for probing collective dynamics such as the interference between two BECs [41] and sound propagation in BECs [42]. These types of measurements often rely on phase-contrast imaging at far-detuning to (1) reduce the absorption of light to a degree that the imaging is nondestructive, allowing for multiple images of the same BEC, and (2) to probe the high optical thickness of a BEC in-situ. The detuning can be hundreds of atomic linewidths, and hence lensing effects due to the index of refraction of the

cloud are typically negligible.

Both absorptive and dispersive techniques can be implemented in a dark-ground configuration, in which unscattered light is suppresses and only light deviating from the incoming probe field mode is detected. By removing the background signal associated with the incident probe beam, dark-ground detection enhances sensitivity to small perturbations of the optical field and can significantly improve the signal-to-noise ratio. This approach was successfully employed for absorption images of ^{23}Na atoms in the early days of BEC physics [43], and has since been used for absorption imaging from ~ 30 atoms [44] to high optical densities on the order of 350 [45]. In the dispersive regime, dark-ground Faraday imaging has been used to estimate atom numbers in-situ during experiments, enabling adaptive evaporation protocols aimed at atom number stabilisation [46].

Our implementation of the dark-ground configurations is conceptually simple and closely related to the used in phase-contrast imaging [41]. Scattered light is separated from the incident probe in the Fourier plane of the imaging system, where the incident beam is tightly focused onto a small opaque object, referred to as the dark-ground target [43, 45, 47]. Replacing this obstacle with a phase retarder, arranged such that only the transmitted probe passes through it, yields a phase-contrast imaging configuration [41, 42]. When combined with a single-photon detector module, the dark-ground configuration enables measurements with a weak probe intensity, allowing for nondestructive in-situ probing of ultracold atomic clouds. This approach permits real-time measurements on a single atomic sample, facilitating the investigation of cloud dynamics and spectroscopic properties.

Figure 2.5 illustrates the distinction between bright- and dark-ground configurations using a simplified optical setup. In both cases, a large waist, collimated, probe beam (red) illuminates an atomic cloud (black dot), and the diffracted field (blue) rapidly diverges due to the small size of the cloud. A lens placed one focal length away tightly focuses the probe beam and collimates the diffracted field. In the bright-field configuration (top), both the probe and diffracted fields are detected. The probe beam provides a bright background, and the presence of the atoms is observed through destructive interference between the two fields, resulting in the shadow of the cloud. The optical density is thus measured on a bright background. In the dark-ground configuration (bottom), an obstacle placed at the focal point of the probe beam blocks the unscattered light. As a result, only the diffracted field reaches the detector, and the atomic signal appears as a positive signal on a zero background.

Representative absorption images for both configurations are shown on Fig. 2.4. Notice the sinc-like side lobes extending horizontally in the dark-ground image. These features resemble the Fourier transform of a rectangular aperture, and originate from the finite size and shape of the dark-ground obstacle, which in this case is a vertically oriented stripped wire. Because the obstacle is extended rather than point-like, its sharp edges introduce diffraction. In contrast, an ideal point-like stop that blocks only the plane-wave mode would produce a uniformly dark background. In early iterations of the experiment, Allan keys with widths ranging from 500 µm to 1200 µm were used; the current implementation employs a 200 µm wide piece of stripped wire. To approximate a point-like target, we tested slabs of glass with painted circular marks, but these were never optically dense enough to fully block the probe light. Another possible approach would be to drill a hole in a glass slab and insert the wire longitudinally, thereby eliminating the rectangular aperture.

2.4.6 Spectra of High-Density Clouds

This section presents theory used for the low intensity probing of high-density clouds, and hence $I \ll I_{\mathrm{sat}}$ is assumed.

Normalised Transmission

For experiments with the single-photon detector, a small pinhole is positioned at an intermediate image plane to filter out background light around the atom cloud. In addition to improving the signal-to-noise ratio, this configuration enables experiments such as live-time measurements of trap frequencies: by moving the pinhole to the edge of the cloud, any motion of the cloud in and out of the pinhole region produces amplitude modulation in the detected signal. The power transmitted through the pinhole in the absence of atoms is $P_{\mathrm{in}} = I_{\mathrm{in}} A_{\mathrm{pinhole}}$, where the effective pinhole area A_{pinhole} accounts for the magnification of the optical setup. In the presence of atoms, the transmitted power is $P = \int_{\mathrm{pinhole}} I \mathrm{d}A$. The normalised transmission, $\mathcal{T} = P/P_{\mathrm{in}}$ plays a central role in the analysis.

Bright-Field Detection

The transmitted light is imaged directly onto a camera or a detector, and the signal is given by Eq. (2.59). The normalised transmission is:

$$\mathcal{T} = \frac{1}{A} \int_{\mathrm{pinhole}} e^{-2\,\mathrm{Im}(\Delta\phi)} \mathrm{d}A\,. \tag{2.69}$$

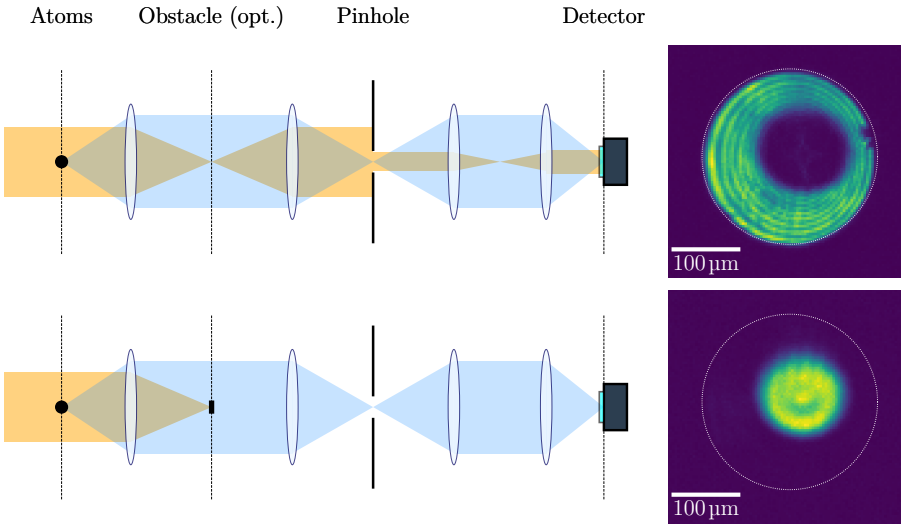

Figure 2.5: *Comparison of the bright- and dark-ground configuration. A large waist probe field, E_{in} (orange) illuminates an atomic cloud and the diffracted field E_{diff} (blue) expands rapidly due to the small size of the cloud. A lens positioned a focal length from the atoms, collimates E_{diff} and strongly focuses E_{in}. (Top) the two fields are superimposed onto a CCD camera, and the destructive interference in the overlap results in a dark shadow of the cloud. (Bottom) a dark-ground obstacle is positioned at the focus, and acts as a spatial filter for E_{in}. Only E_{diff} is transmitted, and the intensity is measured as a bright spot on a zero signal background. Corresponding absorption images of a bimodal cloud are supplied. The imaging setup uses a 75 µm diameter pinhole in an intermediate image plane to spatially filter light outside the cloud region (see Fig. 3.10).*

In the following, the normalised- detuning $\tilde{\delta} = \delta/\Gamma$ and intensity $\tilde{I} = I/I_{\text{sat}}$ is used.

Simulated bright-field signals for thermal clouds with varying atom numbers and temperatures are shown in Fig. 2.6. The top panels display the intensity distribution calculated from Eq. (2.60), evaluated through a pinhole with an effective radius of 75 µm immediately after the atoms. The bottom panels show the corresponding normalised transmission. In the left column, the atom number is varied at a fixed temperature $T = 5\,\mu\text{K}$, while in the right column a fixed atom number of $N = 2 \times 10^6$ is used. For all simulations, the trap frequencies are set to $2\pi \times 100\,\text{Hz}$.

For a thermal cloud at a fixed temperature, and with the probe field tuned on resonance, the centre of the cloud quickly becomes opaque as the atom number

increases. In the extreme case of 2×10^6 atoms, the entire pinhole area is pitch black. At an intermediate detuning, $\tilde{\delta} = -2$, the normalised transmission decreases with increasing atom number in a non-linear fashion. In the far-detuned regime, even the high-density region of the cloud cannot block all of the incoming light, and the absorption approaches a linear response with atom number. In this limit, the exponential in Eq. (2.69) behaves linearly, so that the exponent is much less than 1 everywhere.

For an in-trap thermal cloud, the density allows the approximation given in Eq. (2.56). Similarly to Eq. (2.61), but keeping the density term and neglecting the $\tilde{I}$ for this case, we have

$$2\,\mathrm{Im}\,(\Delta\phi) = \sigma_0 \int_{-\infty}^{z} \frac{\rho}{1+4\tilde{\delta}^2}\mathrm{d}z\,. \tag{2.70}$$

Consequently, the output intensity is,

$$I_{\mathrm{out}} \approx I_{\mathrm{in}}\left(1-\sigma_0\int_{-\infty}^{\infty}\frac{\rho}{1+4\tilde{\delta}^2}\mathrm{d}z\right) = I_{\mathrm{in}}\left(1-\frac{\sigma_0\tilde{\rho}}{1+4\tilde{\delta}^2}\right), \tag{2.71}$$

and the normalised transmission becomes,

$$\begin{aligned} T =& \frac{1}{P_{\mathrm{in}}}\int_{\mathrm{pinhole}} I_{\mathrm{in}}\left(1-\frac{\sigma_0\tilde{\rho}}{1+4\tilde{\delta}^2}\right)\mathrm{d}A = \frac{1}{P_{\mathrm{in}}}\left(P_{\mathrm{in}}-\frac{I_{\mathrm{in}}\sigma_0 N}{1+4\tilde{\delta}^2}\right) \\ =& 1-\left(\frac{I_{\mathrm{in}}N}{P_{\mathrm{in}}}\right)\sigma(\tilde{\delta}), \end{aligned} \tag{2.72}$$

where $\sigma(\tilde{\delta}) = \sigma_0/(1+4\tilde{\delta}^2)$. In the dilute regime, the total probability for a photon to be absorbed by the cloud is simply the single-atom absorption probability, $I_{\mathrm{in}}\sigma(\tilde{\delta})/P_{\mathrm{in}}$, multiplied by the total number of atoms. Consequently, for a cloud fully contained within the pinhole, and with the same number of atoms (right column of Fig. 2.6), all spectra converge in the far-detuned limit.

Around resonance, the spectra are highly sensitive to temperature, because the cross-sectional area of the thermal cloud changes relative to the pinhole area. They are also sensitive to the atom number. However, at far detuning, the spectra depend primarily on atom number. Therefore, fitting the full spectrum allows independent determination of both atom number and temperature.

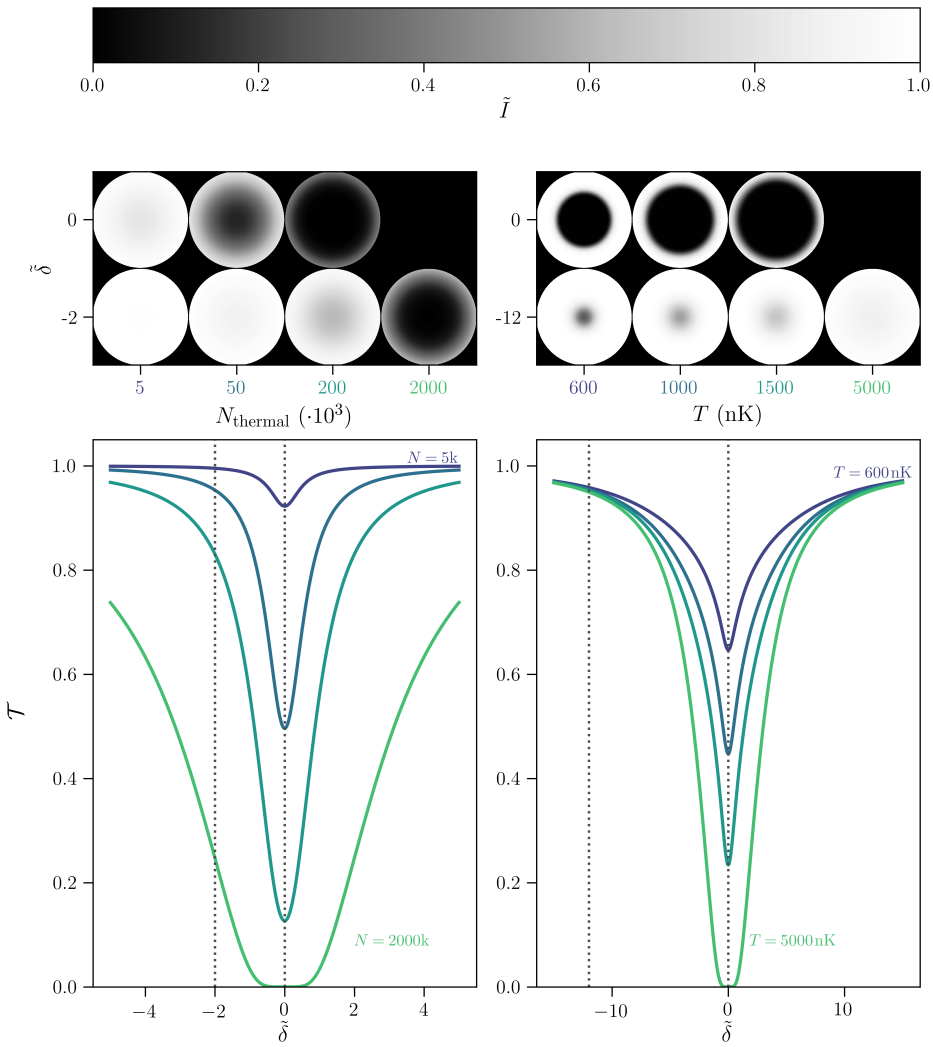

Figure 2.6: *Bright-field signal for thermal clouds of variable atom numbers (left) and temperature (right). (Top) Spatial distribution of output intensity over the pinhole area for variable rescaled detunings $\tilde{\delta} = \delta/\Gamma$ corresponding to dotted lines in the spectra. (Bottom) Normalised transmission spectra corresponding to the upper signals. The pinhole right after the cloud has an effective radius of 75 µm, and the thermal cloud parameters are (left) $T = 5$ µK and (right) $N = 2 \times 10^6$. An increase in parameter value is indicated by a darker green. Figure modified from [48]*

Simulated bright-field signals for bimodal clouds are calculated using the chemical potential and the temperature as degrees of freedom. The chemical potential determines the BEC atom number via the Thomas-Fermi approximation, while the temperature, together with the chemical potential, determines the number of thermal atoms. For these simulations, the effective in-trap pinhole radius is set to 25 µm. The simulations include pure BECs of varying atom numbers (left column) and bimodal clouds with a fixed BEC atom number, $N_0 = 5 \times 10^4$, and varying condensed fraction (right column).

In contrast to thermal clouds, pure BECs increase in size with atom number, according to Eq. (2.43). On resonance, the in-situ od of the BEC is on the order of 100, saturating the signal even for the smallest cloud ($N_0 = 5 \times 10^3$). This is observed in the spectrum as a broadening, with the clouds still clearly visible at $\tilde{\delta} = -10$. However, because the BEC is smaller compared to the pinhole area, the transmission drops only by $\sim 10\,\%$.

In the right column, $N_0 = 5 \times 10^4$ is fixed, and the condensed fraction varies from 100 % to 50 %. At $\tilde{\delta} = -2$ the BEC remains unchanged, but absorption from the thermal component decreases significantly. This produces a bimodal spectrum, where the great od of the BEC gives rise to a wide feature centred on the narrow thermal absorption. Interestingly, this is opposite to the spatial bimodal distribution observed in time-of-flight absorption images, where the BEC appears as a narrow central peak surrounded by a broad thermal tail. In the spectrum, the BEC appears shallow due to its small spatial extent relative to the pinhole, whereas the larger thermal cloud absorbs more light near resonance. However, the thermal component quickly becomes transparent at small detunings compared to the BEC. From the bimodal spectrum, it is possible to fit all relevant cloud parameters in-trap. This approach also simplifies compensation for low optical resolution, as only the total transmitted power needs to be adjusted. Perhaps the greatest benefit is the enhanced sensitivity to thermal atom numbers at high BEC fractions. Standard time-of-flight absorption images struggle to separate the two components at $N_0/N \sim 70\,\%$, as the thermal tail becomes small. By contrast, the spectrum remains highly sensitive to thermal atoms even for $N_0/N \sim 90\,\%$. Furthermore, the method is in-situ and can be performed nondestructively.

Ironically, the approach has a low sensitivity to the BEC component. This can be improved by employing a dark-ground configuration. Chapter 4 investigates the implementation of the dark-ground imaging configuration, and compare it with time-of-flight absorption images.

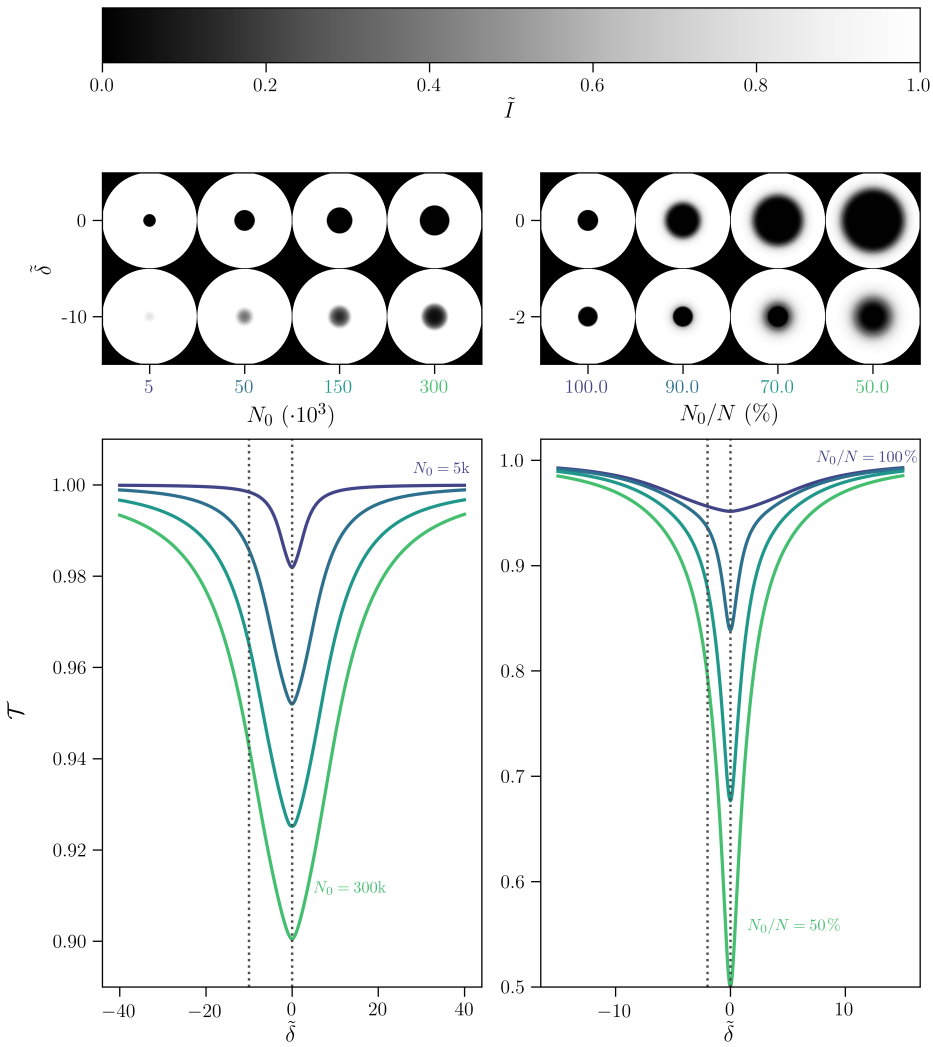

Figure 2.7: *Bright-field signal for pure BECs (left) and bimodal clouds of variable BEC fractions but fixed BEC atom numbers, $N_0 = 50k$ (right). (Top) The output light field intensity over the pinhole area for variable rescaled detunings $\tilde{\delta} = \delta/\Gamma$ corresponding to dotted lines in the spectra. (Bottom) Normalised transmission spectra corresponding to the upper signals. The pinhole right after the cloud has an effective radius of* 25 µm. *Increase in N_0 (left) and condensed fraction (right) is indicated by a darker green. Figure modified from [48]*

Dark-Ground Detection

The formula for dark-ground signals are presented in [47, 49] and the derivation is summarised here.

Consider an incoming linearly polarised probe field, interacting with atoms modelled as two-level systems. Let the probe field before the atoms be E_{in}, and immediately after the cloud it is E_{out}. Then,

$$E_{\text{out}} = E_{\text{in}} + E_{\text{diff}}, \tag{2.73}$$

where E_{diff} is the diffraction field emitted by the atoms. This is the correct description, since Maxwell's equations only contain source terms and no absorption terms. Absorption occurs because the atomic dipoles, driven by the incoming light, re-emit light out of phase with the incident field. In bright-field imaging, the shadow of the cloud arises from this interference of electric fields. In the dark-ground configuration, the unscattered probe E_{in} is filtered out, so only the diffraction field $E_{\text{diff}} = E_{\text{out}} - E_{\text{in}}$ is detected. The time-averaged intensity is then,

$$I_{\text{diff}} = I_{\text{in}} \left| e^{i\Delta\phi} - 1 \right|^2, \tag{2.74}$$

where I_{in} is the time-averaged intensity of E_{in}. Splitting $\Delta\phi = \text{Re}(\Delta\phi) + i\,\text{Im}(\Delta\phi)$ gives,

$$\begin{aligned} I_{\text{diff}} =& I_{\text{in}} \left| \left(e^{-\,\text{Im}(\Delta\phi)} \left[\cos\left(\text{Re}(\Delta\phi)\right) + i \sin\left(\text{Re}(\Delta\phi)\right) \right] \right) - 1 \right|^2 \\ =& I_{\text{in}} \left[\left(-1 + e^{-\,\text{Im}(\Delta\phi)} \cos\left(\text{Re}(\Delta\phi)\right) \right)^2 + e^{-2\,\text{Im}(\Delta\phi)} \sin^2\left(\text{Re}(\Delta\phi)\right) \right] \\ =& I_{\text{in}} \left[1 + T - 2\sqrt{T} \cos\left(\text{Re}(\Delta\phi)\right) \right], \end{aligned} \tag{2.75}$$

where $T = e^{-2\,\text{Im}(\Delta\phi)}$ is the standard transmission from Eq. (2.60). The normalised transmission through the pinhole is:

$$\mathcal{T}_{\text{diff}} = \frac{1}{A} \int_{\text{pinhole}} \left(1 + T - 2\sqrt{T} \cos\left(\text{Re}(\Delta\phi)\right) \right) \mathrm{d}A\,. \tag{2.76}$$

Note the limiting cases of Eq. (2.76). In the absence of atoms, $T = 1$ and $\Delta\phi = 0$, so the normalised transmission for bright-field signal is one and for dark-ground it is zero. Oppositely, in the strongly absorbing regime, the bright-field goes to zero and the dark-ground approaches one. Thus, bright-field and dark-ground signals are complementary and inversely related, though not linearly. Importantly, for small $\mathcal{T}_{\text{diff}}$, the dark-ground configuration significantly improves the signal-to-noise ratio compared to the bright-field configuration.

An important limiting case is the far-detuned region where $|\chi| \ll 1$ and $|\Delta\phi| \ll 1$, then from Eqs. (2.54) and (2.56):

$$\chi \approx \frac{\rho\sigma_0}{k}\left(-\frac{1}{2\tilde{\delta}} + i\frac{1}{4\tilde{\delta}^2}\right) \tag{2.77}$$

$$\tilde{n} \approx 1 + \frac{1}{2}\chi. \tag{2.78}$$

From Eq. (2.53), this leads to a complex phase change of,

$$\Delta\phi \approx k\int_{-\infty}^{\infty}\frac{\chi}{2}\mathrm{d}z = \int_{-\infty}^{\infty}\sigma_0\rho\left(\frac{-1}{4\tilde{\delta}} + i\frac{1}{8\tilde{\delta}^2}\right)\mathrm{d}z = \mathrm{od}\left(-\frac{1}{4\tilde{\delta}} + i\frac{1}{8\tilde{\delta}^2}\right). \tag{2.79}$$

The standard transmission is then given from Eq. (2.59),

$$T = e^{-2\,\mathrm{Im}(\Delta\phi)} \approx 1 - \frac{\mathrm{od}}{4\tilde{\delta}^2}. \tag{2.80}$$

Using the binomial series for the square root, $\sqrt{T} \approx 1 - \mathrm{od}/(8\tilde{\delta}^2)$, and expanding the cosinus in Eq. (2.76):

$$\cos\left(\mathrm{Re}\left(\Delta\phi\right)\right) \approx 1 - \frac{1}{2}\,\mathrm{Re}\left(\Delta\phi\right)^2 \approx 1 - \frac{\mathrm{od}^2}{32\tilde{\delta}^2}, \tag{2.81}$$

which leads to the normalised transmission:

$$\begin{aligned}\mathcal{T}_{\mathrm{diff}} \approx& \frac{1}{A}\int_{\mathrm{pinhole}}\left(1 + \left(1 - \frac{\mathrm{od}}{4\tilde{\delta}^2}\right) - 2\left(1 - \frac{\mathrm{od}}{8\tilde{\delta}^2}\right)\left(1 - \frac{\mathrm{od}^2}{32\tilde{\delta}^2}\right)\right)\\ \approx& \frac{1}{A}\frac{1}{16\tilde{\delta}^2}\int_{\mathrm{pinhole}}\mathrm{od}^2\mathrm{d}A\,.\end{aligned} \tag{2.82}$$

In the far-detuned limit, expanding T, $\sqrt{T}$ and $\cos\left(\mathrm{Re}\left(\Delta\phi\right)\right)$ to lowest order shows that all absorption-related terms cancel, leaving the contribution proportional to $\mathrm{Re}\left(\Delta\phi\right)^2$, and hence od^2. By increasing od, greater detuning will be available for even less absorption, and hence minimal destructivity. In practice, this can be done by lowering the trap frequency along the light propagation, to achieve an elongated, cigar-shaped cloud geometry. This approach is limited by the requirement of keeping a condensed cloud.

The focus now turns to the more complex behaviour observed closer to resonance. When the phase shift exceeds π in parts of the cloud, the dark-ground signal begins to decrease again. In principle, as the phase shift increases further, the signal can alternate repeatedly between low and high values, giving rise to ring-like structures in the dark-ground intensity profile. This is visible on Figs. 2.8 and 2.9.

Simulated dark-ground signals for thermal clouds with varying atom numbers and temperatures are shown in Fig. 2.8. The top panels display the intensity distribution calculated using Eq. (2.75), evaluated through a pinhole with an effective radius of 75 µm at the position of the atom. Note that the colour scale is extended relative to the greyscale by adding a green upper range with a maximum value of 4, which according to Eq. (2.76) corresponds to $T = 1$ and $\mathrm{Re}\,(\Delta\phi) = \pi$. The bottom panels show the corresponding normalised transmission. In the left column, the atom number is varied at a fixed temperature of $T = 5\,\mu\mathrm{K}$, while in the right column, the atom number is fixed at $N = 500\mathrm{k}$. Focusing on the top-left panel, at resonance the diffracted signal increases as more atoms are introduced and eventually begins to saturate at the centre. For each atom number column, increasing the detuning generally leads to a reduced signal, except for the largest cloud, where the spectrum exhibits a slightly enhanced signal at $\tilde{\delta} = -1$. This enhancement is accompanied by the appearance of an interference ring in the intensity profile. However, $\tilde{\delta} = -1$ is not sufficiently large to significantly suppress absorption, and the maximum intensity never reaches the upper limit of 4. The od is not large enough to induce more than a single π phase shift, resulting in only one shoulder on either side of the resonance. At larger detunings, the signal diminishes for all clouds. In the top-right panel, increasing the temperature causes the cloud to expand spatially, leading to an increased on-resonance signal. Some of the clouds have larger od and therefore the signal undergo more than one full phase rotation, which is reflected in the appearance of additional shoulders in the spectrum. Each time a new ring of high intensity occur, the total power increases. This effect is most pronounced for the coldest clouds, which have the highest od. Interestingly, colder clouds are broader and exhibit a larger signal at large detunings due to their higher od. In contrast, hotter clouds show the highest signal near resonance, but quickly diminish as the detuning increases.

Simulated dark-ground signals for bimodal clouds are calculated using an effective in-trap pinhole radius of 25 µm. The BEC component has a particularly strong effect due to its large od, resulting in broader spectra with signals extending well beyond $\tilde{\delta} = 100$. The intensity profiles reveals detailed ring structures, corresponding to shoulder-like features in the spectrum. Similar to the bright-field signal, the thermal component produces a narrow, near-resonance peak in the spectrum. However, the spectral distinction between thermal and BEC components is more pronounced in dark-ground due to the phase shift. The zero background enables higher sensitivity to the weaker BEC component compared to the bright-field.

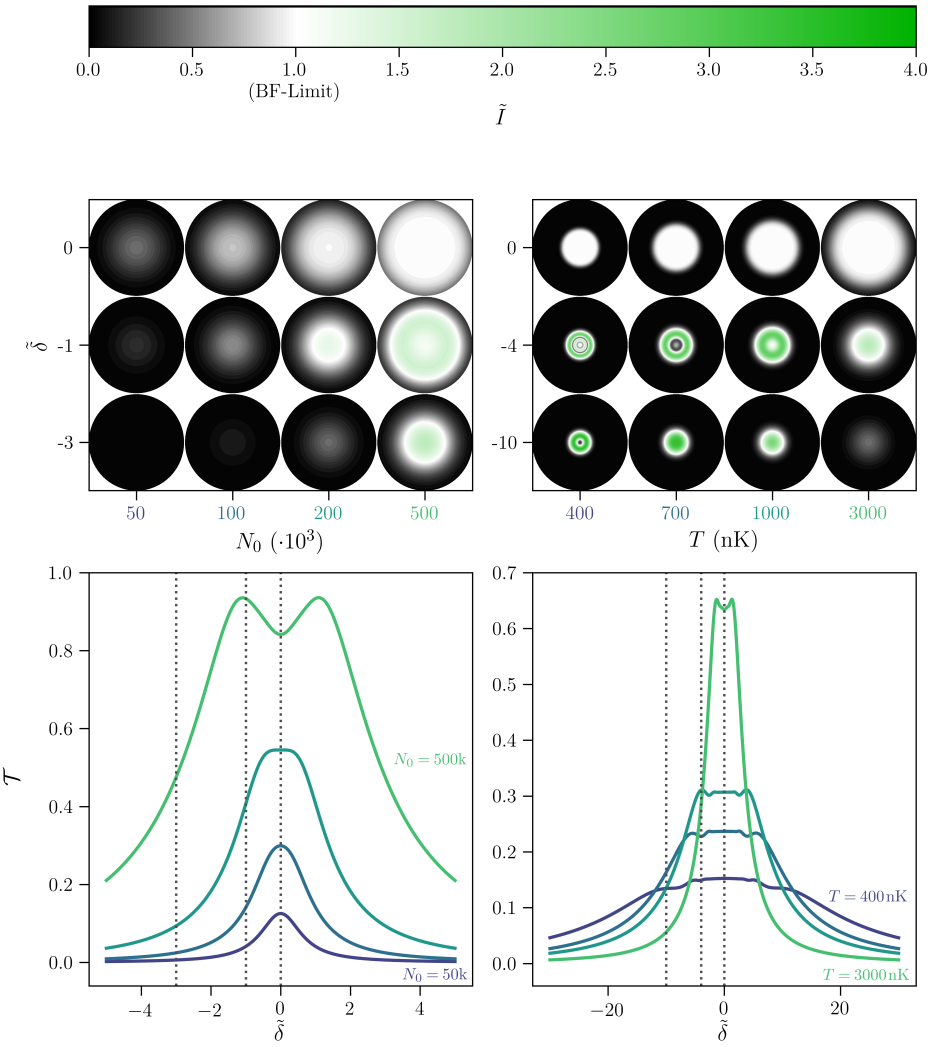

Figure 2.8: *Dark-ground signals for thermal clouds of variable atom numbers (left) and temperature (right). Top panels show the spatial distribution of the light field intensity for variable rescaled detuning, $\tilde{\delta} = \delta/\Gamma$, corresponding to dotted lines in the spectra. Bottom panels show the normalised transmission spectra corresponding to the upper signals. The pinhole right after the cloud has an effective radius of* 75 µm*, and the thermal cloud parameters are (left)* $T = 5\,\mu\mathrm{K}$ *and (right)* $N = 500k$*. Increase in parameter values are indicated from black to green and dashed lines in the spectra indicate the evaluated detunings. Figure from [48]*

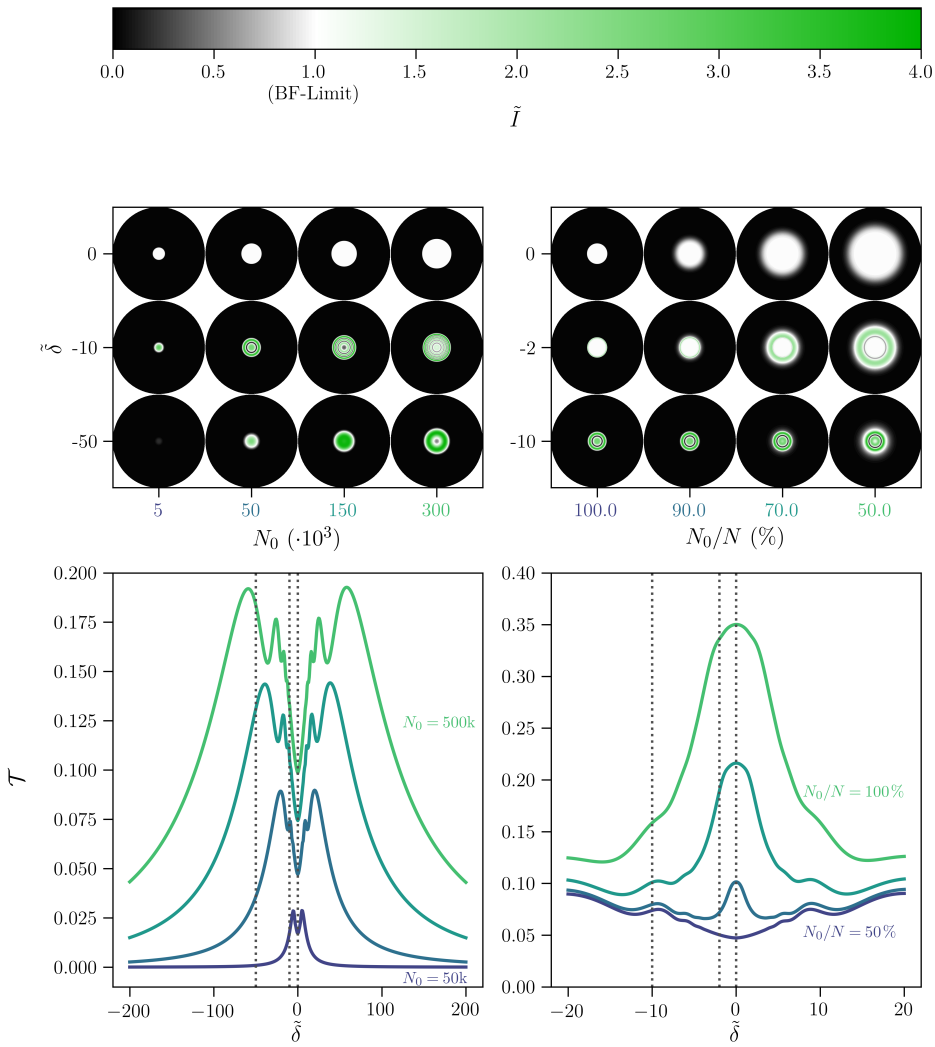

Figure 2.9: *Dark-ground signals for pure BECs (left) and bimodal clouds of variable condensation fractions but fixed BEC atom numbers, $N_0 = 500k$ (right). Top panels show the spatial distribution of the light field intensity for variable rescaled detuning, $\tilde{\delta} = \delta/\Gamma$. Bottom panels show the normalised transmission spectra corresponding to the upper signals. The pinhole right after the cloud has an effective radius of 75 µm. Increase in BEC atom numbers (left) and decrease in BEC fraction (right) is indicated from black to green, and dashed lines in the spectra indicate the evaluated detunings. Figure from [48]*

2.5 Simulation of Experiments

This section introduces the density-matrix simulations used to model the two types of experiments described in subsequent chapters. Despite operating in different physical regimes, both experiments share fundamental grounds in theory from Sections 2.1 and 2.2. They exhibit a high level of complexity arising from their large Hilbert spaces and use of multiple optical fields of variable frequencies, intensities, polarisations and wavevectors.

The first experiment, conducted at Aarhus University, investigates spectroscopies and time-resolved dynamics in ultracold ^{87}Rb. Figure 2.10 displays the D2 spectral line, comprising 24 hyperfine sublevels, which serves as the basis for these studies. Typically, two optical fields with nearly identical wavelengths are applied to connect the two hyperfine ground states through shared excited states in multiple λ-schemes. In some configurations, each transition is uniquely addressed by a single field. However, for detunings comparable to the ground state splitting, particularly relevant for two-photon Raman-Rabi measurements, both optical fields can address each transition. This results in cross-couplings within the interaction Hamiltonian and introduces additional decoherence channels.

The second experiment, conducted at Otago University, employs a Rydberg-atom-based EIT sensing scheme to characterise external MW fields using thermal vapour cells. Figure 2.15 displays the system, comprising 53 quantum states spanning low-lying levels and highly excited Rydberg states. Three fields with widely separated wavelengths connect the system, and each transition pair can be associated with a unique driving field. While this simplifies the connectivity, the Hilbert space is approximately twice as large as that of the D2 system, and the increased number of driving fields significantly enlarges the parameter space as well.

This section is structured as follows. Section 2.5.1 presents a few adjustments to Section 2.1, specifically useful for numerical simulations. Then, Section 2.2 is extended for calculating overlap integrals between low-lying states. This is the groundwork for Section 2.5.2, where the level structure for the D2 line is displayed with typical connectivity, concluding with a density simulation of a two-photon Raman-Rabi experiment. Then, theory for the Rydberg-atom-based experiments is presented in Section 2.5.3, outlining the level structure and connectivities for the full-level system. Finally, density simulations of experiments are presented.

2.5.1 Theoretical Framework

Dipole Operators

The dipole operator was described in Section 2.2.3, but for computational convenience, the Rabi frequencies are factored into a scalar radial component, Ω_{k}^{r}, and an angular component expanded over the spherical basis [14]:

$$\Omega_{\mathrm{k}} = \Omega_{\mathrm{k}}^{r} \sum_{q\in\{0,\pm1\}} A_{\mathrm{k}}^{(q)} u_{\mathrm{k}}^{(q)}. \tag{2.83}$$

The A_{k}^{q} are equivalent to the $\hat{\pi}, \hat{\sigma}^{\pm}$ introduced in Eq. (2.20), where the q index represent the change in angular momentum associated with the transition:

$$A^{(0)} = \hat{E}_{\mathrm{z}} \tag{2.84}$$

$$A^{(\pm1)} = \mp\frac{1}{\sqrt{2}}\left(\hat{E}_{\mathrm{x}} \pm i\hat{E}_{\mathrm{y}}\right). \tag{2.85}$$

The elements of each matrix u_{k}^{q} are found by repeated applications of the Wigner-Eckart theorem, where Ω_{k}^{q} absorbs the reduced matrix element:

$$\begin{aligned}\langle SLJFm_{\mathrm{F}}|u_{\mathrm{k}}^{(q)}|SL'J'F'm_{\mathrm{F}'}\rangle =& (-1)^{1+L'+S+J+J'+I-m_{\mathrm{F}'}} \\ &\times\sqrt{(2J+1)(2J'+1)(2F+1)(2F'+1)} \\ &\times\begin{Bmatrix} L' & J' & S \\ J & L & 1 \end{Bmatrix}\begin{Bmatrix} J' & F' & I \\ F & J & 1 \end{Bmatrix}\begin{pmatrix} F & 1 & F' \\ m_{\mathrm{F}} & q & -m_{\mathrm{F}'} \end{pmatrix}.\end{aligned} \tag{2.86}$$

This allows for calculating the angular components for each transition once, and caching the results for a faster implementation. The radial components are multiplicative factors that can be independently varied over a range of values.

Decay Operators

Decays are categorised into coherent and incoherent decays, where the incoherent operators are simply modelled by a single jump operator for each state pair. For the coherent decays each operator is linked to a photon and not a state pair. Photons have a polarisation and momentum, but the experiments traces out the spatial degrees of freedom and only the frequency and polarisation of the photon is considered. For instance, consider the ladder system in Fig. 2.15, and suppose a σ^{+} photon at $\lambda = 780\,\mathrm{nm}$ is observed. From the observed wavelength the transition is identified to be between the $|i\rangle \to |g\rangle$ manifolds and knowing the polarisation of the photon restricts the atomic transition to $\Delta m_{\mathrm{F}} = -1$. But the specific m_{F}

states are degenerate, and the atom can be modelled to have coherently decayed via all these paths simultaneously. Thus, a photon emission corresponds to a jump operator which represents all the possible paths for $\Delta m_{\mathrm{F}} = -1$ simultaneously. A decay path between two states is described by the collapse operator $L_{\mathrm{k}}^{(q)}$, for each q with elements calculated by [14],

$$\begin{aligned}\langle SLJFm_{\mathrm{F}}|L_{\mathrm{k}}^{(q)}|SL'J'F'm_{\mathrm{F}'}\rangle =&(2L+1) \\ &\times(2J+1)(2J'+1)(2F+1)(2F'+1) \\ &\times\begin{Bmatrix} L' & J' & S \\ J & L & 1 \end{Bmatrix}^2 \begin{Bmatrix} J' & F' & I \\ F & J & 1 \end{Bmatrix}^2 \begin{pmatrix} F & 1 & F' \\ m_{\mathrm{F}} & q & -m_{\mathrm{F}'} \end{pmatrix}^2,\end{aligned} \tag{2.87}$$

which is proportional to the square of Eq. (2.86). Summing over all q and possible jumps from an initial state is normalised to one. The total decay rate γ_{k} in Eqs. (2.10) and (2.12) is shared for all q and sets the radiative lifetime for each initial state.

2.5.2 Dynamics in the D2 Line

In Section 2.2.1, the quantum defect theory and model-potential gave a systematic method to calculate fair approximations to the Rydberg wave functions. However, the quantum defect theory is not designed to reconstruct low-lying wave functions accurately. Moreover, the model-potentials are approximations that build on experimental data, which is less accurate for the low-lying states. Hence, the low-lying states in the spectral D2 line of ^{87}Rb are not expected to be well captured by the model-potentials.

Instead, to calculate dipole transition matrix elements, the well-known linewidth is used, as it relates to the radial overlap integral [50]:

$$\Gamma = \frac{\omega_0^3}{3\pi\varepsilon_0\hbar c^3}\frac{2J+1}{2J'+1}|\langle J||e\boldsymbol{r}||J'\rangle|^2. \tag{2.88}$$

The overlap integral obtained from the quantum defect theory in combination with the model-potentials gives 6.37 a.u. whereas the result from using Eq. (2.88) is 5.17 a.u. With respect to the qualitative behaviour, both values can be used, as the overlap integral plays the role of an overall multiplicative factor. Since the results from simulations can be the starting point for an experiment, the simulations of the D2 spectral line uses Eq. (2.88) for more accurate quantitative results. Figure 2.10 gives an example of the connectivity for an experiment on the D2 spectral line for ^{87}Rb.

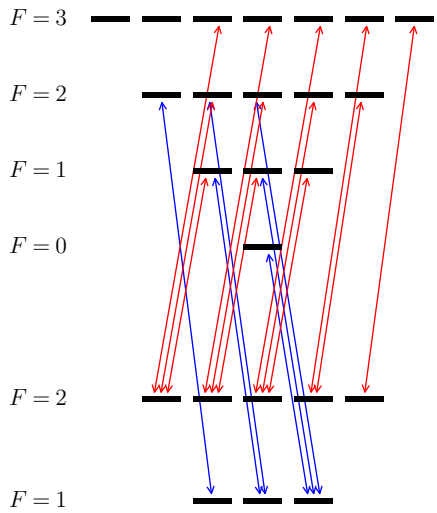

Figure 2.10: *The entire D2 spectral line of* ^{87}Rb *with coherently driven transitions shown. The interaction Hamiltonian takes into account the coupling of each optical field to all ground states, which is not shown on the diagram, although it is relevant for experiments with detunings comparable to the hyperfine ground state splitting. This figure illustrates a co-linearly propagating probe/coupling configuration with opposing, circularly polarisations, which resembles the two-photon Raman-Rabi experiments. However, among detuning, power and beam waists, also the polarisations and wavevectors are variable in the simulation framework.*

Raman-Rabi Oscillations

The developed simulation framework enables the modelling of arbitrary single-atom experiments on the D2 spectral line. These range from the basic transitions relevant for magneto-optical trapping (MOT), optical pumping, and imaging to more advanced configurations involving multiple optical fields, such as EIT, coherent population transfer, and two-photon Raman-Rabi processes.

The simulations are particularly valuable for revealing subtle effects that emerge when a multi-level system is subjected to combinations of light fields. In particular, they allow for the calculation of light-induced shifts that can be difficult to calculate due to the complex connectivity. Moreover, simulations account for multi-level interference effects that are absent in simpler, isolated systems. Although density-dependent interactions are not included in the framework, it nevertheless provides a useful reference for identifying deviations from the ideal single-atom description.

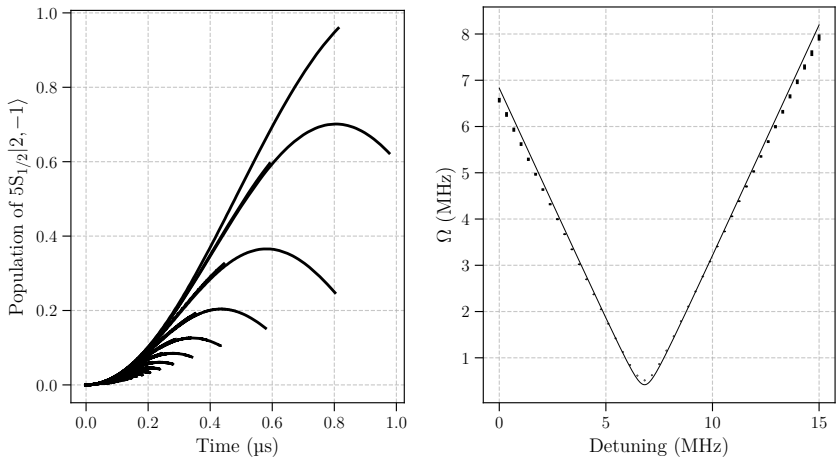

Figure 2.11: *Simulated two-photon Raman-Rabi transitions between the ground state manifolds of* ^{87}Rb. *The atom is initially prepared in the* $|1,1\rangle$ *state, and is predominantly coupled to the* $|2,-1\rangle$ *state via a two-photon transition. Light-induced shifts arise from both optical fields coupling to multiple excited states on the D2 line. (Left): Population of the* $|2,-1\rangle$ *state as a function of time for variable two-photon detuning. The Rabi frequency is extracted by fitting over time windows scaled according to the previously determine Rabi frequency in order to accommodate faster oscillations. (Right): Fitted Rabi frequencies as a function of detuning with errors estimated by the square-root of the covariance diagonal. The two-photon resonance is identified by the minimum, corresponding to a light-induced shift of* 6.82 MHz. *A first-order estimate including only the dominant transitions yields* 4.86 MHz. *The simulation assumes two co-propagating Gaussian beams with* $1/e^2$ *diameters of* 1 mm *and optical powers of* 50 mW, *with opposite circular polarisations, primarily coupling the* $|1,1\rangle$ *and* $|2,-1\rangle$ *states via a* 1 GHz *single-photon detuning.*

In this section, a particular use case of the simulation framework is presented. The simulations are based on a recent experiment investigating two-photon Raman-Rabi oscillations and were developed in parallel with the writing of this thesis. The probe and coupling fields have comparable optical powers and are denoted as Raman 1 and Raman 2 reflecting the nature of the experiment. In the experiment, the two Raman beams co-propagate along the $\hat{z}$ direction with opposite circular polarisations. Both optical fields are Gaussian with $1/e^2$ diameters of 1 mm and optical powers of 10 mW.

The atoms are initially prepared in the $|F, m_F\rangle = |1,1\rangle$ ground state, and the two Raman fields couple this state to the $|2,-1\rangle$ ground state via the shared $|1,0\rangle$ excited state. Both Raman fields are detuned by 1 GHz from their respective

single-photon resonance. The chosen λ scheme is magnetically insensitive to first order, as the two ground states experience equal and opposite Zeeman shifts, while the excited state remains unshifted [4].

Initial analysis using the simulation framework failed to reveal any significant Rabi oscillations. This discrepancy was traced to the omission of induced light shifts in the model. Without accounting for this effect, the time evolution exhibits high frequency and low amplitude oscillations that closely resemble numerical noise. Figure 2.11 shows a calibration of the simulation framework, closely analogous to an experimental procedure. For these simulations, the optical powers of both fields were increased to 50 mW in order to induce faster oscillations. This choice reflects the stiffness of the differential equation describing the system. Slow dynamics require the time-dependent master equation to be integrated up over long time periods and is computationally heavy. Furthermore, the faster oscillations arising from detuning allow for shorter time windows without compromising the Rabi frequency fit. To exploit this, an adaptive approach is employed for setting the integration time window of the simulation: the previously fitted Rabi frequency is used to estimate the oscillation period, and the system dynamics are integrated up to a fixed scaling of this period. The fitted Rabi frequencies are plotted as a function of the two-photon detuning, with the two-photon resonance corresponding to the minimum of the curve. All detunings are defined relative to the light shifted resonance. The induced light shift is 6.82 MHz. Without resorting to the full simulation framework, the light shift can be estimated to first order by considering the two dominant transitions, $|2,-1\rangle \rightarrow |1,0\rangle$ and $|1,1\rangle \rightarrow |1,0\rangle$. Each transition induces a light shift on the ground state, and the effective two-photon resonance shift is 4.86 MHz.

After applying the light induced correction to the two-photon resonance, the system was simulated at resonance over longer times to resolve the time dynamics. Figure 2.12 shows the population distribution across all levels of the D2 spectral line. First, a clear two-photon Raman-Rabi oscillation is observed between the two coupled ground states. Second, single-photon transitions connect to all $|F',0\rangle$ states, with the allowed couplings dictated by the selection rule $\Delta F \in \{0,\pm 1\}$. The separation between $|F'=0\rangle$ and $|F'=1\rangle$ is 72.22 MHz which is negligible compared to the single-photon detuning of 1 GHz, and the single-photon transitions are almost identical from the perspective of $|F=1\rangle$. Spontaneous decay from the excited states gives rise to small population built up in the remaining ground

[4] This transition is used for measuring non-linear Zeeman shifts at low magnetic field strengths in Chapter 4.

states of both manifolds. Most notable is a weak optical pumping effect into the $|1,-1\rangle$ ground state. This state couples via one Raman beam to a closed transition $|1,-1\rangle \rightarrow |2,-2\rangle$, while the second Raman beam is suppressed by the ground state hyperfine splitting of 6.834 GHz. Consequently, the $|1,-1\rangle$ state behaves as a semi-dark state. Figure 2.13 shows a zoomed-in view of the ground state manifolds, in particular the population dynamics of the $|1,1\rangle$ ground state.

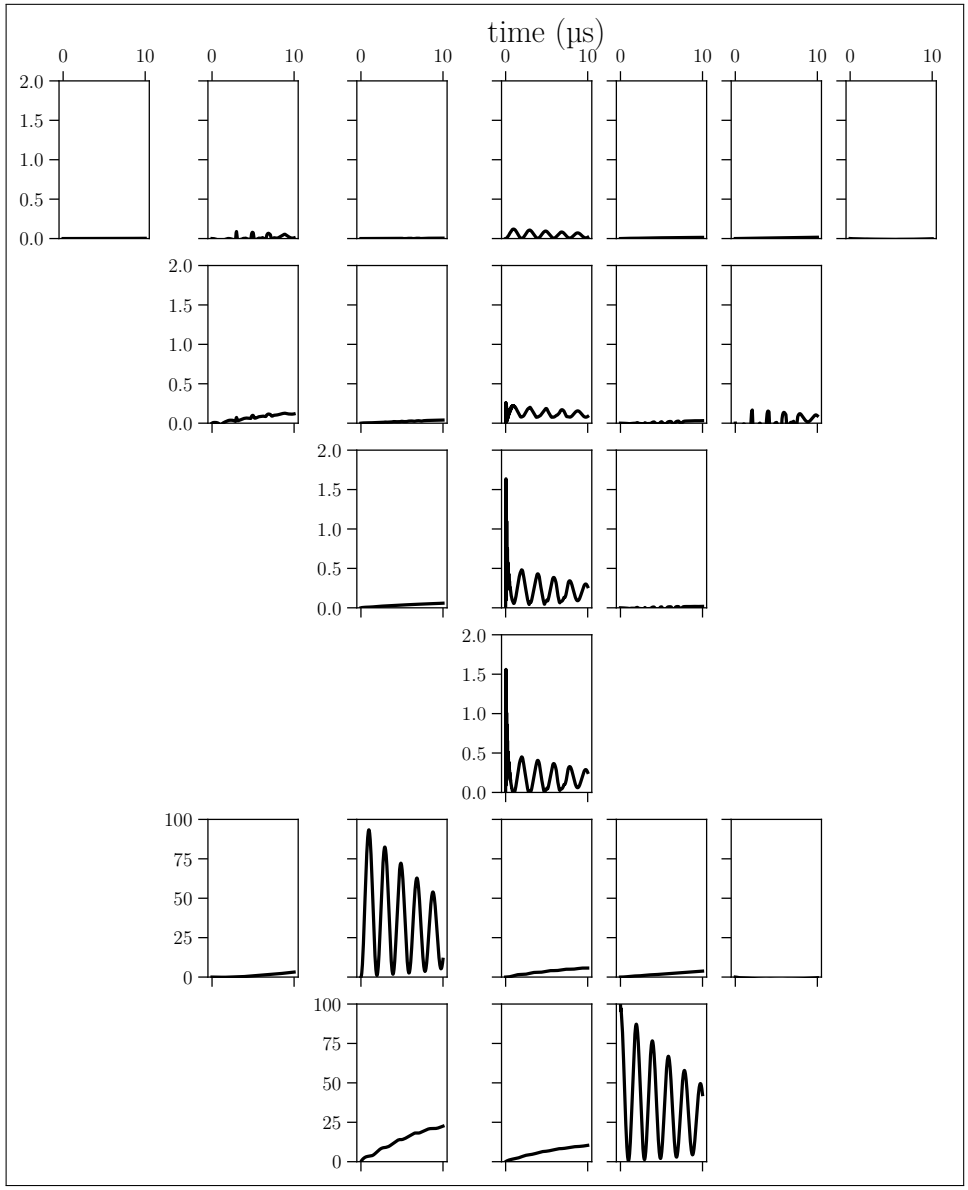

Figure 2.12: *Simulated Raman-Rabi oscillations on the two-photon resonance accounting for the light-induced shift from Fig. 2.11. Time resolved distribution of populations between all* 24 *substates of the D2 spectral line, ordered in accordance to the* $|F, m_\mathrm{F}\rangle$ *state, from left to right in increasing* m_F*, and from bottom to top in increasing* F*, with the ground state manifolds at the bottom. All populations are indicated in percentages. Note the difference in y-axes: ground-states oscillate from* 0 % *to* 100 %*, whereas the excited states are capped at* 2 %*. This indicates the relative transition strengths of the single-photon process compared to the two-photon absorption at the field properties indicated in Fig. 2.11.*

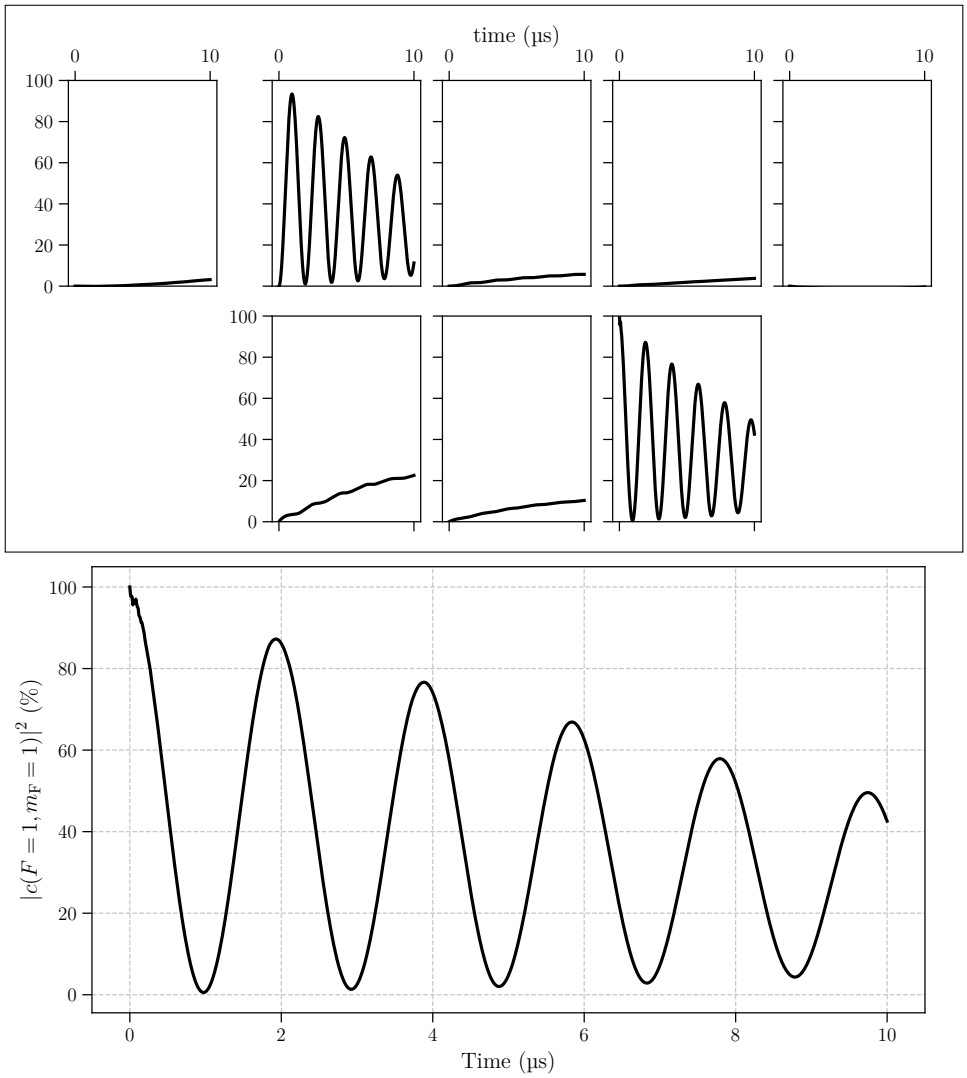

Figure 2.13: *Zoomed-in view of the population distribution in the ground state manifolds (top) and the* $|1,1\rangle$ *ground state (bottom) from Fig. 2.12. All populations are plotted as percentages. Note the small amount of optical pumping into the fully-stretched* $|1,-1\rangle$ *state.*

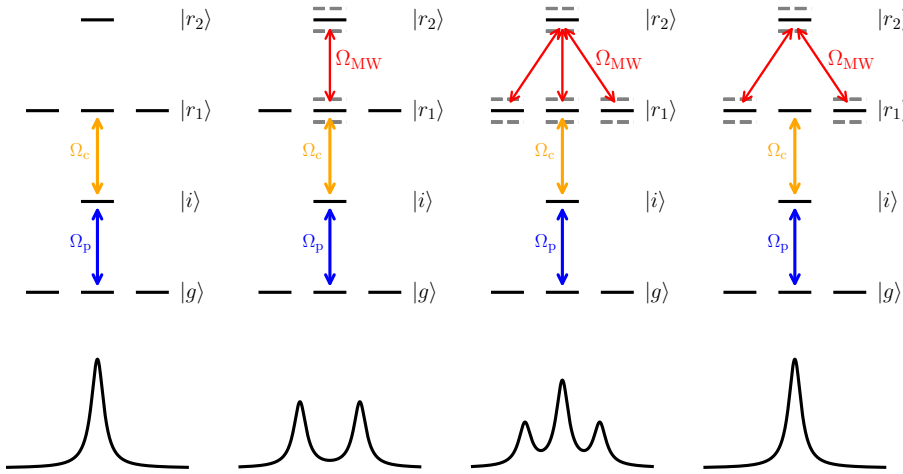

Figure 2.14: *Level diagrams of a four-level model atom (top) with the corresponding probe field transmission spectra (bottom). A linearly polarised probe field couples the* $|g\rangle \rightarrow |i\rangle$ *transition, while a coupling field is frequency swept across the* $|i\rangle \rightarrow |r_1\rangle$ *resonance. In the absence of MW fields (first from the left), an EIT peak is observed in the probe transmission. Dressing the threefold-degenerate* $|r_1\rangle$ *state with an external MW field of parallelly polarised (*$\theta = 0°$*), orthogonally polarised (*$\theta = 90°$*) or at an intermediate angle (*$\theta = 45°$*) with respect to the optical fields gives rise to an AT splitting, indicated by dashed lines. The probe transmission spectra for* $\theta \in \{0°, 45°, 90°\}$ *illustrate the transition from a doublet to a triplet and finally to a single EIT peak as the MW polarisation is rotated. The sketch is inspired by work from [14].*

2.5.3 Rydberg Simulations

Figure 2.14 presents a model atom consisting of four levels, $\{|g\rangle, |i\rangle, |r_1\rangle, |r_2\rangle\}$. A linearly polarised probe field resonantly couples the $|g\rangle \rightarrow |i\rangle$ transition, while a coupling field is frequency swept across the $|i\rangle \rightarrow |r_1\rangle$ resonance. In the absence of MW fields, the condition for EIT is satisfied at the two-photon resonance, resulting in a transmission peak in the recorded probe signal. An external MW field couples the two Rydberg states, imprinting an AT splitting onto the EIT spectrum. When the MW field is parallelly polarised ($\theta = 0°$), the AT splitting breaks the EIT condition, and the spectrum exhibits two distinct peaks. In contrast, orthogonal polarisation ($\theta = 90°$), preserves the EIT condition and a single transmission peak is observed. Intermediate polarisation angles display a triple-peak structure, with the ratio between the central- and the side peaks increasing with θ.

Extension to the Real Atomic System

Take the four level basis $\{|g\rangle, |i\rangle, |r_1\rangle, |r_2\rangle\}$ from Section 2.1.1, and suppose each level contains a set of sub-states. Let $|g\rangle$ and $|i\rangle$ be the $5S_{1/2}|F = 2\rangle$ and $5P_{3/2}|F = 3\rangle$ manifolds each containing 5 and 7 resolved hyperfine states. These are then connected to two Rydberg manifolds, which are not hyperfine resolved. Let $|r_1\rangle$ and $|r_2\rangle$ be the Rydberg states $49D_{5/2}$, $F \in \{1, 2, 3, 4\}$, and $50P_{3/2}$, $F \in \{0, 1, 2, 3\}$, each including 24 and 16 unresolved hyperfine states respectively. All in all, the Hilbert space now consists of 52 states, as shown in Fig. 2.15. To include decay channels from the Rydberg states, which are primarily incoherent, a dummy state is added, to which the Rydberg states decay to, and which immediately decays to the ground state with a lifetime negligible compared to the D2 lifetime, populating the sub-states with equal probability. This describes the full atomic system.

The Hamiltonian is a square 53-dimensional matrix that resembles Eq. (2.9). The diagonal detuning blocks are square "*identity*" blocks, and the off-diagonal Ω_k blocks are rectangular with elements calculated by Eq. (2.86). Adding the two optical probe and coupling fields, as shown in Fig. 2.15, connects the 3-level ladder structure as described in Section 2.1.1. Each optical field is characterised by its wavevector, polarisation, field strength and detuning, and all parameters can be independently varied. For a given set of optical field parameters, the full set of differential equations governed by Eq. (2.12) can be solved in the steady-state limit, $\dot{\rho} = 0$, which is equivalent to finding the null space of $\mathcal{L}$.

The transmitted probe light is modelled by the Beer-Lamberts law from Eq. (2.64), which can be written $I = I_0 e^{-\alpha L}$, where L is the sample length and the extinction coefficient is calculated by the coherences of the levels in the transition [14]:

$$\alpha = \frac{2n\omega_p}{c\varepsilon_0\hbar} \sum_{g,i} |\boldsymbol{\mu}_{i,\,g}|^2 \mathrm{Im}\left(\frac{\rho_{gi}}{\Omega_{ig}}\right). \tag{2.89}$$

The high dimensionality of the underlying parameter space motivates a systematic investigation. The system is first simulated in the absence of MW fields, probing the fundamental three-level system comprising $5 + 7 + 24 + 1 = 37$ hyperfine sub-states. Fig. 2.16 presents such simulated spectra. In all experiments, the probe transmission is recorded, and different spectral responses are observed depending on which optical field is scanned. When the coupling is held fixed on resonance and the probe field frequency is scanned across the transition, a broad absorption background is observed. In contrast, when the probe field is fixed on resonance and the coupling field frequency is scanned, the probe transmission is strongly

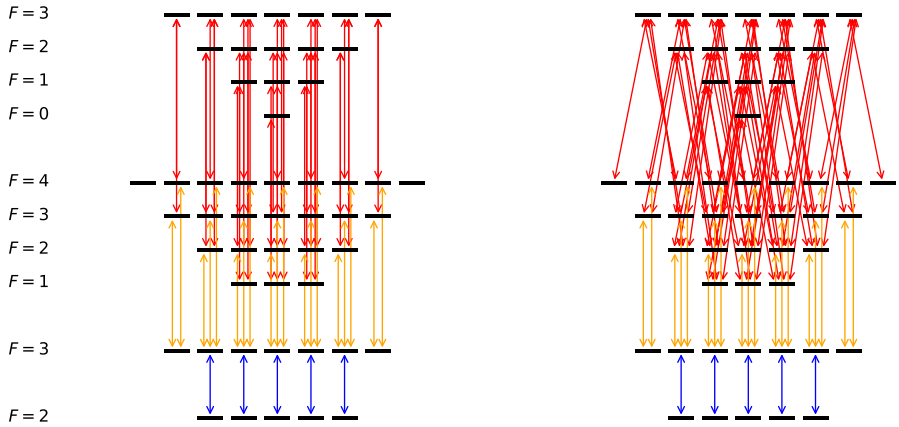

Figure 2.15: *The atomic level structure considered for the Rydberg experiments. The probe field (blue), coupling field (orange) and MW field (red) addresses distinct transition between each rung of the ladder. The hyperfine sub-levels of both highly excited Rydberg levels are unresolved, so relative vertical offsets have been added to enable a visual tracking. For experiments, the optical field polarisations are fixed, whereas the MW field polarisation can be varied from driving π transitions (left) to a combination of $\sigma^{\pm}$ transitions (right).*

suppressed except at the two-photon resonance. Both the EIT and AT regimes are simulated and the clear distinction is shown in the spectra. There is a subtle but important distinction to be made regarding the AT regime. When viewed in the frequency domain of the probe field, the AT regime display a strong absorption on resonance with either dressed-state, resulting in two distinct transmission minima. In contrast, when the probe field is fixed on resonance and the coupling field detuning is scanned, only a single transmission peak is observed. Physical intuition for this behaviour can be obtained from the avoided-crossing splitting given in Eq. (2.5). For $\Delta_c = 0$, the dressed-states are symmetrically split by $\Omega_c/2$ around the bare excited state. In this case, the probe field is not resonant with either dressed-state and is therefore transmitted. As the coupling field is detuned, one dressed-state shifts towards the probe resonance while the other moves further away. Consequently, the probe transmission decreases with increasing coupling detuning. For sufficiently large detunings, the system effectively reduces to an uncoupled two-level atom driven resonantly by the probe field, leading to strong absorption.

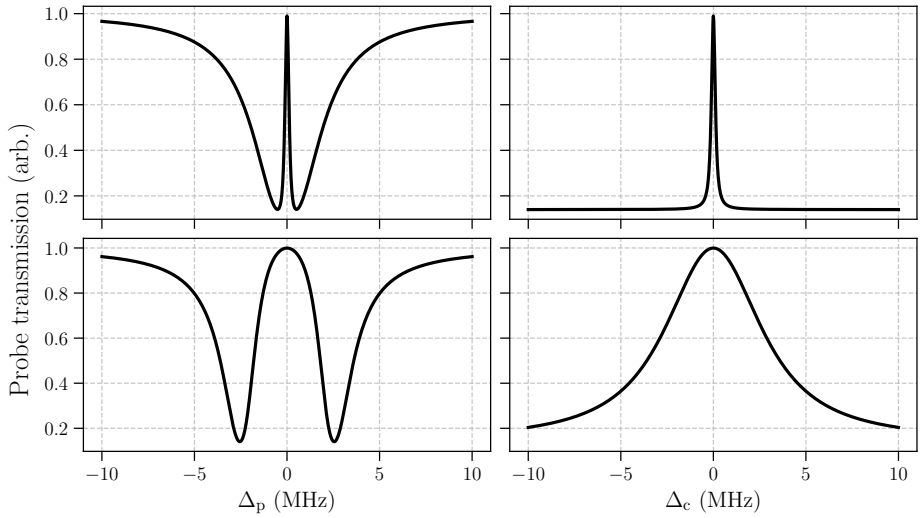

Figure 2.16: *Simulated probe transmission as a function of two-photon detuning at variable coupling field strengths for EIT (top) or AT (bottom) conditions, in the absence of an external MW field. A clear distinction is observed between varying the probe frequency (left) or the coupling frequency (right), while keeping the opposite optical field resonant. A broad absorption background is seen for the probe scan. In contrast, the coupling frequency scan exhibit a suppressed probe transmission except at the two-photon resonance.*

Introducing Microwave Fields

The Rydberg-atom-based EIT detection scheme measures the transmission of a weak probe field under EIT conditions. In the recorded spectra, the coupling laser frequency is scanned while the probe frequency is kept resonant. When a MW field is present, it modifies the transmission spectrum through its interaction with the highly excited Rydberg states. Depending on the dipole-allowed MW couplings between the involved Rydberg states, the system can exhibit either a single EIT resonance or multiple resonances arising from AT splitting. This effect forms the basis for determining the state of polarisation of the MW field, as discussed in Chapter 5. The probe and coupling lasers are co-linearly polarised, and their common polarisation axis defines the quantisation axis of the system. In all experiments except those dedicated to MW polarimetry, the MW field polarisation is fixed to be co-linear with the optical fields. Under these conditions, the MW field drives only π-transitions between the Rydberg states, as illustrated in the left column of Fig. 2.15. The resulting dressed-state structure is then

investigated by varying the MW frequency and field amplitude.

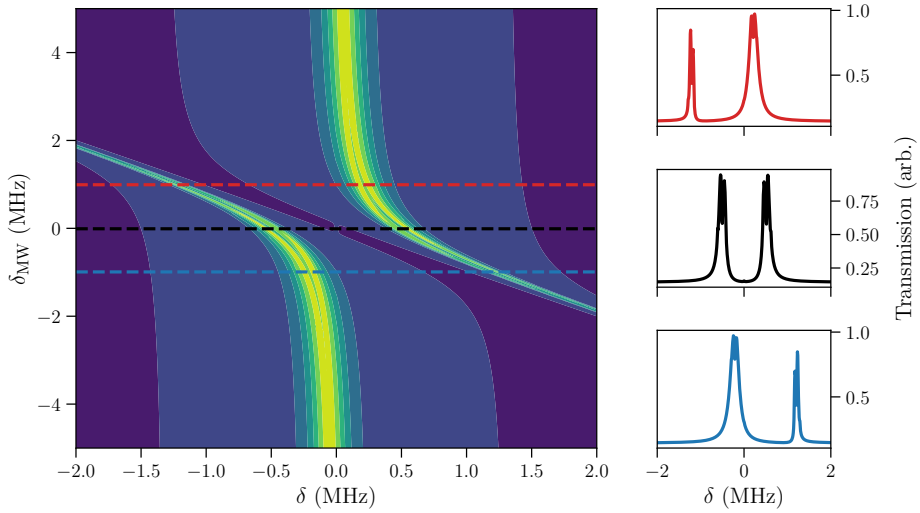

Figure 2.17: *Simulated two-photon spectroscopy ($\delta_p = 0$) at variable MW detuning exhibits an avoided-crossing, with dressed-states separated by the generalised MW Rabi frequency, which is minimum at resonance. The dashed lines indicate horizontal slices corresponding to the spectra shown in the right panel, where both colour and vertical ordering establish the correspondence between the two panels.*

Figure 2.17 shows a scan of the MW frequency exhibiting the expected avoided-crossing, as predicted by the dressed-state picture introduced in the derivation of Eq. (2.5). As the AT splitting reaches a minimum at resonance, this procedure provides a calibration of the MW frequency, which is necessary for the experiments presented in Chapter 5. With the MW field tuned to resonance, exploration of the strong-field regime reveals additional spectral features in the dressed-state structure, as shown in Fig. 2.18. These features appear as a sub-branching of the otherwise linear AT splitting. They arise from the m_J-dependent interaction strength between pairs of Rydberg sub-states within the coupled manifold [14]. This dependence can be understood in terms of variations in the MW coupling strength caused by differing Clebsch-Gordan coefficients for the allowed transitions. Figure 2.19 illustrates this for the case of a MW field driving pure π-transitions. Because the MW Rabi frequency scales with the magnitude $|m_J|$ through these coefficients, the MW coupling induces different AT splittings across the $|r_1\rangle$ manifold. This behaviour is shown in Fig. 2.19 (b), where the $\pm$ labels denote the symmetry of the dressed superposition states represented by the black and

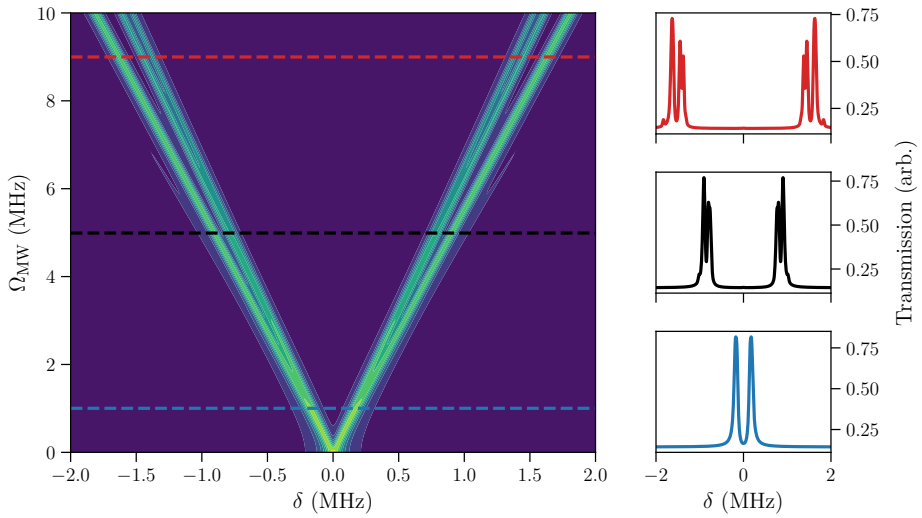

Figure 2.18: *Simulated two-photon spectroscopy ($\delta_P = 0$) in the presence of a resonant MW field of variable strengths exhibits an AT splitting with substructure due to an m_J-dependent coupling strength inherent to the dressed-states. This is theoretically predicted in [14] and the mechanism is shown in Fig. 2.19. The dashed lines indicate horizontal slices corresponding to the spectra shown in the right panel, where both colour and vertical ordering establish the correspondence between the two panels.*

grey lines. Notice the two spectator states, corresponding to the extremal m_J components, which remain uncoupled by the MW field.

Since the low-lying states are hyperfine resolved and the coupling laser specifically drives the transition from $5P_{3/2}$ ($F = 3$) to $|r_1\rangle$, electric dipole selection rules (Laporte's rule) excludes direct optical coupling to $|r_2\rangle = 50P_{3/2}$, for which $\Delta L = 0$. Consequently, only the lower Rydberg state is considered in the expansion shown in Fig. 2.19 (c). Because the system involves a $J = 5/2 \leftrightarrow J' = 3/2$ structure, five dressed-states arise in the lower Rydberg manifold. These are labelled by their angular momentum projections $|m_J, m_I\rangle$, with $m_F = m_J + m_I$. In principle, all five dressed-states exist in the manifold. However, their visibility in the EIT spectrum depends on the optical coupling strength to the specific intermediate state $|i\rangle$, which can be denoted with its quantum numbers $|J'F'm_{F'}\rangle$. As discussed in [14], the optical coupling of the dressed Rydberg states to the intermediate state is proportional to:

$$|\langle J'F'm_{F'}| - er_0|Jm_JIm_I; s\rangle|^2 \propto \begin{pmatrix} J' & J & 1 \\ -m_{J'} & m_J & 0 \end{pmatrix}, \tag{2.90}$$

which vanishes when $|m_J| > J'$. For the present case, $J' = 3/2$, so the extremal components $m_J = \pm 5/2$ have zero dipole matrix element. These states therefore do not couple to the optical EIT ladder and are true spectator states of the detection scheme. Although five dressed states are present in the Rydberg manifold, only four are optically active. The spectator states do not contribute to the EIT signal and, consequently, no central peak associated with the uncoupled state appears in the simulated spectrum. This behaviour is experimentally demonstrated in Chapter 5, where a sub-structure of the AT splitting is observed in the strong MW field regime without any contribution from the spectator state.

Finally, a polarimetric study of the MW field is performed in Fig. 2.20. In this case, the MW field is again fixed on resonance, albeit not operated in the strong field regime. As the polarisation changes, so does the state connectivity and the spectrum exhibits a transformation from a single EIT peak to the multiple peaks in the AT regime. This is similar to the simpler model system depicted in Fig. 2.14.

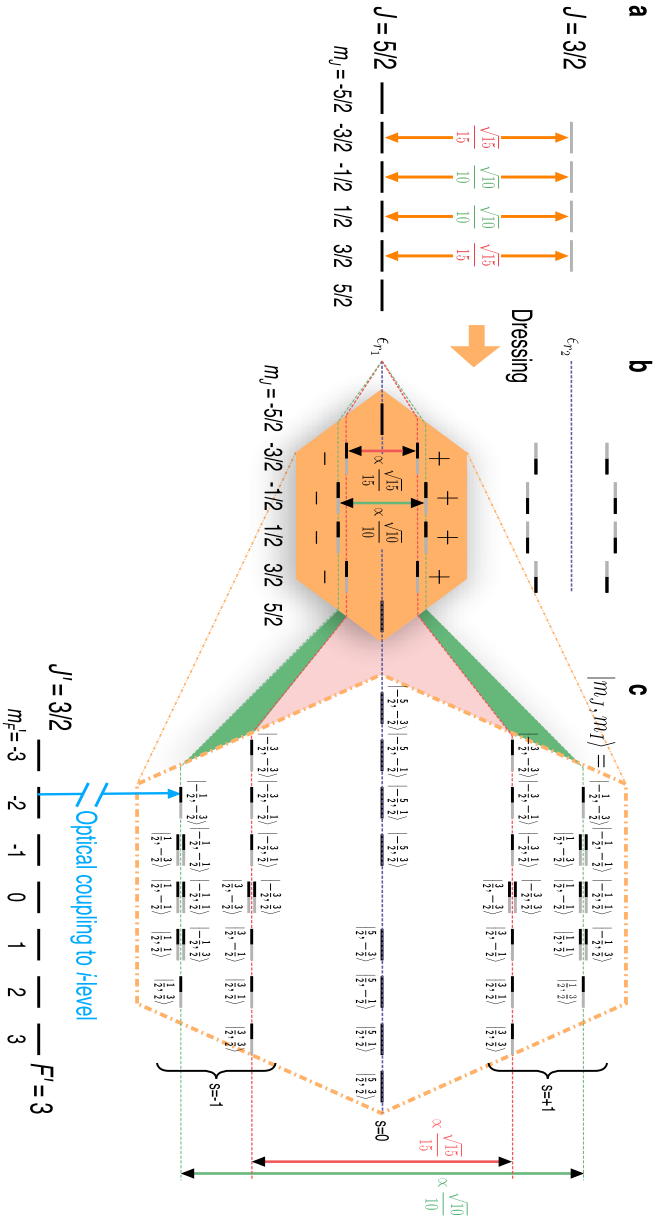

Figure 2.19: *(a): A linearly polarised MW field couples the two Rydberg levels via π-transitions with the dipole matrix elements indicated. (b) The transition pairs are subjected to a $|m_J|$-dependent AT splitting, and the $\pm$ indicates the symmetry of the superposition of Rydberg states represented by the black-grey lines. (c) Zoom in on the lower dressed manifold of (b) and labelling states with possible values of the nuclear spin projection, $|m_J, m_I\rangle$ (and hence $m_F = m_J + m_I$) as well as the symmetry of the superposition. The figure is from [14]*

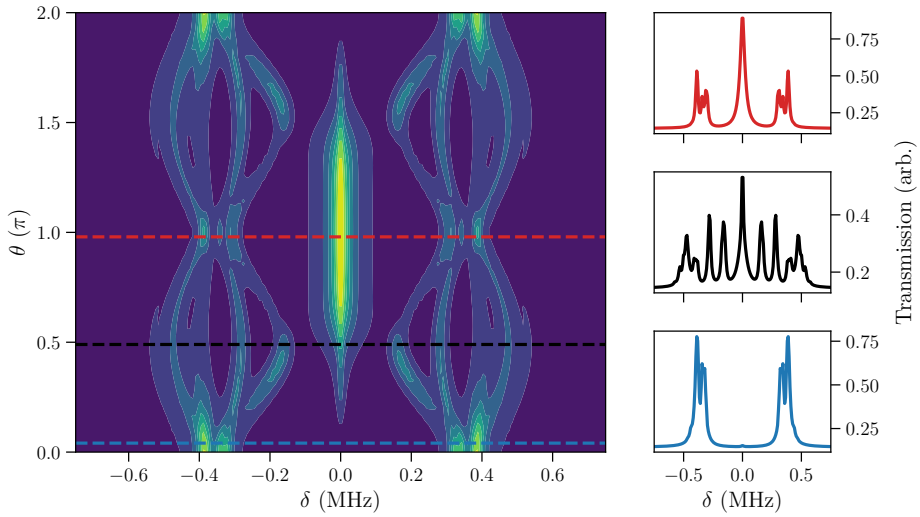

Figure 2.20: *Simulated two-photon spectroscopy ($\delta_P = 0$) in the presence of a resonant MW field with variable polarisation. The MW polarisation is controlled by scanning the relative phase θ between the two input ports of a dual-ridged MW Horn antenna oriented at 45° with respect to the quantisation axis. A phase of $\theta = 0°$ corresponds to linear polarisation driving pure π-transitions. Increasing θ introduces ellipticity into the MW field, as described in detail in Chapter 5. The dashed lines indicate horizontal slices corresponding to the spectra shown in the right panel, where both colour and vertical ordering establish the correspondence between the two panels.*

CHAPTER 3

Production of Ultracold Atom Gases

The ultracold quantum gas group at Aarhus University operates two active laboratories producing ultracold clouds of either pure ^{87}Rb or mixed ^{87}Rb-^{40}K clouds. This thesis focuses on work with pure ^{87}Rb clouds, and the purpose of this chapter is to provide a concise overview of the key elements of the experimental apparatus. The experiment was initially built in 2003 and has been producing BECs since 2006 [51, 52]. Over the past two decades, a wide range of experiments has been performed, including studies of optical lattices [51, 53, 54] and optimal control for quantum gates [55]. More recently, research has focused on the characterisation of BEC atom number fluctuations using a microcanonical ensemble description [33–35], as well as spatial alpha calibration for time-of-flight absorption imaging of ultracold gases [1]. These latter studies were completed at the beginning of this research project [1, 2].

This chapter reflects the changes to the laboratory carried out as part of this research project. It begins with an overview of the experimental sequence used to produce ultracold atomic clouds, providing the framework for the chapter. During my employment, all optical setups were redesigned and rebuilt to improve stability and flexibility. Therefore, the configuration of each laser is outlined together with the ^{87}Rb level scheme and relevant transitions for the experiment. New equipment for nondestructive measurements is introduced, including the imaging

optics, the single-photon detector module (SPDM), and the dark-ground imaging configuration. Although a substantial portion of this research project involved laboratory redevelopment, most notably the implementation and programming of a FlexDDS unit, which now lies at the core of the experiment by controlling both MW sweeps for state preparation and the optical phase-lock loop (OPLL) reference for probe frequency stabilisation, these developments were recently described in detail elsewhere [48]. The FlexDDS was integrated into a control framework that also manages motorised mirrors for the optical dipole trap, enabling straightforward beam realignment and optimisation. Integration of the PicoScope (3406D) for SPDM data acquisition has further simplified day-to-day operation of the experiments.

Finally, the chapter summarises the improvements achieved during this project and presents an outlook, outlining how the high-density regime can be realised to enable further experimentation.

3.1 Overview of the Experiment

3.1.1 Experimental Sequence

Briefly, the experiment loads a magneto-optical trap (MOT) of approximately 10^9 ^{87}Rb atoms which are optically pumped to the $|2,2\rangle$ state, then caught in a magnetic quadrupole trap (QPT) on conveyor belts and transported to an ultra-high vacuum chamber. Here the cloud is subjected to active RF-evaporation in the tight QPT, and before Majorana spin-flip losses sets in, the atoms are transferred and further cooled in a hybrid trap configuration that combines the magnetic field from the QPT and a Gaussian dipole laser beam at 1064 nm along the $\hat{z}$-direction, tightly focused to beam waist diameters of approximately 80 µm, and vertically offset by approximately 100 µm under the magnetic zero point using an optical power of 7 W. Evaporation is continued by lowering the optical power gradually at a magnetic field gradient slightly below the levitation threshold. The atoms are transferred to a crossed optical dipole trap (cODT) in the overlap of an orthogonal pair of Gaussian beams of similar characteristics. For this step, the QPT magnetic field is ramped to zero and the atomic spin projection is preserved by adding a background magnetic field from a pair of Helmholtz coils. A MW frequency sweep prepares the atoms in the $|1,1\rangle$ ground state, which has an enhanced lifetime in the trap of 12.4 s compared to the 3.2 s for the $|2,2\rangle$ state. The final evaporation step is adjusted for producing a thermal, bimodal or condensed cloud of variable size. The experiment reliably produces fair sized

BECs of approximately 600k atoms.

3.1.2 Optical Tables

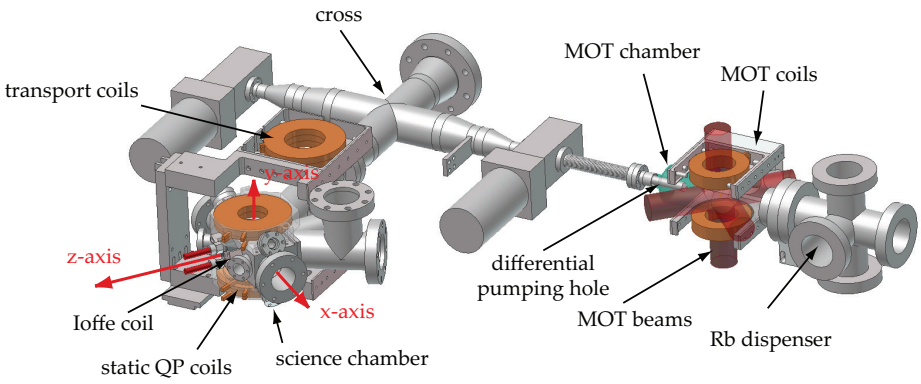

Figure 3.1: *Overview of the vacuum chambers and magnetic coils configurations. The experiment begins in the MOT chamber, where a cloud of* ^{87}Rb *atoms is laser cooled and trapped. Magnetic transport coils then convey the atomic cloud through a differential pumping tube into the science chamber. There, initial RF-evaporation is performed in a tight magnetic QPT. Optical dipole trapping beams are available along both the* $\hat{x}$ *and* $-\hat{z}$ *directions. Imaging is performed along these same axes using two CCD cameras, while a single-photon detector is positioned along the* $-\hat{z}$ *direction.*

Figure 3.1 displays the vacuum chamber central to the experiments, together with the surrounding configuration of magnetic coils. The experiment is distributed across two optical tables, referred to as the *laser table* and the *science table*, as illustrated in Fig. 3.2. The laser table stores the resonant laser systems, and equipment for light preparation, whereas the science table houses the vacuum chambers, magnetic coils and a mechanical positioning system with a translational stage used to move the magnetic coils between vacuum chambers. The resonant lasers are separated from the science table for two main reasons. First, and most importantly, stray resonant light heats the atomic ensemble and inhibits the formation of a large BEC. To mitigate this effect, all resonant light is guided to the science table by polarisation-maintaining single mode (PM-SM) optical fibres, and any stray light is blocked by curtains at the science table. These curtains also provide partial protection of the optical components against dust and other contamination. A secondary, though less critical, point for separating the laser systems from the science table is the reduction of acoustic and mechanical noise. Motion of the magnetic coils can introduce vibrations that couple into the laser systems, potentially destabilising the laser modes.

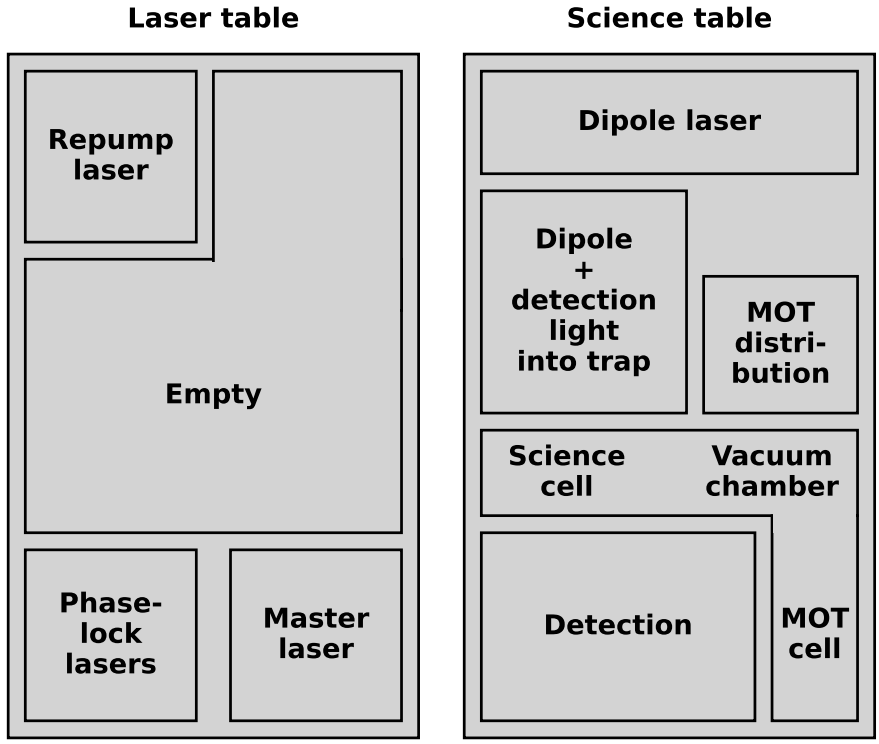

Figure 3.2: *The two optical tables containing the experimental apparatus, lasers and optics.*
(Left): The laser table primarily contains three modules, all constructed during this research project . The master laser provides light for the 3D MOT, imaging along both horizontal directions, optical pumping for magnetic trapping, and depumping to enable fast acquisition of absorption images with and without atoms. The phase-lock lasers system consists of two optically phase-locked lasers, providing a Raman laser setup as well as a tunable probe laser capable of scanning $9\,\mathrm{GHz}$ *within approximately* $100\,\mathrm{ms}$. *The repump laser addresses the* $|F = 1\rangle \rightarrow |F' = 2\rangle$ *transition in both the MOT glass cell and the science chamber. The rework of the laser table has cleared up space, and unnecessary optics and electronics was removed to accommodate future experimental upgrades.*
(Right): The science table contains the far-detuned optical dipole laser and a MOT distribution board used to balance optical power among the six MOT telescope beams. All PM-SM optical fibres guide light from the laser table to the science table, where final preparations are done for detection and dipole optics before the light is directed into the vacuum system. Two CCD cameras enable absorption imaging of the atomic clouds along each of the horizontal directions, and a single-photon detector module is setup in the $\hat{z}$ *detection branch for nondestructive probing. The vacuum chamber has an L-shaped geometry and the partition of the MOT and science chambers is also shown in Fig. 3.1.*

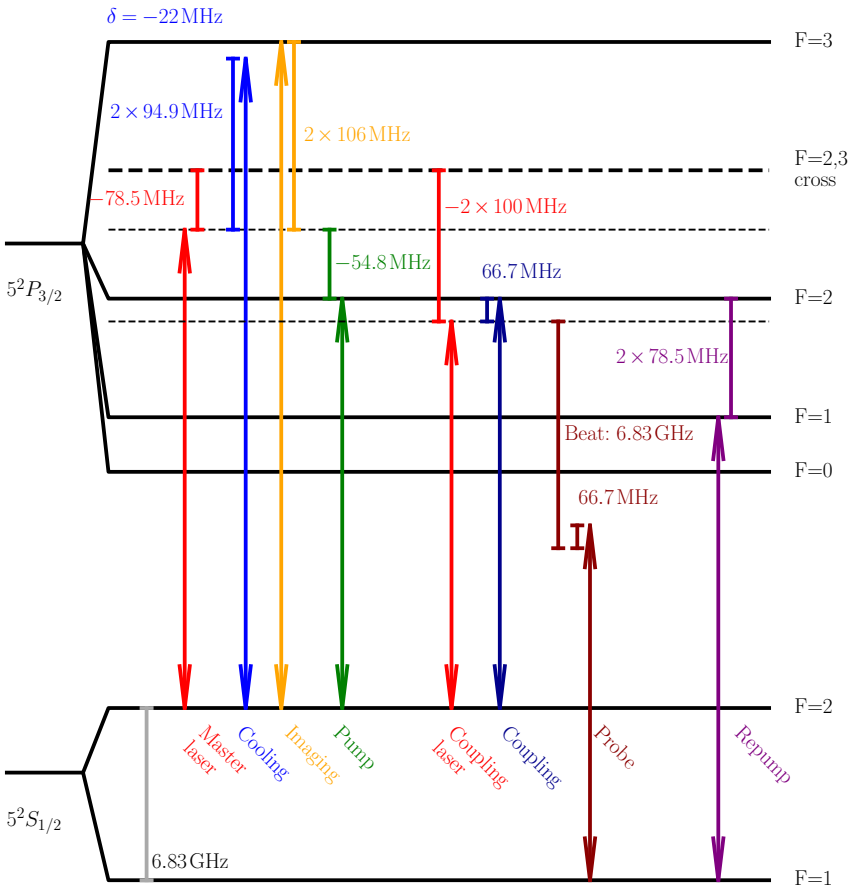

Figure 3.3: *The* ^{87}Rb *D2 level diagram including the optical transitions used as laser locks for the master, coupling and repump laser. The master laser provides light for laser cooling, absorption imaging and optical pumping. The probe and coupling lasers are optically phase-locked, and the repump laser addresses a single transition used for both the MOT cell and science chamber.*

3.1.3 Laser Systems

All resonant lasers are controlled by Toptica DLC units and are, with the exception of the probe laser, frequency stabilised using a Doppler-free saturation spectroscopy setup. An overview of the ^{87}Rb D2 level diagram with each laser transition is presented in Fig. 3.3, and representative spectroscopy signals are shown in Fig. 3.4. This section presents each laser system and its role in the experiment.

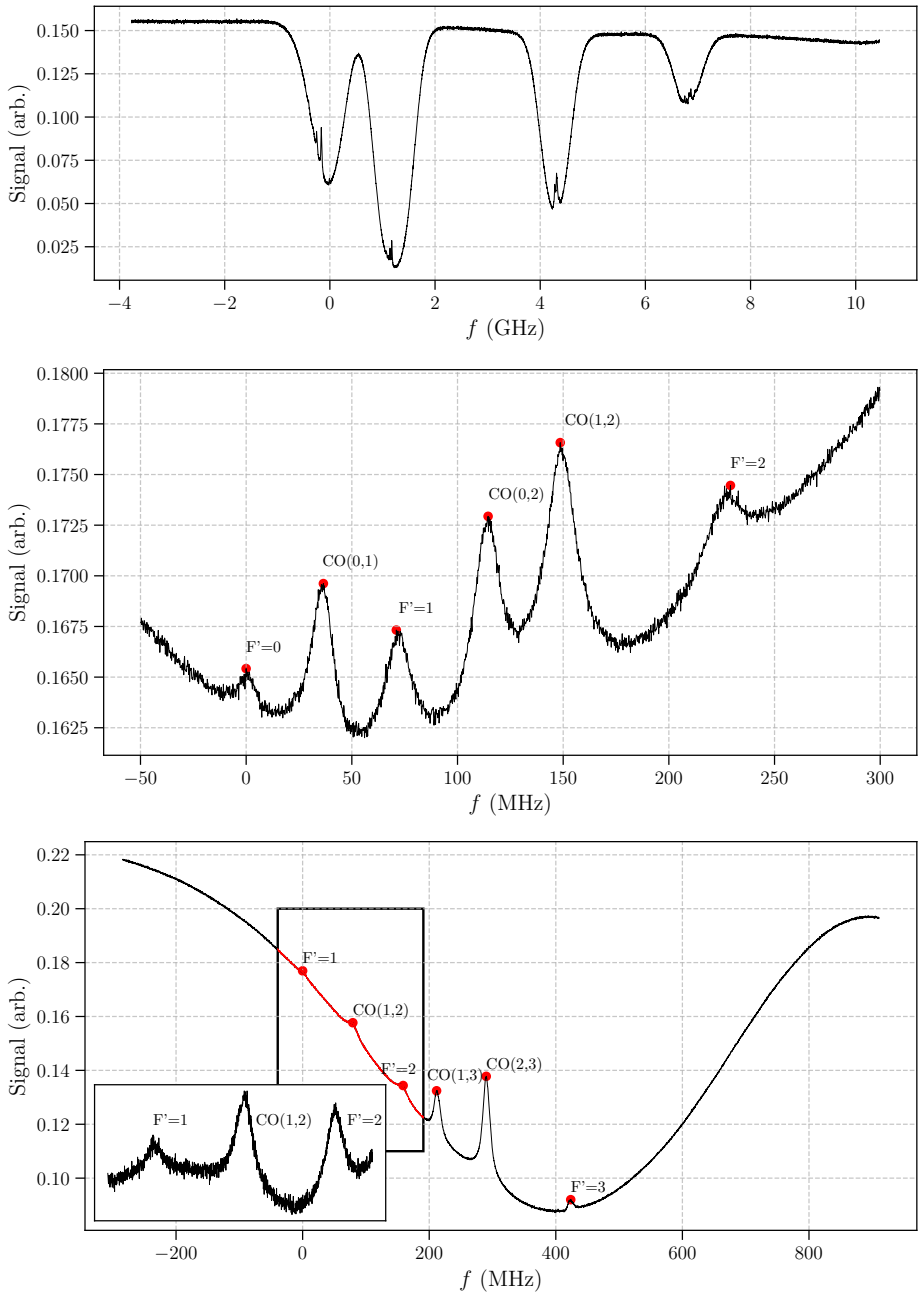

Figure 3.4: *Doppler-free saturation spectroscopy signals of Rb. (Top): Spectrum covering all four ground-state hyperfine levels of both isotopes, showing absorption dips corresponding (from left to right) to* $^{87}\mathrm{Rb}|F=2\rangle$, $^{85}\mathrm{Rb}|F=2\rangle$, $^{85}\mathrm{Rb}|F=1\rangle$, *and* $^{87}\mathrm{Rb}|F=1\rangle$. *(Centre): Zoom in on the* $^{87}\mathrm{Rb}|F=1\rangle$ *manifold. (Bottom): Zoom in on the* $^{87}\mathrm{Rb}|F=2\rangle$ *manifold. The inset shows weak spectral features in the red-marked region that become visible after detrending the data within the rectangle. All frequency axes are calibrated using reference data from [50]*

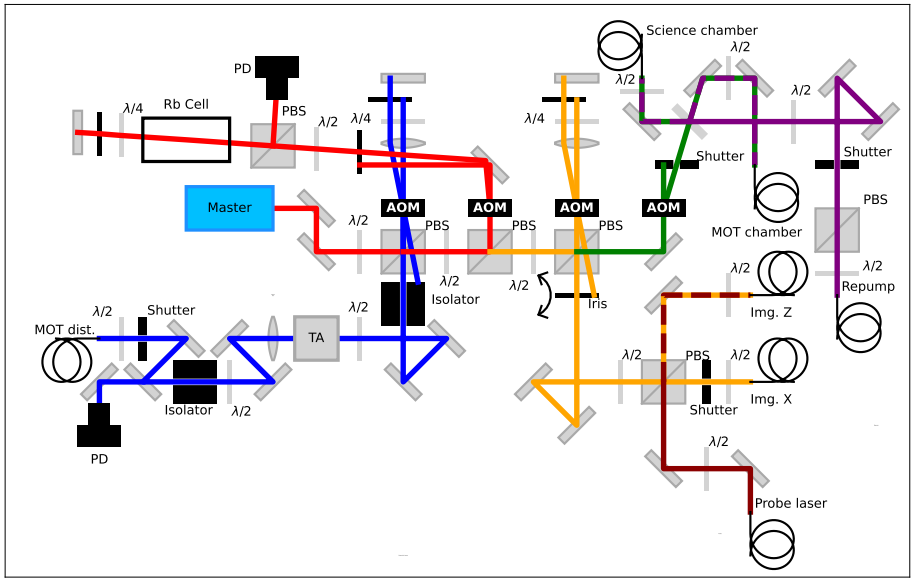

Figure 3.5: *The master laser setup provides MOT cooling (blue), absorption imaging (yellow) and optical pumping (green). It is frequency locked using a Doppler-free saturation spectroscopy setup (red), and each branch is frequency shifted according to Fig. 3.3. Probe light is coupled into the $\hat{z}$-imaging fibre, and repump light is delivered to both the MOT cell and the science chamber via the optical pump fibres.*

Master Laser System

The master laser is frequency locked to the $|F = 2\rangle \rightarrow |F' = 2/3\rangle$ cross-over transition indicated in Fig. 3.4. The laser output is divided into three frequency-shifted branches for laser cooling in the MOT, absorption imaging in the two horizontal directions, and optical pumping in both the MOT cell and science chamber. The exact transition addressed by each branch is indicated in Fig. 3.3 and a schematic of the master laser setup is shown in Fig. 3.5.

The optical layout is designed for robustness and ease of maintenance, two qualities that are easy to overlook until they are missing. The previous master laser setup occupied roughly half of the optics table, with meter-scale distances between mirrors [34, 35]. In contrast, the current design fits into a small corner of the table and requires significantly less effort to optically couple and maintain long-term stability. In addition, all AOM drivers and monitoring oscilloscopes are located directly above the setup, creating a compact and convenient workstation.

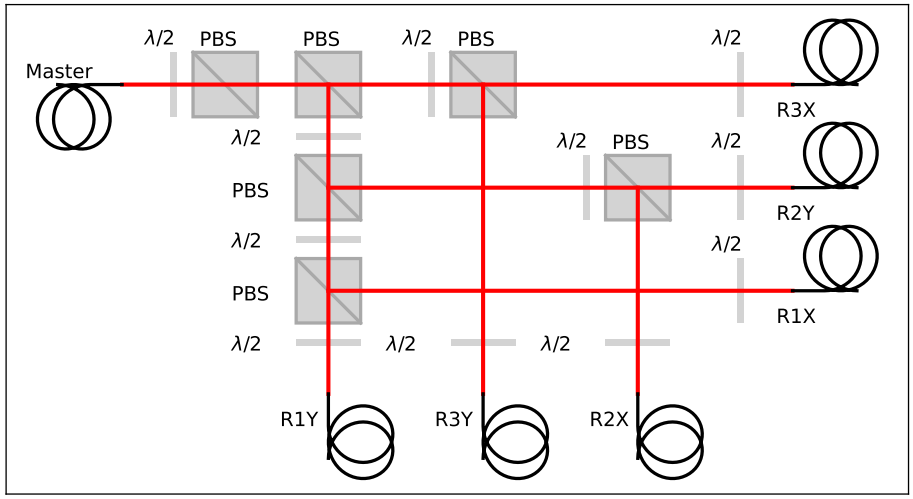

Figure 3.6: *Schematic of the MOT distribution board. The cooling light from the Master laser system is split into three pairs of telescopes for the MOT, and power balancing is provided by the λ/2 plate and PBS cube pairs. The first PBS cleans the polarisation to mitigate effects on the optical power balancing from polarisation drift.*

The layout achieves this robustness by using a minimal number of components arranged much closer to each other. Despite the new level of compactness, the layout deliberately preserves some free space around each optical element to facilitate diagnostics and simplify future alignment while allowing additional components to be integrated with minimal reconfiguration. The setup is based on a backbone of PBS cubes combined with a parallel row of AOMs to provide the required frequency shifts for each branch. Double-pass AOM configurations enable tunable frequency offsets without introducing significant variations in output optical power, both during experiments and between experimental cycles.

The MOT cooling light is typically detuned by $-22\,\mathrm{MHz}$ from the closed cycling transition $|F = 2\rangle \rightarrow |F' = 3\rangle$. After amplification to approximately 700 mW using a tapered amplifier (TA), the light is directed to the MOT distribution board as shown in Fig. 3.6, where it is coupled into the six MOT telescopes. Two Faraday isolators are required around the TA. One suppresses amplified spontaneous emission propagating in the backward direction, which would otherwise leak into the other branches and degrade, in particular, the spectroscopy signal. The second isolator protects the TA from back-reflected light, most notably from a closed shutter.

The absorption imaging light is resonant to the cycling transition $|F = 2\rangle \rightarrow |F' = 3\rangle$ and is distributed into two PM-SM optical fibres with adjustable power control using a $\lambda/2$ plate and a PBS cube. The optical pumping light is frequency shifted into resonance for the $|F = 2\rangle \rightarrow |F' = 2\rangle$ transition. This branch employs a single-pass since the transition is already close to the lock-point, and to minimise optical power losses. A 50/50 BS cube directs the pumping beam into two PM-SM optical fibres. One fibre delivers light for optical pumping in the MOT cell, preparing the atoms in the most magnetically trappable state $|2, 2\rangle$ before transfer into the tight magnetic QPT generated by the transport coils. The second fibre supplies light to the science chamber for depumping atoms away from the cycling transition, enabling faster acquisition of absorption images with and without atoms. This way, the images can be taken within 340 µs limited by the camera shift-speed [33].

Raman Laser System

The Raman laser system consists of two lasers. Depending on the context, these are referred to as the probe and coupling lasers (two-photon spectroscopies), Raman 1 and Raman 2 lasers (Raman transitions) or the primary and secondary lasers (phase-lock context).

The primary laser is typically frequency-locked to a Doppler-free saturation spectroscopy signal, although the specific transition depends on the experiment. For far-detuned Raman experiments, the primary laser can be left free-running at the far edge of the Rb spectrum, as the laser output is relatively stable and measured frequency drift over a single experimental cycle is negligible compared to detunings on the order of GHz. In Fig. 3.3, the coupling laser is considered to be frequency stabilised to the $|F = 2\rangle \rightarrow |F = 2/3\rangle$ cross-over transition, and this is the general assumption unless specified otherwise. The primary laser serves as the reference (beating) laser. The secondary laser is locked to the primary using an OPLL with a variable lock point controlled by a FlexDDS unit. The OPLL implementation is based on previous work [56] and was recently described in detail in [48].

A schematic of the Raman laser setup is shown in Fig. 3.7. Each laser is split into three branches: one for the spectroscopy cell, one for the frequency-mixing input to the OPLL box, and one for delivering light to the experiment. A 10 % sampler splits the output from each laser for the spectroscopy branch. The coupling laser, however, is first directed to a double-pass AOM for a total frequency shift of

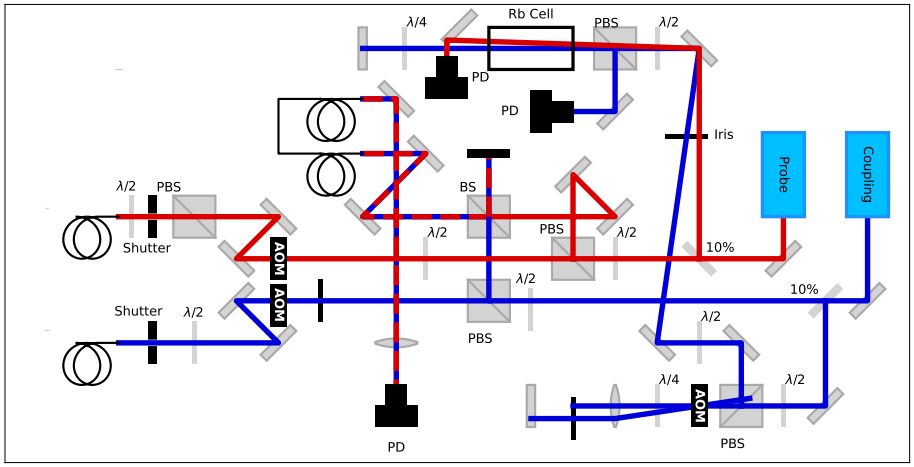

Figure 3.7: *The Raman laser system consists of two lasers. The primary (blue) is frequency stabilised using a Doppler-free saturation spectroscopy setup. It is combined with the secondary laser (red) and the beat frequency is given as input to an OPLL to frequency lock the secondary laser. Both are optically coupled to individual PM-SM optical fibres, providing two phase-locked lasers to the experiment for either two-photon resonances, or using only the secondary laser as a versatile probe laser that can scan* 9 GHz *in approximately* 100 ms.

approximately 200 MHz before the cell. The spectroscopy cell provides a reference for frequency-locking the primary laser and provides monitoring for diagnostics of both laser outputs. If the probe laser is not blocked by an iris before the Rb cell, room-temperature EIT is observed in the spectrum.

For the OPLL branch, a $\lambda/2$ plate and PBS cube pair splits each laser, enabling individual power control, and ensuring identical polarisations of the two fields for beating. The laser fields are combined on the surface of a 50/50 BS cube before coupling into a PM-SM optical fibre to ensure spatial mode matching. The fibre output is directed to a fast photodiode with a bandwidth of 12 GHz that measures the beat frequency between the two lasers. The signal is compared to a variable reference frequency in the OPLL electronics, which controls the secondary laser injection current and piezo voltage. As a result, the system can operate either as a pair of phase-locked lasers for EIT experiments or as a highly versatile probe laser that can be locked to arbitrary frequencies and swept over a variable range. The current configuration of the OPLL provides stable probe frequency sweeps of up to 9 GHz over a time scale of 100 ms, where the sweep duration is limited by the laser lock. Compared to the typical tuning range on the order of hundreds of

MHz provided by AOMs, this represents a substantial increase in flexibility.

The third branch directs each laser field to the experiment and employs a single-pass AOM configuration for a frequency shift of 66.67 MHz. The single-pass AOMs enable fast switching of the laser fields, and the frequency shift is fixed, such that fine frequency adjustments are done via the double-pass AOM. The single-pass AOMs are daisy-chained, with the monitoring output of one driving the frequency input of the other, ensuring identical frequency shifts and preserving the phase relation of the two fields.

This system enables both a versatile probe laser as well as phase-locked laser pairs for two-photon spectroscopy and time-resolved dynamics. Applying triangular waveforms to the OPLL reference frequency allows for multiple spectra to be recorded, and when combined with nondestructive techniques, complete calibration datasets can be acquired from a single cloud, opening a wide range of experimental possibilities. A catalogue of such experiments is presented in Chapter 4.

Repump Laser Setup

The repump laser was reworked twice over the course of this thesis. Initially, the repump light was provided by a home-built ECDL. This system suffered from recurring issues with the laser diode, and repairs to the optical components inside the ECDL were time-consuming. In many cases, they required up to a full day for adhesives to set, followed by realignment of the output beam. Monitoring the output with a Fabry-Perot cavity revealed multiple modes and overall worse spectral quality compared to a commercial Toptica DL. After the Raman laser system was constructed for the first iteration of the EIT experiments, an alternative source for the repump light became available. At that time, all experiments employed the same λ-scheme, where the coupling laser drove the $|F = 2, m_{\mathrm{F}}\rangle \rightarrow |F' = 2, m_{\mathrm{F}'} = 2\rangle$ π-transition, while the probe laser addressed the $|F = 1, m_{\mathrm{F}} = 1\rangle \rightarrow |F' = 2, m_{\mathrm{F}'} = 2\rangle$ σ^+-transition. As a result, the probe laser was already frequency stabilised to the repump transition. Since the EIT experiments required less than 1 mW of probe power, the remaining ~ 40 mW of optical power was free for repumping purposes. This configuration proved to be stable and reliable over an extended period. However, this approach constrained the experiments to probe frequencies connected to the $|F = 1\rangle$ ground-state. To lift this restriction, together with giving more optical power for each purpose, the repump was decoupled from the Raman laser system, and a dedicated Toptica DL Pro unit was acquired to provide the repump light.

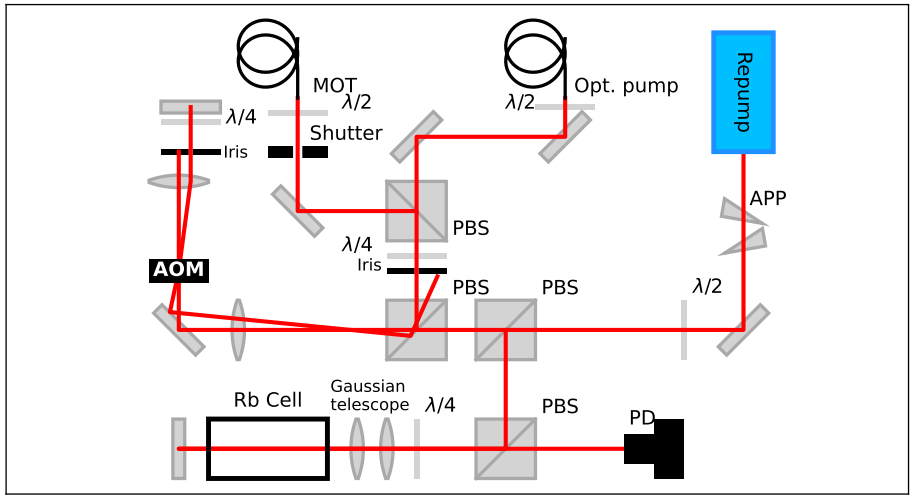

Figure 3.8: *Overview of the repump laser setup. An anamorphic prism pair reshapes the rectangular laser profile to improve coupling efficiencies. For spectroscopy, a Gaussian telescope expands the beam for improved signal-to-noise ratio. A double-pass AOM configuration frequency shifts by* 157 MHz *and two PM-SM optical fibres provides light to the MOT cell and the science chamber.*

A schematic of the repump laser system is shown in Fig. 3.8. An anamorphic prism pair (APP) reshapes the laser's rectangular output profile. This step is necessary because, unlike the other laser systems, the APP is not integrated into the repump laser head. The beam is then split into two branches using a $\lambda/2$ plate and a PBS cube. The reflection is directed to a Doppler-free saturation spectroscopy setup, where the beam is expanded with a Gaussian telescope to significantly improve the signal-to-noise ratio of the spectroscopy signal. The transmitted light passes through a double-pass AOM for a total frequency shift of 157 MHz, corresponding to the energy difference between the $5P_{3/2}$ $|F' = 1\rangle$ and $|F' = 2\rangle$ excited states. A two-lens configuration is employed for the double-pass AOM. The first lens focuses the beam to match the small AOM aperture, ensuring that it remains within the active region of the crystal. After the first pass, a second lens collimates and refocuses the beam for the second pass, after which the first lens collimates the output beam once more. This configuration improves coupling efficiency not only for the AOM but also into the PM-SM optical fibres that provide light to the MOT cell and the science chamber. The enhancement is likely due to better preservation of the beam profile after the AOM interaction, which results in a more effective mode matching to the fibre.

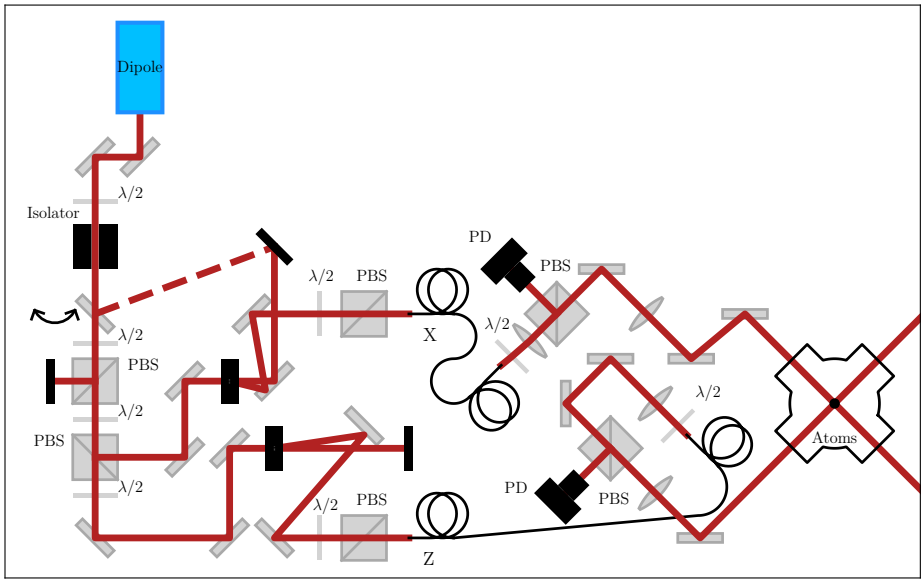

Figure 3.9: *Overview of the optical dipole laser system. A mirror mounted in a motorised flip mount enables safe dumping of the full optical power when the system is not in use. During operation, the beam is split into two branches, each providing one trapping beam. Two AOMs enable fast switching and frequency-shift the dipole beams in opposite directions by* $\pm 100\,\mathrm{MHz}$ *to suppress interference effects at the spatial overlap of the beams. Optical power control is implemented using a photodiode placed after the NKT hollow-core fibres. The photodiode signal is calibrated to absolute optical power and used in a PID feedback loop for active power stabilisation.*

Optical Dipole Laser System

The optical dipole trap was implemented in 2022 and has been characterised for experimental use in previous work [57]. The system employs a single high-power Azurlight systems fibre laser delivering up to 20 W of optical power at a wavelength of 1064 nm [1]. The choice of high intensity and far-detuning reflects the two key parameters: the absorption rate $R_{\mathrm{abs}} \propto I/\Delta^2$, and the trapping potential $U \propto I/\Delta$. Hence, it is possible to minimise the absorbed photons while keeping the trap potential useful by detuning the light field and cranking up the power

[1] During this thesis, while the unit was shipped for repairs, a similar 50 W unit was tested for continuation of experiments. It served as the dipole laser for some time, but the photodiode failed and the unit would turn off during experiments. This problem was fixed after the return of the 20 W, and hence the 50 W unit is currently not in use. Potentially, it can provide much tighter traps for high-density clouds, or provide enough power to load the MOT cooled cloud directly into a cODT, skipping the magnetic trap.

accordingly.

A schematic of the optical dipole laser system is shown in Fig. 3.9. The beam is elevated to a standard beam height of 7.5 cm using a periscope, and the laser head is protected from back-reflections by an optical isolator. A mirror mounted in a motorised flip mount enables safe dumping of the full optical power when the system is not in use. The first $\lambda/2$ plate and PBS cube pair is used for power adjustment, and enables a controlled fraction of the light to be safely dumped. This is particularly useful during system alignment. Once preliminary optical coupling is achieved at low optical powers and at minimum seed laser current, the full beam is transmitted and the seed laser is increased. As slight changes in the laser mode are expected at high output powers, the optical coupling efficiencies are re-optimised under high-power operation. In laboratory terms, this corresponds to a "*hot*" coupling of the system, which is always performed following the low power "*cold*" coupling. The laser output is split into two branches, each providing a trapping beam along one of the horizontal directions, $\hat{x}$ and $\hat{z}$. A second $\lambda/2$ plate and PBS cube pair balances the optical power between the two dipole beams. Each branch is frequency-shifted in opposite directions to minimise low-frequency beating at the spatial overlap of the trap. The AOMs also provide fast switching of the beams and, in combination with photodiodes and PID feedback loops, enable active stabilisation of the optical power. The reference voltages supplied by the experimental control system are calibrated to physical optical powers using power meters placed at the entrance to the vacuum chamber.

The optical fibres used in this laser system are hollow core fibres (NKT HC-1060) with a mode field diameter of $6.7\,\mu\text{m} \pm 1\,\mu\text{m}$, in which the majority of the optical mode propagates in air. This design makes them well suited for the high optical powers required for the dipole trap. The optical fibres divide the optical dipole setup in two, and optimisations can be performed on the input side without misaligning the cODT at the atoms. On the output side, the optical paths contain a $\lambda/2$ plate and a cleaning PBS cube, two lenses, the power monitoring photodiode and mirrors to direct the beams into the trap. The two beams are orthogonally polarised to mitigate beating between the dipole beams. To achieve this, the PBS cube in the $\hat{x}$-direction is rotated 90° around the beam axis. The first lens after each fibre is exchangeable and can be selected to set the final beam waist at the position of the atoms. Currently, an $f = 50\,\text{mm}$ ($f = 60\,\text{mm}$) out-coupling lens with a diameter of $1''$ is used in the $\hat{x}$ ($\hat{z}$) direction. The final convex lens has a diameter of $2''$ and a focal length of $f = 500\,\text{mm}$, and is mounted on a translational stage to allow fine adjustment of the beam focus position. The choice

of lens and distances is constrained by access to the vacuum chamber and, in particular, by the transport coils. Shorter distances would allow for smaller beam waists and improve the stability of the setup. Both dipole arms are equipped with a motorised mirror on the output side of the optical fibre, enabling fine positioning of the dipole beams inside the vacuum chamber with high reversibility, limited only by the small hysteresis of the Pico-motors. These mirrors are integrated into the same control environment as the PicoScope unit and FlexDDS unit, which allows straightforward optimisation of dipole beam overlap using absorption images as feedback. During setup, the beam waists are estimated by imaging each dipole beam onto a CCD camera and fitting the Gaussian intensity profile. After the cODT is realised, a collection of trap frequency measurements at variable intensities is acquired, and the beam waists are more accurately determined by modelling the trap [48].

3.1.4 Detection Setup

Two detection methods are employed to probe the atomic samples, and the complete optical setup for both detection methods is shown in Fig. 3.10. The first method is the well-established absorption imaging technique, described in Section 2.4.4. For this purpose, two CCD cameras (Andor iXon Ultra 897 EMCCDs) are arranged to image the atoms along each horizontal direction, using above-saturation imaging intensities typically after a time-of-flight expansion. The experimental implementation of this method has been thoroughly described in previous works [1, 2, 33]. The second method employs a nondestructive detection scheme using an attenuated weak probe field combined with a free-space avalanche single-photon detector module (Thorlabs SPDMH2). In this approach, the transmitted probe field consisting of either the diffracted probe field (dark-ground) or the sum of transmitted and diffracted probe fields (bright-field), is detected at the single-photon level, allowing measurements with minimal perturbation of the atomic ensemble.

The $\hat{x}$-direction is the primary imaging axis used for absorption images both in-situ and after time-of-flight expansion. Figure 3.11 shows the imaging system consisting of four lenses to relay the image of the atoms onto the CCD camera. Figure 3.15 illustrates the opposing $\hat{z}$-direction, which provides access to both absorption imaging and nondestructive detection in either bright-field or dark-ground configurations. A pinhole is placed in the intermediate image plane to spatially filter light around the atomic cloud, before the image is relayed onto a light-sensitive chip.

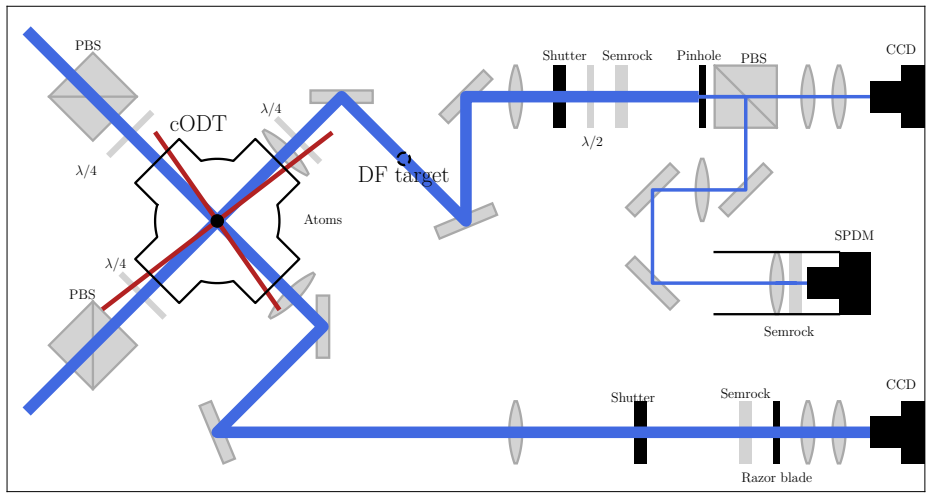

Figure 3.10: *Schematic of the detection system. Detection light (blue) combined with a pair of CCD cameras allow for absorption imaging along both horizontal directions. The CCD chips are partially masked by four razorblades ($\hat{x}$) or a pinhole ($\hat{z}$) placed at the intermediate image plane for faster data acquisition. The image is relayed onto the CCD chip by another pair of lenses. Slightly offset optical dipole beams (red) are safely dumped after the vacuum chamber, and residual dipole light in the detection mode is nulled by optical filters to properly protect all light-sensitive chips. An single-photon detector module is implemented in the $\hat{z}$-direction together with an optional dark-ground target, placed at the focus of the first lens.*

Absorption Imaging

As mentioned in Section 2.4.4, four images are acquired in two consecutive pairs. The first pair is taken in the presence of atoms. After the first image, the atoms are optically depumped into the dark state $|F = 1\rangle$, and the illuminated pixels are shifted into a dark region of the CCD chip. This allows the second image of the imaging beam to be acquired within approximately 340 µs, a timescale limited only by the pixel shift speed of the camera. Acquiring the two images in rapid succession significantly reduces fringe effects and noise originating from mechanical vibrations or laser intensity fluctuations. The images are transferred to the computer memory in ~ 500 ms. Subsequently, a second pair of images is acquired in an analogous manner, but with the imaging light switched off using AOMs while keeping all mechanical shutters open. These images account for the camera offset and dark-counts, as well as any residual background light present in the optical path. To further reduce dark-count noise, the CCD chip is cooled to $-40\,^{\circ}$C. The four images are used to construct the absorption image

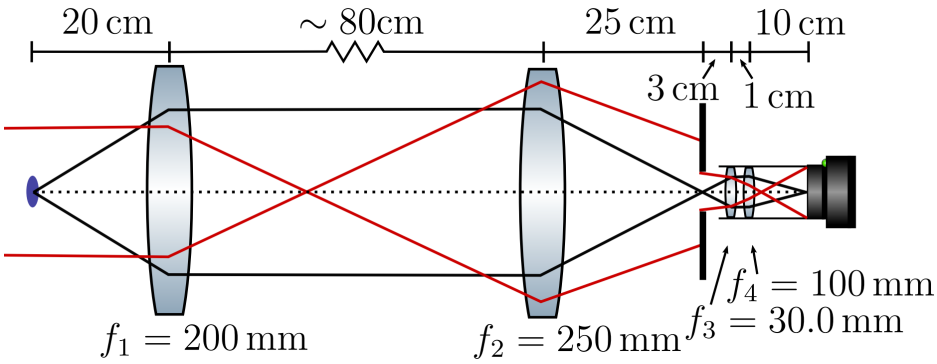

Figure 3.11: *Sketch of the imaging optics along the $\hat{x}$-direction. An intermediate atom image is cut by razor blades to black out part of the CCD chip to allow for two images to be taken quickly in succession. The intermediate image plane is imaged onto the CCD camera by another pair of lenses. The magnification of the ideal optical system is* 4.17. *Figure from [33].*

by subtracting the background contributions and calculating the optical density according to the standard absorption imaging formalism. The processed image of the column densities can be fitted to Eqs. (2.65) to (2.67) for information on atom numbers and temperatures. The details of the fitting procedure are described in previous works [33, 48].

For diagnostics and monitoring of the atomic cloud, absorption imaging can be performed simultaneously along both directions. However, an improved signal is achieved by imaging along only a single direction at a time. By employing magnetic field shim coils in an anti-Helmholtz configuration, the quantisation axis can be rotated along the imaging direction. This allows the imaging light to drive the closed cycling transition $|2,2\rangle \rightarrow |3,3\rangle$ as shown in Fig. 3.3. Figure 3.11 shows the optical system for imaging along the $\hat{x}$-direction. As shown in Fig. 3.10, it consists of two $2''$ mirrors, four lenses, a large-aperture shutter, a Semrock 780 nm single-band bandpass filter, and a set of four razorblades for blocking unwanted stray light and to partially mask half of the camera chip. This enables faster acquisition by shifting the illuminated pixels into a dark region on the sensor [35]. The intermediate image is relayed by the second pair of lenses onto the CCD chip. The final pair of lenses is mounted in a tube directly attached to the CCD camera, forming a fixed imaging unit. The alignment of the imaging branch requires careful optimisation to avoid clipping of the imaging beam, which would reduce the effective numerical aperture. To focus the camera, the objective is to overlap the camera focal plane with the intermediate image plane. This is achieved in

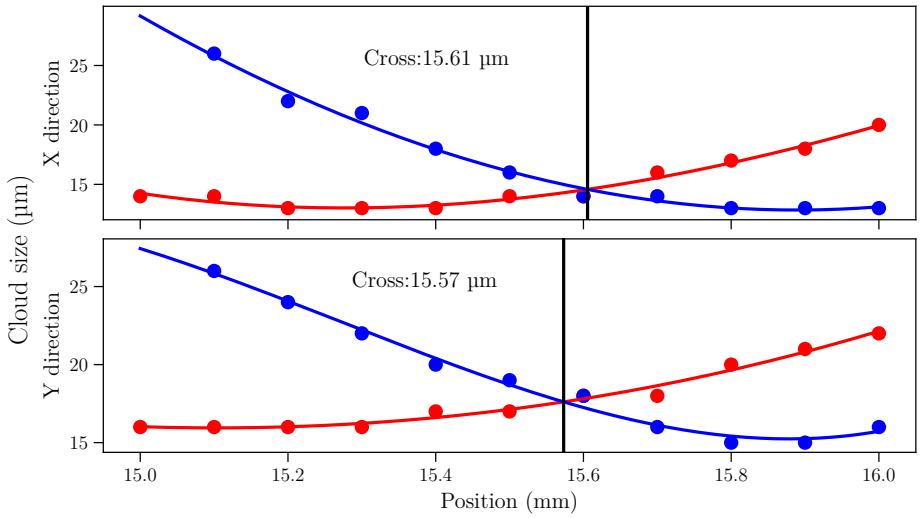

Figure 3.12: *Data obtained during the standard procedure for camera focusing. Absorption images are taken in both the red-detuned and blue-detuned regime at variable camera position, which is adjustable using a translational stage with a micrometre adjuster. The atomic cloud acts as a converging (diverging) lens for red (blue) detuned light. As shown in Fig. 3.13, the apparent cloud exhibits a broadened doughnut geometry or becomes narrowed, depending on the light detuning and camera focus with respect to the cloud position. When the camera is focused on the atomic cloud, the apparent cloud size in both detuning regimes agrees.*

two steps. First, the apparent size of a compact object in the intermediate image plane, such as a BEC, is minimised using resonant absorption imaging. This provides a coarse adjustment of the focus. In a second step, a translational stage equipped with a micrometre adjuster is used to systematically vary the camera position allowing fine-tuning of the focal plane. Due to the dispersive nature of the atomic refractive index near resonance, the atomic cloud acts as a weak lens. For red-detuned light it behaves as a converging lens, whereas for blue-detuned light it acts as a diverging lens. This effect, illustrated in Fig. 3.13, can be exploited to optimise the camera focus. To this end, absorption images are recorded with detuned imaging light (approximately $\pm 2\Gamma$) while varying the camera position. The optimal focus is determined by minimising distortions caused by atomic lensing. This procedure is illustrated in Fig. 3.12. When the cloud size extracted from red-detuned and blue-detuned images agrees, the dispersive lensing effects are minimised, and the camera is considered to be properly focused [33, 51].

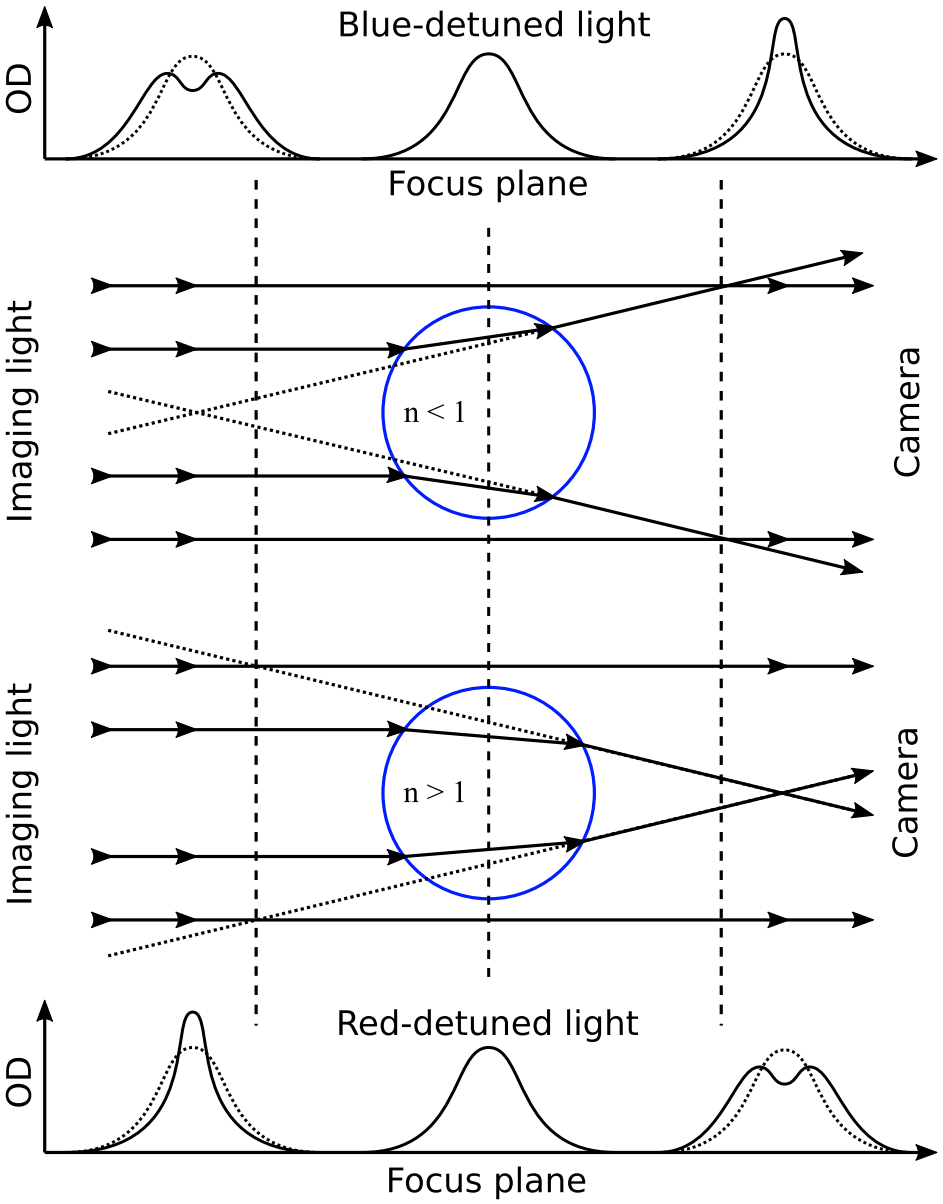

Figure 3.13: *The dispersive nature of the refractive index near a resonance can be used to focus the camera onto the atomic cloud. The cloud acts as a weak lens, which goes from converging for red-detuned to diverging for blue-detuned light. The apparent optical densities for a camera focused behind, on-top and infront of the cloud is shown for both the red-detuned and blue-detuned regimes. This phenomenon allows for a fine-tuning of the camera focus, as illustrated in Fig. 3.12.*

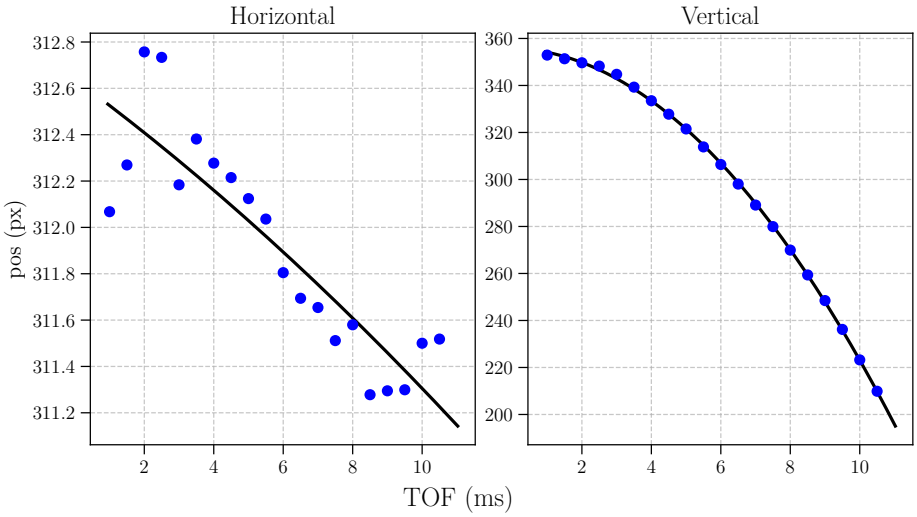

Figure 3.14: *Data obtained during a standard pixel size calibration. The centre-of-mass dynamics of an ultracold gas subject to gravitational free fall fitted in both the horizontal (left) and vertical (right) directions. The acceleration,* $a = \sqrt{a_x^2 + a_y^2}$ *is fitted to* $2.55(5)\,\mathrm{px\,ms^{-2}}$*. A pixel size of* $3.84(7)\,\mu\mathrm{m\,px^{-1}}$ *is determined by comparing the acceleration with the expected gravitational acceleration* $9.82\,\mathrm{m\,s^{-1}}$*. This is in fine agreement with a pixel size of* $3.837\,\mu\mathrm{m\,px^{-1}}$ *from the expected optical system magnification and the physical pixel size of* $16\,\mu\mathrm{m}$*.*

From the optical design in Fig. 3.11, the calculated magnification of the imaging system is 4.170. With a physical pixel size of 16 µm on the CCD, this corresponds to an effective pixel size in the atom plane of $3.837\,\mu\mathrm{m\,px^{-1}}$. However, this value does not account for imperfections in alignment and lens positioning. Therefore, an experimental pixel-size calibration is performed.

The calibration is based on time-of-flight expansion measurements. After release from the trap, the atoms are subjected to gravitational free fall. By acquiring a series of absorption images at varying time-of-flight durations and tracking the centre-of-mass position of the cloud, the acceleration due to gravity can be extracted. The magnitude of the acceleration is determined from the components along each direction via $a = \sqrt{a_x^2 + a_y^2}$. The measured acceleration is compared to the expected gravitational acceleration, $9.82\,\mathrm{m\,s^{-2}}$. An example calibration is shown in Fig. 3.14. From this procedure, the effective pixel size is determined to be $3.84(7)\,\mu\mathrm{m\,px^{-1}}$, corresponding to a magnification of 4.16(8), which is in good agreement with the optical design.

Absorption imaging is a standard technique that has been highly successful in the field of ultracold atoms. However, it suffers from the fundamental disadvantage of being destructive, as the resonant, above-saturation imaging light significantly perturbs the atomic cloud. Also, the method often requires releasing the atoms for a time-of-flight expansion for reliable probing of the high optical densities. Accurately modelling this expansion is computationally demanding, as it must account for interactions in high-density regions, light pressure from the imaging light, and cloud motion during imaging, and such analysis is unsuitable for fast analysis of everyday experiments.

Reconstructing real-time dynamical processes using absorption imaging requires a sequence of independent experimental cycles, preparing a new atomic cloud for each image. Consequently, preparation noise is introduced to the experiments. To mitigate this effect, technical atom number stabilisation methods have been developed. An example is the real-time analysis of Faraday imaging for control of an adaptive final evaporation ramp using an FPGA [34, 35, 55].

Such methods utilise far-detuned imaging methods that are less destructive. These alternatives rely on probing in the far-detuned regime and are therefore not suitable for resonant spectral measurements.

One of the main goals of this thesis is the development of a nondestructive measurement technique that extends from the far-detuned regime into the resonant regime. To qualify as a nondestructive measurement, the probe must interrogate the atomic cloud in-situ without causing significant atom loss or heating. For imaging-based approaches, this typically requires a high numerical aperture optical system and careful alignment to achieve sufficient spatial resolution at low probe intensities. In contrast, a single-photon detector module (SPDM) effectively operates as a single-pixel camera. While spatial resolution is compromised, the signal-to-noise ratio at a given optical power can be significantly higher. Furthermore, the effective frame rate is limited only by the detector dead time, which is substantially shorter than the frame rate of most CCD cameras.

The improved signal-to-noise ratio, particularly when combined with a dark-ground configuration, enables measurements at sufficiently low probe power to approach the nondestructive regime even with near-resonant light. In practice, no measurement is perfectly nondestructive and in this context, nondestructive means that no measurable atom loss or significant heating per probe pulse is observed.

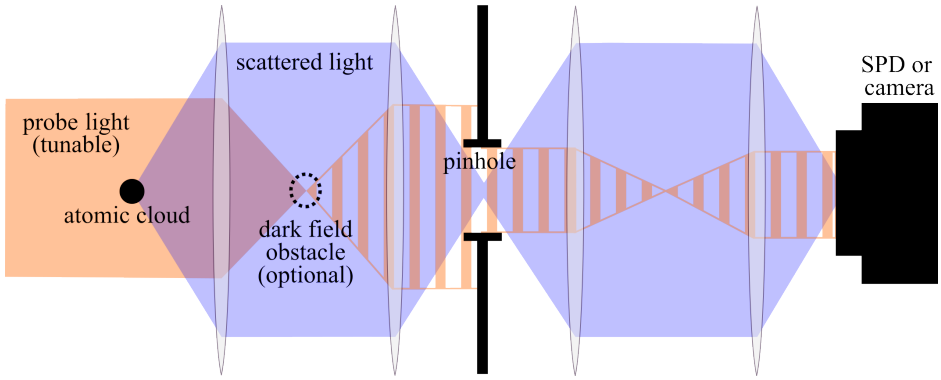

Figure 3.15: *Schematic of the detection setup along the $\hat{z}$-direction. Collimated probe light (orange) illuminates a cloud of trapped atoms that emit a scattered light field (blue). At the focus plane of the probe beam, an optional dark-ground obstacle can be placed to toggle between the bright-field and dark-ground configuration. In addition, a pinhole spatially filters the background light signal at the intermediate image plane. The configuration can be toggled between a single-photon detector module (SPDM) or a CCD camera during experiments.*

Single-Photon Detection

To measure the weak probe intensities used in nondestructive measurements a single-photon detector module (Thorlabs SPDMH2) is employed. The module consists of a silicon avalanche photodiode (APD) with a 100 µm diameter circular active area.

The APD is operated in Geiger mode, where the applied reverse bias voltage is set slightly above the avalanche breakdown voltage. In this regime, the absorption of a single photon generates a primary charge carrier (an electron-hole pair), triggering a measurable avalanche that produces a macroscopic current pulse [58]. To prevent damage to the APD and to extinguish the avalanche, the module employs active quenching electronics. Once an avalanche is detected, the bias voltage is lowered below the breakdown voltage, terminating the avalanche current. During this recovery period the detector is blind to incoming photons and this duration defines the detector dead time which is approximately 45 ns for the SPDMH2. This corresponds to a maximum count rate of approximately 22 MHz.

Typical experiments operate below a count rate of 10 MHz to improve the measured count rate accuracy. The dark-count rate is 100 Hz and mainly depends on thermally generated carriers. The active region is thermoelectrically cooled to mitigate the dark-counts and is placed in a sealed housing to protect it from

humidity and contamination. The photon detection efficiency depends on the wavelength (70 % @ 670 nm and 60 % @ 810 nm). For each photon detected, the SPDM outputs a TTL pulse lasting 15 ns with a 30 ns delay from photon impact. The signal is available for readout via an SMA connection.

The TTL pulses were recorded by a PicoScope 3406D oscilloscope for a significant portion of this thesis. While this approach worked for initial experiments, the PicoScope is fundamentally the wrong acquisition tool for this type of data. As a waveform digitiser, the PicoScope records the full voltage trace of the TTL signals, whereas only the timestamps corresponding to photon arrival events are required for analysis. Consequently, the majority of the recorded data is irrelevant.

Moreover, the "*streaming mode*", which transfers data to the computer in real-time, is too slow for the typical count rates encountered in experiments. Instead, the PicoScope was operated in "*block mode*", in which the voltage trace is recorded over a fixed duration and transferred to the main computer only after the acquisition is complete. Photon arrival timestamps are then extracted on the main computer in post-processing by identifying the rising edges of the TTL pulses. To resolve the 15 ns pulses, the PicoScope was configured with a 4 ns time base, restricting the acquisition window to a maximum of 512 ms due to the PicoScope's limited memory. To find a more suitable tool for data acquisition, the primary challenge is achieving nanosecond time resolution over probe durations on the order of several seconds.

This problem was resolved by implementing a time-tagger. Specifically, a Red Pitaya-125-14 unit. This is a development board based on a system-on-a-chip (SoC) that combines a processor with an FPGA. The FPGA is programmed to act as a time-tagger for processing TTL signals from the SPDM. It records timestamps corresponding to the rising edges of the square pulses with a 8 ns time resolution. The external software handles the time-tagging in parallel with a remote server that queries the tags, and passes the timestamps to the main computer.

The Red Pitaya has two inputs: one receives the TTL signals from the SPDM, and the other triggers the counting gate. Once the device is prepared, it waits for the counting gate to open. When the gate opens, it begins recording the timestamps of each rising edge from the SPDM signal, and when the gate closes, it stops counting. Counts are sent as 32-bit unsigned integers with an 8 ns time resolution. These counts are transferred in real-time to the main computer. This approach eliminates the post-processing of irrelevant data and removes the restriction on

the acquisition window.

A sketch of the optical setup is shown in Fig. 3.15. All optical components before the intermediate image plane were recently replaced with 3″ optics in order to increase the numerical aperture[2]. The detection arm branches to the SPDM after the intermediate image plane. A $\lambda/2$ waveplate mounted in a motorised flip mount, in combination with a PBS cube, enables controlled switching of the optical path, allowing the light to be directed either to the CCD camera or to the SPDM. The camera is focused using the same procedure described in Fig. 3.12. In contrast, the SPDM operates as a single-pixel detector, and hence its positioning is less constrained, provided that the light is accurately focused onto the active area of the chip. To maximise the SPDM detection efficiency, the alignment is optimised with feedback from the SPDM in real-time.

After the intermediate image plane, the light is first collimated by a lens and subsequently focused onto the active region of the detector by a second lens. The SPDM is shielded from ambient light by a protective tube, which also contains a narrowband pass filter to suppress stray light and residual dipole light in the detection mode before it reaches the detector. Since the SPDM branch is comparatively short and the first lens is positioned close to the intermediate image plane, 2″ optics are sufficient for this part of the optical system.

3.2 Experimental Improvements

Typically, the time spent on producing BECs far outweighs the time for a corresponding experiment. There are two ways to address this problem: either reduce the experimental duty cycle, thereby shortening the time required per data point, or extract multiple data points within a single preparation cycle. The latter approach naturally motivates the development of nondestructive measurement techniques. This thesis focuses on both strategies.

Prior to my tenure as a PhD fellow, the experimental duty cycle was approximately 90 s [33]. Through extensive optimisation, the duty cycle was reduced to about 30 s for a single run, and to 25 s per run in continued-mode operation. The continued-mode operation is employed for repeated experiments and systematic scans of predefined parameter spaces. This improvement can not be attributed to a single effort. On the contrary, it includes the redesigning of the MOT phase,

[2]This effort was motivated by numerical simulations of nondestructive spectroscopy experiments using the optical setup, which suggested the change would increase the detected signal significantly [48].

which enabled faster and more efficient loading, optimising the velocities and accelerations of the magnetic transport coils between the vacuum chambers, and refining the overall experimental sequence from the inital loading stage to the final release of the BEC. In addition to reducing the cycle time, these optimisations led to a substantial increase in BEC atom numbers, from approximately 100k to 700k atoms. The following section outlines the experimental sequence and highlight the key improvements that contributed to both the reduced cycle time and the greater BEC atom numbers.

3.2.1 MOT Improvements

The MOT phase was optimised, and every optical component surrounding the MOT cell has been rebuilt. This includes upgraded laser systems providing optical power for both cooling and repumping. The introduction of a MOT distribution board has improved stability, simplified maintenance, and enabled precise balancing of the optical power between each pair of telescopes. In addition, all telescopes were fully disassembled, cleaned, and reconfigured to ensure optimal beam quality and alignment.

As part of the redesign, the vertical telescope previously suspended from the ceiling above the MOT cell has been relocated onto the optical table to improve mechanical stability. In the previous configuration, the springs in the adjustable mount were nearly fully extended, reducing stability and limiting fine control. By mounting the telescope on the optical table, the mechanical support is improved and the adjustment range is better utilised. The beam is subsequently redirected into the MOT cell using mirrors.

The Rb dispensers were replaced, and the ion pump was "*hi-potted*" using 12 kV to intentionally generate arcs inside the vacuum chamber[3]. This procedure removes accumulated sputtered material, also known as whiskers, from the pump electrodes. As a result, the vacuum pressure in the MOT cell could be monitored more reliably. This, in turn, enables a more informed choice of dispenser current, balancing rapid MOT loading against atom losses during magnetic transport through the chamber and into the differential pumping tube. The high-voltage procedure was carried out using a power supply provided by the electronics department.

To monitor the fluorescence of the MOT cloud and to facilitate alignment and diagnostics, two CMOS cameras were installed in addition to the photodiode.

[3]Although hi-potting seems invasive to the vacuum chamber, the alternative is knocking a rubber hammer on the sides of the ion pump, potentially damaging the fragile glass MOT cell.

The photodiode provides a measure of the total atom number, while the cameras supply spatial information for beam alignment, power balancing of the MOT telescopes and optimisation of the overlap between the MOT centre and the high-field QPT centre.

Following the initial telescope alignment, the spatial overlap is fine-tuned using adjustable irises on all telescopes. This approach enables optimisation with a reduced cloud size while providing real-time camera feedback. The two cameras are aligned along the horizontal cooling beam axes, which is particularly useful for balancing the optical power between opposing telescopes. In this configuration, any cloud displacement along a horizontal axis directly indicates an imbalance in cooling beam intensity. To balance the cooling powers, the cloud fluorescence is monitored with the cameras while the magnetic field is abruptly switched off. Any imbalance in optical power results in a net radiation pressure force that blows the cloud along the dominant beam direction. When symmetric expansion is observed, the cooling beam powers are considered balanced.

The cameras are also used to align the optical overlap with the magnetic field centre at high coil currents. For this purpose, the displacement of the cloud position after transfer into the high-field QPT is compared to the original MOT centre. Ideally, this displacement is minimised, as any offset results in heating due to the sudden increase in potential energy. In addition, the cameras assist in monitoring the MOT cloud geometry, which is useful for diagnostic purposes. Subsequent efforts focused on the implementation of sub-Doppler cooling. The present configuration of the compressed MOT (CMOT) phase is described in recent work [48], where the next steps towards implementing an optical molasses stage are also outlined.

3.2.2 Improvements of Atom Transport

After the MOT phase, the atoms are optically pumped to the most magnetically trappable state $|2, 2\rangle$ and subsequently transferred into a dark QPT. The QPT is transported to the higher-quality vacuum science chamber using a conveyor belt controlled by a mechanical postioning system. Transporting the MOT-cooled cloud through the vacuum chamber inevitably leads to atom losses due to background gas collisions. In particular, the differential pumping tube, a long cylindrical orifice that maintains a pressure gradient between the two chambers without the need for valves, introduces significant losses. To improve the transfer efficiency through the differential pumping tube, the magnetic transport coils were vertically

repositioned.

The number of atoms in the MOT cell can be monitored by applying a short pulse of cooling light and measuring the resulting fluorescence signal on a photodiode. This method enables a systematic recapture measurement for monitoring relative atom numbers. In such measurements, the MOT cloud is prepared and transferred into the QPT, held for a variable time or transported a variable distance, and then returned to the MOT region, where the atoms are subsequently illuminated with cooling light, and the fluorescence signal is recorded. This procedure allows verification of optical pumping efficiency and identification of loss mechanisms during transport. Prior to optical pumping, the atoms are equally distributed among the eight ground-state Zeeman sublevels. However, only three of these states are magnetically trappable in the QPT. Failure to prepare the MOT cloud in the stretched $|2, 2\rangle$ state therefore results in a loss of roughly 5/8 of the atoms.

Recapture measurements were also performed for varying transport distances, as shown in Fig. 3.16. A significant loss occur at approximately 20k motor steps, which is indicated by a vertical line in the figure. This corresponds to the position of the differential pumping tube. At this stage, the confined cloud in the tight QPT is partially clipped by the narrow aperture, making the differential pumping tube the dominant source of loss during transport.

Although the absolute fluorescence levels depend on the MOT loading conditions, the background pressure, the cooling light intensity and detuning, the relative changes provide insight into lifetimes and transfer efficiencies. For reference, the background pressure in the MOT cell is typically between 10^{-10} Torr to 10^{-8} Torr. Fitting the fluorescence decay to an exponential model indicates that approximately 91 % of the MOT fluorescence is initially transferred into the QPT, and about 76 % of the atoms reach the entrance of the differential pumping tube. After passage through the tube, the recapture fraction drops to approximately 30 %. This is a significant loss, but the advantage of the science chamber is the substantially longer lifetime due to the improved vacuum conditions.

Recapture measurements are an essential diagnostic tool for assessing early stage efficiencies in transfers and optical pumping. It quantifies the performance of each stage in the transfer from the MOT cell to the science chamber.

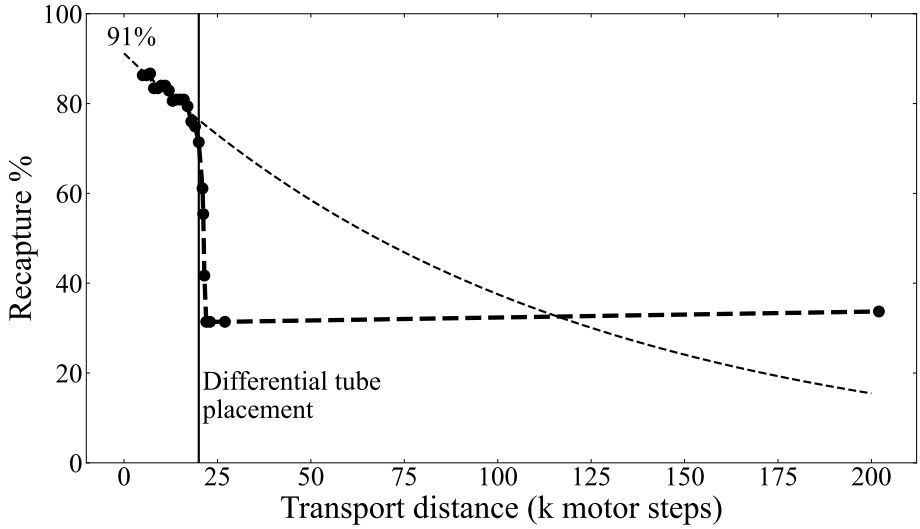

Figure 3.16: *Data obtained during a recapture experiment. The fluorescence level is monitored after a variable transport length and compared to the signal of the MOT fluorescence level for a relative measure of atom numbers. Losses in the MOT cell are primarily due to background gas collisions. Approximately* 91 % *of the cloud is transferred into the QPT, and about* 76 % *of the atoms reach the entrance of the differential pumping tube. After passage through the tube, the recapture fraction has dropped to approximately* 30 %*. The advantage of the differential pumping tube is the substantially longer lifetime in the science chamber due to the improved vacuum conditions.*

3.2.3 Improvements to the Experimental Sequence

With the atoms transferred into the science chamber, the next step is RF evaporative cooling in the QPT. This technique exploits the spatially varying Zeeman splitting in the QPT to drive spin-flip transitions at selected energy surfaces addressed by resonances in the RF regime [30]. Atoms with energies above the RF-defined threshold are transferred into untrapped states and removed from the trap. Subsequent elastic collisions lead to rethermalisation of the remaining ensemble at a lower temperature, thereby realising active evaporative cooling. The RF field is often referred to as an RF knife that is lowered into the high-energy tail of the Boltzmann distributed thermal cloud to reduce the temperature.

Besides the experimental simplicity in realising a QPT, it provides a large trapping volume and deep trap depth, making it well suited for the early evaporation stage of a MOT-cooled cloud. The large mode-matching volume allows efficient capture of atoms after transport [59]. However, the magnetic trap is sensitive to the

atomic state and relies on the condition that the atomic magnetic moments adiabatically follows the local magnetic field direction. Near the centre of the QPT, where the magnetic field strength vanishes, this condition breaks down. Atoms passing through this region can undergo non-adiabatic spin flips, known as Majorana spin-flip losses, and are ejected from the trap. These losses become increasingly significant at low temperatures, where the atomic cloud is localised near the field zero. This ultimately limits the efficiency of evaporation in a pure QPT. Since the Majorana spin-flip losses prohibit an efficient evaporation path to achieve BEC, the goal of the RF evaporation is to cool the atomic cloud to a temperature compatible with the trap depth of the cODT, where evaporation can be continued without Majorana losses. The entire evaporation sequence was systematically optimised, resulting in both larger BECs and a substantially reduced total experimental cycle time.

RF evaporation in a QPT is controlled by several interdependent parameters. The magnetic field gradient determines the trap stiffness and cloud density. Increasing the confinement enhances the elastic collision rate, which improves rethermalisation and accelerates evaporation. However, higher density also increases inelastic collision rates, particularly three-body recombination, whose rate scales with density cubed. As evaporation proceeds and the cloud becomes colder and denser, three-body losses can significantly reduce efficiency. For this reason, the magnetic field gradient is dynamically lowered during evaporation, weakening the confinement, reducing density-dependent losses, and modifying the evaporation dynamics. In addition, to the QPT parameters, each RF frequency ramp is controlled by a duration, the rate of change, and the total frequency range. Consequently, the RF evaporation sequence represents a trajectory through a high-dimensional parameter space, where many parameters are strongly correlated. Optimising such a sequence requires a systematic approach.

The initial RF frequency is determined experimentally by applying RF radiation and gradually lowering the frequency while monitoring atom loss via absorption imaging. A dataset is shown in Fig. 3.17. A sharp onset of loss indicates the energy threshold corresponding to the cloud edge. The evaporation sequence is initiated slightly above this threshold to account for preparation instabillities.

Then, an exponential ramp is approximated by a number of linear steps[4] each characterised by a frequency range and a time duration. Each evaporation step is

[4]A single exponential RF sweep was tested, but the linear ramps are robust, they provide similar efficiency, and importantly, they are much simpler to optimise and modify.

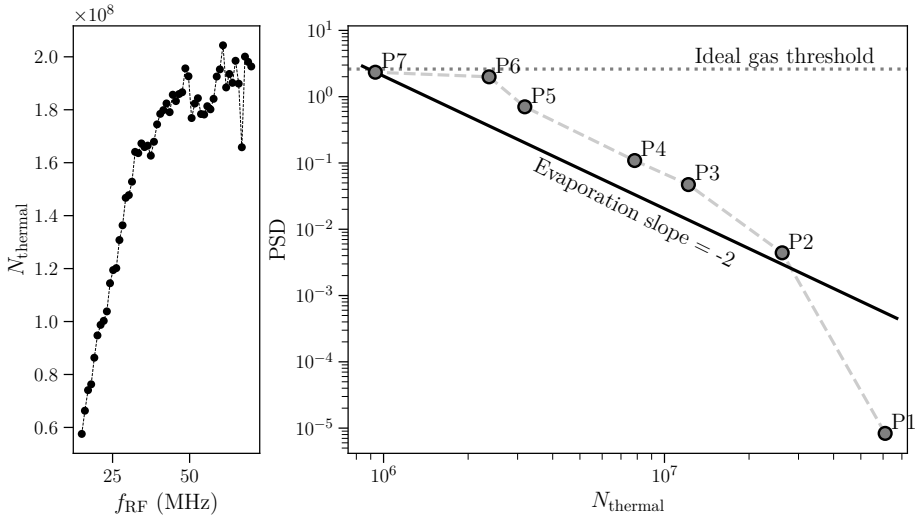

Figure 3.17: *Evaporation maps. (Left): The initial RF frequency for the evaporation map is determined via absorption imaging, by lowering the RF frequency until a significant atom loss occurs. (Right): The entire phase-space density vs. atom number map of the experimental evaporation sequence from the initial thermal cloud to the final BEC on a log-log plot. Points along the evaporation ramp is annotated by Px for integer x. Points with $x < 3$ correspond to the pure magnetic QPT, $x = 3$ marks the hybrid trap stage and $x > 3$ corresponds to the pure optical cODT. A slope of -2 represents the empirical scaling for efficient evaporation: losing one order of magnitude of atoms increases the phase-space density by two orders of magnitude. The critical phase-space density for a uniform 3D ideal gas is* 2.61*, indicated by the dotted line.*

evaluated on a log-log plot of phase-space density (PSD) versus atom number (N), where an efficient evaporation is expected to follow a slope of -2. This corresponds to two orders of magnitudes gain in phsae-space density per magnitude lost in atom number. Optimisation proceeds iteratively, and each ramp duration is scanned while evaluating the cloud parameters on a PSD vs. N log-log plot. A deviation from the efficient evaporation, typically appearing as a kink in the evaporation path, signals the onset of Majorana spin-flip losses. This point defines the practical lower temperature limit of evaporation in the pure QPT. More details on the optimisation procedure is found in [57].

Above the Majorana threshold, the atoms are transferred to a hybrid trap following the procedure described in [59]. The transfer is performed by reducing the magnetic field gradient below the levitation threshold such that the atoms fall in a gravitationally mitigated free fall into the optical dipole beam, where they

are caught. The hybrid trap configuration combines a tightly focused, red-detuned, high optical power Gaussian dipole beam for radial trapping with longitudinal confinement provided by the weak QPT. Typical beam waists lie between 50 µm to 100 µm. The hybrid trap is still state-sensitive. Hence, the vertical offset should be larger than the beam waist to reduce atom losses, while not too large to heat up the cloud during transfer. The evaporation continues by lowering the optical dipole power while gravity assists the removal of energetic atoms. The levitation condition is determined by balancing the magnetic force with gravity, $B' = mg/(m_\mathrm{F} g_\mathrm{F} \mu_\mathrm{B})$, which is approximately $15.3\,\mathrm{G\,cm^{-1}}$ for $m_\mathrm{F} = 2$. An experimental measurement of this is described in [57]. Operating below this threshold ensures that atoms leaving the optical potential are not re-captured by magnetic confinement. This continues until the dominant dipole beam is comparable in optical power to the secondary dipole beam. At this point, the magnetic field is gradually nulled, while the atoms are transferred into the spatial overlap of a cODT.

A MW sweep prepares the cloud in the $|1,1\rangle$ ground-state, which has a measurably longer lifetime ($\tau \sim 12.4\,\mathrm{s}$) in the cODT compared to the $|2,2\rangle$ ground-state ($\tau \sim 3.2\,\mathrm{s}$). Obviously, the indicated lifetimes are dependent on the specific trap configuration, but the key difference remains the same: one ground-state is more stable than the other. The $F = 2$ state carry extra internal energy equivalent to the hyperfine splitting of 6.834 GHz, and during spin-exchange collisions, the energy is converted into kinetic energy. The hyperfine splitting corresponds to about 330 mK, which is way above the typical cODT trap depth on the order of µK. The MW state preparation is only possible in the state-insensitive cODT, as the $|1,1\rangle$ is not magnetically trappable. This, together with the magnetic field degree of freedom, is among the advantages of a cODT. For reference, an asymmetry in the MW frequency sweep direction is presented and explained in Chapter 4 alongside experiments that utilise MW pulses to drive MW Rabi transitions. Evaporation in the optical trap continues until the desired regime is observed via absorption imaging, be it thermal, bimodal, or pure BEC. After the final image is acquired, the MOT loading phase is immediately initiated while the remaining experimental systems are reset and data is transferred to the computer. The MOT reloading significantly reduces the effective cycle time in the continued-operation mode, often saving the entire MOT stage of 10 s to 15 s for consecutive runs.

This experimental sequence primarily describes the production of an ultracold atomic sample. In practice, however, the actual physical investigation using the

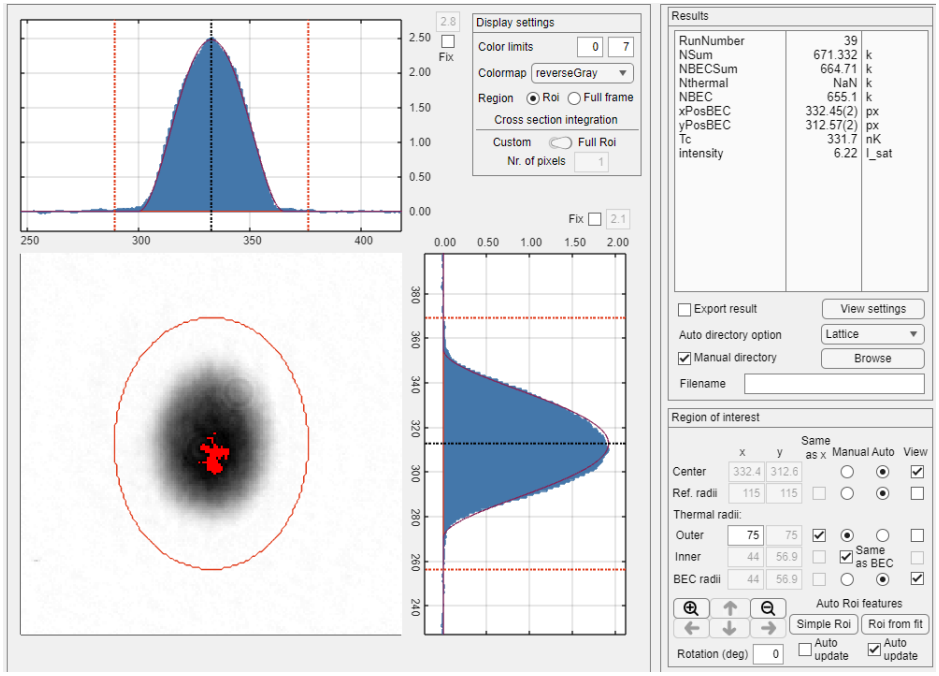

Figure 3.18: *An absorption image of the greatest BEC produced during my employment as a PhD student. The image was captured following a full calibration procedure of the CCD camera, and the produced BEC was measured after a* 38 ms *time-of-flight expansion. This represents the largest BEC produced in the group over the past* 20 *years.*

ultracold gas is performed after the final evaporative cooling stage and before the first destructive absorption image is captured.

The central objective of this thesis has been the implementation of a novel detection technique capable of probing the atomic cloud in-situ. Thus, the preparation sequence is followed by the experimental probing stage, and only afterwards by standard detection, providing more data per cloud. Figure 3.19 presents a representative in-situ probe spectroscopy measurement obtained while varying the coupling field strength. In the absence of the coupling field, the probe exhibits a Lorentzian absorption profile characteristic of a two-level transition. For weak coupling strengths, a narrow transparency window emerges due to EIT. At higher coupling strengths, the system enters the AT regime, where the excited state is dressed by the strong coupling field, resulting in a clearly resolved doublet in the absorption spectrum.

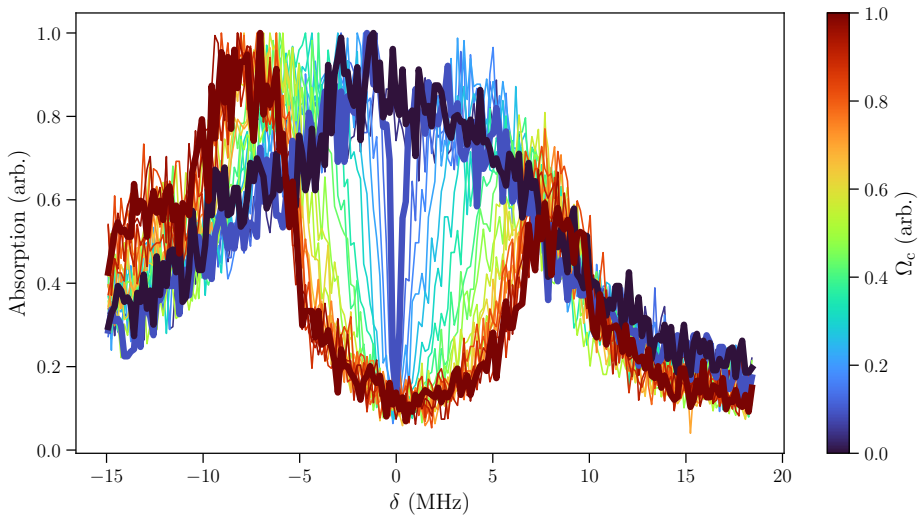

Figure 3.19: *Two-photon spectroscopy on a three-level system at varying coupling field strength in the dark-ground imaging configuration. In the absence of a coupling field, the Lorentzian absorption profile is observed (black), while the spectroscopy exhibits an EIT transparency window at weak coupling fields, and at increasing coupling strength it transforms into two split Lorentzians in the AT regime.*

3.2.4 Tight cODT Configuration

Part of this thesis focused on investigating the light-induced dipole-dipole interaction. Initially, this effect was probed using the EIT transparency window. In the absence of dipole-dipole effects, the EIT bandwidth scales[5] with $1/\sqrt{\text{od}}$, equivalent to a scaling with density of $1/\sqrt{n}$, arising purely from the cumulative effect of the single-atom absorption line profile to the total absorption of the cloud. However, a theoretical simulation framework developed by Prof. Thomas Pohl and Dr. Jan Kumlin from TU Wien predicts that in the presence of light-induced dipole-dipole interactions, this scaling should be modified to approximately $1/n$. To probe this effect experimentally, the high peak densities in BECs were initially exploited. Achieving densities on the order of $n \sim 100/\lambda^3$ was of a particular interest, as this regime is theoretically predicted to enhance dipole-dipole interaction effects. According to Eq. (2.44), the peak density of the condensate scales as:

$$n_0 \propto N_0^{2/5} \bar{\omega}^{6/5} \propto \frac{N_0^{2/5} P^{3/5}}{w_0^{12/5}}, \tag{3.1}$$

[5]From Lambert-Beers law, $T \propto e^{-\text{od}}$, and expansion of the transmission window to second order around $\delta = 0$, gives an approximate Gaussian with a width of $1/\sqrt{\text{od}}$.

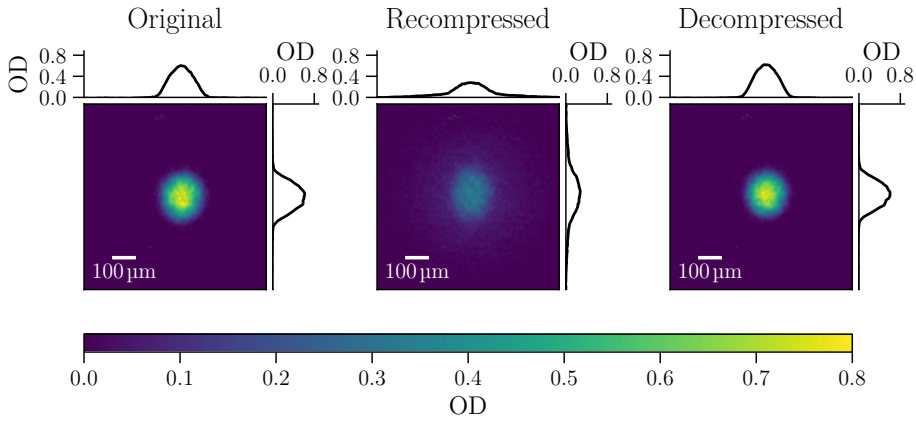

Figure 3.20: *Absorption images of a purely condensed atomic cloud in a cODT during a recompression cycle. The sequence shows the cloud before compression (left), at compression (centre) and after decompression (right). Cross-sectional optical densities (OD) are supplied alongside each image, representing the mean signals within a* $\pm 20\,\mathrm{px}$ *window around the cloud centre. This technique allows for the production of ultra-high density samples required for investigating light-induced dipole-dipole effects.*

where the second proportionality relates the mean trap frequency to the optical power and beam waist for an ideal cODT in the absence of gravity [57]. Although this is an idealised estimate, it provides a clear roadmap for identifying the experimental parameters that most strongly influence the peak density.

Atom number: The experiment is already optimised for BEC atom number, making further gains in N_0 difficult. Furthermore, Eq. (3.1) demonstrates that the peak density scales weakly with atom number. This is not a suitable parameter for substantially increasing the density.

Optical power: During evaporation, the power must be ramped down below a critical threshold to obtain a BEC. Nevertheless, as shown in Fig. 3.20, the power can be increased after condensation to adiabatically compress the cloud. While this strategy successfully enhances density, it comes at the cost of modest heating.

Beam waist: Eq. (3.1) reveals that the beam waist is the most critical parameter. Consequently, reducing the beam waist is the most effective approach for generating high-density samples.

During the course of this thesis, the optical dipole setup was modified, and stable operation was demonstrated for beam waists between 50 µm to 100 µm.

The fundamental lower limit on the waist is governed by geometric constraints, specifically, the transport coils prevent the final focusing lens from being positioned close to the vacuum chamber.

At a working distance of approximately 500 mm, the optical setup becomes increasingly sensitive to beam-pointing drifts. Despite these challenges, BECs were successfully produced using final beam waists of approximately 15 µm, achieving peak number densities between $200/\lambda^3$ to $300/\lambda^3$. Operating at such small beam waists places stringent requirements on stability and alignment, and even minor drifts translate into significant spatial displacements at the position of the atoms. Consequently, maintaining efficient atom transfer between the trapping stages, from the QPT to the hybrid trap and subsequently from the hybrid trap to the cODT, requires careful optimisation. In particular, the spatial overlap of the tightly focused cODT beams is highly sensitive to small misalignments and angular drifts and therefore requires *daily* optimisation. This is in stark contrast to when the experiment is operated with larger beam waists, where the increased trap volume provides substantially greater alignment tolerance.

Although reaching such high atomic densities was a prerequisite for observing light-induced dipole-dipole broadening of the EIT transparency window, the actual measurements proved significantly more challenging than initially anticipated. Three main arguments will now be presented.

(1): The Raman laser system was originally constructed to probe EIT, exploiting its narrow spectroscopic feature to achieve high precision in measuring the weak broadening phenomenon. In practice, however, EIT offers no intrinsic metrological advantage for this purpose: the change in linewidth scales relative to the EIT window itself. Consequently, the required *relative* precision remains unchanged, while the experimental complexity increases substantially compared to standard absorption spectroscopy.

(2): Utilising EIT introduces several additional parameters, such as the coupling Rabi frequency, two-photon detuning and ground-state dephasing, which complicates both the experimental operation and theoretical modelling.

(3): Complete transparency is never achieved due to residual dephasing processes. Even if the extreme optical density in-situ for a BEC, which can easily be on the order of 300 to 500, is reduced by 99% via EIT, the integrated attenuation is still far too large. For instance, suppose the reduction in OD is from 300 to an OD of 3, then the transmission is $T = e^{-3} \approx 5\,\%$, and the "*strong*" transparency is yet far from complete transparency. Consequently, at the large optical densities, the

atomic cloud remains optically thick even under EIT conditions: EIT is simply not transparent enough.

For bimodal clouds, the observed transmission, which is the integrated transmission over the pinhole area, is dominated by the lower-density thermal component, effectively masking the contribution from the high-density condensate that is of primary interest in the context of the light-induced dipole-dipole effect. Previous investigations [60–62] have circumvented this obstacle by using very tight dipole traps of waists of approximately 1 µm. Consequently, the atom number can be reduced to a few hundred, yielding high atom density at a low optical density.

Recognising that EIT is not the appropriate tool for probing the effect, the investigation of light-induced dipole-dipole interactions was ultimately paused. Subsequently, the experiment was reoriented towards probing simpler absorption spectra of atomic clouds at variable densities. This shift of gears led to the development of a nondestructive probing technique that required a detailed characterisation of the observed dark-ground spectra. After demonstrating this detection technique, high-density experiments can be resumed using the nondestructive technique to probe the clouds.

CHAPTER 4

Few-Photon Probing of Ultracold Atoms

This chapter presents the main results obtained from nondestructive measurements, organised into two articles. All experiments are enabled by three newly implemented modules: the Raman laser system with its versatile probe laser, a single-photon detection system providing high temporal resolution, and a dark-ground imaging configuration that enhances the signal-to-noise ratio and offers sensitivity to dispersive phase shifts.

The first article employs spectroscopic measurements to estimate thermodynamic quantities such as the atom number and temperature. Results from in-situ probing are shown to be in quantitative agreement with those obtained using standard absorption imaging after time-of-flight expansion. Importantly, the method extends beyond the conventional imaging regime, providing enhanced sensitivity to weak thermal components even at high condensate fractions.

The second article presents a catalogue of a new class of in-situ minimally destructivity measurements enabled by the setup. Time-resolved measurements performed on a single atomic cloud demonstrate the flexibility of the technique, and show accelerated experiments with calibrations and parameter optimisations completed in minutes rather than hours. The probe pulse can be configured either as a single fixed-frequency pulse or as a frequency sweep over a defined range, with adjustable contributions from resonant and far-detuned components.

However, specifying a single quantitative measure of destructivity is challenging. A comprehensive characterisation would require systematic measurements across a range of temperatures, frequencies, and probe intensities. In practice, no measurement is perfectly nondestructive. In this chapter it implies negligible atom loss and minimal heating per probe pulse. For the experiments presented in this chapter, the degree of destructivity depends on factors such as trap configuration, atomic density distribution, temperature and probe parameters. Qualitatively, the probe pulse intensity was chosen such that the atom loss per pulse, measured via absorption imaging, remained below 10 %, which is on the same order as typical preparation noise. This choice reflects the fact that the experiments are performed on a single atomic cloud, mitigating the impact of preparation noise. The probe intensity can be reduced significantly below this threshold while maintaining acceptable data quality, albeit at the cost of signal-to-noise ratio. If needed, experiments can be repeated at much weaker probe intensities, introducing preparation noise but further decreasing the destructivity. Other possibilities for reducing destructivity include the use of detuned single fixed-frequency pulses and spectroscopy restricted to frequency spans far from resonance.

Few-photon spectroscopy of Bose-Einstein condensates

R. M. F. Andersen,[1] L. N. Stokholm,[1] I. Zebergs,[1] N. R. Neubert,[1] A. S. Chatterly,[1] N. Kjærgaard,[2] and J. J. Arlt[1]

[1] *Center for Complex Quantum Systems, Department of Physics and Astronomy, Aarhus University, Ny Munkegade 120, DK-8000 Aarhus C, Denmark.*

[2] *Department of Physics, Quantum Science Otago (QSO), and Dodd-Walls Centre for Photonic and Quantum Technologies, University of Otago, Dunedin, New Zealand.*

Ultracold quantum gases are typically detected by using destructive absorption imaging. Here, a complementary spectroscopic detection technique is presented that enables minimally destructive measurements of the ensemble parameters, without relying on spatially resolved imaging. The method uses few-photon detection in bright field and dark field configurations based on a frequency-agile laser system. The light propagation through a bimodal density distribution is modeled to describe the measured spectra. The method is experimentally implemented for ultracold ^{87}Rb clouds in a crossed optical dipole trap and benchmarked against conventional absorption imaging after time-of-flight expansion. Both configurations are shown to contain distinct signatures of the condensed and thermal components, and in particular, the dark field technique allows for precise measurement of the cloud parameters. The spectroscopically obtained temperatures and thermal atom numbers agree with time-of-flight results within $\pm 10\,\mathrm{pm}$ across a broad parameter range. Importantly, spectroscopic measurements show superior sensitivity to small thermal fractions in nearly pure condensates. This allows the measurement of very low temperatures, which are typically difficult to access. The technique operates at low probe powers and avoids modeling of expansion dynamics, and thus it provides a complementary method for characterizing ultracold gases at low temperatures.

I. INTRODUCTION

Extracting information about ultracold clouds is typically achieved by exploiting the physics of light-matter interaction. There are many alternative methods with their own advantages and disadvantages.

The most common method is absorption imaging in a bright field (BF) configuration after time-of-flight (TOF) expansion [1–5]. Other BF techniques include frequency modulation imaging [6], dual-port Faraday imaging [7], partial-transfer absorption imaging [8], imaging with a phase spot [9], off-resonant defocus-contrast imaging [10], and inverse holography [11].

Additionally, there are many dark field (DF) techniques which have been used on resonance [12, 13] as well as far-off resonant to achieve phase contrast imaging [14–17], spatial heterodyne imaging [18], and Faraday imaging [7, 19, 20]. All the DF methods listed here use post-processing of the light, for example by placing an opaque target in the point of the imaging beam focus after a lens. However, it is also possible to a non-Gaussian incoming light beam such that the resulting image becomes DF, which is more common in fields outside of ultracold atoms [21].

Each of the imaging techniques referenced here use only one specific imaging light detuning, and most have implemented cameras to obtain spatial resolution. This paper investigates the signals from ultracold atom clouds across the full spectrum in in-trap BF and DF scalar imaging setups using a single-photon detector (SPD) instead of cameras. Section II introduces the theoretical framework and experimental techniques necessary to measure the spectra and extract cloud parameters from spectroscopic fits, and Section III compares the extracted cloud parameters from fitted spectra to the established TOF imaging method.

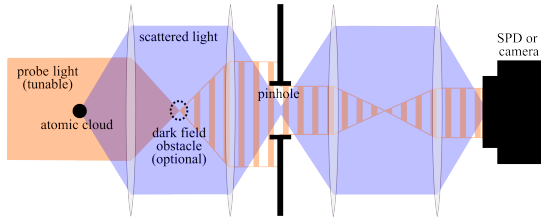

FIG. 1: Schematic of the detection setup. Collimated probe light (orange) is sent through a cloud of trapped atoms, and some of the light is scattered (blue). At the focus plane of the probe beam, an optional small dark field obstacle can be placed to block only the unscattered light. Additional filtering is achieved by a pinhole at an intermediate image plane. Either a single photon detector (SPD) or a camera is placed at the second image plane.

II. SPECTROSCOPY OF PARTIALLY CONDENSED ATOMIC CLOUDS

A. Detection system

The spectral characterisation method uses a $4f$ imaging setup as depicted in FIG. 1, and combines a CCD camera for spatially resolved images with a single-photon detector (SPD) that can record the power integrated over the imaged area with high sensitivity. The light used

for spectroscopic measurements will be referred to as the probe light. In a perpendicular direction, a second CCD camera is positioned to take images after time-of-flight (TOF), and the light used in this direction will be referred to as the imaging light.

By inserting a DF obstacle, the unscattered light is spatially filtered [22], which increases the SNR for the recorded spectra and allows experiments to use weaker probe powers for less destructive measurements. The DF obstacle inserted and removed easily allowing the possibility of both BF and DF configurations. A pinhole is placed in the intermediate image plane to select an effective area around the atoms that contributes to the recorded spectrum. While the pinhole is imperative in the BF configuration, it is also helpful for the DF spectra, since the obstacle never blocks all of the light.

To measure the spectra, the experiment uses ultracold ^{87}Rb in a crossed optical dipole trap (cODT) with approximately 80 µm waists. The atoms are prepared in the $|F = 2, m_F = 2\rangle$ ground state, and a weak light field is used to probe the cloud with σ^+-polarization, such that it can interact only with the cycling transition. The probe laser frequency is beat-locked to a second laser with an optical phase-lock loop (OPLL) [23], allowing for a wide frequency span. The atoms can be released for TOF imaging, where a second laser field resonant with the cycling transition is used to image the cloud. The pinhole has a diameter of 150 µm, and the DF target is a metal wire with a width of 200 µm. The numerical aperture (NA) of the described setup in the probe field direction is 0.18, and Rayleigh's criterion [24] predicts a resolution of 2.6 µm. Thus, the NA is not sufficient to resolve the in-trap distribution of atoms, which also affects the measured spectra, but is simple to account for with a model discussed in Section II E. A complete description of the experiment to produce partially condensed ultracold atomic samples can be found in [25, 26].

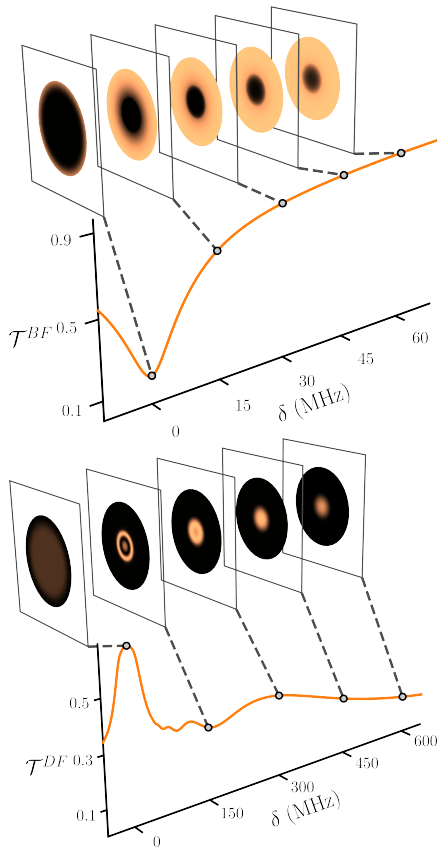

FIG. 2: Simulated bright field (top) and dark field (bottom) spectrum of an exemplary bimodal cloud with $1.7 \cdot 10^5$ condensed atoms, $5 \cdot 10^4$ thermal atoms, and a temperature of 130 nK in a symmetrical harmonic trap with trap frequencies $2\pi \cdot 100$ Hz. Insets show corresponding intensity profiles of the light in bright field and dark field configurations immediately after the cloud at different detunings.

B. Ultracold cloud spectra

The intensity profile $I(x, y)$ of the light field in a plane immediately after a bimodal cloud is illustrated in the top panel of FIG. 2 at various detunings of the probe light δ. The intensity profile is plotted only within the region of the pinhole, which is chosen to be only 75 µm here for clearer illustrations.

Since the SPD detects the entire intensity profile simultaneously, any modelling of the observed spectroscopic signals requires the intensity profile to be integrated over the recorded area. The incoming probe light has an initial intensity of I_0, and is assumed to be constant over the pinhole region, which has an area A when it is back-propagated through the optics to the atomic plane. The transmitted light recorded by the SPD in BF is denoted by $\mathcal{T}^{BF}$, which is normalized to the incoming probe power $I_0 A$. Then,

$$\mathcal{T}^{BF} = \frac{1}{A} \int_{\text{pinhole}} t(x, y)^2 \, \mathrm{d}x\mathrm{d}y, \tag{1}$$

where $t(x, y)$ is the spatially dependent electric field transmission coefficient through the cloud. This can be calculated as

$$t(x, y) = \exp\left(- \int_{-\infty}^{\infty} \mathrm{Im}\left(n(x, y, z)\right) k \mathrm{d}z \right), \tag{2}$$

where [9, 27]

$$n(x, y, z) = \sqrt{1 + \frac{\chi(x, y, z)}{1 - \frac{1}{3}\chi(x, y, z)}}, \tag{3}$$

is the Lorentz-Lorenz model for the complex index of refraction, and the susceptibility $\chi(x,y,z)$ is given by [28]

$$\chi(x,y,z) = -\frac{\sigma\rho(x,y,z)}{k}\frac{1}{2\tilde{\delta}+\mathrm{i}}, \tag{4}$$

where σ_0 is the resonant photon absorption cross section, ρ is the number density of atoms, $\tilde{\delta} = (\omega-\omega_0)/\Gamma$ is the normalized detuning with ω_0 being the resonance frequency and Γ is the FWHM of the transition. The probe light intensity is assumed to be much lower than the saturation intensity. Effects due to bosonic statistics [29, 30] are not included in this model, and neither are dipole-dipole interactions [31–34] or the non-coherent emission signal from the atoms [12].

The number density is given by $\rho = \rho_0 + \rho_{th}$ where the BEC density ρ_0 is [35]

$$\rho_0(x_i) = \frac{15}{8\pi}\frac{N_0}{R_1R_2R_3}\cdot\Theta\left(1-\sum_{i=1}^{3}\frac{x_i^2}{R_i^2}\right), \tag{5}$$

where Θ is the Heaviside-step function, x_i refer to the three directions with corresponding Thomas-Fermi radius $R_i = \sqrt{2\mu/(m\omega_i^2)}$, and the chemical potential μ related to the condensed atom number in the Thomas-Fermi approximation by $\mu = \frac{1}{2}\left(15N_0a/a_{\mathrm{ho}}\right)^{2/5}\hbar\bar{\omega}$. Here, a is the s-wave scattering length, $a_{\mathrm{ho}} = \sqrt{\hbar/(m\bar{\omega})}$ is a characteristic length in the harmonic oscillator, and $\bar{\omega} = (\omega_1\omega_2\omega_3)^{1/3}$ is the geometric mean of the trap frequencies. The thermal density ρ_{th} is given by the semi-ideal model [36]

$$\rho_{th}(x_i) = \lambda_T^{-3}g_{\frac{3}{2}}\left(\mathrm{e}^{\left|V(x_i)-\mu\right|/k_BT}\right), \tag{6}$$

where $\lambda_T = \left(2\pi\hbar/(mk_BT)\right)^{3/2}$ is the thermal de-Broglie wavelength, $V(x_i)$ the trapping potential, and where $g_\gamma = \sum_{i=1}^{\infty}\frac{x^i}{i^\gamma}$ is the Polylogarithm function.

The resulting BF spectrum, shown in the top panel of FIG. 2, contains a bimodal structure with each contribution to the spectrum characterized by its optical density (*od*) and cross sectional size. The condensate has a high *od* and therefore is broad in frequency, but the physical size is small. Thermal component, which has a much larger cross-sectional area, has a narrower spectrum due to its lower *od*, but results in a more significant dip in the signal. The bimodal structure in the spectrum can be compared to the spatial bimodal density profile observed in TOF images, however, with reversed roles. The distinction in the transmission profiles in the top panel of FIG. 2 can be observed. The the light field on resonance is almost entirely absorbed by the thermal cloud, while at probe detunings of 15 MHz to 30 MHz or larger, only signs of the BEC remain.

The bottom panel of FIG. 2 illustrates the scenario in the DF configuration. A series of scattered light field intensity profiles immediately after the atomic cloud is shown at various detunings, together with the spectroscopic signal measured on a SPD. The DF signal, normalized to the incoming probe power I_0A, is given by [37]

$$\mathcal{T}^{DF} = \frac{1}{A}\int_{\text{pinhole}} 1 + t(x,y)^2 - 2t(x,y)\cos\left(\phi(x,y)\right)\ \mathrm{d}x\mathrm{d}y, \tag{7}$$

where $t(x,y)$ is the electric field transmission coefficient from Eq. (2), and $\phi(x,y)$ is the spatially dependent phase-shift, relative to vacuum, given by

$$\phi(x,y) = \int_{-\infty}^{\infty}\left(\mathrm{Re}\left(n(x,y,z)\right)-1\right)k\ \mathrm{d}z. \tag{8}$$

Because DF is sensitive to phase-shifts, the spectra become much broader and contain more complex structures. The spectrum is separated into a strong, narrow peak caused by the thermal component, and a broad, shallow peak caused by the BEC, for the same reasons as was discussed in the BF case. Since the peak phase-shift is typically several π, the spectrum contains troughs and peaks. A noticeable feature is the large shoulder at the intermediate detuning around 150 MHz. This occurs when a ring of phase-shift equal to π appears such that the integrated signal is maximized, while the peak phase-shift at the center is not enough to reach 2π.

Thus, both BF and DF spectra contain information about the spatial distribution of the clouds including the thermal atom numbers, BEC atom numbers, and the temperature. This probing method can be used on a wide range of in-trap clouds since the optical densities probed span from the resonant value to almost zero over the entire spectrum. Section III investigates how well these parameters can be extracted.

C. Experimental measurement sequence

For all measurements, the light probes the cycling transition $|F=2, m_F=2\rangle \leftrightarrow |F'=3, m_F'=3\rangle$. Probing other transitions is equally possible as long as the theoretical cross section is updated.

The measurement sequence differs slightly between BF and DF methods. The experimental sequence used to acquire BF data is illustrated in FIG. 3, where an exemplary signal is shown together with the measurement intervals. The signal is derived from the individual photon arrival times recorded by the SPD as follows. The photon arrival times are first binned into intervals, and then the record number is divided by the bin duration, this, giving the rate R of detected photons.

The BF technique performs measurements during three time intervals to obtain the normalized transmission spectrum, indicated with "A", "B", and "C". The signal in the presence of atoms denoted is P_A during which the

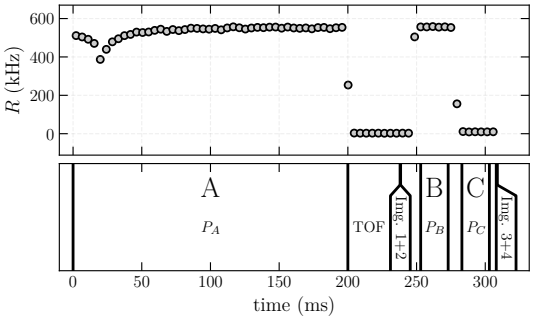

FIG. 3: Measurement sequence of a BF spectrum and the following absorption images after TOF. The top panel shows an example dataset from the SPD, while the bottom panel labels the different time-intervals. Three intervals, named "A", "B", and "C", are highlighted and used to calculate $\mathcal{T}^{BF}$.

frequency of the probe light is being swept. The mean signal without atoms, but with detection and trapping light on, denoted $\overline{P}_B$ is measured to obtain the probe light intensity. Finally, the mean signal without the detection light, but with the trapping light on, is denoted $\overline{P}_C$ and is used to extract the background signal. With these a normalized transmission is calculated as

$$\mathcal{T}^{BF} = \frac{P_A - \overline{P}_C}{\overline{P}_B - \overline{P}_C}. \tag{9}$$

The value of $\mathcal{T}^{BF}$ lies between 0 (when there is no absorption of light) and 1 (when all light in the pinhole region has been absorbed), in units of the incoming power $I_0 A$ as described in Section II B, where the back-propagated pinhole area A is given by the physical area divided by the square of the magnification between the atoms and the pinhole. All signals together with the images after TOF are measured on the same cloud, which requires the probe light intensity to be as low as possible to cause only minimal destruction to the cloud.

The DF measurement is similar to BF, but requires a separate measurement of the probe light intensity due to the presence of the DF target. The experimental sequence used to acquire DF data is illustrated in FIG. 4 which again shows an example of a detected photon rate together with labels of all the time intervals. Four powers are measured to obtain a normalized transmission spectrum, and the time intervals are indicated with "A", "B", and "C" in the figure. The signal in the presence of atoms, P_A with sweeping probe light frequency. The mean signal without atoms, but with both trapping and probing light on, $\overline{P}_B$ is measured to get the background signal in the DF setup. The mean of this signal without the DF target inserted is measured separately, denoted $\overline{P}_B^{BF}$, and gives the incoming light intensity. Finally, the mean of the signal without the probe light and without the dark field obstacle, but with the trapping light on, denoted

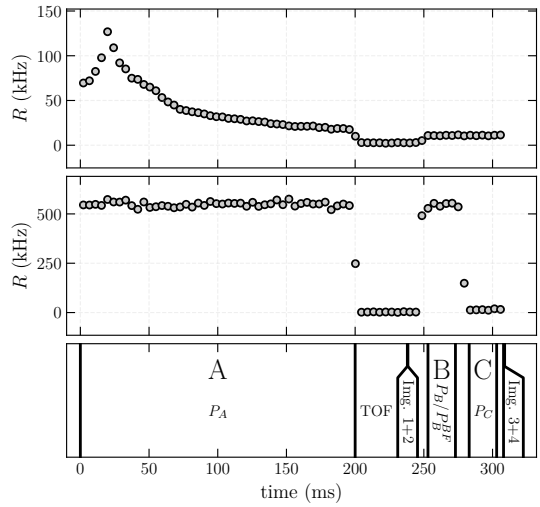

FIG. 4: Measurement sequence of a DF spectrum and the following absorption images after TOF. The top panel shows an example dataset from the SPD, the middle panel shows the measurement of I_0, and the bottom panel labels the different time-intervals. Three intervals, named "A", "B", and "C", are highlighted and used to calculate $\mathcal{T}^{DF}$.

$\overline{P}_C^{BF}$, is measured to get the background signal of the light intensity measurement. With these measurements a normalized transmission signal for the DF setup $\mathcal{T}^{DF}$, is given by

$$\mathcal{T}^{DF} = \frac{P_A - \overline{P}_B}{\overline{P}_B^{BF} - \overline{P}_C^{BF}}. \tag{10}$$

In the following, the normalized transmissions $\mathcal{T}^{BF}$ and $\mathcal{T}^{DF}$ allow for a comparison between the experimental results and the theoretical spectra.

D. Time-of-flight image analysis

Absorption imaging after TOF is a standard technique [37] and is only outlined briefly here. It provides spatial information of the light intensity $I(x, y)$ after passing through the atomic cloud. The optical density $od(x, y) = \sigma_0 \tilde{\rho}(x, y)$, where $\tilde{\rho}$ is the atom number column density, is calculated from the images using the method described in [2]. In FIG. 3 and FIG. 4, the timing of these images is indicated.

The cloud parameters μ and T are extracted from the images as follows. First, the average imaging intensities in a region without atoms (outside the radius R_{ref}) are compared, and scaled to match. A second region centered on the atoms with a manually set radius R_{atom}, fully within the first region, is used to fit the od with the parameters

μ and T, using the in-situ distributions from Eq. (5) and Eq. (6) to calculate the atom numbers N_0 and N_{th} to guarantee the result follows the semi-ideal curve and is comparable to the model used for spectroscopic analysis. The BEC column density after TOF is given by

$$\tilde{\rho}_0 = \frac{5}{2\pi}\frac{N_0}{R_1 R_2}\cdot\Theta\left(1-\sum_{i=1}^{2}\frac{(x_i-x_{i,0})^2}{R_i^2}\right)^{3/2}, \quad (11)$$

where the Thomas-Fermi radii R_i, positions $x_{i,0}$ are free parameters and the atom number N_0 calculated from μ. The thermal column density after TOF is given by

$$\tilde{\rho}_{th} = \begin{cases} c_+ g_2\left(\exp\left(-\sum_{i=1}^{2}\frac{(x_i-x_{i,0})^2}{2\beta_i^2 w_i^2}\right)\right), & \mu > 0 \\ c_- g_2\left(\exp\left(\frac{\mu}{k_B T}-\sum_{i=1}^{2}\frac{(x_i-x_{i,0})^2}{2\beta_i^2 w_i^2}\right)\right), & \mu \leq 0 \end{cases}, \quad (12)$$

where $w_i = 1/\omega_i \cdot \sqrt{k_B T/m}$, $\beta_i = \sqrt{1+\omega_i^2 t^2}$, t is the TOF, $c_+ = N_{th}/(2\pi w_x\beta_x w_y\beta_y g_3(1))$, and $c_- = \sqrt{2\pi}/(\lambda_T^3\beta_x\beta_y)$. The free parameters are μ, and T, while the positions $x_{i,0}$ are the same as for the BEC component. It is necessary to limit $\mu \leq 0$ in the Bose-enhanced distribution if the repulsive forces between atoms are not taken into account, which results in two separate thermal distributions below and above the BEC transition.

The image is fitted with the sum of the two components simultaneously and the fit contains six parameters in total. After a fit, the value of R_{ref} is updated to be $4w_i\beta_i$ in each direction, the value of R_{atom} is updated to be $3w_i\beta_i$ in each direction, and the region is centered on $x_{i,0}$. The fit is then repeated with the new ROI. A cloud is fitted a total of 3 times before the final result is read out.

E. Spectral calibration

To calculate the normalized transmission, it is necessary to measure the area A of the image of the pinhole when it is back-propagated to the plane of the atoms, see eq. (1), (7). This is determined by the magnification of the first half of the $4f$-setup in FIG. 1. The total magnification of the setup can be measured by varying the TOF and comparing the motion with theoretical free fall. The magnification of the second half of the $4f$-setup can be directly measured by the size of the image of the pinhole on the camera. Thus, the magnification of the first half can then be calculated giving 1.442, which is near the theoretically estimated value of 1.429.

Furthermore, two parameters are calibrated to take into account the experimental imperfections. Firstly, the numerical aperture of the imaging system is not designed for in-trap measurements and must be taken into account. This is done by propagating the DF electric field from the atoms to the first Fourier plane and calculating the fraction of power, $\mathcal{P}$ falling within a radius R_{NA} and outside the dark field target. Since the DF electric field is collimated in this section, this allows for taking into account apertures between the first and second lens of the setup as well as the blockade of the DF target, while requiring minimal computational resources. The radius R_{NA} is a free parameter to be calibrated. The propagation is evaluated numerically according to

$$E_{\mathcal{F}}(x,y) = \frac{1}{\lambda f}\mathcal{F}[E_0]\left(\frac{x}{\lambda f},\frac{y}{\lambda f}\right), \quad (13)$$

where $E_0 = 1-\mathrm{e}^{-t+\mathrm{i}\phi}$ is the DF electric field just after the atoms, with t given by eq.(2) and ϕ given by eq.(8), and where f is the focal length of the first lens in the setup, λ is the wavelength of the light, and $\mathcal{F}$ is a Fourier transform. The amplitude of the incoming field cancels out in the calculation of the fraction of blocked power and can be left out. Since t and ϕ depend on the detuning of the light, the limited numerical aperture alters the shape of the spectra. The aperture transmission function $\mathcal{P}^{DF}$ to be multiplied with DF spectra $\mathcal{T}^{DF}$ is given directly by the fraction of power $\mathcal{P}$. In BF, the lost power of the DF electric field is also missing, giving a different aperture transmission function $\mathcal{P}^{BF}$

$$\mathcal{P}^{BF} = 1-(1-\mathcal{P}^{DF})\frac{\mathcal{T}^{DF}}{\mathcal{T}^{BF}}. \quad (14)$$

This can be understood as follows; the fraction of lost DF signal is given by $1-\mathcal{P}^{DF}$. To calculate the fraction of lost BF signal, this should be rescaled by a factor $\mathcal{T}^{DF}/\mathcal{T}^{BF}$. Finally, the transmitted fraction of power is given by 1 minus the lost fraction.

Secondly, a calibration of the cross section of light-atom interactions $\sigma = \sigma_0/\alpha$, where the theoretical value σ_0 scaled by a parameter α is performed. This is similar to a technique used in absorption imaging[2], and takes into account numerous imperfections in the light causing a reduction in the interaction strength.

To calibrate R_{NA} and α two DF datasets representing different regions of cloud parameters are fitted with varying values of the calibration parameters, and the extracted cloud parameters are compared to the values from time-of-flight imaging. The calibration parameters are chosen such that the two techniques agree maximally. The optimal value for R_{NA} was found to be 3.6 mm and the optimal value for α was found to be 1.27.

The result of the calibration is shown in FIG. 6, where the two datasets used for calibration (top and bottom panel) are compared with two curves with $\alpha = 1$ and infinite aperture radius and with the optimized values. The same calibration is used for BF spectra. The cloud parameters used to plot the model were taken from the time-of-flight images of the corresponding clouds and are not yet fitted spectroscopically. The result of the calibration is a significant increase in agreement between the expected and measured spectra.

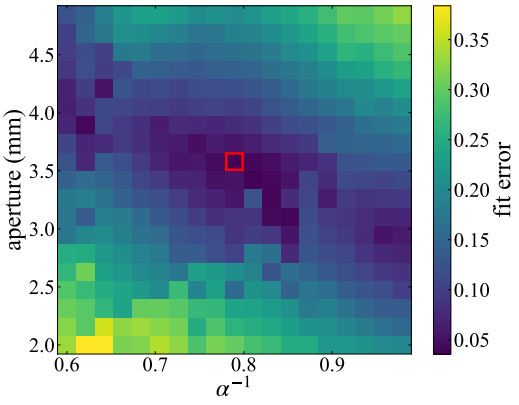

FIG. 5: Calibration parameter landscape. The two calibration parameters are scanned and used to fit spectra. The extracted parameters T, N_{th}, and N_0 are compared to the values extracted from absorption images of the same clouds, and the mean relative error is plotted. The minimum position is indicated with a red square.

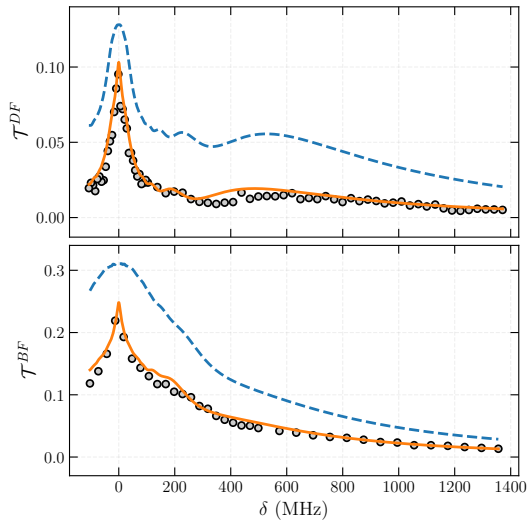

FIG. 6: The two datasets used for calibration. The top panel has $T = 125\,\mathrm{nK}$, $N_{th} = 130 \cdot 10^3$, and $N_0 = 490 \cdot 10^3$. The bottom panel has $T = 380\,\mathrm{nK}$, $N_{th} = 100 \cdot 10^3$, and $N_0 = 160 \cdot 10^3$. A blue, dashed line illustrates the predicted spectrum from the model assuming infinite aperture radius and $\alpha = 1$, and using the absorption imaging extracted loud parameters. An orange, solid line shows the predicted spectrum with the calibrated values for NA and α.

III. SPECTROSCOPIC DETECTION

This section presents the analysis of the spectra and benchmarks the extracted cloud parameters – N_0, N_{th}, and T – against time-of-flight imaging data. Spectra and images are always taken on the same cloud, and the experiment is repeated at different points in the evaporation sequence to probe various regimes. The light intensity is chosen such that a maximum of 10% of atoms are lost in the most shallow trap and the coldest clouds during the measurement of a spectrum, while the destructivity is smaller for all other measurements.

The spectra are fitted with the two cloud parameters; the chemical potential μ and the temperature T and the spectral resonance frequency. The BF spectra are fitted with Eq. (1) multiplied by the BF aperture transmission function $\mathcal{P}^{BF}$ in Eq. (14), and DF spectra are fitted with Eq. (7) multiplied by the DF aperture transmission function $\mathcal{P}^{DF}$.

Figure 7 shows DF and BF fit examples for bimodal and hot clouds. The model is able to replicate the structures that are measured in all four spectra.

A. Evaluation of spectroscopic detection

Using spectroscopy for characterization gives an alternative approach to absorption imaging in detection of thermal atoms in cloud with high condensate fractions. Especially for bimodal clouds with a high condensed fraction, the spectroscopic approach offers a significant advantage. Figure 8 compares absorption images and DF measurements of the coldest cloud in the dataset. The top panel shows the one-dimensional integrated atom number density of 18 averaged images, and the bottom panel shows the average spectroscopic signals of the same clouds before the trap was released.

The spectrum shows a fitted curve, which extracts the temperature $T = 47\,\mathrm{nK}$, corresponding to a condensed fraction of 97 %. To illustrate which part of the signal arises from the small thermal component of the cloud, a curve with the same number of BEC atoms, but $T = 0\,\mathrm{nK}$, and thus zero thermal atoms, is also included. Around resonance, there is a clear signal from the thermal atoms in the spectrum which is well separated from the pure BEC signal.

The fit of the absorption images is plotted against the data in the top panel and results in a physically implausible temperature of 0.6 nK since there is no clear thermal tail in the bimodal cloud, even after averaging 18 images. Two insets in the panel show a region around the tail of the cloud, and a fit function with the spectroscopically fitted temperature is included for reference, once again illustrating the infeasibility of extracting the thermal cloud parameters from the images.

The spectrum has a second advantage since it is being measured in-trap. This completely removes the need of modelling the expansion dynamics of the clouds, which

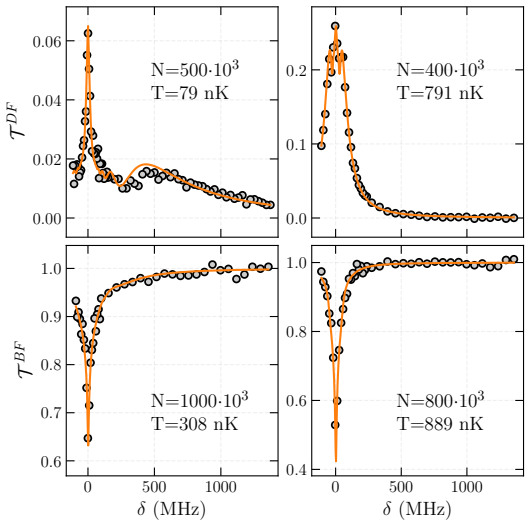

FIG. 7: Four spectroscopic fit examples. The top row shows DF spectra and the bottom row shows the BF. The left column shows colder clouds and the right column shows hotter clouds.

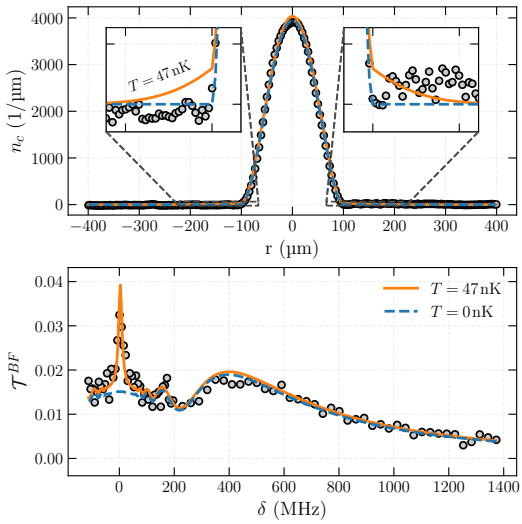

FIG. 8: Comparison between absorption imaging after 36 ms TOF (upper) and DF spectrum (lower) for a very cold cloud. Blue, dashed lines in both panels show the models using the absorption imaging fitted parameters, and orange, solid lines show the models using the spectroscopically fitted parameters. The absorption image shows no sign of a thermal component. In contrast, the spectroscopic method shows a clear signal around the resonance.

can be especially complicated for bimodal clouds with high condensate fractions [38]. It also allows for continued measurements of the same cloud because it is not released from the trap.

Since the spectrum is measured across a wide frequency span, the high optical density of in-trap clouds is not problematic. However, clouds with peak *od* much less than one cannot be measured in this way, since the signal reduces to a linear regime and reveals no spatial information. In this particular trap setup, the regime would be reached around 1000 atoms, and it would require fewer atoms in tighter traps.

B. Comparison to time-of-flight imaging

To investigate the accuracy and precision of spectral fits, the method is compared to the fits of images after TOF. A dataset that spans a wide variety of atom numbers, temperatures, trap frequencies, and condensate fractions is used to investigate the comparison in a large parameter space.

In the following, parameters extracted from spectra are indicated with a superscript S and parameters extracted from absorption images after TOF are indicated with a superscript A. The differences between the two methods is given by

$$\Delta T = T^S - T^A, \quad \Delta N_{th} = N_{th}^S - N_{th}^A,$$
$$\Delta N_0 = N_0^S - N_0^A. \tag{15}$$

Figure 9 shows the comparison between the two methods. Consider first FIG. 9(a). BF and DF methods agree with the absorption imaging for all points except the coldest with the highest condensed fraction (see FIG. 8). The disagreement here is not caused by the spectroscopic fits but instead by the absorption imaging method which is unable to detect the small remaining thermal component. This is clearer in FIG. 9(b), where the relative disagreement of all points are withing ±10 %, except for the coldest point which is off by ≈ 100 % since the absorption image fit estimates $T \approx 0$ K.

In FIG. 9(c)-(d), the thermal atom number extraction is compared. The DF spectroscopic method once again displays good agreement with the absorption image method within ±10 %, except for the coldest point. The BF method follows the same trend as the absorption imaging method, but with a constant offset of ≈ 30 % and more noisy parameter extraction. This is most likely caused by the limited NA of the setup, which has a larger relative effect on BF since it is not sensitive to the phase-shift of the light. The coldest point again disagrees between the two methods because the extraction of thermal atom number fails with absorption imaging.

Figure 9(e)-(f) shows the extracted condensed atom number obtained with the BF and DF methods. Both methods show reasonably good agreement with absorption imaging, however the DF technique clearly outperforms

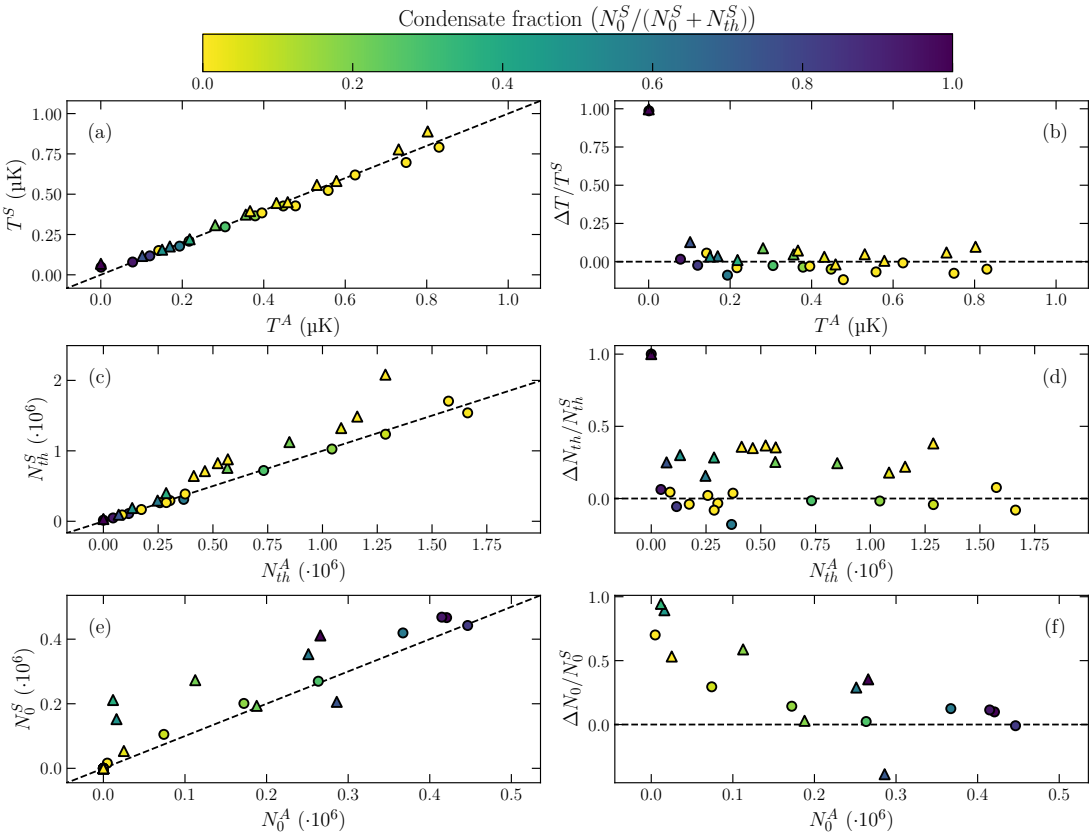

FIG. 9: Comparison between absorption imaging and spectroscopy. Direct (left) and relative (right) comparison of temperature (a)-(b), thermal atom number (c)-(d), and condensed atom number (e)-(f). The △ - markers indicate results via the BF configuration, while the ○ - markers represent the DF results. A color scale indicates the condensed fraction as calculated from the spectral fits. Notably, the relative deviation for temperature (b) and thermal atom number (d) diverges for the coldest atomic samples, when absorption imaging fails to recognise the thermal cloud in both BF and DF configuration.

the BF method. The BF method suffers from the limited NA and its insensitivity to phase-shifts, affecting the precision of extracting N_0 from the BEC's broad but shallow spectroscopic signal. The DF result agrees considerably better with absorption imaging at all condensed atom numbers. Significant relative errors only arise for condensed fractions less than $\approx 20\,\%$, close to the critical temperature. For large condensed fractions, the relative difference is again within $\pm 10\,\%$

IV. CONCLUSION AND OUTLOOK

In conclusion, a complementary spectroscopic detection technique was demonstrated, which enables minimally destructive measurements of ensemble parameters without requiring spatially resolved imaging. The approach relies on few-photon detection in both bright-field and dark-field configurations, based on broad frequency scans. The light propagation through a bimodal density distribution was modeled to quantitatively describe the measured spectra. The method was explored experimentally with ultracold ^{87}Rb clouds confined in a crossed optical dipole trap.

The spectroscopically extracted parameters were compared to the results from absorption imaging after time-of-flight for a variety of experimental parameters. The temperature extraction was shown to perform well for both BF and DF methods, and both showed increased sensitivity to the small thermal component of very pure BECs compared to absorption imaging. The same is true

for the extraction of the thermal atom numbers, while the DF method performs better than the BF method in this case. Only the DF method was able to reliably measure condensed atom numbers, since the limited NA proved too detrimental for the BF method to estimate this parameter.

Since the spectra can be measured in-trap without the need of high-resolution imaging optics, the method provides an alternative path for weakly destructive measurements of the cloud parameters while avoiding the need to model the expansion dynamics.

Spectroscopic measurements can be susceptible to complicated light-atom interaction effects such as bosonic enhancements [29, 30] or dipole-dipole interactions [31–34]. In fact, dipole-dipole interactions are expected to play a role in these measurements since they become important at densities larger than $\approx 1\,\lambda^{-3}$ and the peak density of atoms in these measurements can be greater than $100\,\lambda^{-3}$, where λ is the wavelength of the probe light. This will be subject to further investigations.

ACKNOWLEDGMENTS

We acknowledge support from the Danish National Research Foundation through the Center of Excellence "CCQ" (DNRF152) and by the Novo Nordisk Foundation NERD grant (Grantno. NNF22OC0075986).

[1] T. Vibel, M. B. Christensen, M. A. Kristensen, J. J. Thuesen, L. N. Stokholm, C. A. Weidner, and J. J. Arlt, Spatial calibration of high-density absorption imaging, Journ. of Phys. B **57**, 145301 (2024).
[2] G. Reinaudi, T. Lahaye, Z. Wang, and D. Guéry-Odelin, Strong saturation absorption imaging of dense clouds of ultracold atoms, Opt. Lett. **32**, 3143 (2007).
[3] T. Vibel, M. B. Christensen, R. M. F Andersen, L. N. Stokholm, K. Pawłowski, K. Rzążewski, M. A. Kristensen, and J. J. Arlt, Atom number fluctuations in Bose gases—statistical analysis of parameter estimation, Journ. of Phys. B **57**, 195301 (2024).
[4] M. H. Anderson, J. R. Ensher, M. R. Matthews, C. E. Wieman, and E. A. Cornell, Observation of Bose-Einstein condensation in a dilute atomic vapor, Science **269**, 198 (1995).
[5] K. B. Davis, M. O. Mewes, M. R. Andrews, N. J. van Druten, D. S. Durfee, D. M. Kurn, and W. Ketterle, Bose-Einstein condensation in a gas of sodium atoms, Phys. Rev. Lett. **75**, 3969 (1995).
[6] K. S. Hardman, P. B. Wigley, P. J. Everitt, P. Manju, C. C. N. Kuhn, and N. P. Robins, Time-of-flight detection of ultra-cold atoms using resonant frequency modulation imaging, Opt. Lett. **41**, 2505 (2016).
[7] F. Kaminski, N. S. Kampel, M. P. H. Steenstrup, A. Griesmaier, E. S. Polzik, and J. H. Müller, In-situ dual-port polarization contrast imaging of Faraday-rotation in a high optical depth ultracold 87Rb atomic ensemble, The Eur. Phys. Journ. D **66**, 10.1140/epjd/e2012-30038-0.
[8] A. Ramanathan, S. R. Muniz, K. C. Wright, R. P. Anderson, W. D. Phillips, K. Helmerson, and G. K. Campbell, Partial-transfer absorption imaging: A versatile technique for optimal imaging of ultracold gases, Rev. of Scient. Inst. **83**, 083119 (2012).
[9] R. Meppelink, R. A. Rozendaal, S. B. Koller, J. M. Vogels, and P. van der Straten, Thermodynamics of Bose-Einstein-condensed clouds using phase-contrast imaging, Phys. Rev. A **81**, 053632 (2010).
[10] L. D. Turner, K. P. Weber, D. Paganin, and R. E. Scholten, Off-resonant defocus-contrast imaging of cold atoms, Opt. Lett. **29**, 232 (2004).
[11] L. D. Turner, K. F. E. M. Domen, and R. E. Scholten, Diffraction-contrast imaging of cold atoms, Phys. Rev. A **72**, 031403 (2005).
[12] M. Pappa, P. C. Condylis, G. O. Konstantinidis, V. Bolpasi, A. Lazoudis, O. Morizot, D. Sahagun, M. Baker, and W. von Klitzing, Ultra-sensitive atom imaging for matter-wave optics, New Journal of Physics **13**, 115012 (2011).
[13] A. Reinhard, J. Riou, L. A. Zundel, and D. S. Weiss, Dark-ground imaging of high optical thickness atom clouds, Opt. Comm. **324**, 30 (2014).
[14] M. R. Andrews, M.-O. Mewes, N. J. van Druten, D. S. Durfee, D. M. Kurn, and W. Ketterle, Direct, nondestructive observation of a Bose condensate, Science **273**, 84 (1996).
[15] M. R. Andrews, D. M. Kurn, H.-J. Miesner, D. S. Durfee, C. G. Townsend, S. Inouye, and W. Ketterle, Propagation of sound in a Bose-Einstein condensate, Phys. Rev. Lett. **79**, 553 (1997).
[16] C. C. Bradley, C. A. Sackett, and R. G. Hulet, Bose-Einstein condensation of lithium: Observation of limited condensate number, Phys. Rev. Lett. **78**, 985 (1997).
[17] M. F. Fernandez, P. G. S. Dias, P. H. N. Magnani, M. do A. Martins, M. Hugbart, A. Cipris, P. W. Courteille, and R. C. Teixeira, Phase-contrast imaging of a dense atomic cloud (2025).
[18] S. Kadlecek, J. Sebby, R. Newell, and T. G. Walker, Nondestructive spatial heterodyne imaging of cold atoms, Opt. Lett. **26**, 137 (2001).
[19] M. Gajdacz, P. L. Pedersen, T. Mørch, A. J. Hilliard, J. Arlt, and J. F. Sherson, Non-destructive Faraday imaging of dynamically controlled ultracold atoms, Rev. of Scient. Inst. **84**, 083105 (2013).
[20] M. A. Kristensen, M. Gajdacz, P. L. Pedersen, C. Klempt, J. F. Sherson, J. J. Arlt, and A. J. Hilliard, Sub-atom shot noise Faraday imaging of ultracold atom clouds, Journ. of Phys. B **50**, 034004 (2017).
[21] P. F. Gao, G. Lei, and C. Z. Huang, Dark-field microscopy: Recent advances in accurate analysis and emerging applications, An. Chem. **93**, 4707 (2021), pMID: 33620210.
[22] M. Pappa, P. C. Condylis, G. O. Konstantinidis, V. Bolpasi, A. Lazoudis, O. Morizot, D. Sahagun, M. Baker,

and W. von Klitzing, Ultra-sensitive atom imaging for matter-wave optics, New Journal of Physics **13**, 115012 (2011).
[23] J. Appel, A. MacRae, and A. I. Lvovsky, A versatile digital GHz phase lock for external cavity diode lasers, Meas. Scien. and Tech. **20**, 055302 (2009).
[24] E. Hecht, *Optics*, third edition ed., edited by J. Berrisford (Addison Wesley Longman, 1998).
[25] M. Andersen, *Spectrally Probing Ultra-Cold Bosonic Clouds*, Ph.D. thesis, Aarhus University (2025).
[26] L. Stokholm, *Real-Time Quantum Sensing in Rubidium: Few-Photon Probing of Ultracold Gases and Rydberg Microwave Polarimetry*, Ph.D. thesis, Aarhus University (2026).
[27] J. D. Jackson, *Classical Electrodynamics*, 3rd ed. (John Wiley & Sons, New York, 1999).
[28] R. W. Boyd, Chapter 6 - nonlinear optics in the two-level approximation, in *Nonlinear Optics* (Academic Press, Burlington, 2008) third edition ed., pp. 277–328.
[29] K. Konstantinou, Y. Zhang, P. H. C. Wong, F. Wang, Y.-K. Lu, N. Dogra, C. Eigen, T. Satoor, W. Ketterle, and Z. Hadzibabic, How interacting Bose gases scatter light (2025).
[30] O. Morice, Y. Castin, and J. Dalibard, Refractive index of a dilute Bose gas, Phys. Rev. A **51**, 3896 (1995).
[31] L. Brossard, *Study of light-induced dipolar interactions in cold atoms assemblies*, Ph.D. thesis, Université Paris-Saclay (2020).
[32] J. Pellegrino, R. Bourgain, S. Jennewein, Y. R. P. Sortais, A. Browaeys, S. D. Jenkins, and J. Ruostekoski, Observation of suppression of light scattering induced by dipole-dipole interactions in a cold-atom ensemble, Phys. Rev. Lett. **113**, 133602 (2014).
[33] S. Jennewein, M. Besbes, N. J. Schilder, S. D. Jenkins, C. Sauvan, J. Ruostekoski, J.-J. Greffet, Y. R. P. Sortais, and A. Browaeys, Coherent scattering of near-resonant light by a dense microscopic cold atomic cloud, Phys. Rev. Lett. **116**, 233601 (2016).
[34] M. Maiwöger, M. Sonnleitner, T. Zhang, I. Mazets, M. Mallweger, D. Rätzel, F. Borselli, S. Erne, J. Schmiedmayer, and P. Haslinger, Observation of light-induced dipole-dipole forces in ultracold atomic gases, Phys. Rev. X **12**, 031018 (2022).
[35] C. J. Pethick and H. Smith, *Bose-Einstein condensation in dilute gases*, second edition ed. (Cambridge, 2008).
[36] M. Naraschewski and D. M. Stamper-Kurn, Analytical description of a trapped semi-ideal Bose gas at finite temperature, Phys. Rev. A **58**, 2423 (1998).
[37] W. Ketterle, D. S. Durfee, and D. M. Stamper-Kurn, Making, probing and understanding Bose-Einstein condensates (1999).
[38] R. M. F. Andersen, S. Frederiksen, L. Stokholm, I. Zebergs, M. Kristensen, C. Weidner, and J. J. Arlt, Cloud parameter estimation for interacting BEC after time-of-flight (2026), arXiv:2601.10415 [cond-mat.quant-gas].

Observation of Dynamics in Ultracold Gases using Dark-Ground Detection

L. N. Stokholm,[1] R. M. F. Andersen,[1] I. Zebergs,[1] N. R. Neubert,[1] A. S. Chatterly,[1] N. Kjærgaard,[2] and J. J. Arlt[1]

[1] *Center for Complex Quantum Systems, Department of Physics and Astronomy, Aarhus University, Ny Munkegade 120, DK-8000 Aarhus C, Denmark.*

[2] *Department of Physics, Quantum Science Otago (QSO), and Dodd-Walls Centre for Photonic and Quantum Technologies, University of Otago, Dunedin, New Zealand.*

A minimally destructive detection platform for ultracold atomic gases based on time-resolved dark-ground (TRDG) imaging combined with single-photon detection is presented. The method integrates a dark-ground spatial filter and intermediate pinhole, strongly suppressing probe light while transmitting phase- and density-dependent scattered fields. Coupled to a single-photon detector, this enables minimally destructive time-resolved in-situ measurements of ultracold atoms. The technique allows for both broadband and sub-kHz-resolution measurements on a single atomic cloud based on an optical phase-locked loop. The capabilities of the platform are demonstrated through single-shot extraction of trap frequencies from real-time motional dynamics. Moreover, it is shown that the internal dynamics can be monitored, showing time-resolved microwave Rabi oscillations which can be used for adiabatic state transfer and rapid magnetic-field calibration on a single cloud, The systemalso enables direct detection of Raman-Rabi oscillations via monitoring of the driving optical fields, and sub-kHz electromagnetically induced transparency spectroscopy with a 360 Hz linewidth. Finally, broadband hyperfine spectroscopy across the full ground-state splitting of ^{87}Rb, and continuous spectral monitoring during evaporative cooling are demonstrated. These measurements show that the system provides a complementary alternative to destructive absorption imaging for coherent control of quantum gases.

I. INTRODUCTION

Ultracold neutral atoms form a cornerstone of modern physics. Their high degree of experimental control enables precise engineering and probing of quantum matter, establishing them as a powerful platform for quantum simulation and precision measurements. Applications in quantum technologies have catalysed advancements in the field of quantum metrology, sensing [1, 2] and computing [3]. Experimental access to ultracold gases relies on probing the atoms with light fields, and absorption imaging has long served as the workhorse technique for estimating atom number and temperature [4–6]. Absorption imaging, however, employs resonant light at intensities above saturation and typically requires releasing the atomic cloud for a time-of-flight expansion to reduce the high in-situ optical density and improve spatial resolution [5]. Its inherently destructive nature necessitates a new atomic cloud for each measurement, introducing preparation noise and placing strong demands on experimental cycle times. To overcome this limitation, alternative dispersive techniques such as phase-contrast imaging [7, 8] and Faraday imaging [9, 10] have been developed. While such methods can be minimally destructive, they generally operate in the far-detuned regime to suppress absorption, limiting their applicability for resonant or near-resonant spectroscopy. In recent work [11], a novel approach was demonstrated, combining a single-photon detector (SPDM) with a dark-ground (DG) target for non-destructive, in-situ spectroscopy of ultracold gases, enabling atom number and temperature extraction in quantitative agreement with absorption imaging. The current work shows that this technique makes for a new class of minimally destructive in-situ measurements. This allows for time-resolved interrogation of internal and external dynamics on a single ultracold atomic cloud. These measurements provide complete-datasets from a single preparation cycle, reducing calibration and parameter optimisation times from hours to minutes.

II. EXPERIMENTAL SETUP

A. Detection System

Figure 1a shows the detection system along two directions in the horizontal plane. Two imaging paths enable spatially resolved absorption images of the atoms either in-situ or after a variable time-of-flight expansion. A four-lens configuration is used to relay the image of the atoms onto the CCD camera. In the first focus, the DG obstacle can be placed, rendering the imaging configuration from bright-field (BF) to DG, and in the intermediate image plane a pinhole can be placed which reduces the image to an area around the cloud position in-situ. The CCD camera is used to align the probe beam and position the pinhole. The pinhole diameter is chosen to match the in-trap size of the cloud; typically we use 75 µm for BECs and 150 µm for a pure thermal cloud.

In addition, a single-photon detector module (SPDM) is integrated into an imaging direction, enabling time-resolved, dark-ground (TRDG) measurements at the few-photon level. In contrast to the CCD cameras, the SPDM is a single-pixel detector, and requires that the light is accurately focused onto the active area of the chip. The SPDM records the optical power integrated

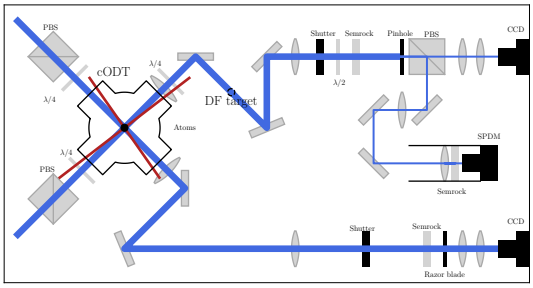

(a)

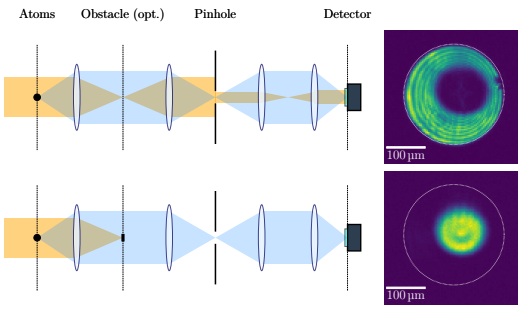

(b)

FIG. 1. Panel (a) top-view of the optical setup. Atoms are stored in the overlap of two tightly focused dipole beams (dark red), which are slightly off-axis from the two imaging directions (blue). Two CCD cameras provide spatially resolved absorption images taken in-situ and after time-of-flight. A SPDM enables non-destructive probing of the cloud and provides temporal resolution. Panel (b) images without the DG target (top) and with the DG target (bottom). The length scale indicates the size of the in-situ atoms. A dotted circle indicates the edge of the pinhole. A DG target can be inserted at the small probe beam waist focus to block out background light.

over the imaging region with high sensitivity. The experiment can switch between the two detection schemes during operation via two motorised flip mounts: one inserts neutral density filters to attenuate the probe light before it reaches the atoms, and the other toggles between the SPDM and the CCD camera using polarising optics. Specifically, a $\lambda/2$ waveplate mounted in a motorised flip mount enables controlled switching of the optical path. The detection arm branches to the SPDM after the intermediate image plane. Both CCD cameras are capable of capturing a series of images, however, typically, only a single image of the atomic cloud is obtained per experimental run. In contrast, the SPDM collects minimally destructive datasets using a single atomic cloud, eliminating run-to-run preparation noise. Alternatively, data from multiple atomic samples can be combined improving counting statistics at the cost of reintroducing preparation noise. Moreover, the probe detuning can be varied over a frequency range of 9 GHz within 100 ms. This allows for both resonant and far-detuned interrogations, and is particularly useful for spectroscopic measurements, as it enables scanning the entire frequency range required.

The SPDM records photon arrival times, providing temporal resolution to the experiment. The single-pixel detection provides no spatial resolution in itself, and therefore the detector is easily saturated. Consequently, spatial filtering of light is essential for weak probe measurements. This is achieved in two ways: first by the DG obstacle placed in the probe field focus to remove background light, and second by implementing a narrow pinhole at the intermediate image plane to filter light outside the cloud region, and further suppress residual unscattered light. The DG configuration used here was introduced in recent work on few-photon spectroscopy of BECs [11]. Figure 1a also shows the tightly focused trapping light which is slightly off-axis and is primarily dumped. Any small amount of trapping light that is transmitted through the detection system and reaches the SPDM is fully removed by a single low-pass filter.

The two lasers used for imaging and probing differs in both intensity and frequency-stabilisation methods. The absorption imaging laser is locked to the closed cycling transition $|2,2\rangle \rightarrow |3,3\rangle$, using saturated Doppler-free spectroscopy, while the probe laser is beat-locked to a reference laser via an optical phase-lock loop (OPLL) [12]. The degree of freedom in probe frequency is key for most experiments presented in this work, and the specific probe transition is stated for each experiment. Moreover, the two phase-locked lasers enables investigations of coherent interactions in a multi-level system, including electromagnetically induced transparency (EIT), the Autler-Townes (AT) regime and Raman transitions.

B. Dark-Ground Spectroscopy

A probe beam with transverse intensity profile $I(x, y)$ and detuning δ is directed through an atomic cloud confined in the trap. The atom-light interaction is treated within a two-level approximation. The probe beam is assumed to have a transverse extent sufficiently large that its intensity can be taken as constant I_0 over the region selected by the pinhole aperture. The atomic cloud is characterised by a spatially dependent elecric-field transmission coefficient $T(x, y)$ and an associated dispersive phase-shift $\phi(x, y)$ imparted to the transmitted light. After interaction with the atoms, the probe field therefore acquires both amplitude attenuation and phase modulation across its transverse profile. In the DG configuration, the detected photon count rate R is determined

by [13]

$$R = \frac{I_0}{\hbar\omega}\int_{\text{pinhole}} 1 + T^2 - 2T\cos(\phi)\mathrm{d}A, \tag{1}$$

where $\hbar\omega$ is the energy of a probe photon. Because the DG configuration is sensitive to phase-shifts, significant signal can be generated even when absorption is weak. Consequently, the signal obtained per absorbed photon can substantially exceed that of bright-field detection schemes. In the ideal case, the DG background vanishes in the absence of atoms, allowing operation with a signal-to-noise ratio approaching the photon shot-noise limit. Further details on DG spectroscopy can be found in [11], and a broader comparison of signal-to-noise ratios in different detection configurations is given in [9]. In the far-detuned limit, the DG signal is given by [14]

$$R = \frac{I_0}{\hbar\omega}\frac{\Gamma^2}{16\delta^2}\int_{\text{pinhole}} \mathrm{od}^2\ \mathrm{d}A, \tag{2}$$

where Γ is the natural linewidth and od is the optical density, proportional to the atomic column density. The far-detuned DG signal is therefore directly related to the number of atoms present in states coupled to the probe light field. This proportionality is exploited in measurements to monitor population dynamics and track the evolution of the system in real time while maintaining minimal destructivity.

C. Production of Ultracold Gases

The experimental apparatus was recently described in [14]. In short, the experiment loads a magneto-optical trap (MOT) with approximately 10^9 ^{87}Rb atoms which are optically pumped to the $|F = 2, m_F = 2\rangle$ state, then caught in a magnetic quadrupole trap (QPT) and transported to an ultra-high vacuum chamber. The cloud is subjected to active RF-evaporation in the tight QPT, and the atoms are further cooled in a hybrid trap configuration that combines the QPT and a dipole laser beam at 1064 nm tightly focused to about 80 µm and vertically offset by 100 µm under the magnetic zero point. Finally, the atoms are transferred to a crossed optical dipole trap (cODT) based on an orthogonal pair of almost identical Gaussian beams. A microwave (MW) frequency sweep prepares the atoms in the $|1, 1\rangle$ ground-state, which has an enhanced lifetime in the trap of 12.4 s compared to the 3.2 s for the $|2, 2\rangle$ state. The final evaporation steps result in a Bose-Einstein condensates (BEC) of up to 650k atoms.

III. CATALOGUE OF EXPERIMENTS

This section presents a series of measurements designed to illustrate the performance and versatility of the TRDG platform. The experiments span motional, internal-state and spectroscopic dynamics, demonstrating that the setup enables real-time, high-sensitivity measurements across a broad range of time- and frequency scales within a single experimental realisation. Together, these results establish TRDG as a unified tool complementary to conventional imaging procedures. The section begins with trap frequency measurements (Section III A), in which the spatial motion of a single atomic cloud is encoded as amplitude modulations of the TRDG signal through a pinhole aperture. This approach enables complete extraction of trap frequencies from a single experimental run, eliminating the need for repeated time-of-flight measurements and significantly reducing the experimental overhead. Attention then turns to MW-driven internal-state dynamics. Real-time observation of MW-driven Rabi oscillations between two hyperfine ground-states is demonstrated (Section III B), providing direct determination of the MW Rabi frequency and transition frequency. Adiabatic MW frequency sweeps are subsequently used to monitor population transfer in-situ (Section III C), illustrating continuous tracking of coherent state evolution. Building on this capability, repeated sawtooth MW frequency sweeps applied to a single cloud enable full magnetic-field calibration within one experimental cycle (Section III D), reducing what is typically a multi-run procedure to a single-shot measurement. Optical two-photon measurements are demonstrated using the phase-locked Raman laser system. Raman-Rabi oscillations are directly detected by monitoring the driving optical fields themselves (Section III E). By exploiting the strong background suppression inherent to the DG configuration, signals at the 10^{-6} level relative to the driving fields are clearly resolved, underscoring the high dynamic range and sensitivity of the TRDG detection scheme. To highlight the spectral versatility of the phase-locked laser system, measurements are presented at both extremes of resolution and bandwidth. In the narrowband regime (Section III F) the system is used for two-photon spectroscopy in the EIT configuration, resolving sub-kHz transmission windows and enabling precise determination of the nonlinear Zeeman shift via the Breit-Rabi formula. At the opposite extreme (Section III G), broadband spectroscopy spanning 9 GHz across the ground-state hyperfine splitting of ^{87}Rbis performed within 100 ms, demonstrating rapid tunability across a wide spectral range. Finally, the low-destructivity of the TRDG platform is illustrated through continuous spectral monitoring of a cloud during evaporative cooling (Section III H). This enables real-time tracking of the transition from a thermal gas to a BEC, demonstrating the capability of the system to probe dynamical processes without interrupting or resetting the experimental sequence.

A. Trap Frequency Measurement

Extracting trap frequencies from experiments provide the basis for theoretical models and analysis of ultracold clouds. Using the TRDG method, a trap frequency measurement can be performed on a single cloud.

A pinhole is placed in the intermediate image plane, at a position, such that the image of the cloud is partially cut. Then, continuously probing the cloud with a weak, far-detuned probe field, encodes the motional cloud dynamics as amplitude modulation of the detected signal as the cloud moves in and out of the pinhole region. Although the method is most effective for detecting motion transversal to the light beam, oscillations along the beam also induce small changes in the signal. A Fourier analysis can in principle separate simultaneous oscillations along all directions at the same time, the clearest data is achieved by observing oscillations in each direction separately.

To induce oscillations, the atoms are pulled upwards with a magnetic field gradient, which is then abruptly turned off, such that the atoms start oscillating in the cODT. The best data quality is obtained by initiating purely single-dimensional oscillations, although it is also possible to measure several trap frequencies at once by initiating oscillations in multiple directions. The probe light is turned on 10 ms before the oscillation is initiated, and the SPDM records the dynamics.

Figure 2 shows two examples of measured trap frequencies in the cODT for a thermal cloud (top) and a purely condensed cloud (bottom). Previous absorption imaging methods required the acquisition of a series of images, where each image records the instantaneous centre-of-mass coordinates at variable wait times. Performing this type of experiment requires repeated measurement on a new cloud due to the destructivity of the imaging technique. In contrast, the TRDG method enables reliably extraction of complete-dataset using a single cloud. This is complementary to other methods of measuring trap frequencies on a single cloud with imaging techniques [9].

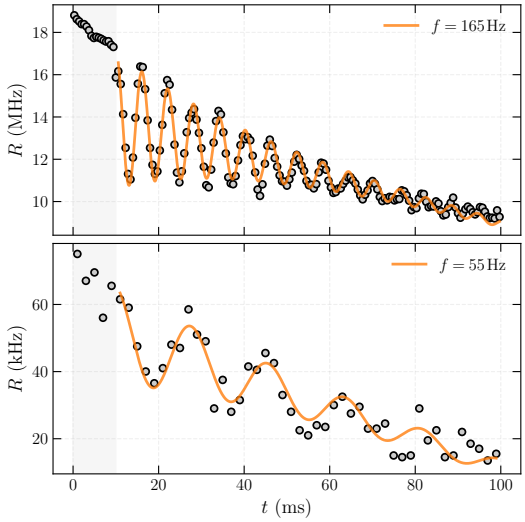

FIG. 2. Real-time measurements of trap frequencies at variable trap configurations: (top) a thermal cloud, and (bottom) a purely condensed cloud. The atomic cloud is trapped in an optical trap, and set in motion via a QP field, which is abruptly turned off at $t = 10\,\mathrm{ms}$. A weak probe field illuminates the cloud, and motion in and out of the pinhole is recorded by the SPDM. Trap frequencies can be measured over single experimental runs by detrending with an experimental decay and fitting to a harmonic oscillation.

B. Microwave Induced Rabi Frequencies

Measuring microwave (MW) induced Rabi frequencies provides a direct and accurate characterization of the coherent coupling between internal states in ultracold gases. Such measurements enable precise quantum-state control by providing a calibration of the MW field at the atomic sample, and are therefore essential for reliable state preparation and precision spectroscopy. For these experiments, the atoms are prepared in the state $|F, m_F\rangle = |2, 2\rangle$. A resonant or near-resonant MW field is then applied at fixed frequency to drive Rabi oscillations on the $|1, 1\rangle \leftrightarrow |2, 2\rangle$ transition. The resulting population dynamics are detected using the optical probe field, that selectively addresses only the lower hyperfine ground-state. The TRDG signal hence provides a time-resolved readout of the state populations. An example of the measured Rabi oscillations is shown in the top inset of Fig. 3, which illustrates the TRDG signal over time with the background offset subtracted. The generalised Rabi frequency Ω of the MW-driven transition depends on the MW detuning as

$$\Omega = \sqrt{\Omega_{\mathrm{MW}}^2 + \delta_{\mathrm{MW}}^2}, \tag{3}$$

where Ω_{MW} is the resonant Rabi frequency and δ_{MW} is the MW frequency detuning. Consequently, varying the MW frequency between experimental runs, the generalised Rabi frequency is measured as a function of MW detuning, as shown in the top panel of Fig. 3. Fitting this dependence allows Ω_{MW} and δ_{MW} to be extracted precisely. The bottom panel shows the residuals from the fit, which remain below the sub-kHz level. This shows that the measured values for Ω agree well with the theoretical prediction, and that the method provides an accurate characterisation of the MW field.

From the Rabi frequency measurements, the instantaneous frequency can be extracted using standard analytic signal representation [15–18] since the signal is real-

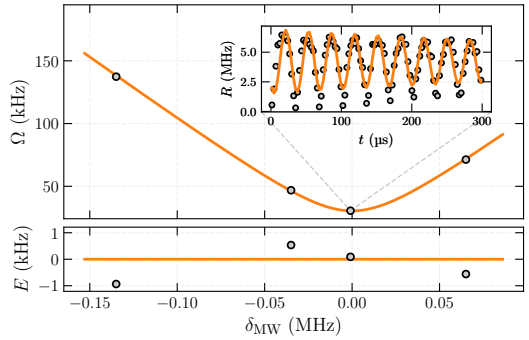

FIG. 3. Real-time measurements of MW-induced generalised Rabi oscillations on the $|1,1\rangle \leftrightarrow |2,2\rangle$ transition. To detect the population transfer an optical probe laser selectively addresses the $F = 1$ ground-state, such that the TRDG signal oscillates as the atomic population is driven between the two hyperfine states. The top panel shows the extracted generalised Rabi frequency Ω as a function of MW frequency detuning δ_{MW} with the fit to Eq. (3). The inset shows a representative time trace of Rabi oscillations near resonance with the corresponding fit. The bottom panel shows the residuals of the fit, which is seen to be below the sub-kHz level.

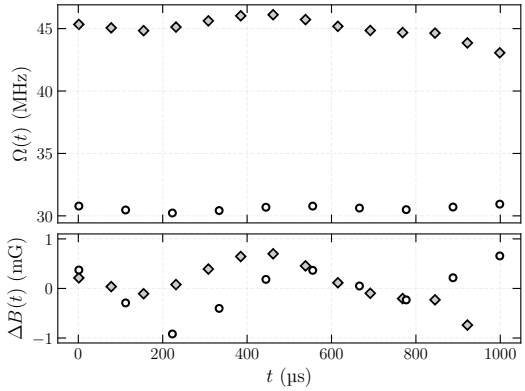

FIG. 4. Instantaneous Rabi frequency extracted from analytic signal analysis and the estimated magnetic field fluctuations causing the instability in frequency. The top panel shows the extracted time-dependent Rabi frequencies for the most resonant point in Fig. 3 (circles), and for the second most resonant point (diamonds). The bottom panel shows an estimate of the magnetic field fluctuations, assuming the instabilities are caused solely by these.

valued. Given a raw signal $S(t)$ from the SPDM, the analytic signal is defined as

$$\overline{S}(t) = S(t) + \mathrm{i}\mathcal{H}\left[S\right](t), \tag{4}$$

where $\mathcal{H}$ is the Hilbert transform. The instantaneous phase $\phi(t)$ is then the argument of the complex-valued $\overline{S}(t)$, and its derivative,

$$\Omega(t) = \frac{1}{2\pi}\frac{\mathrm{d}\phi(t)}{\mathrm{d}t}, \tag{5}$$

yields the instantaneous frequency $\Omega(t)$. This gives the frequency content of the signal as it evolves in time, and any oscillations or instabillities in the signal will show up as variations in $\Omega(t)$. The result of this analysis on the two datasets closest to resonance in Fig. 3 is shown in Fig. 4. Attributing the instability to magnetic field fluctuations only, the instantaneous deviation in the magnetic field from the mean value $\Delta B(t)$ can be calculated from the generalised Rabi frequency formula and is shown in the bottom panel of the same figure. The result under these assumptions is a fluctuation on the order of 1 mG in the magnetic field over a period of 1 ms.

C. State Preparation

Essential to experiments is the control and state manipulation of the atomic cloud. A particularly robust technique involves MW frequency sweeps to adiabatically transfer atoms between hyperfine ground-state manifolds. Compared to using π-pulses, frequency sweeps are more stable against small drifts in experimental parameters, such as stray magnetic fields that shifts the resonance.

Similar to Section III B, the preparation dynamics can be recorded using TRDG detection. Figure 5 shows the TRDG signal during MW frequency sweeps for two distinct scenarios, each measured on a single cloud using weak optical probe light addressing the $F = 1$ ground-state manifold. Initially, the atoms are in the state $|F, m_F\rangle = |2,2\rangle$, and a schematic level diagram indicating the relevant transitions, labelled (1) through (6), is shown at the top of Fig. 5. In the first scenario, the MW frequency is swept upward across the hyperfine ground-state resonances. With the atoms in the $|2,2\rangle$ state, MW radiation transfers population to the $|1,1\rangle$ state as soon as the resonance is reached. No further transitions occur at higher frequencies, resulting in the binary sigmoid signal in the TRDG signal as shown in the top panel of Fig. 5. In the second scenario, the MW frequency is swept downward from above the $|2,2\rangle \rightarrow |1,1\rangle$ resonance. Multiple resonances are sequentially crossed during the sweep. The first corresponds to the $|2,2\rangle \rightarrow |1,1\rangle$ transition, followed by the $|1,1\rangle \rightarrow |2,1\rangle$ transition and additional transitions occur until the atoms reach the final $|2,-1\rangle$ state. Consequently, the cloud is visible to the probe field a total of three times during the MW frequency sweep, corresponding to the three m_F states of the $F = 1$ ground-state manifold.

The amplitude of the TRDG signal varies due to several factors. Each state has an energy shift determined by the magnetic field, although this effect is negligible

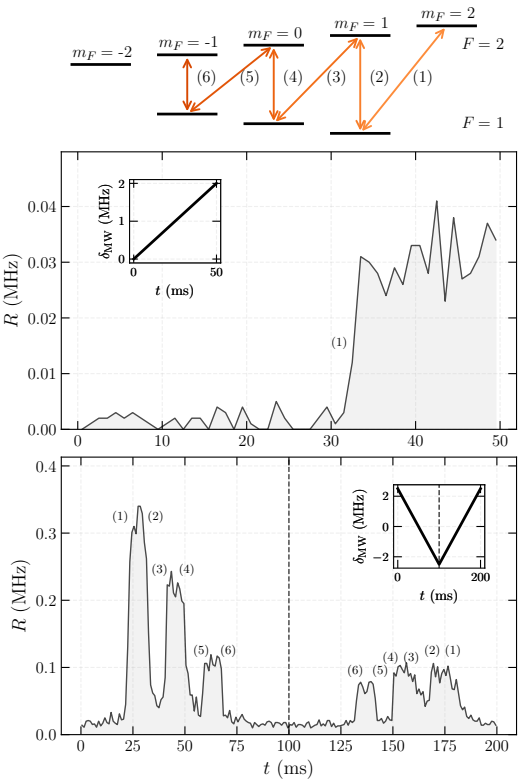

FIG. 5. Measured TRDG signal recorded during MW frequency sweeps on single atomic clouds. The optical probe field selectively addresses the $F = 1$ ground-state, and the atoms are initially prepared in the $|2, 2\rangle$ state. The upper schematic indicates the relevant transitions, labelled (1) to (6). In the top panel the MW frequency is swept upward from below resonance, resulting in adiabatic transfer to the $|1, 1\rangle$ state as the resonance is crossed. In the lower panel, the MW frequency is swept downward from above resonance, leading to sequential transitions as multiple resonances are crossed. The cloud becomes visible to the probe field three times during the sweep, corresponding to the three m_F states of the $F = 1$ manifold that couple to the detection.

for far-detuend probe light. Variations in optical coupling strengths governed by the Clebsch-Gordan coefficients, also contribute, as does the finite lifetime of the trapped cloud. Reversing the MW sweep reproduces the three observed peaks, with progressively increasing amplitudes consistent with the Clebsch-Gordan coefficients, while the overall reduction in signal reflects the cloud's limited lifetime.

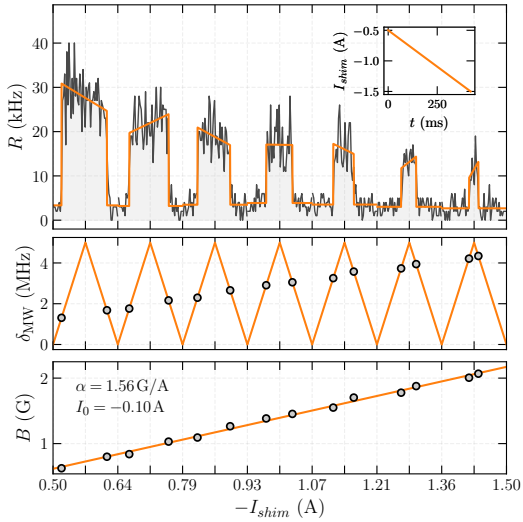

FIG. 6. Continuous monitoring of a single cloud during repeated sawtooth MW frequency sweeps while ramping a shim magnetic field. Atoms are here prepared in the $|2, 2\rangle$ state. Top panel shows the TRDG signal recorded using a weak optical probe field addressing the $F = 1$ ground-state. Each transition appears as a square-shaped pulse in the TRDG signal and these are fitted to Eq. (6) to extract the transition times. Middle panel shows these transition times plotted against the corresponding MW frequencies. As the magnetic field is ramped, the resonance frequency is shifted, leading to progressively narrower square-pulses. Lower panel shows the magnetic field (inferred from the resonance frequencies) versus the shim currents. A linear fit yields the current-to-field conversion factor and the field-nulling current, providing a full calibration of the magnetic field from a single cloud.

D. Magnetic Field Calibration

Experiments are typically characterised by a set of parameters whose influence on the atomic system must be carefully calibrated. This can be accomplished by monitoring the evolution of an atomic resonance while systematically varying the parameter of interest. Calibration of a magnetic field provides a representative example. The technique introduced in Section III C enables repeated measurements of the resonance frequency on a single atomic cloud by employing a sawtooth waveform for the MW frequency sweep.

The atoms are initially prepared in the $|2, 2\rangle$ state, and the MW frequency is ramped up from below the $|2, 2\rangle \leftrightarrow |1, 1\rangle$ resonance. As the resonance is crossed, the atoms are transferred adiabatically to the $|1, 1\rangle$ state. Reversing the direction of the ramp transfers the atoms back to $|2, 2\rangle$. Repeated application of a sawtooth frequency sweet therefore shuttles the atoms deterministically be-

tween the $|2,2\rangle$ and $|1,1\rangle$ states, enabling multiple resonance crossings, and thus multiple resonance measurements within a single experimental realisation. Performing this procedure while continuously recording the TRDG signal enables real-time monitoring of the transition resonance. This approach can be used to quantify the influence of external noise and experimental drifts, as well as to track the transition frequency while other experimental parameters are actively varied.

An example is shown in Fig. 6, where the magnetic offset field is slowly ramped while the MW frequency is swept back and fourth over a fixed range using a sawtooth waveform. The corresponding TRDG signal is displayed in the top panel. Each time the MW frequency crosses the resonance, the TRDG signal switches between low and high values. These switching events mark the instantaneous resonance frequency, which shifts due to the linear ramp of the magnetic field (top inset of Fig. 6). As the magnetic field increases, the resonance occurs at progressively different positions within the sawtooth sweep. Consequently, the square-shaped pulses in the TRDG signal become narrower in the time domain. Each pulse is fitted with the piecewise-defined function

$$C(t) = \begin{cases} at + b, & t_0 \leq t \leq t_1 \\ c, & \text{else} \end{cases}, \tag{6}$$

where, the parameters a, b, c, t_0, and t_1 are fit parameters. The timestamps, t_0 and t_1 define the transition moments and thus determine the resonance frequency for each sweep. These extracted frequencies are shown as markers overlaid on the MW frequency ramps in the middle panel of Fig. 6.

For magnetic-field calibration in the low-field regime, the measured transition frequencies are converted to magnetic-field values and plotted as a function of shim current (lower panel of Fig. 6). A linear fit yields the current-to-field conversion factor α and the field-nulling current I_0, thereby providing a complete calibration of the magnetic field generated by the coils. This demonstrates that full magnetic-field calibration can be performed using a single atomic cloud with the TRDG method.

E. Raman-Rabi Oscillations

This section demonstrates that the TRDG setup enables direct measurement of optical Raman-Rabi oscillations. Optical Rabi oscillations are typically measured by monitoring state populations, either via fluorescence detection or by using an additional probe field. Fluorescence signals are often weak, and require high numerical aperture systems, while auxiliary probe beams may perturb the atomic system.

The setup in Fig. 1 is modified by introducing a second laser field co-propagating with the probe beam. The original probe field is phase-locked to this additional field, and the two optical fields enter the setup with orthogonal circular polarisation. Together, these two phase-coherent fields drive a two-photon Raman transition. In the following, the original probe field is denoted R1 (Raman 1), and the additional field R2 (Raman 2). For these measurements, the SPDM is replaced by an avalanche photodiode (APD) to achieve improved time-resolution. In principle, slower Rabi oscillations could also be resolved using the SPDM. Using the TRDG detection scheme, only those components of the driving fields whose spatial modes are modified by interaction with the atoms, due to refraction, diffraction or spontaneous processes, are transmitted to the detector. These altered modes carry the relevant dynamical information, while the unperturbed background is strongly suppressed, thereby improving the signal-to-noise ratio. The flippable waveplate, which was previously used to direct light to either the CCD camera or the SPDM, can now be used to monitor either R1 or R2, separately, mimicking a dual-port detection setup.

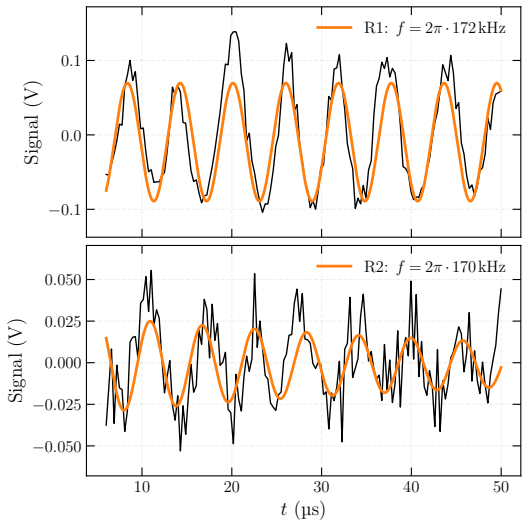

FIG. 7. Real-time measurements of optical Raman-Rabi oscillations on an avalanche photodiode (APD). Signal from either beam is measured at each output port a PBS cube, which filters the two Raman laser fields. Both panels illustrate the detrended signal of the Raman 1 (top) and Raman 2 (bottom panel). From the sinusoidal fits the frequencies and relative phase-relation are extracted. Notice the signals being out of phase, due to absorption from one is followed by stimulated emission into the other. Fitted phase difference around 200° and Raman-Rabi frequency around $2\pi \cdot 170\,\text{kHz}$.

Direct measurements on one of the two Raman fields have previously been demonstrated in a different setup [19], but direct detection in free space has not been performed

to our knowledge, and neither have measurements of both Raman light fields in a co-propagating setup.

To perform these measurements, the atoms are prepared in the state $|1,1\rangle$, R1 has σ^--polarisation, and R2 has σ^+-polarisation leading to a connection on the magnetically insensitive $|1,1\rangle \leftrightarrow |2,-1\rangle$ transition. Both optical fields are red-detuned $\approx 137\,\mathrm{MHz}$ from their respective single-photon transition to the excited $|1,0\rangle$ state on the D_2-line.

The TRDG signals for R1 and R2 are expected to contain two frequency components. The first arises from far-detuned single-photon transitions. This component reflects the population in $|1,1\rangle$ for R1 and in $|2,-1\rangle$ for R2, and will be referred to as the population signal. The second component arises from the transfer process of atoms between the two states, which involves absorption and stimulated emission in the two fields. In the TRDG setup, any changes in the light fields will be detected, producing signal that peaks when the transfer occurs at maximum rate, which occurs exactly at twice the transfer frequency itself, and will be referred to as the field signal. The population signal between R1 and R2 is expected to be out of phase, since they each detect different population states. In contrast, the field signal is in phase, because both emission and absorption of fields lead to signals in the TRDG setup. The relative magnitude of the two fields depend on the Raman-Rabi frequency, which scales with the square root of the power in each light field, the resonant optical density of the cloud, the single-photon detuning of each light field from the many allowed transitions, and the absolute power of the fields, which directly determines the population signal strength.

The result of one such measurement can be seen in Fig. 7, which displays the signal of the APD over time, with an exponential background subtracted. The experiment is performed twice, giving the signals of both R1 (top panel) and R2 (bottom panel), and the data is fitted with a decaying sinusoidal function. The fitted sinusoidal signals between R1 and R2 are 200° out of phase, close to the expected 180°, where the discrepancy is attributed to noise in the data and the fit. Additionally, the two signals have nearly identical frequencies. This indicates that the population signal is the main contribution to the TRDG signal. No clear sign of a double frequency signal is observed on top of the carrier signal. This suggests that the relative strength of the field signal is too weak to be detected with current data quality and experimental parameters.

Although the field signal was not detected, this measurement demonstrates the possibility of the TRDG setup. The signal reaching the APD is estimated to be $\approx 10^{-6}$ weaker than the driving fields, yet it is still clearly distinguishable from the background, which is strongly suppressed by the DG target and pinhole. Consequently, only a small fraction of background signal persists, while almost all signal is transmitted.

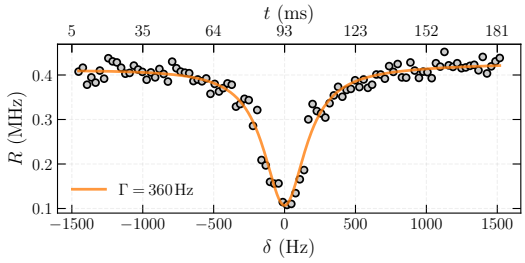

FIG. 8. Two-photon spectroscopy of an ultracold cloud above T_c. Attenuating both probe and coupling fields, the system is capable of resolving spectral features sub-kHz. This EIT transmission window FWHM is fitted to 360 Hz.

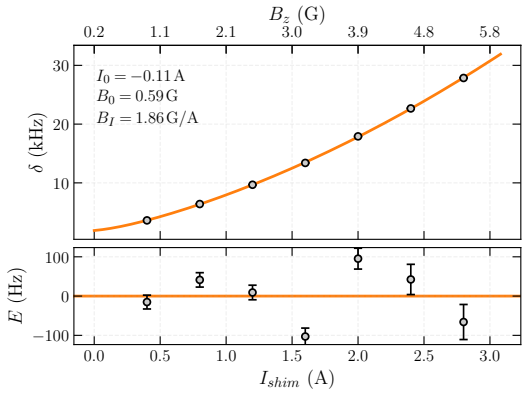

FIG. 9. Weak magnetic field Breit-Rabi measurement of the $|1,1\rangle \leftrightarrow |2,-1\rangle$ non-linear Zeeman shift. The top panel shows a series of fitted EIT resonances, each averaged over ten measurements on a single cloud, for different magnetic fields, and bottom shows the residuals. The shim-coil parameters are fitted using the theoretical prediction from the Breit-Rabi formula. The statistical uncertainty of each point is not visible. The second panel shows the residuals from the fit, which have an average magnitude of 53 Hz.

F. Narrow Spectroscopy: Resolving Sub-kHz EIT

For electromagnetically induced transparency (EIT) measurements, the phase-locked Raman laser system is used as described in Section III E. The two optical fields are co-propagating with opposing circular polarisation. The R2 laser field acts as a coupling field resonant to the $|2,-1\rangle \rightarrow |2,0\rangle$ transition, while the R1 field serves as the probe field at much lower optical power than R2, and frequency swept across the single-photon transition $|1,1\rangle \rightarrow |2,0\rangle$ (and consequently, the two-photon reso-

nance) by adjusting the beat-lock. Since the two-photon resonance is magnetically insensitive, the decoherence between the ground levels in this lambda-scheme is greatly reduced compared to other level schemes. This allows for measurements of sub-kHz EIT-transmission windows.

Figure 8 shows a dataset measured on a single cloud, illustrating the narrowest measurement possible with the experiment to date. A Lorentzian fit yields a full width at half maximum (FWHM) of 360 Hz, placing it in sub-kHz regime. To achieve the best resolution, the frequency generator, which provides the reference signal to the OPLL for the beat-frequency lock, is operated with the smallest possible frequency step-size and the longest possible time step-size.

The fact that the spectrum must be taken in steady-state, puts a lower limit on the observable linewidth using the built-in function of the frequency generator, and the data displayed in Fig. 8. The consequence of measuring narrow spectral features at time-scale limit is that the system has not had the time to decohere to steady-state during the sweep, leading to the appearance of Raman-Rabi oscillations in the spectrum. This effect can be mitigated, if necessary, by using a different frequency generator or manually encoding the sweep steps in the frequency generator.

The narrow spectral feature allows for precise measurements of the $|1,1\rangle \leftrightarrow |2,-1\rangle$ resonance frequency. To demonstrate this, the non-linear Zeeman shift is measured at a low absolute magnetic field of a few Gauss. Similar to the approach in Fig. 6, the magnetic field can be swept during continuous measurements to obtain a full dataset using a single cloud. Here, instead, the magnetic field is held constant and the resonance is measured 10 times on a single cloud. The fitted resonances $\delta_{0,i}$ are then used to find a mean value δ_0 and an uncertainty, σ, as

$$\sigma = \frac{\sqrt{\sum_i^N (\delta_{0,i} - \delta_0)^2}}{N}, \tag{7}$$

where $N = 10$. The experiment is then repeated with different magnetic fields. The results are displayed in the top panel of Fig. 9, and the data are fitted using the predicted frequency shift relative to the hyperfine splitting, calculated from the Breit-Rabi formula [20, 21]. The lower panel shows the residuals E of the fit, with an average magnitude of deviation of 53 Hz, corresponding to a relative frequency accuracy of $7.2 \cdot 10^{-6}$.

Currently, the spectral resolution is hardware limited, specifically by the frequency generator register design, which uses a 16-bit encoding for the time-step size of the sweep. This constraint sets a limit on how narrow a spectrum can be measured, but is very feasible to improve in future measurements. Ultimately, the physical limit on minimum achievable linewidth with EIT is set by the phase-decoherence between the $|1,1\rangle$ and $|2,-1\rangle$ states, which is the most complex parameter to optimise, as it involves hard-to-control sources of noise from the lab environment and laser systems. The measurements displayed here show no sign of having reached that limit yet.

G. Broadband Spectroscopy

In the previous Section III F the optical phase-locked loop (OPLL) was shown to enable sub-kHz-resolution. An equally important capability for many applications is the ability to tune the optical probe frequency rapidly and continuously over a wide spectral range. Here it is demonstrated to also be capable of broad spectroscopy across the entire ground-state hyperfine structure of ^{87}Rb. Following similar techniques as in Section III B, the atoms are prepared in an equal mixture of $|1,1\rangle$ and $|2,2\rangle$, and spectroscopy is carried out by sweeping the reference beat-frequency of the OPLL-circuit to change the probe frequency.

Figure 10 presents the spectrum obtained from probing the atomic sample with a weak light field of either σ^+ or σ^- polarisation. These experiments were performed by sweeping the probe frequency over a 9 GHz range within 100 ms. Each polarisation shows distinct spectral features corresponding to the electric dipole-allowed transitions. Specifically, as the atoms are prepared in a superposition state of $|1,1\rangle$ and $|2,2\rangle$ ground states, the σ^+ transition restricts the coupling between the fully stretched states with $\Delta F = +1$ only, namely $|F, m_\mathrm{F}\rangle \rightarrow |F+1, m_\mathrm{F}+1\rangle$. In contrast, σ^- transitions exhibit three dominant transitions with $\Delta F = 0, \pm 1$ for each of the ground-states. Since the optical density depends on the transition, and particularly the Clebsch-Gordan coefficient for the relevant transition, the σ^+ transition is spectrally broader and with higher amplitude than the much weaker σ^- transition.

Interestingly, side-lobes are observed in the DG spectrum, corresponding to the constructive interference effect of the DG method, as discussed in [11]. Physically, the SPDM records the integrated intensity in the pinhole area, and since the DG signal is sensitive to dispersive phase shifts, ring-like structures are observed in the intensity profile across the pinhole [11]. At certain detunings, constructive interference rings appear, which give rise to shoulder peaks in the absorption spectrum. This is spectrally enhanced for the σ^+ transition, as the phenomenon scales with optical density.

Another interesting phenomenon is the destructive interference between peaks observed in the σ^--spectra. This effect is only visible in DG measurements and is caused by the phase-shift sign, which depends on the sign of the detuning. That is, while absorption from different resonances always adds up, the phase-shift induced signal in the DG configuration cancels out in between two resonances.

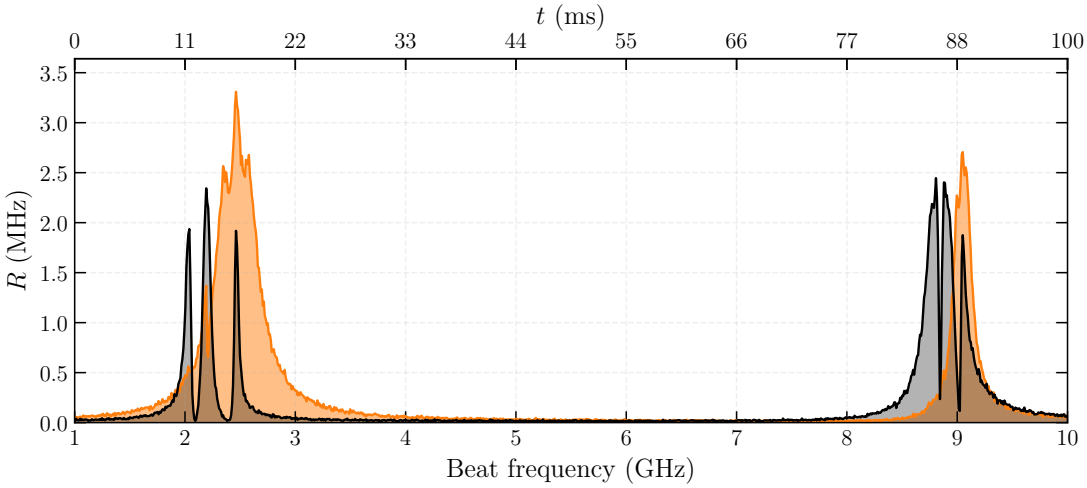

FIG. 10. Spectroscopy of an ultracold cloud prepared in a superposition state of the $|1,1\rangle$ and $|2,2\rangle$ hyperfine ground-states, interrogated with a probe laser that spans approximately 9 GHz within 100 ms. Both hyperfine manifolds exhibits a single dominant peak for σ^+ polarisation (orange), corresponding to the $\Delta F = 1$ transition between fully stretched states, or three peaks for the σ^- transitions (black) with $\Delta F = 0, \pm 1$. Small impurities in polarisation or the atomic state give rise to weak signals in σ^+ that align with the σ^- case. The atomic clouds are identical, but the spectral peaks are distinctly different in both height and widths due to the differences in transition strengths. In particular, the Clebsch-Gordan coefficients corresponding to each transition reflects the differences in the observed optical density. Interestingly, since the SPDM records the integrated intensity in the pinhole area, and as the dark-ground signal is sensitive to dispersive phase shifts, ring-like structures is observed in the intensity profile across the pinhole [11]. At certain detuning, new constructive interference rings appear, which gives rise to shoulder peaks in the absorption spectrum. This is spectrally enhanced for the σ^+ transition, as the phenomenon scales with optical density.

Currently, the main limiting factors to achieving broader sweeps are (i) avoiding mode jumps in the laser light during the sweep, and (ii) bandwidth of electrical components in the OPLL circuit. Mode jumps are circumvented by using feed-forward mechanisms from the piezo-voltage to the diode current. This has the slight disadvantage of altering the laser power during the measurement; however, this is negated with a power-stabilising circuit (not shown in Fig. 1). The upper limit is therefore currently hardware-limited by the bandwidth of the electrical components, which significantly deteriorates above 10 GHz. Achieving broader scans is thus feasible with different electrical components.

H. Detection During Evaporative Cooling

Since the presented detection setup can work in a minimally destructivity regime, it is possible to perform multiple measurements on a single cloud. This is illustrated in Fig. 11 for two different scenarios. In both cases, the probe light sweeps across the $|2,2\rangle \leftrightarrow |3,3\rangle$ resonance within a frequency interval $-150 < \delta/\Gamma < 100$, and the atoms are prepared in the $|2,2\rangle$ state.

Both panels illustrate a continuous triangular frequency sweep of the probe light. The top panel is a measurement performed with a constant cODT depth for a thermal cloud at 380 nK. Within a total duration of ≈ 34 s, the sweep was repeated 70 times. After this sequence, $77 \cdot 10^3$ atoms were still present in the trap, compared to $125 \cdot 10^3$ if the same experiment was repeated without probe light. The temperature increased from 380 nK to 450 nK when using the probe light. The TRDG method recorded a total of $6 \cdot 10^5$ counts, after subtracting the background signal, which results in about 13 counts per lost atom or $8.5 \cdot 10^3$ counts per nK increase in temperature.

The bottom panel shows a similar measurement performed during a slow evaporative cooling ramp over ≈ 5 s in the cODT. During the evaporation, the total number of atoms decreases, resulting in a decreasing TRDG count rate. Additionally, as the cloud cools, its size decreases, leading to fewer probe photons interacting with the atoms, contributing to the observed decrease of the signal. This effect is especially important when the cloud condenses and forms a BEC towards the end of the measurement. The optical density of the cloud is, however, relatively unchanged during the sweep, since both the atom number and temperature decrease, which compen-

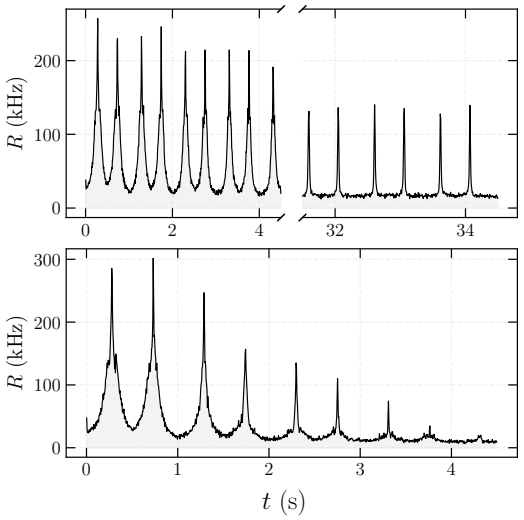

FIG. 11. Continuos spectral sweeps performed on single clouds during two scenarios: constants trap configuration (top) and in an evaporation sequence (bottom). In both cases the weak optical probe field is sweeping across the $|2,2\rangle \leftrightarrow |3,3\rangle$ cycling transition. In the evaporation step of the lower panel, the atomic cloud crosses the transition from a thermal gas to a condensed BEC.

sate each other. Consequently, the width of spectral features shrinks at a much slower rate than the signal amplitude. After the data acquisition, the cloud was released for time-of-flight absorption imaging, which showed that a BEC cloud was still intact after the measurement sequence.

IV. CONCLUSION

This work demonstrates the versatility of the novel TRDG detection platform based on DG imaging in a $4f$-setup in combination with a pinhole, single photon detection and a broadband laser system. One of the advantages of the DG configuration is the ability to obtain many measurements from single atomic clouds, which significantly reduces shot-to-shot noise and measurement times.

We successfully demonstrated real-time monitoring of motional dynamics, and internal state evolution. This included oscillations in the harmonic trap, microwave-induced Rabi oscillations, and state transfers. A successful measurement of Raman-Rabi oscillations was performed by measuring directly on the driving fields. In particular, it was demonstrated that signals from either of the two driving fields can be measured individually. Based on the phase-locked detection laser system, we achieved sub-kHz spectral resolution in EIT measurements and successfully probed the system across a 9 GHz frequency range within 100 ms. By employing repeated frequency sweeps on a single cloud, we demonstrated a fast, high-precision measurement of the non-linear Zeeman shift at low magnetic fields.

The technique presented here offers several promising avenues for future research. The capability to repeatedly scan narrow spectral features, such as EIT peaks, on a single cloud enables the investigation of density-dependent effects without the atom-number fluctuations due to preparation noise. The high temporal resolution and non-destructive nature of the signal can also be used for active feedback to stabilise experimental parameters or to steer quantum states during an experiment. In-particular, this platform is very well suited for studying multi-level coherent interactions, including e.g. EIT, the Autler-Townes regime, and resonant Rabi oscillations, with high sensitivity. Thus this method provides a robust, complementary alternative to destructive imaging, serving as a potential tool for the next generation of precision measurements with ultracold quantum gases.

ACKNOWLEDGMENTS

We acknowledge support from the Danish National Research Foundation through the Center of Excellence "CCQ" (DNRF152) and by the Novo Nordisk Foundation NERD grant (Grantno. NNF22OC0075986).

[1] K. Bongs, M. Holynski, J. Vovrosh, P. Bouyer, G. Condon, E. Rasel, C. Schubert, W. P. Schleich, and A. Roura, Taking atom interferometric quantum sensors from the laboratory to real-world applications, Nature Reviews Physics **1**, 731 (2019).

[2] B. Stray, A. Lamb, A. Kaushik, J. Vovrosh, A. Rodgers, J. Winch, F. Hayati, D. Boddice, A. Stabrawa, A. Niggebaum, M. Langlois, Y.-H. Lien, S. Lellouch, S. Roshanmanesh, K. Ridley, G. de Villiers, G. Brown, T. Cross, G. Tuckwell, A. Faramarzi, N. Metje, K. Bongs, and M. Holynski, Quantum sensing for gravity cartography, Nature **602**, 590 (2022).

[3] D. Bluvstein, S. J. Evered, A. A. Geim, S. H. Li, H. Zhou, T. Manovitz, S. Ebadi, M. Cain, M. Kalinowski, D. Hangleiter, J. P. Bonilla Ataides, N. Maskara, I. Cong, X. Gao, P. Sales Rodriguez, T. Karolyshyn, G. Semeghini, M. J. Gullans, M. Greiner, V. Vuletić, and M. D. Lukin, Logical quantum processor based on reconfigurable atom arrays, Nature **626**, 58–65 (2023).

[4] G. Reinaudi, T. Lahaye, Z. Wang, and D. Guéry-Odelin, Strong saturation absorption imaging of dense clouds of ultracold atoms, Optics letters **32**, 3143 (2007).

[5] T. Vibel, M. B. Christensen, M. A. Kristensen, J. J. Thuesen, L. N. Stokholm, C. A. Weidner, and J. J. Arlt, Spatial calibration of high-density absorption imaging, Journal of Physics B: Atomic, Molecular and Optical Physics (2024).

[6] W. Ketterle, D. S. Durfee, and D. Stamper-Kurn, Making, probing and understanding Bose-Einstein condensates, in *Bose-Einstein condensation in atomic gases* (IOS Press, 1999) pp. 67–176.

[7] R. Meppelink, R. A. Rozendaal, S. B. Koller, J. M. Vogels, and P. van der Straten, Thermodynamics of Bose-Einstein-condensed clouds using phase-contrast imaging, Phys. Rev. A **81**, 053632 (2010).

[8] M. R. Andrews, M.-O. Mewes, N. J. van Druten, D. S. Durfee, D. M. Kurn, and W. Ketterle, Direct, nondestructive observation of a Bose condensate, Science **273**, 84 (1996).

[9] M. Gajdacz, P. L. Pedersen, T. Mørch, A. J. Hilliard, J. Arlt, and J. F. Sherson, Non-destructive Faraday imaging of dynamically controlled ultracold atoms, Rev. of Scient. Inst. **84**, 083105 (2013).

[10] F. Kaminski, N. S. Kampel, M. P. H. Steenstrup, A. Griesmaier, E. S. Polzik, and J. H. Müller, In-situ dual-port polarization contrast imaging of Faraday-rotation in a high optical depth ultracold 87Rb atomic ensemble, The Eur. Phys. Journ. D **66**, 10.1140/epjd/e2012-30038-0 (2012).

[11] R. M. F. Andersen, L. N. Stokholm, I. Zebergs, N. R. Neubert, A. S. Chatterly, and J. J. Arlt, Spectrally probing ultra-cold clouds, arXiv (2026).

[12] J. Appel, A. MacRae, and A. I. Lvovsky, A versatile digital GHz phase lock for external cavity diode lasers, Measurement Science and Technology **20**, 055302 (2009).

[13] W. Ketterle, D. S. Durfee, and D. M. Stamper-Kurn, Making, probing and understanding Bose-Einstein condensates (1999).

[14] R. M. F. Andersen, *Spectrally probing ultracold bosonic clouds*, Phd thesis, Aarhus University (2025).

[15] B. Boashash, Estimating and interpreting the instantaneous frequency of a signal. i. fundamentals, Proceedings of the IEEE **80**, 520 (1992).

[16] B. Boashash, Estimating and interpreting the instantaneous frequency of a signal. ii. algorithms and applications, Proceedings of the IEEE **80**, 540 (1992).

[17] L. Cohen, *Time-Frequency Analysis* (Prentice Hall, Upper Saddle River, NJ, 1995).

[18] P. Flandrin, *Time-Frequency/Time-Scale Analysis* (Academic Press, San Diego, 1999).

[19] C. Liedl, S. Pucher, P. Schneeweiss, L. P. Yatsenko, and A. Rauschenbeutel, Observation of oscillatory Raman gain associated with two-photon Rabi oscillations of nanofiber-coupled atoms, Journal of Physics B: Atomic, Molecular and Optical Physics **55**, 234005 (2022).

[20] D. A. Steck, Rubidium 87 D Line Data, `http://steck.us/alkalidata` (2025), revision 2.3.4, 8 August 2025.

[21] G. Breit and I. I. Rabi, Measurement of nuclear spin, Phys. Rev. **38**, 2082 (1931).

CHAPTER 5

Quantum Sensing using Rydberg Atoms

This chapter presents a series of experiments performed with a Rydberg-atom-based EIT sensing scheme conducted during a seven-week long research stay abroad. The experimental work was carried out at Otago University, New Zealand, under the supervision of Prof. Niels Kjærgaard, whose expertise and guidance were essential for the execution and interpretation of the measurements.

Central to this chapter is the realisation of a Rydberg-atom-based EIT scheme for sensing and characterising external MW fields. This represents a clear shift from the Aarhus experiment, and the approach does not rely on elaborate infrastructure such as ultra-high vacuum systems, laser cooling and trapping of atoms. Instead, the experiments are based on a room-temperature ^{87}Rb vapour cell, significantly simplifying the experimental platform while retaining high sensitivity to MW fields. Two optical lasers provide the probe and coupling fields required to address a three-level ladder scheme, enabling EIT as a readout mechanism. The interaction of the Rydberg states with external MW radiation changes the spectral features forming the basis for atomic MW polarimetry in a compact architecture. The experiments led to two main results: the first being the result from a follow-up experiment on previous works [14] investigating the Autler-Townes (AT) splitting at strong MW fields, and in particular resolving substructure of the highly excited Rydberg states; and the other revolving on state of polarisation measurements of

MW fields. The latter is being published as of writing [6].

This chapter is divided into three sections. The first describes the experimental design, the second presents a catalogue of the experiments conducted, and the third includes the resulting publication from the investigations on MW polarimetry. The structure of this chapter reflects the work carried out during my time in the laboratory. My first task was constructing the experiment on a cleared optical bench, and hence the chapter begins with laying out technical considerations behind the setup and characterising its stability. This is followed by the presentation of experimental results, beginning with frequency calibrations of both optical and MW fields to ensure resonance conditions for subsequent experiments; followed by the strong MW field regime investigations, particularly the AT splittings of the Rydberg states which is shown to exhibit substructure. This observation in itself constitutes a significant result, supplementing results that were absent from [14]. Finally, polarimetric measurements were carried out using the Rydberg-EIT sensing scheme; marking the final results of my stay and laying the basis for the work presented in [6], which is added as an appendix to this chapter. As a conclusion of my research abroad, I developed a simulation framework for data analysis. Although initially intended for the Rydberg experiments described here, this work motivated several modifications that enabled its application to experiments conducted in Aarhus. These developments are not discussed in this chapter, and the reader is referred to Section 2.5 for theoretical details. The density simulations will be presented in parallel with the experimental results.

5.1 Experimental Setup

Highly excited Rydberg states were introduced in Section 2.2. These states are characterised by large transition dipole moments to neighbouring Rydberg states, which can be addresed with resonant radiation in the MW domain. The high sensitivity to electromagnetic fields can be exploited for applications in precision metrology, communiation and quantum sensing and offers a replacement to classical components, like the metallic antenna wire, with miniature vapour cells. A common approach for sensing external MW fields exploits Rydberg EIT [14, 63–66], resulting in an AT splitting of the transmission feature proportional to the MW field amplitude. This method offers a self-calibrated, SI-traceable atomic probe, which motivates the following experiment.

5.1.1 Overview

The experiment consists of two modules: one for generating external MW fields of variable frequency, field strength, polarisation and wavevector; and the other comprises the Rydberg-atom-based sensor that utilises EIT to measure these fields. For MW field emission, two homebuilt configurations were tested. First iteration of experiments used helical antennas. They are quick to produce, consisting of a conducting wire wound in a helix, and emit circularly polarised fields along the antenna axis. Moreover, a horn antenna design was made for a standard 3D printer using light-weight plastic material. The interior surface serves as a waveguide for the field emitted by a coaxial probe at the horn throat, and hence the surface was copper-electroplated to add conductivity. Generally, the horn antenna emits MW fields that are highly directive, typically linearly polarised, and can be considered ideal plane waves in the far field. Both types of antennas are low-cost and offer fast prototyping. However, the final setup uses an industrially manufactured, dual polarised, quad ridged horn antenna (RF SPIN, QRH40C) connected to a MW signal generator (Agilent E8257D). An additional MW signal generator (HP 83732B) is used for the polarisation measurements in Section 5.2.4. All experiments employ the same Rydberg-atom-based MW field probe. It consists of two optical fields and the atomic sample.

Unlike previous experiments which require laser cooled atoms in an elaborate ultra-high vacuum setup, this work employs a simple, sealed bubble cell with a diameter of 10 mm containing a room-temperature gas of ^{87}Rb atoms. Although

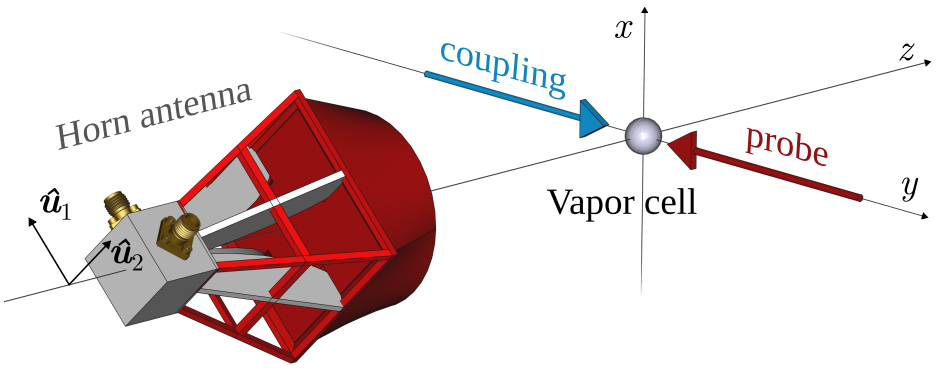

Figure 5.1: *The key components for the experiments on Rydberg-atom-based EIT sensing. Two counter propagating light fields achieve EIT conditions in an atomic sample that is subjected to MW fields generated in the far-field of a quad ridged horn antenna.*

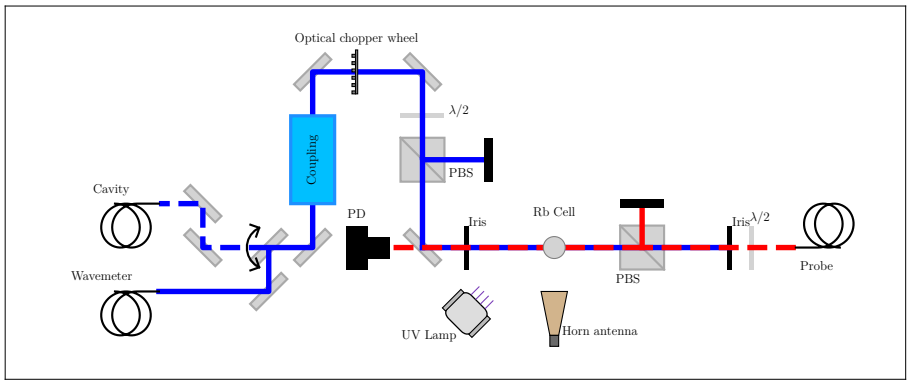

Figure 5.2: *Sketch of the experimental configuration. The setup is centred around a vapour cell, in which counter propagating probe and coupling beams establish EIT conditions. The probe laser (Toptica DL-pro @ 780 nm) is locked to the* $5S_{1/2}|F = 2\rangle \rightarrow 5P_{3/2}|F = 3\rangle$ *transition and guided to the experiment via a PM-SM optical fibre. Beam alignment is ensured using two pinholes, while combinations of waveplates and PBS cubes provide polarisation cleaning and independent light power control for both optical fields. The probe light power is* $\sim 1.0\,\mathrm{mW}$ *and the transmitted probe light is separated from the coupling beam by a dichroic mirror and detected using a photodiode (Thorlabs, PDA100A-EC). The coupling laser (MOGLab injection-locked @ 480 nm) connects the* $5P_{3/2}|F = 3\rangle \rightarrow |r_1\rangle$ *transition, where* $|r_1\rangle$ *is a highly excited Rydberg level. It provides* $\sim 330\,\mathrm{mW}$ *of amplified light, optically chopped at 6 kHz, enabling the use of a lock-in-amplifier (SR810 DSP) to detect the weak EIT signal. The coupling laser has a second output for its seed laser at* $\sim 10\,\mathrm{mW}$*, which is directed either to a wavemeter (Bristol 621) for initial frequency tuning and mode-jump monitoring; or to a high-finesse optical cavity (Stable Laser Systems), where changes in the transmission or reflection signal is used in a feedback-loop to improve long term frequency stability.*

a larger cell provides better signal-to-noise ratio, the small spherical cell confines the sample to a region where the MW field, generated in the far field of the horn antenna, can be considered homogeneous. However, the small cell's large radius of curvature, can lead to undesirable lensing effects on both laser beams. Time was not spent investigating such effects during my stay, and will be omitted in this thesis, although it might be taken into account for future experiments. The counter-propagating, optical fields "*wire-up*" the atoms for the EIT readout, which motivates an outline of the optical setup.

5.1.2 Lasers and Optics

The experimental setup, shown in Fig. 5.2, is centred on a vapour cell in which counter-propagating probe- and coupling beams establish EIT conditions. The

probe laser is at 780 nm provided by a Toptica DL-pro, frequency stabilised to the $5S_{1/2}|F = 2\rangle \rightarrow 5P_{3/2}|F = 3\rangle$ resonance using a Doppler-free saturated spectroscopy setup. The light is guided to the experiment via a PM-SM optical fibre, and collimated with a $1/e^2$ diameter of ~ 5 mm at the atomic plane, not accounting for lensing effects at the vapour cell surface. The probe power is ~ 1.0 mW. A waveplate and PBS cube pair facilitate polarisation cleaning, independent light power control and easy alignment of the polarisation axis for both optical fields. Behind the atoms, a dichroic mirror separates the probe and coupling beams, and a photodiode detects the transmitted probe light.

The coupling field is provided by a 480 nm MOGLab injection-locked amplified laser, which provides a beam with a $1/e^2$ diameter of ~ 5 mm and ~ 330 mW light power for the experiment. The coupling laser connects the $5P_{3/2}|F = 3\rangle \rightarrow |r_1\rangle$ transition, where $|r_1\rangle$ is a highly excited Rydberg state. For most of the experiments in this work, $|r_1\rangle \in \{49D_{3/2}, 49D_{5/2}\}$, and these states are not hyperfine resolved, since the splitting is much smaller than the interaction with external fields, making the fine structure basis sufficient. With a choice of the $|r_1\rangle$ level, the resonance frequency is calculated using the ARC (Alkali Rydberg Calculator), which computes atomic energies from literature quantum defects [67]. The coupling laser frequency is tunable by adjusting the ECDL parameters, namely the injection current, diode temperature and piezo offset, while the output frequency is continuously monitored using a wavemeter (Bristol 621). When the laser frequency is within the anticipated range, a sawtooth waveform is applied to the piezo controlling the grating position, modifying the external cavity length and hence enables very broad[1] frequency scans of ~ 100 GHz. Then, the piezo DC offset and diode current can be adjusted until the spectral EIT features are observed, corresponding to the two-photon resonance. An optical chopper periodically blocks the coupling beam at 6 kHz[2], which enables the use of lock-in detection. The recorded probe transmission feeds into a SR810 DSP lock-in-amplifier with a reference frequency input from the optical chopper controller. The output of the lock-in-amplifier is recorded by a 2 GSa/s oscilloscope (Agilent MSO-X-2000). The coupling seed laser is send to a ultra-high finesse optical cavity (from Stable Laser Systems), where both reflected and transmitted signals are monitored and used for a feedback-loop to stabilise the frequency output described in Section 5.1.4. A CMOS camera recorded the spatial cavity mode shown in Fig. 5.3.

[1] Compared to the usual ~ 10 GHz range for Toptica DLs
[2] A high pitched sound started above this value, otherwise limited by 10 kHz

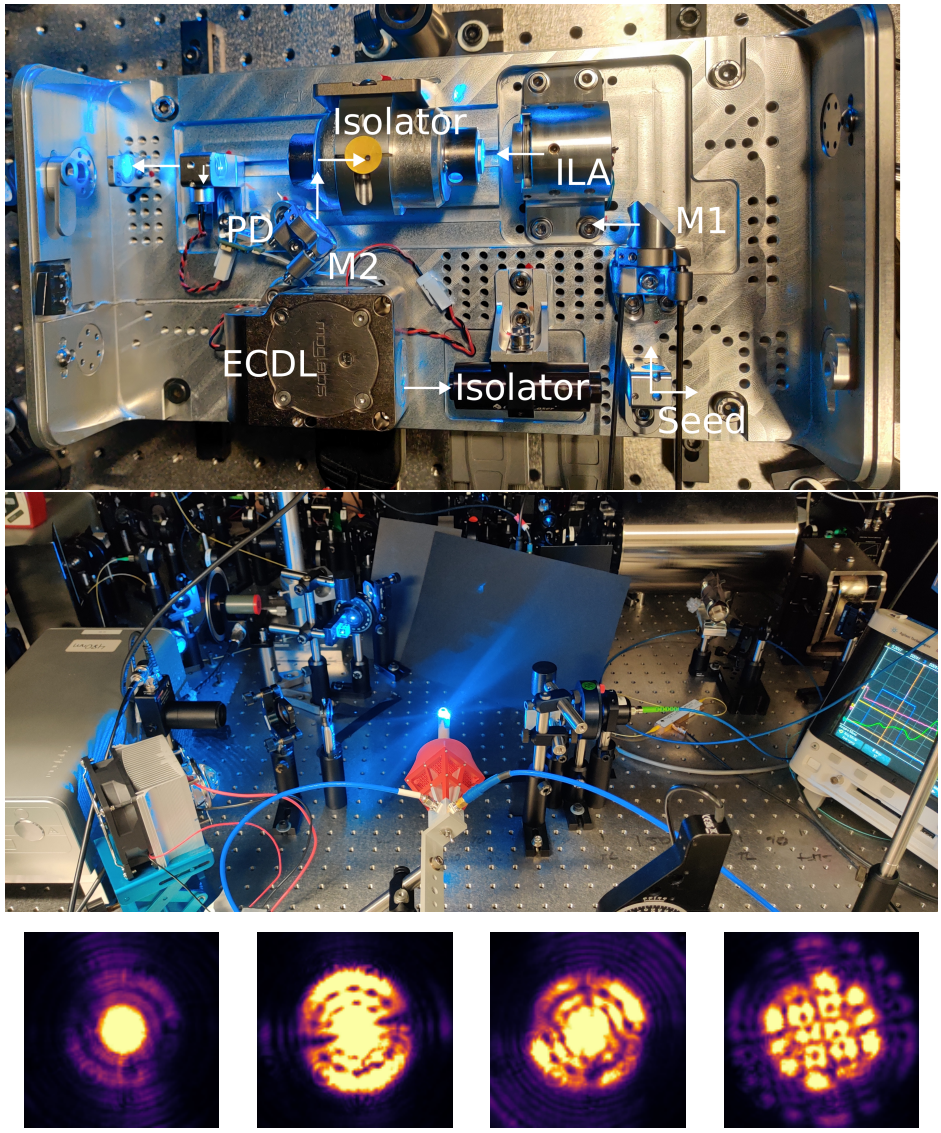

Figure 5.3: *(Top) The MOGLabs injection-locked amplified laser module consists of an ECDL seed laser (primary laser) that provides reference light for the injection-locked amplifier diode (secondary laser). Both diodes are temperature stabilised and the secondary diode has an integrated aspheric lens to focus the seed laser. An anamorphic prism pair is used for beam-shaping the output. (Centre) Photograph of the final experimental setup. (Bottom): Examples of transverse modes measured after reflections in the ultra-high finesse cavity. Different families of higher-order Gaussian beams can be seen, including the Hermite-Gaussian (cartesian), Laguerre-Gaussian (cylindrical), and Ince-Gaussian (elliptical) modes. Zero orders are the same for all families, and each family constitutes a basis to re-express any general solution in.*

5.1.3 Experiment Control System

After assembling the equipment, the system was nearly ready for operation. However, an experimental control system was still required to enable automated experiments with communication between the various instruments. For these experiments, the key components are: (1) the MW generator, used for varying external MW field parameters such as frequency, power and sweep parameters; (2) the lock-in-amplifier that enables detection of the weak EIT signal and (3) the oscilloscope, which is used for averaging traces and to store and save the data for later computer analysis. Additionally, for a stable experiment: (4) the MOGLab laser driver can be used for logging the coupling laser and ensuring that it remains locked during experiments; and (5) the signal generator, which produces the piezo ramp for scanning the coupling laser frequency can be actively controlled to adjust the piezo DC offsets, which is essential for the feedback loop that maintains long-term stability of the coupling laser frequency.

All experimental control programmes are build modularly and therefore share the same structure. At the start of each experiment, the relevant instruments are initialised and configured. This typically involves setting the MW power and frequency, defining the desired sweep parameters, configuring the oscilloscope, and adjusting the filter settings and gain for the lock-in-amplifier, sometimes using a variable gain over the course of an experiment. Moreover, the control programme is threaded, so that the stabilisation routine can run in parallel with the experiment.

After establishing communication with all instruments, a single coupling laser frequency sweep is performed with the MW fields off, and the resulting EIT trace is saved for calibration of the ramp. A more detailed description is given in Section 5.2.1, and an exemplary trace is shown in Fig. 5.10. The parameter space is then investigated iteratively, with all data stored alongside relevant metadata for each instrument.

All recorded spectra result from averaging over a number of repeated experiments. In this thesis, the standard number of repetitions varied from 2 to 512 traces, in multiplicative steps of 2. For testing purposes, the data was averaged over 8 or 16 traces, whereas larger numbers were used when time permitted to achieve higher data quality. Suppose a single frequency scan takes $\sim 500\,\mathrm{ms}$, the acquisition time for an averaged trace then ranges from approximately 2 s to 4 minutes. Most experiments involve scanning two variables, typically showing spectral features as a function of MW power, frequency or polarisation. Investigating such parameter

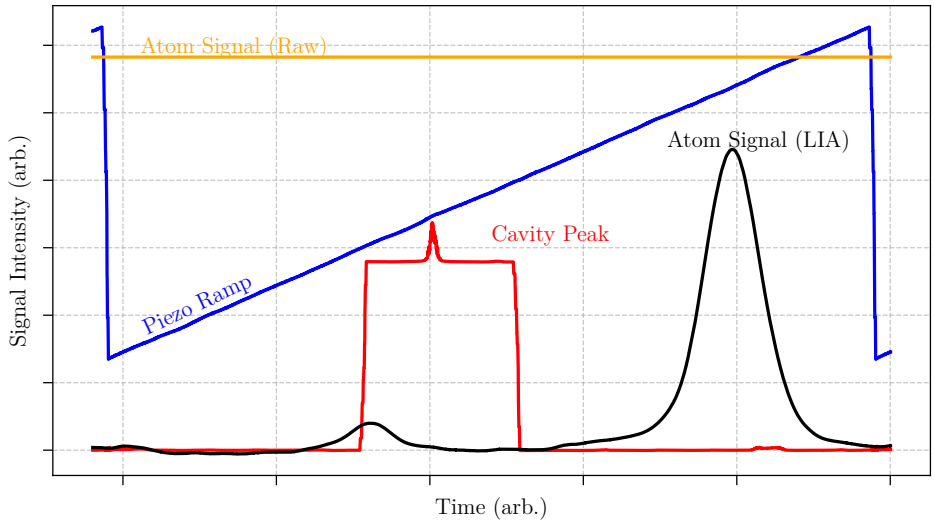

Figure 5.4: *Snapshot of the four oscilloscope traces before an experiment. A sawtooth ramp (blue) drives the coupling laser frequency sweep. Probe transmission is directly measured by the photodiode signal (orange), while the weak EIT signal is detected using a lock-in-amplifier (black), clearly indicating the two-photon resonance for each* $|r_1\rangle \in \{49D_{3/2}, 49D_{5/2}\}$ *level in the absence of external MW fields. A square wave added to the reflected cavity peak (red) provides a stable frequency reference used to generate an error signal for a feedback loop that stabilises the coupling frequency against long-term drift.*

spaces can easily require 100 scans or more, meaning that experiment durations can range from 3 minutes to about 7 hours, often running overnight. Hence, it is crucial to maintain a stable coupling laser frequency sweep for long periods of time. To this end, a feedback loop was developed to correct for any drift in the coupling laser frequency.

5.1.4 Long Term Stability

The four channels on the oscilloscope record: (1) the bare photodiode signal measuring probe transmission, (2) the lock-in amplifier output signal, (3) the cavity transmitted or reflected peaks, and (4) the piezo ramp. Although, the sensing scheme only relies on the second channel for measuring the EIT signal, the other channels are useful for monitoring purposes. Figure 5.4 exemplifies a snapshot of the oscilloscope traces.

A dual-port signal generator produces: (1) a sawtooth ramp driving the coupling

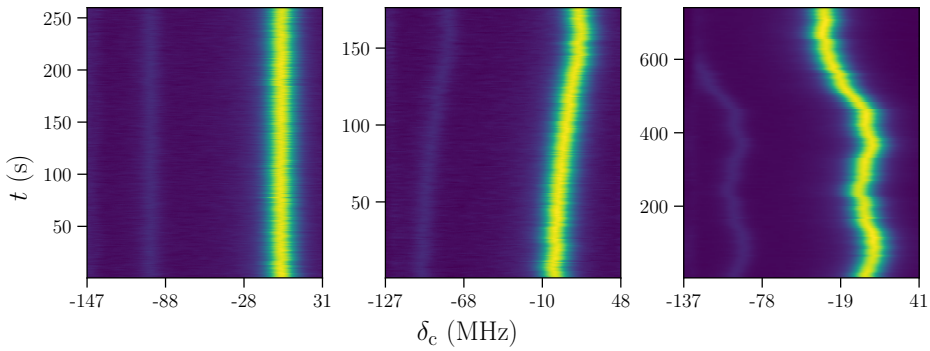

Figure 5.5: *Characterising the frequency stabilisation of the coupling laser, by repeated measurements on the three-level EIT system in the absence of external MW fields. (left): using a frequency-locked laser with the stabilisation method, (centre) using a frequency-locked laser without the stabilisation method, (right) using a free-running laser without the stabilisation method.*

laser frequency sweeps, and (2) a square pulse, serving as a frequency reference for a feedback loop that stabilises the coupling laser frequency against long-term drift.

For the initial setup, the oscilloscope is triggered by the piezo ramp. The square pulse is then configured at the same frequency as the sawtooth ramp so that it appears within the oscilloscope time window. This pulse is added to the cavity reflection signal. By adjusting both the pulse width and the relative phase between the square pulse and piezo ramp, the pulse is modified to centre, and fully encompass a single cavity resonance peak. The oscilloscope is subsequently set to trigger on the edge of the cavity peak. As the laser frequency drift over time, the cavity peak moves relative to the square pulse. Since the oscilloscope triggers on the cavity peak, this drift corresponds to a change in the relative position of the square pulse edge. By comparing the initial distance between the pulse edge and the cavity peak, with subsequent measurements, an error signal is obtained for the feedback loop, which is then used to adjust the piezo DC voltage offset accordingly. Implementing the feedback loop is straightforward and is achieved using a multithreaded programme. One thread continuously calculates the error and stabilises the coupling laser in the background, while a second thread controls the experimental sequence.

To characterise the frequency stabilisation method, repeated measurements on the three-level EIT system in the absence of external MW fields are performed.

Ideally, since no experimental parameters are actively scanned, identical spectra should be obtained in each measurement. Temporal variations therefore provide a measure of the experimental precision, and drifting values indicate experimental instability. Figure 5.5 shows the effect of implementing the stabilisation method by directly comparing the time evolution of the EIT spectrum with and without stabilisation method. For context, data acquired with an unlocked coupling laser is also displayed, illustrating the worst-case scenario. Figure 5.5 qualitatively indicates, in all three cases, the amplitude and width of the EIT peak remain relatively stable. Only the centre frequency is modified using the stabilisation routine, as expected, since the piezo offset is used to control the laser frequency.

In the absence of stabilisation, a clear drift of the EIT peak position is observed, which is strongly suppressed when stabilisation is applied demonstrating the effectiveness of the method.

For each spectrum, the position, width and amplitude of the EIT peak is estimated by fitting a Gaussian. The fit parameters form a time series reflecting how the peak properties vary over time. Figure 5.6 quantifies the temporal stability of the EIT resonance by plotting the standard (Z-) score,

$$z_{\mathrm{P}} = \frac{x_{\mathrm{P}} - \mu_{\mathrm{P}}}{\sigma_{\mathrm{P}}}, \tag{5.1}$$

where μ is the weighted arithmetic mean and σ is the standard deviation for each parameter, P. In the bottom panel, the relative deviation, $(x - \mu)/\mu$ for both transmission signals are shown. It is important to note from Fig. 5.4 that the lock-in amplifier output signal clearly shows EIT features, whereas the raw photodiode signal is flat. To compare the two transmission signals, the raw photodiode signal is averaged to get a measure of the probe transmission per trace, whereas the maximum value (not fitted) for the EIT peak is used for the lock-in amplifier signal to indicate maximum probe transmission. Although the two values are different in nature, both give a measure of probe transmission per trace. Most importantly, Fig. 5.6 shows that although the output of the lock-in-amplifier is relatively stable, the raw photodiode signal can change drastically. Variations in the raw transmission signal can be due to unstable probe power, either due to fluctuations in output laser power, optical coupling efficiency at the PM-SM fibre or polarisation drift leading to changes in transmission at the PBS cube. These possibilities are each easy to characterise with a powermeter, but was not done during my stay and arguably irrelevant, as data is acquired from the stable lock-in amplifier signal.

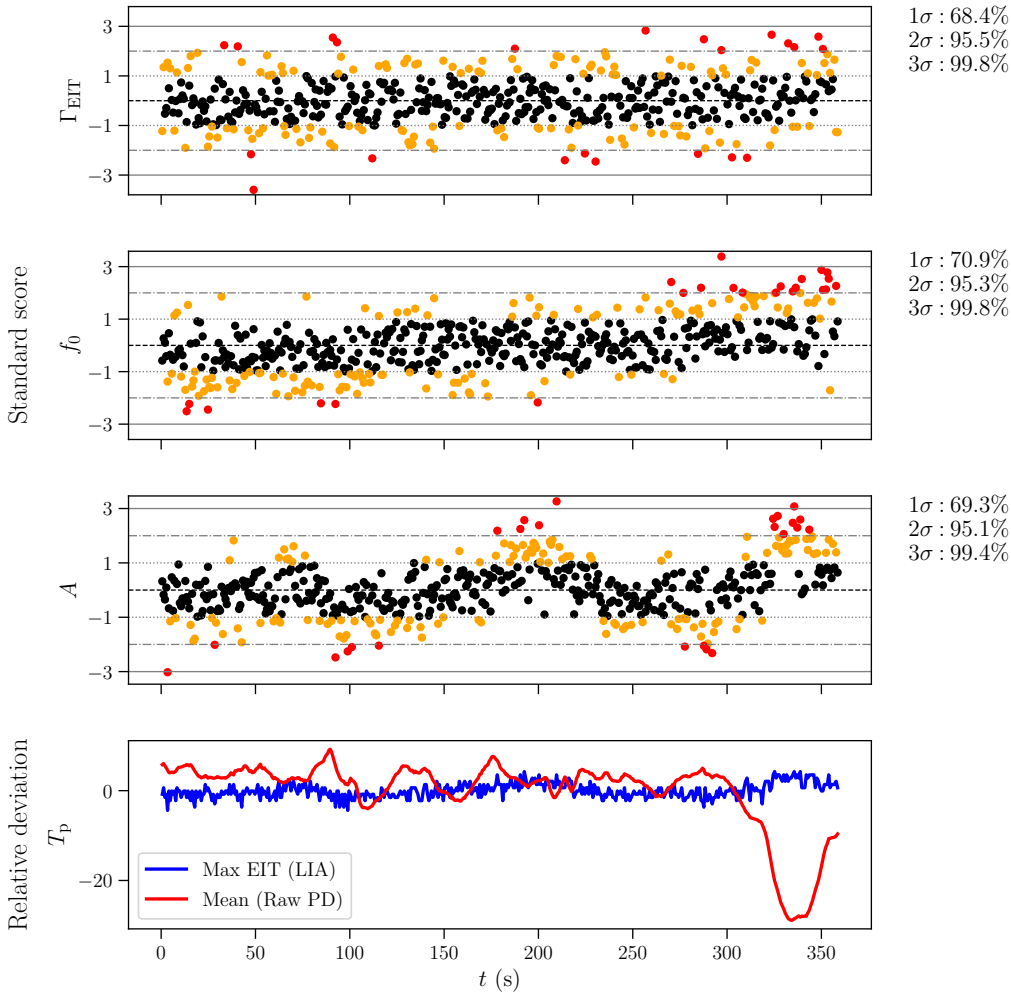

Figure 5.6: *Repeated measurements on the three-level EIT system in the absence of external MW fields. (Top): The time evolution of the standard (Z-) score for each fitting parameter characterising the EIT peak. The number of points measured within* 1σ *(black dots),* 2σ *(orange dots) and* 3σ *(red dots) is indicated in the right most column. (Bottom): The relative deviation from the mean over time for the two probe transmission signals. To get a transmission per trace, the flat signal from the raw photodiode output is averaged, whereas the maximum value is used for the detected EIT signal. Notice, the lock-in amplifier output is stable against drastic changes in the raw photodiode signal.*

For this experiment, the detuning from the expected resonance and the EIT linewidth are estimated using weighted arithmetic means, yielding $\tilde{\delta}_0 = 321.5(1)\,\mathrm{kHz}$, and $\tilde{\Gamma}_{\mathrm{EIT}} = 9.089(1)\,\mathrm{MHz}$.

Figure 5.7 shows the Allan deviation $\sigma_{\mathrm{P}}(\tau)$, applied to the time series of each fitted parameter, P, as a function of the averaging times τ. This analysis is a useful tool to characterise the dominant noise processes in the experiment. On a (σ, τ) log-log plot, a straight line means a power-law noise process, $\sigma_{\mathrm{P}}(\tau) \propto \tau^{\alpha}$, where, α is the slope that determines how the signal stability scales with averaging time. White phase noise, corresponding to completely uncorrelated phase fluctuations, exhibits a steep slope of -1. Flicker phase noise and white frequency noise show slopes of $-1/2$. A summary of these regimes along with other noise types can be found in the literature [68]. In Fig. 5.7, a straight line is fitted to the Allan deviation data, and the extracted slope is tagged for each dataset. The observed -1 slope indicates that the experiment is dominated uncorrelated, short-timescale noise that averages down quickly.

Each saved spectrum corresponds to the photodiode signal internally averaged on the oscilloscope before being timestamped in Python. Each fitted parameter set $(A, f_0, \Gamma_{\mathrm{EIT}})$ therefore represents one estimate per effective measurement interval. While oscilloscope averaging reduces high-frequency measurement noise in the raw signal, the Allan deviation compares the stability of fitted parameters over increasing time windows. The base Allan sampling period is related to the averaging times used for calculating the Allan deviation by $\tau = m\tau_0$, where m is an integer. Due to small relative timing jitter arising from data transfer latency and software overhead, there is no exact sampling rate, and a mean sampling interval is used to estimate τ_0. Moreover, the overlapping Allan deviation is used as it averages over many more pairs than the regular Allan deviation.

Interestingly, the Allan deviation of all fitted parameters except the centre frequency is nearly identical with and without frequency stabilisation, consistent with the qualitative behaviour discussed in Fig. 5.5. This indicates that the stabilisation loop primarily affects the laser frequency and does not significantly influence other parameters. At short averaging times, the frequency stabilisation leads to a slightly larger Allan deviation, which can be attributed to the active feedback process injecting noise into the system, however, at rather short timescales of about 6 s. Beyond this, the stabilisation suppresses slower frequency fluctuations and improves long-term stability.

Notably, the extracted slopes remain constant over the entire acquisition dura-

tion. This robustness indicates that successive measurements are statistically independent and that further averaging continues to reduce the Allan deviation over the measured timescales. Such behaviour is characteristic of white phase noise. Extending the measurement duration would be of interest in future work, as it may reveal a transition to slower noise processes at longer averaging times.

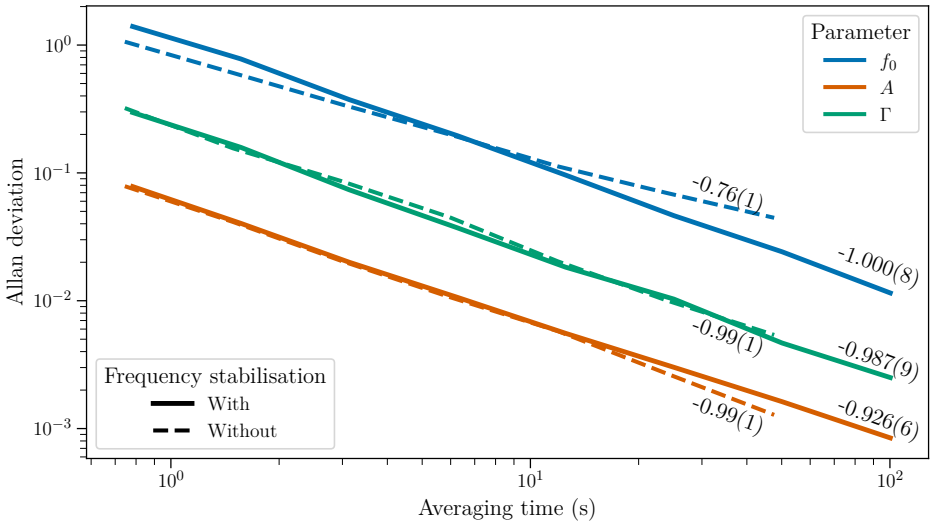

Figure 5.7: *Allan deviations as a function of averaging time for the fitted parameters on a log-log plot. Fitting the Allan deviations for each time series of parameters with a straight line determines the power-law noise process, and the slope that determines how the signal stability scales with averaging time is tagged for each dataset. Errors are estimated by a standard propagation of error using the square-root of the covariance matrix elements from the polynomial fit weighted by the errors from the allan deviation routine. The slope of approximately -1, indicates very fast noise that averages down quickly. This is characteristic for white phase noise and it is shown that successive measurements are statistically independent and that further averaging continues to reduce the Allan deviation for any extended period of time throughout the experiment. Moreover, the noise from the stabilisation method exceeds the free-running noise for very short times $\tau \leq 6\,\mathrm{s}$, beyond which the stabilisation suppresses slower frequency fluctuations and improves long-term stability.*

5.1.5 Atomic Desorption of Glass Cell

When a Rb atom collides with the glass wall, it can donate its valence electron to the surface, becoming ionised and subsequently bound to the charged glass via a van der Waals like process known as chemisorption. Some adsorbed Rb atoms migrate along the surface, diffuse into the glass crystal or form stable compounds, resulting in long-term atom loss from the vapour. Over time, this accumulation on the cell walls leads to a reduction in the free Rb density. An effective method for releasing these atoms back into the vapour is light-induced atomic desorption, which can be achieved using UV light. When the UV light is applied, the desorption rate exceeds the adsorption rate, causing an increase in the vapour density. For experiments, this is seen as an improved signal-to-noise ratio, particularly advantageous for the weak EIT signals occurring at strong MW fields. Figure 5.8 shows the effect of UV light on the glass cell. Repeated measurements on the three-level EIT scheme, reveal a (dis)charging effect on the signal strength when the UV light is switched on (off). The characteristic $1/e$ time constant extracted from the fit is approximately 1.5 minutes.

While the UV lamp is beneficial for measuring weak signals, an additional layer of complexity is also introduced to the experiment: photoionisation of Rb leads to free charges inside the cell and additional E-fields that can induce perturbations like the Stark DC shift. Rydberg states with their great polarisabilities are particularly susceptibile for such energy shifts. Any subtleties regarding the UV light will not be treated in this work, although it might be relevant for further investigations.

The temporal evolution of the EIT peak when switching the UV lamp on/off is characterised by the time series of Gaussian fit parameters presented on Fig. 5.9. The charging experiments are initiated with the UV lamp off. After three spectroscopies, the UV lamp is abruptly turned on, releasing adsorbed atoms and increasing the gas pressure slightly in the cell, corresponding to an increase in signal which is then fitted with a charging time of (95 ± 10) s. After a long time, to ensure saturation, the discharging experiments are performed. When discharging measurements are initiated, three spectroscopies are saved with UV light on before the UV lamp is abruptly turned off, and in a similar fashion, the discharge time is fitted to (85 ± 20) s.

The UV light is particularly useful for measurements at strong MW fields where the EIT signal is ultra weak.

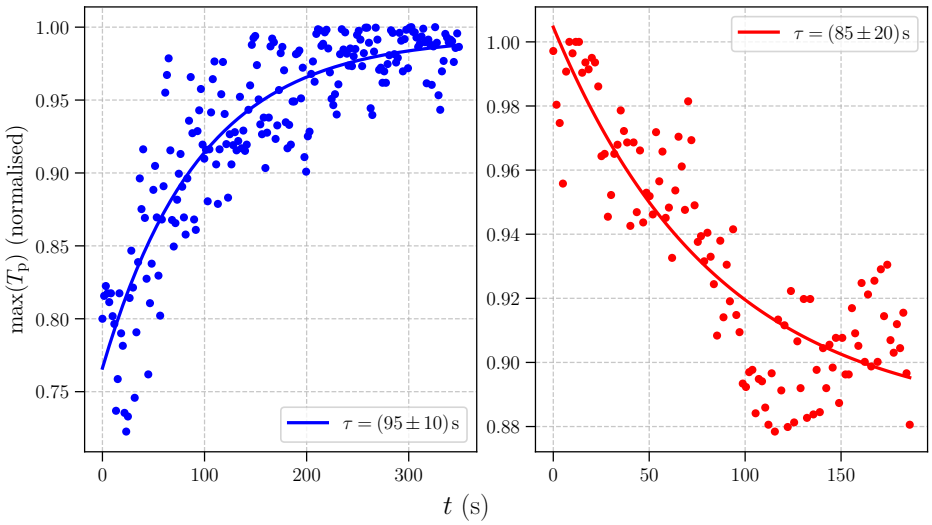

Figure 5.8: *Switching the UV lamp on/off (left/right) during repeated measurements on the three-level EIT system. The time series of EIT peak values indicate the signal strength per trace. Estimating the characteristic* $1/e$ *time by fitting an exponential tells that* $\tau \approx 1.5\,\mathrm{min}$. *for atoms to adsorp onto- or desorp from the glass surface under the presence of UV light.*

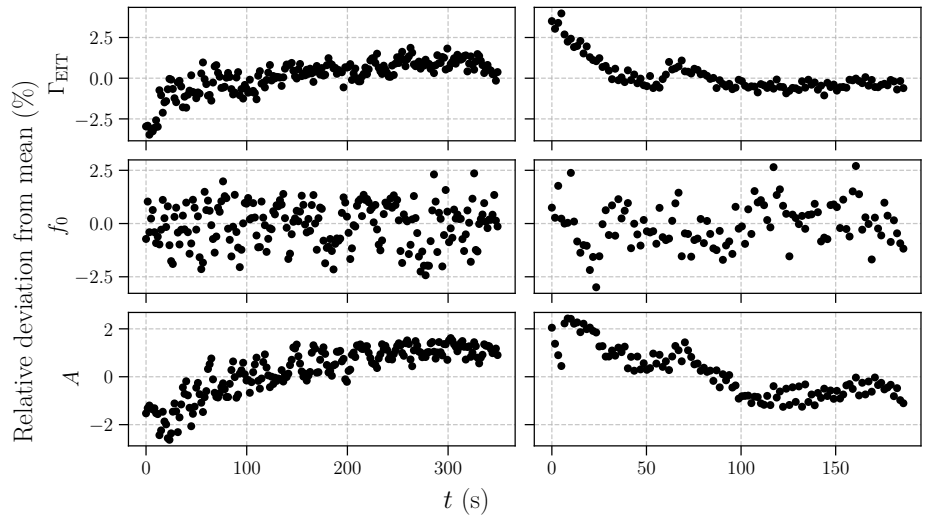

Figure 5.9: *Time series of the fitted parameters characterising the evolution of the EIT peak when switching the UV lamp on/off (left/right). (Top): Changes in* Γ_{EIT} *indicates a broadening due to the presence of UV light. This is not investigated further in this thesis.*

5.2 Experiments

5.2.1 Coupling Laser Frequency Calibration

Without external fields, the two highly excited Rydberg states, $|r_1\rangle$ and $|r_2\rangle$ do not interact. The coupling laser therefore addresses the electric dipole transitions to $49\mathrm{D}_{3/2}$ and $49\mathrm{D}_{5/2}$, connecting two independent three-level ladder schemes for EIT. The two fine-structure levels are separated by a well-known frequency that can be calculated following [67]. Hence, any piezo ramp spanning both transitions can be calibrated. For the mentioned states, the separation is 98.681 85 MHz and data from a calibration routine is shown on Fig. 5.10.

5.2.2 Microwave Frequency Scan

For the following experiments, $49\mathrm{D}_{3/2}$ is a spectator state, $|r_1\rangle = 49\mathrm{D}_{5/2}$ and $|r_2\rangle = 50\mathrm{P}_{3/2}$. Applying MW radiation near the $|r_1\rangle \leftrightarrow |r_2\rangle$ resonance couples the two Rydberg states, and by tuning the MW frequency around the resonance, an avoided crossing appears. As discussed in Section 2.1.1, the resulting dressed states are separated by the generalised MW Rabi frequency, allowing for a MW frequency calibration which is essential for subsequent experiments. In these measurements, the MW field strength is a free parameter. Stronger fields produce greater AT splittings, but increasing the power too much causes an overlap with

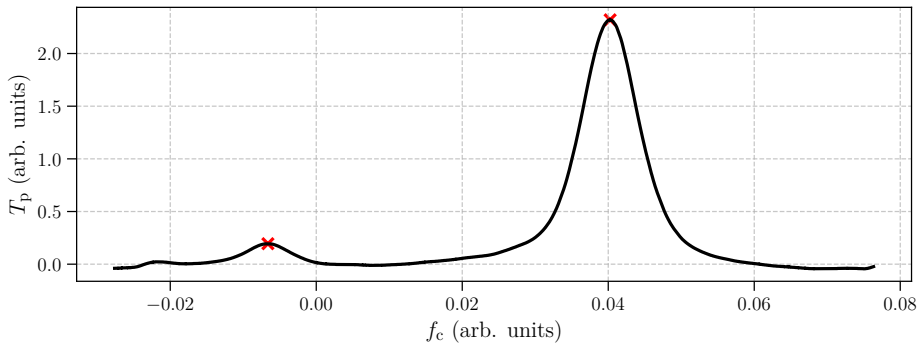

Figure 5.10: *A coupling frequency sweep spanning the two-photon resonances associated with the fine-structure Rydberg states $49D_{3/2}$ and $49D_{5/2}$, with the probe laser held on resonance and no external MW field applied. Two distinct EIT peaks are observed, each corresponding to a two-photon resonance for the two independent three-level systems accessible via the coupling laser. The piezo ramp is calibrated using the well known frequency separation between the $49D_{3/2}$ and $49D_{5/2}$ Rydberg levels,* 98.681 85 MHz *[67]*

the $49D_{3/2}$ spectator state, introducing interference between dressed states and potentially adding an error to the measured resonance. A weak MW field was used, such that the spectator state can be neglected. Figure 5.11 compares scans at weak and strong fields and Fig. 5.12 tracks the EIT peak position at variable MW frequencies. The MW resonance is fitted by:

$$f_{\mathrm{EIT}} = f_0 + \frac{1}{2}\left(\Delta_{\mathrm{MW}} \pm \sqrt{\Delta_{\mathrm{MW}}^2 + \Omega_{\mathrm{MW}}^2}\right), \tag{5.2}$$

where f_0 is the two-photon resonance without MW fields, whereas Δ_{MW} and Ω_{MW} are the MW- detuning and Rabi frequency. Eq. (5.2) contains the bare-energy term and the interaction term from Eq. (2.5). The MW resonance frequency is fitted to be 18.146(6) GHz corresponding to a relative deviation of 0.025(3) % from the tabulated resonance of 18.141 48 GHz. The fitted frequency slightly above the tabulated value is consistent with positive systematic shifts, such as the Zeeman or Stark shifts. Since stray magnetic fields can induce Zeeman shifts at the MHz level, the measurement accuracy is expected to improve with magnetic shielding, which was not implemented in this experiment. Despite the absence of magnetic shielding, the observed agreement at the 10^{-4} level highlights the robustness of the Rydberg-atom-based EIT scheme.

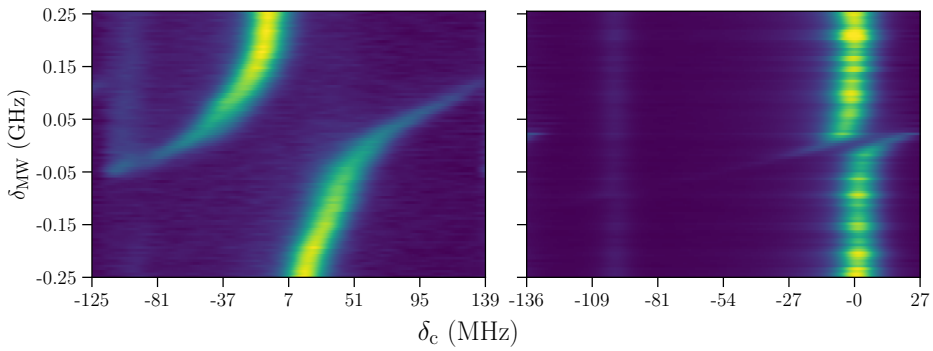

Figure 5.11: *Tuning the MW frequency over the resonance* $49D_{5/2} \rightarrow 50P_{3/2}$. *(Left): For a strong MW field, the AT splitting is comparable to the fine structure splitting of the lower Rydberg state and the spectra overlap considerably. (Right): A weaker MW field is preferred such that the spectator state can be neglected. Notice that the EIT peak in the strong field case is significantly shifted away from zero field resonance, already at* $\delta_{\mathrm{MW}} = -250\,\mathrm{MHz}$.

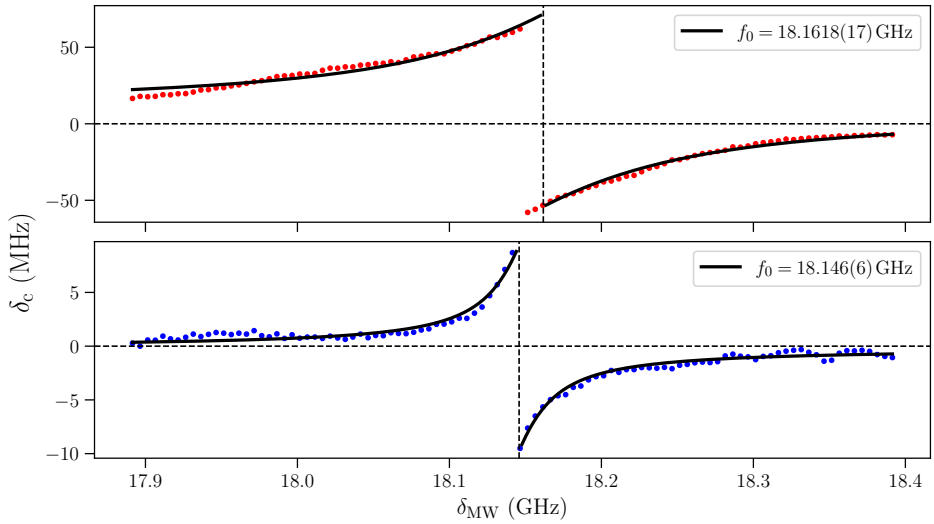

Figure 5.12: *Tracing the EIT resonance frequency at variable MW frequencies show an avoided crossing, where the splitting is* $\tilde{\Omega}_{\mathrm{MW}}$ *which is minimum at resonance. Fitting the avoided crossing with Eq.* (5.2) *for the high and low MW powers give a resonance of* 18.1618(17) GHz *and* 18.146(6) GHz*, deviating from the tabulated* 18.141 48 GHz *by a relative error of* 0.112(9) % *and* 0.025(3) % *respectively. The greater resonance for the strong MW field regime is consistent with a Stark shift. The dashed lines indicate the two-photon resonance at zero MW fields and the fitted MW resonance. Note that the strong MW field regime suppresses the quadratic dependence on detuning in the generalised Rabi frequency.*

5.2.3 Microwave Power Scan

In the presence of an external MW field, the spectrum exhibits AT splitting, with the magnitude of the splitting proportional to the generalised MW Rabi frequency. However, the Rydberg-atom-based sensing scheme does not consist of a simple 4-level system, and the full level scheme is presented in Section 2.5.3. The dressed-state structure probed by EIT is discussed in Section 2.5.3, and specifically Fig. 2.19 illustrates the MW field dressing resulting from coupling the two highly excited Rydberg states $|r_1\rangle = 49\mathrm{D}_{5/2}$ and $|r_2\rangle = 50\mathrm{P}_{3/2}$ using a linearly polarised MW field. The allowed π-transitions and corresponding dipole matrix elements are indicated in Fig. 2.19 (a). Importantly, the MW Rabi frequency depends on $|m_J|$ and consequently the MW coupling produces different AT splittings across the $|r_1\rangle$ manifold, as shown in Fig. 2.19 (b). Due to the $J = 5/2 \leftrightarrow J' = 3/2$ structure, five dressed states are present for the EIT scheme to resolve. However, the optical coupling of the dressed Rydberg states to the

intermediate state is proportional to the Wigner-3j symbol in Eq. (2.90), which vanishes when $|m_J| > 3/2$, so the extremal components $m_J = \pm 5/2$ have zero dipole matrix element. Consequently, the spectator states do not contribute to the EIT signal and no central peak associated with the uncoupled state appears in the simulated spectrum in Fig. 2.18.

During the final two weeks of my stay, a newly acquired variable-gain amplifier from Mini-Circuits (ZVA-18443VG+) became available providing up to 47 dB of gain at the relevant frequency of 18 GHz. This amplifier enabled a continuation of previous investigations [14] which had been limited by insufficient MW power, and were therefore unable to resolve the sub-structure of the AT splitting. The amplifier was initially operated in analogue-control mode for quick setup and proof-of-concept measurements, while the final implementation used a USB-to-TTL converter to configure the amplifier via the control system described in Section 5.1.3. Transmission losses in the experimental setup were minimised by measuring the transmission and reflection coefficients of all accessible cables at the relevant MW frequency, using a vector network analyser. In addition, an armored low-loss cable (KBL-1.5FT-LOW+) connected the antenna to the amplifier. These efforts resulted in the data shown in Fig. 5.13.

To track the AT splitting from zero amplification up to the strong MW field regime, a broad frequency scan of the coupling field is required. For improved resolution at high MW powers, a smaller range is useful. However, failing to scan both resonances of the Rydberg fine-structure compromises the coupling frequency calibration, as described in Section 5.2.1.

The MW powers in Fig. 5.13 are the sum of the output power from the MW generator, the transmission loss over cables (measured to -12 dB) and the amplification ($+40$ dB). The positive branch is tracked in Fig. 5.13, where the y-axis is transformed using $P_{\mathrm{mW}} = 10^{P_{\mathrm{dBm}}/10}$ and the square root to relate it to Rabi frequencies, $\Omega_{\mathrm{MW}} \propto \sqrt{P_{\mathrm{mW}}}$. This provides a relative axis, where the scaling is expected to be linear. An absolute reference is required for calibrating the axis to MHz.

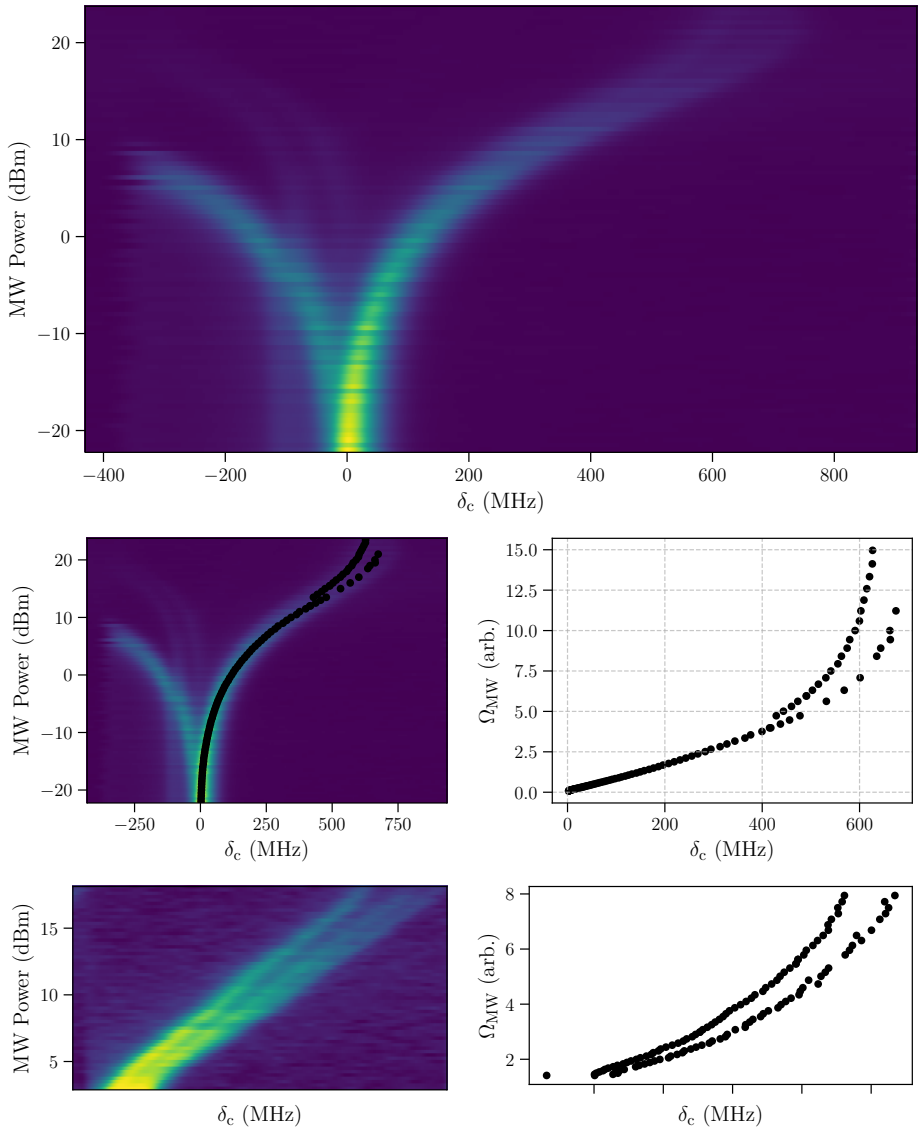

Figure 5.13: *(Top) Broad scan of both the MW power and two-photon detuning. At higher MW powers each branch indicates sub-structure, due to the m_J dependent Rabi frequencies of the MW coupling, as argued in [14]. (Centre) Tracking the right branch (positive AT shift), clearly demonstrates the sub-structure at sufficiently high MW powers. This is the first experimental demonstration of the sub-structure of $|r_1\rangle$ to my knowledge. (Bottom) A narrow frequency scan at high MW powers. Notably the smaller coupling frequency range compromises the calibration. All MW powers are presented as the direct output from the MW generator with the measured loss over cables and the amplification, which was* $-12\,\mathrm{dB}$*, and* $40\,\mathrm{dB}$ *respectively.*

5.2.4 Phase Mixing

With the Quad Redged Horn Antenna (RF spin broadband antenna QRH40C), a new line of experiments became possible. This broadband dual-polarised horn antenna has two ports. By connecting two MW frequency generators (Agilent E8257D and HP 83732B) to the antenna ports, it is possible to mix two MW fields of identical frequency and power, but orthogonal linear polarisation. The superposition of two orthogonally polarised linear fields with a variable relative phase produces elliptically polarised MW fields of tunable ellipticity. The output MW power from the generators was balanced by measuring the transmission losses over the connecting cables from each generator to the antenna.

Figure 2.19 indicates that the probe transmission spectrum is highly dependent on the two Rydberg levels characterised by the angular momentum of the two Rydberg states. The transition between $|r_1\rangle = 49\mathrm{D}_{5/2}$ and $|r_2\rangle = 50\mathrm{P}_{3/2}$, is simply denoted by $J = 5/2 \rightarrow J' = 3/2$, and changing the two Rydberg states allows for an investigation of the probe transmission against the MW polarisation for variable $J \rightarrow J'$ transition types.

5.3 Publication

The phase mixing measurements mark the conclusion of my work with the Light and Matter group at the University of Otago. The experimental work was continued by Dr. Matthew Chilcott and the investigations resulted in the publication [6].

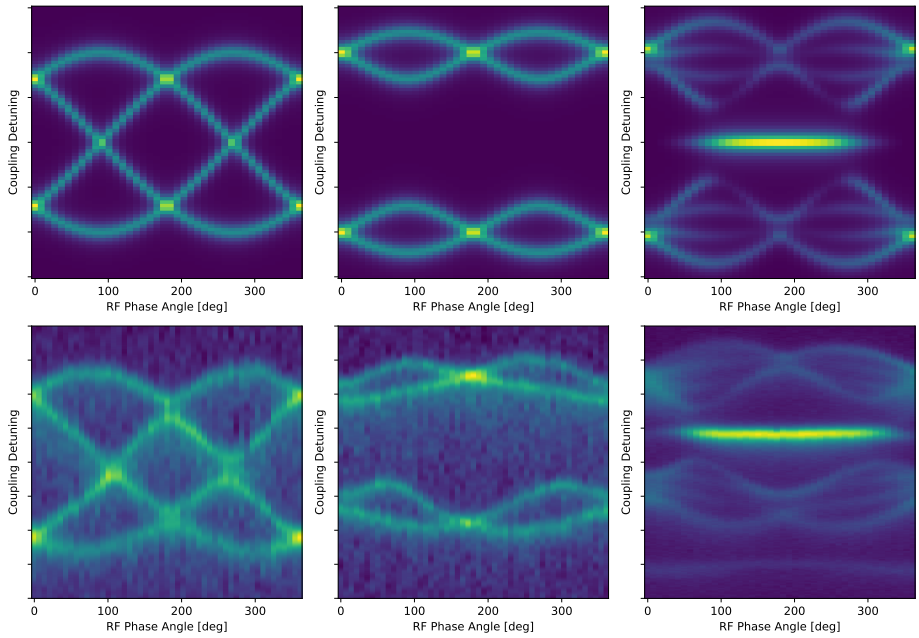

Figure 5.14: *Density matrix simulations (top) with corresponding measurements (bottom) of the phase-mixing experiment for three different Rydberg transitions, characterised by their angular momentum, $J \leftrightarrow J'$. (Left): $J = 1/2 \leftrightarrow J' = 1/2$, (Centre): $J = 1/2 \leftrightarrow 3/2$, and (Right): $J = 3/2 \leftrightarrow J' = 5/2$.*

Quantum-enabled complete RF-polarimetry

Matthew Chilcott,[1,*] Laurits N. Stokholm,[2,*] Matthew Cloutman,[1] J. Susanne Otto,[1] Amita B. Deb,[3] and Niels Kjærgaard[1,†]

[1] *Department of Physics, QSO—Quantum Science Otago, and Dodd-Walls Centre for Photonic and Quantum Technologies, University of Otago, Dunedin 9016, New Zealand*
[2] *Department of Physics and Astronomy Aarhus University, Denmark*
[3] *School of Physics and Astronomy, University of Birmingham, Edgbaston, Birmingham B15 2TT, United Kingdom*

(Dated: January 30, 2026)

Rydberg atomic electrometry leverages the extreme sensitivity of highly excited alkali atoms for calibration-free electric field measurements. The techniques uses a non-metallic vapour cell to link properties of an RF field to a read-out in the optical domain. Most demonstrations have so far focussed on detecting linearly polarized fields for which the induced splitting of dressed atomic levels is rotationally invariant. Here we report Rydberg atomic measurements on RF fields in an entirely general state of polarization (SOP) and demonstrate a complete polarimeter capable of mapping the RF polarization state onto the Poincaré sphere through a unique spectroscopic fingerprint. This includes ascertaining the helicity of circularly polarized light. For a Stokes vector circumnavigating a Poincaré sphere meridian, we witness a continuous transformation of the Rydberg atomic eigenenergy spectrum when optically probing the dressed atoms in an electromagnetically induced transparency scheme. Since the SOP can be determined from the relative positions of eigenenergy peaks and because these peaks are locked in place by the quantization of angular momentum the method is calibration free.

State of polarization (SOP) measurements of electromagnetic fields are used in many scientific, industrial, and technological applications including material characterization, chemical analysis, and remote sensing. In the optical domain, the mapping onto the Poincaré sphere [1, 2] of a light field's SOP is typically achieved through measurements with a rotating-element polarimeter. The simplest *complete* polarimeter—one that can determine all four components of the Stokes vector—is realized by passing the light through a rotating quarter-wave retarder and a linear polarizer while recording the varying transmitted intensity on a photodetector [3]. In the RF domain, where polarization for example plays an important role in analyzing radar echoes [4], polarimetry is typically carried out by means of dual-polarized metallic antennas that measure the amplitude and phase for two orthogonal components of the field [5]. Due to their conducting nature such antennas inevitably distort an incoming RF field.

Rydberg atomic vapour cells open up the possibility of a non-metallic sensor for electromagnetic fields with frequencies falling below the optical domain [6]. We shall invariably refer to such fields as RF fields even when their frequencies extend into the GHz and THz region. The prospect of SI-traceable and calibration-free RF electric field measurement based on the quantized energy-level structure of atoms [7] has attracted considerable interest from metrology laboratories and beyond [8]. Studies concerned with Rydberg atomic sensing of polarization

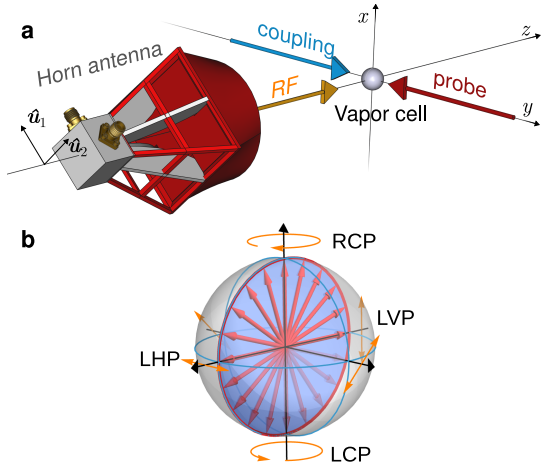

Fig. 1 | Rydberg atomic SOP analyzer. a, Schematic for SOP measurement. The RF field produced by a dual-polarized ($\hat{\mathbf{u}}_1/\hat{\mathbf{u}}_2$) lensed horn antenna propagates in the z-direction towards an atomic vapour cell located at the origin. Coupling and probe laser beams counter-propagate along the y-axis. **b** Poincaré sphere showing the trajectory of the RF-field's Stokes vector (red arrow) when $\phi = 0 \rightarrow 2\pi$ in Eq. (1). As ϕ polarization state from linear-vertical (LVP) to left-cicular (LCP) to linear-horizontal (LHP) to right-circular (RCP), and back to LVP.

* These authors contributed equally to this work.
† niels.kjaergaard@otago.ac.nz

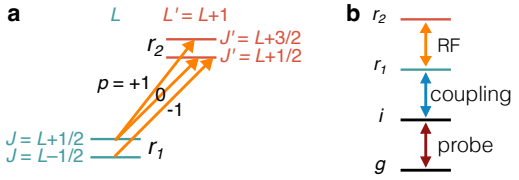

Fig. 2 | Atomic level diagrams. a, The three dipole-allowed transitions ($L \to L+1$) between the two Rydberg levels r_1 and r_2 are designated by $p = 0, \pm 1$. **b**, Schematic energy level scheme for ladder-type EIT-sensing of an RF field showing how the optical probe and coupling fields connect the atomic ground level g to the RF-field-dressed Rydberg levels r_1 and r_2 via an intermediate level i.

have however mainly been limited to linearly polarized fields [9–16]. A first demonstration involving elliptical polarized fields only emerged very recently [17, 18] and required no less than three auxiliary local oscillator fields produced by separate microwave antennas to operate in addition to two lasers establishing the electromagnetically-induced transparency (EIT) optical readout scheme.

In this Letter, we demonstrate that a complete Rydberg atomic RF polarimeter can be implemented without relying on any auxillary RF fields. Instead, a spectroscopic vapour cell, "wired up" with two laser beams, inherently processes the device-under-test (DUT) field and maps its SOP onto an optically recorded spectrum. More specifically, the polarimetric signal will be encoded in the quantum states of two Rydberg levels r_1 and r_2 of an alkali atom with total electronic angular momenta J and J', respectively. Without loss of generality, we shall assume $J' \geq J$ and selection rules then dictate that the coupling is dipole-forbidden unless either $J' = J$ or $J' = J+1$ [19]. Crucially, this establishes an iterative transition hierarchy, where the algebra of quantized angular momentum uniquely and explicitly defines families of SOP-dependent spectroscopic "fingerprints".

We produce the first four members of the angular momentum transition hierarchy in experiments and discuss how their associated spectrograms are tied to the SOP and direction of an incoming RF field dressing the atomic states. We also show how properties of the optical fields interrogating the RF-dressed atoms can be selected to break the symmetry of potentially duplicate SOP fingerprints to obtain an unambiguous mapping onto the Poincaré sphere.

TRANSITION HIERARCHY

In our demonstration of an atomic SOP analyzer, a microwave field that resonantly couples states between r_1 and r_2 is emitted by a dual-polarized horn antenna [see Fig. 1(a)]. The antenna has two input ports, connected to orthogonally oriented stubs in the waveguide region near the horn throat, which we drive with two equal-amplitude phase-synchronous sinusoidal signals of frequency f. Each stub generates a linearly polarized field of amplitude E_0 propagating on the axis of the horn, which we take to be along $\hat{\boldsymbol{z}}$. Denoting the two orthogonal directions of polarization as $\hat{\boldsymbol{u}}_1$ and $\hat{\boldsymbol{u}}_2$, respectively, the resultant electric component of the field emitted by the antenna can be expressed as

$$\boldsymbol{E}(z,t) = \frac{E_0}{\sqrt{2}} \,\mathrm{Re}\left[(\hat{\boldsymbol{u}}_1 + e^{i\phi}\hat{\boldsymbol{u}}_2)e^{-i(kz+\omega t)}\right], \qquad (1)$$

where $k = 2\pi f/c$, and ϕ describes the phase of the second signal source with respect to the first. By adjusting the phase ϕ we can control the polarization state of the microwave impinging on the atoms to reside anywhere on the meridian of the Poincaré sphere shown in Fig. 1(b).

In our experiment, the atomic sensing cell is located at the origin of a Cartesian coordinate system, with the antenna producing the device-under-test (DUT) field oriented such that $\hat{\boldsymbol{u}}_{1,2} = (\hat{\boldsymbol{x}} \mp \hat{\boldsymbol{y}})/\sqrt{2}$. For $\phi = 0$, the resultant field is linearly polarized along $\hat{\boldsymbol{x}}$—the vertical direction of our setup [cf. Fig. 1(a)]. Expressed in terms of covariant spherical-basis unit vectors $\hat{\boldsymbol{e}}_{\pm 1} = \mp(\hat{\boldsymbol{x}} \pm i\hat{\boldsymbol{y}})/\sqrt{2}$, an atom located at the origin will experience an RF field

$$\boldsymbol{E}(t) = \frac{E_0}{\sqrt{2}} \,\mathrm{Re}\left\{\left[\left(\cos\frac{\phi}{2} + \sin\frac{\phi}{2}\right)\hat{\boldsymbol{e}}_+ + \left(\cos\frac{\phi}{2} - \sin\frac{\phi}{2}\right)\hat{\boldsymbol{e}}_-\right]e^{-i\omega t}\right\}. \qquad (2)$$

By choosing $\hat{\boldsymbol{z}} = \hat{\boldsymbol{e}}_0$ as the quantization axis for the atomic system, and working in the dipole and rotating wave approximations, the angular part of the coupling Hamiltonian, which describes allowed transitions between r_1 and r_2, can be represented by a matrix $\boldsymbol{M}^{(Jp)}$ of dimension $(2J+2J'+2) \times (2J+2J'+2)$ with entries

$$M_{ij}^{(Jp)} = \sqrt{\tfrac{(2J+1)}{4(J+1)}}\sqrt{\tfrac{(2J+3)|p|}{J(1-|p|)}} \sum_{q=\pm 1} \left[\begin{pmatrix} J & 1 & J+|p| \\ J+1-j & q & -3J-|p|-2+i \end{pmatrix} + \begin{pmatrix} J & 1 & J+|p| \\ J+1-i & q & -3J-|p|-2+j \end{pmatrix}\right]\left[\cos\left(\frac{\phi}{2}\right) + q\sin\left(\frac{\phi}{2}\right)\right]. \qquad (3)$$

where $p = 0, \pm 1$ is defined in Fig. 2(a) and Supplementary note 1. In deriving Eq. (3), we have made use of the condition $J' - J = 0, 1$ and have assumed an alkali atom with electronic spin quantum number $S = 1/2$ [20].

By diagonalising $\boldsymbol{M}^{(Jp)}$ it is possible to find analytic expressions for the variation in eigenvalues with ϕ. For

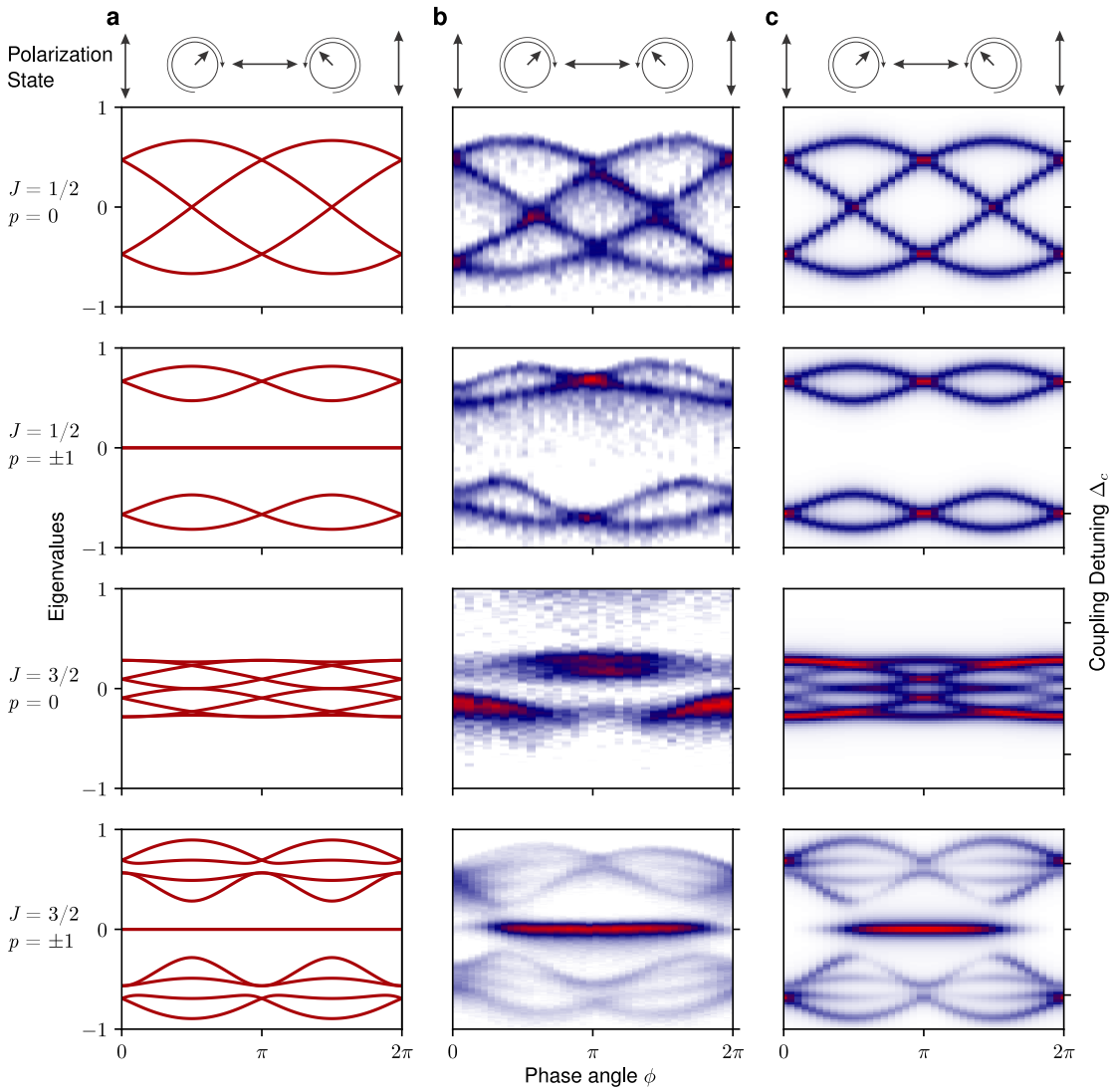

Fig. 3 | Spectrograms for RF dressed Rydberg atomic transitions. Eigenvalue spectra for resonantly coupled manifolds $\updownarrow_J^{J'} = \left\{\updownarrow_{1/2}^{1/2}, \updownarrow_{1/2}^{3/2}, \updownarrow_{3/2}^{3/2}, \updownarrow_{3/2}^{5/2}\right\}$ as a function of the phase angle ϕ defined in Eq. (1). **a**, Analytic eigenvalues found by diagonalizing the coupling matrices $\mathbf{M}^{(Jp)}$ with entries defined by Eq. (3). The SOP of the RF dressing field is shown at the top. **b**, Experimentally acquired spectrograms. **c**, Simulated spectrograms from density matrix calculations on optically interrogated two-level Rydberg manifolds.

example, the simplest member of the iterative hierarchy established by Eq. (3), $J^p = \frac{1}{2}^0$, gives the four angular-dependent eigenvalues $\pm\sin(\phi/2+\pi/4)/\sqrt{2}$ and $\pm\cos(\phi/2+\pi/4)/\sqrt{2}$. Moving up in the hierarchy increases the complexity with the number of eigenvalues growing linearly with J. Figure 3(a) presents the angular variation in eigenenergies for the cases of the coupled manifolds $\updownarrow_J^{J'} = \left\{\updownarrow_{1/2}^{1/2}, \updownarrow_{1/2}^{3/2}, \updownarrow_{3/2}^{3/2}, \updownarrow_{3/2}^{5/2}\right\}$, corresponding to $J^p = \{\frac{1}{2}^0, \frac{1}{2}^\pm, \frac{3}{2}^0, \frac{3}{2}^\pm\}$. In accordance with the rule for linear polarized RF fields given in [12], for $\phi = 0$ (vertical linear polarization) and $\phi = \pi$ (horizontal linear polarization) the number of unique eigenvalues are $N_{\text{eig}}^{\text{lin}} = 2, 3, 4, 5,$

respectively, with non-zero eigenvalues doubly degenerate. For $\phi \neq 0, \pi$, these degeneracies are lifted by the chirality acquired by the field, when its SOP moves off the equator of the Poincaré sphere. The maximum number of unique eigenvalues that can be encountered for our cases is therefore $N_{\rm eig}^{\rm max} = 4, 5, 8, 9$.

EXPERIMENTS

The above treatment leading to Fig. 3(a) elucidates how the SOP of the DUT field is imprinted on the energy spectrum of the dressed states hybridized out of substates of r_1 and r_2. We assess the prospect of utilizing the analytically predicted SOP-dependence of eigenenergies in a real-world sensor by conducting experiments on ^{87}Rb atoms in a vapor cell. Specifically, we make use of a DUT RF field with a frequency around 18 GHz and consider its effect on Rydberg states with principal quantum numbers around 50, but the results established will be of generally validity as the scheme hinges on universal results on quantized angular momentum structure.

The RF-dressed manifold of atomic energies are probed optically via an electromagnetically-induced transparency (EIT) ladder scheme [see Fig. 2(b)]. Details of our detection scheme has been described elsewhere[12, 15]. In brief, a beam of ~ 780 nm probe laser light along the y-axis addresses the transition from the Rb ground level $5S_{1/2}$ to an intermediate $5P_{3/2}$-level, which is further connected to a Rydberg level r_1 by a ~ 480 nm counter-propagating coupling laser [see Fig. 1(a)] with some detuning Δ_c. Both probe and coupling light fields are linearly polarized in the $\hat{\boldsymbol{x}}$-direction. When Δ_c is scanned over a ~ 200 MHz range, EIT peaks will emerge in the detected probe field whenever the coupling laser resonantly links a state of the intermediate level to a dressed state hybridized of the Rydberg levels.

In Fig. 3(b) we show spectrograms resulting from EIT-probing the dressed manifolds $\left\{\updownarrow^{59P_{1/2}}_{59S_{1/2}}, \updownarrow^{59P_{3/2}}_{59S_{1/2}}, \updownarrow^{49D_{3/2}}_{50P_{3/2}}, \updownarrow^{49D_{5/2}}_{50P_{3/2}}\right\}$ as ϕ is scanned from 0 to 2π. In doing so, the Stokes vector describing the field-SOP circumnavigate a meridian on the Poincaré sphere [cf. Fig. 1(b)]. The four Rydberg transitions are particular incarnations of $J^p = \left\{\frac{1}{2}^0, \frac{1}{2}^+, \frac{3}{2}^0, \frac{3}{2}^+\right\}$. Figure 3(c) shows the result of density matrix simulations which unlike the analytic results incorporate effects pertaining to the optical fields. We note how the simulated spectra replicate the peak positions of the analytical predictions in Fig. 3(a), while also capturing the change in prominence of the moving spectral features as ϕ is varied. The SOP of the RF field entirely locks in the relative positions of spectral peaks, but for a given ϕ the observed intensity for each peak will depend on properties of the optical fields such as polarization and propagation direction.

In discussing our experimental results in Fig. 3(b), we consider first the simplest case of a $\updownarrow^{59P_{1/2}}_{59S_{1/2}}$-transition

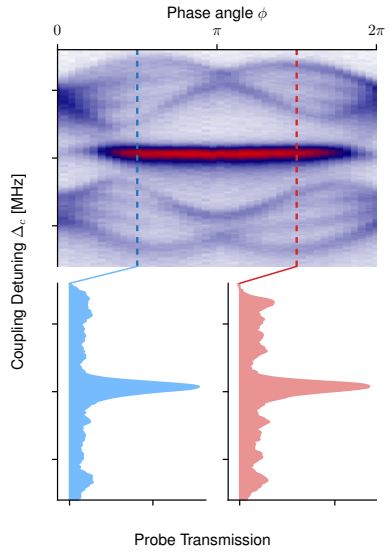

Fig. 4 | EIT spectra for atoms dressed with circularly polarized RF fields. Full blue line shows laser probe transmission as a function of coupling laser detuning for an LCP RF-field ($\phi = \pi/2$) and dashed red the result RCP RF-field ($\phi = 3\pi/2$).

(i.e. $J^p = \frac{1}{2}^0$) for which we find excellent agreement between experiment and the analytically predicted pattern of Fig. 3(a) which is paralleled in Ref. 21. In particular we note how pure linear and circular RF polarization gives rise to exactly two and three spectral peaks, respectively, with the maximum four peaks attained for elliptical polarization. Meanwhile, the simulated spectrum captures the increase in peak intensity, when eigenvalue degeneracy occurs. For the dressed $59S_{1/2} \leftrightarrow 59P_{3/2}$ transition (i.e., $J^p = \frac{1}{2}^+$) the agreement with the analytical prediction is also good. For the experimental spectrum, we note an absence of a central peak at $\Delta_c = 0$ so that the number of coupling matrix eigen-energies exceeds the number of spectral peaks by one everywhere: any state corresponding the central eigenenergy will exclusively have r_2-character and the coupling field can therefore not make a connection to the $5P_{3/2}$ level (Laporte's rule). The absence of a central peak is captured by the density matrix simulations along with an increase in peak intensity for degenerate eigenenergies. We note how both types of $J = 1/2$ spectra display mirror symmetries about integer multiples of $\pi/2$. This introduces a four-fold ambiguity in inferring ϕ from a given spectrum. For example $\phi = \pi/4, 3\pi/4, 5\pi/4, 7\pi/4$ display identical spectra.

The spectral SOP-ambiguity is reduced when proceeding to the cases of $J = 3/2$ where experiment as well as density matrix simulation reveal a simple mirror symmetry about $\phi = \pi$. The recorded experimental spectrum

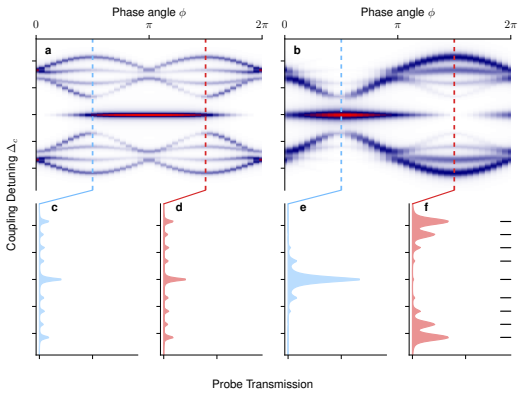

Fig. 5 | Breaking spectrogram symmetry. Simulated EIT probing of a RF-dressed $J^p = \frac{3}{2}^+$ transition with the optical fields counter-propagating along the direction $\hat{\mathbf{z}} + \hat{\mathbf{y}}$. **a** Spectrogram for optical field polarized along $\hat{\mathbf{x}}$. As shown in (**b**) the spectra for $\phi = \pi/2$ (full blue line) and $\phi = 3\pi/2$ (red dashed line) are identical due to the symmetry about $\phi = \pi$. **c**, Spectrogram obtained with circularly polarized optical fields, breaking the symmetry about $\phi = \pi$. **d**, The corresponding spectra at $\phi = \pi/2$ and $\phi = 3\pi/2$ are clearly distinguishable.

for the dressed $\updownarrow^{49D_{3/2}}_{50P_{3/2}}$ transition shows limited resemblance to the analytical $J^p = \frac{3}{2}^0$ prediction in Fig. 3a and the density matrix simulation Fig. 3c. The discrepancy results from dealing with a real atom and is caused by interference from the nearby $49D_{5/2}$ departure from the idealized case of an isolated $\updownarrow^{49D_{3/2}}_{50P_{3/2}}$. The Extended Data Fig. 1 details the effect of adding a third level to the problem while also showing that by expanding the density matrix to include the $49D_{5/2}$ state agreement between experiment and simulation is established. In contrast, the $\updownarrow^{49D_{5/2}}_{50P_{3/2}}$ -transition is well described within the simpler framework of Fig. 3 and excellent correspondence between analytical theory, experiment, and simulations is found. For the purpose of demonstrating Rydberg atomic SOP measurements, we shall therefor focus our attention to the case of $J^p = \frac{3}{2}^+$ and discuss strategies to establish an unambiguous assignment to the Poincaré sphere.

RESOLVING AMBIGUITY FOR A $J^p = \frac{3}{2}^+$ SYSTEM

The mirror symmetry about π for the $J^p = \frac{3}{2}^+$spectrogram of Fig. 3 implies a twofold spectral degeneracy for the probing configuration Fig. 1(a). Indeed, Fig. 4 shows the nominally identical $J^p = \frac{3}{2}^+$ spectra for circularly polarized RF fields of opposite helicities (i.e., $\phi = \pi/2$ and $3\pi/2$) on the basis of which it is not possible to discern the handedness of the DUT field.

To obtain a complete SOP measurement on the DUT field the symmetries encountered in $J^p = \frac{3}{2}^+$ spectrograms of Fig. 3 needs to be broken. One way of achieving this is by going to a configuration where the probe and coupling beams counter-propagate along $\hat{\mathbf{z}} + \hat{\mathbf{y}}$. Figure 5a shows the simulated spectrogram for $J^p = \frac{3}{2}^+$ probed with linearly polarized optical fields along the x-axis while Fig. 5b extracts the associated EIT spectra for $\phi = \pi/2$ and $\phi = 3\pi/2$. The results match those obtained in the orthogonal-axes configuration Fig. 1 including the inability to assign the handedness of a circularly polarized RF-field. However, by switching to using circularly polarized optical fields in the non-orthogonal-axes configuration, the spectrogram symmetry about π becomes broken as shown in Fig. 5(c). Indeed, the corresponding spectra for LCP ($\phi = \pi/2$) and RCP ($\phi = 3\pi/2$) polarized shown in Fig. 5(d) can clearly be discriminated, for example through the increase or suppression of the central spectral peak.

DISCUSSION AND OUTLOOK

This work has demonstrated how the SOP for an incoming RF DUT field imprints on the Rydberg states of atoms of a vapour cell sensor and that this imprint can be read out via optical spectroscopy. In general, a recorded spectrum may not be unique to a single SOP, inverting to multiple points on the Poincaré sphere. However, through suitable choices for the propagation direction of the interrogating optical fields and the polarization, such ambiguity can be resolved as illustrated in the case of a dressed $\updownarrow^{5/2}_{3/2}$ transition.

As a natural extension of our work we envisage the directions of the optical beams to be scanned in conjunction with scanning their states of polarization. Such a tomographic approach might be used to compensate for the effect of a possible background magnetic field and other symmetry-breaking perturbations. It may also be used to infer an unknown direction of arrival (DoA) for the incoming RF field—a core diagnostics within RF antenna engineering [22]. While conventional DoA estimation typically makes use of an array of antennas [23] to infer a transmitter location, Rydberg atomic sensors offers a solution for carrying out this task based on a single detection element [24–26]. The framework presented in this Letter may allow for a particular simple implementation of a Rydberg atomic DoA sensor which like our SOP measurements hinges on proper understanding of how an atom via its quantized angular momentum structure processes a DUT dressing field [27].

This work was supported by the Marsden Fund of New Zealand (Contract No. UOO2421).

[1] M. Born and E. Wolf, *Principles of Optics* (Cambridge University Press, 1999).
[2] E. Collett, *Field Guide to Polarization* (SPIE, 2005).
[3] P. Hauge, Recent developments in instrumentation in ellipsometry, Surf. Sci. **96**, 108 (1980).
[4] S. Drabowitch, A. Papiernik, H. Griffiths, and J. Encinas, *Modern Antennas* (Springer US, 1998) Chap. Fundamentals of polarimetry.
[5] Y. Inoue, L. E. Perez, R. T. Kelly, A. Jemcov, T. G. Pratt, and S. C. Morris, Non-intrusive radio frequency polarimetry measurements of rotor whirl using artificial neural networks, Meas. Sci. Technol. **36**, 035904 (2025).
[6] J. Sedlacek, A. Schwettmann, H. Kübler, R. Löw, T. Pfau, and J. Shaffer, Microwave electrometry with Rydberg atoms in a vapour cell using bright atomic resonances, Nat. Phys. **8**, 819 (2012).
[7] C. L. Holloway, J. A. Gordon, S. Jefferts, A. Schwarzkopf, D. A. Anderson, S. A. Miller, N. Thaicharoen, and G. Raithel, Broadband Rydberg atom-based electric-field probe for SI-traceable, self-calibrated measurements, IEEE Trans. Antennas Propag. **62**, 6169 (2014).
[8] N. Schlossberger, N. Prajapati, S. Berweger, A. P. Rotunno, A. B. Artusio-Glimpse, M. T. Simons, A. A. Sheikh, E. B. Norrgard, S. P. Eckel, and C. L. Holloway, Rydberg states of alkali atoms in atomic vapour as SI-traceable field probes and communications receivers, Nat. Rev. Phys. **6**, 606 (2024).
[9] J. A. Sedlacek, A. Schwettmann, H. Kübler, and J. P. Shaffer, Atom-based vector microwave electrometry using rubidium Rydberg atoms in a vapor cell, Phys. Rev. Lett. **111**, 063001 (2013).
[10] Z. Song, W. Zhang, Q. Wu, H. Mu, X. Liu, L. Zhang, and J. Qu, Field distortion and optimization of a vapor cell in Rydberg atom-based radio-frequency electric field measurement, Sensors **18**, 3205 (2018).
[11] Y. Wang, F. Jia, J. Hao, Y. Cui, F. Zhou, X. Liu, J. Mei, Y. Yu, Y. Liu, J. Zhang, F. Xie, and Z. Zhong, Precise measurement of microwave polarization using a Rydberg atom-based mixer, Opt. Express **31**, 10449 (2023).
[12] M. Cloutman, M. Chilcott, A. Elliott, J. S. Otto, A. B. Deb, and N. Kjærgaard, Polarization-insensitive microwave electrometry using Rydberg atoms, Phys. Rev. Appl. **21**, 044025 (2024).
[13] W. Yin, J. Zhang, F. Jia, Y. Wang, Y. Wang, J. Hao, Y. Cui, Y. Liu, and Z. Zhong, Measurement of microwave polarization using two polarization orthogonal local microwave electric fields in a rydberg atom-based mixer, Opt. Express **32**, 38372 (2024).
[14] S. H. You, M. H. Cai, H. A. Zhang, Z. F. Song, and H. Liu, RF spectra induced by different polarized microwave, AIP Adv. **14**, 015245 (2024).
[15] M. Cloutman, M. Chilcott, A. Elliott, J. S. Otto, A. B. Deb, and N. Kjærgaard, Quantum-enabled rydberg atomic polarimetry of radio-frequency fields 10.48550/ARXIV.2503.17997 (2025), arXiv:2503.17997 [quant-ph].
[16] M. Cai, A. Wei, S. Chen, and Y. Huang, Polarization impact on sensitivity measurement of Rydberg atom-based microwave sensors, Chin. Phys. B **34**, 083201 (2025).
[17] P. K. Elgee, K. C. Cox, J. C. Hill, P. D. Kunz, and D. H. Meyer, Complete three-dimensional vector polarimetry with a Rydberg-atom rf electrometer, Phys. Rev. Appl. **22**, 064012 (2024).
[18] P. K. Elgee, K. C. Cox, J. C. Hill, P. D. Kunz, and D. H. Meyer, Electrically small Rydberg sensor for three-dimensional determination of radio-frequency k -vectors, Phys. Rev. Appl. **23**, 064012 (2025).
[19] I. I. Sobelman, *Atomic Spectra and Radiative Transitions* (Springer Berlin Heidelberg, 1992).
[20] See Supplemental Material [url] for [brief description], which includes Ref. [28].
[21] A. Chopinaud and J. Pritchard, Erratum: Optimal State choice for Rydberg-atom microwave sensors [Phys. Rev. Appl. 16 , 024008 (2021)], Phys. Rev. Appl. **22**, 029902 (2024).
[22] Z. Chen, *Introduction to Direction-of-Arrival Estimation.*, 1st ed., edited by G. K. Gokeda and Y. Yu (Artech House, Norwood, 2010) description based on publisher supplied metadata and other sources.
[23] A. M. Molaei, B. Zakeri, S. M. H. Andargoli, M. A. B. Abbasi, V. Fusco, and O. Yurduseven, A comprehensive review of direction-of-arrival estimation and localization approaches in mixed-field sources scenario, IEEE Access **12**, 65883 (2024).
[24] A. K. Robinson, N. Prajapati, D. Senic, M. T. Simons, and C. L. Holloway, Determining the angle-of-arrival of a radio-frequency source with a rydberg atom-based sensor, Appl. Phys. Lett. **118**, 114001 (2021).
[25] N. Schlossberger, R. Talashila, N. Prajapati, and C. L. Holloway, Angle-of-arrival detection of radio-frequency waves via Rydberg-atom fluorescence imaging of standing waves in a glass vapor cell, Phys. Rev. Appl. **24**, 024056 (2025).
[26] R. Talashila, W. J. Watterson, B. L. Moser, J. A. Gordon, A. B. Artusio-Glimpse, N. Prajapati, N. Schlossberger, M. T. Simons, and C. L. Holloway, Determining angle of arrival of radio-frequency fields using subwavelength, amplitude-only measurements of standing waves in a Rydberg atom sensor, J. Appl. Phys. **138**, 114402 (2025).
[27] M. Chilcott and N. Kjærgaard, Comment on "Determining angle of arrival of radio-frequency fields using subwavelength, amplitude-only measurements of standing waves in a Rydberg atom sensor" [J. Appl. Phys. 138, 114402 (2025)], J. Appl. Phys. (2025).
[28] D. A. Varshalovich, A. N. Moskalev, and V. K. Khersonskii, *Quantum Theory of Angular Momentum* (World Scientific, 1988).
[29] W. J. Thompson, *Angular Momentum: An Illustrated Guide to Rotational Symmetries for Physical Systems* (Wiley, 1994).

EXTENDED DATA

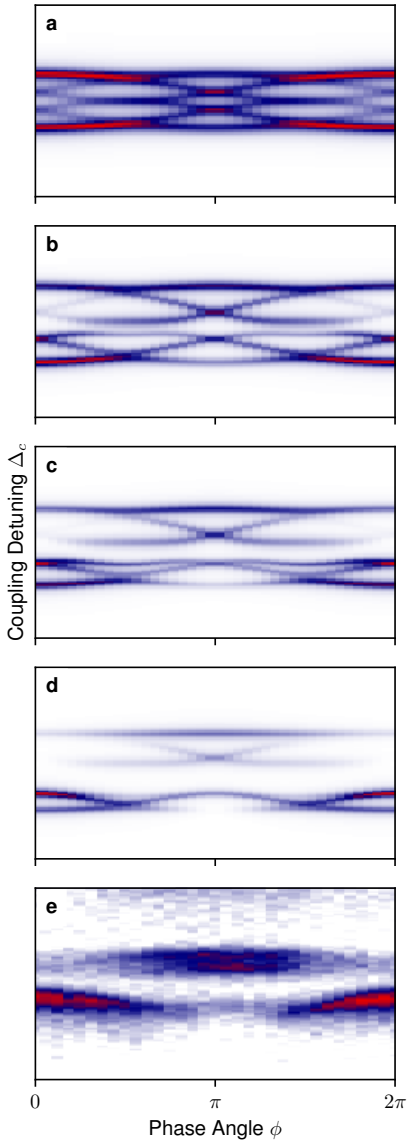

Extended Data Fig. 1 | Beyond a dressed two-level system. Effect of coupling off-resonantly to a third level. **a**, Simulated spectrogram for an isolated $J^p = \frac{3}{2}^0$-transition nominally occurring between the two levels $49D_{3/2}$ and $50P_{3/2}$. **b-d** spectrograms including coupling to the $49D_{5/2}$ placed, respectively, 350 MHz, 200 MHz, and 100 MHz above the $49D_{3/2}$ -state. **e** Experimentally observed spectrogram when resonantly dressing the $49D_{3/2} \leftrightarrow 50P_{3/2}$ transition. In doing so the $49D_{5/2} \leftrightarrow 50P_{3/2}$ transition is off-resonantly dressed (with ∼100 MHz detuning) and correspondence with **d** rather than **a** is found.

SUPPLEMENTARY NOTE 1

Matrix elements of r_q

We want to calculate the dipole matrix element between an initial quantum state $|i\rangle$ and a final state $|f\rangle$ in the $J = L + S$ coupled basis under the assumptions

1. $S = S' = 1/2$.
2. For the dipole matrix element to be non-zero, L and L' must differ by 1 (Laporte's rule). Without loss of generality we will assume $L' = L + 1$. This implies that for allowed transitions, we either have $J' = J$ or $J' = J + 1$.
3. The wavefunction for the Rydberg level corresponding to a principal quantum number n and orbital angular momentum L is described by a radial component $R_{nL}(r)$.

Using the Wigner-Eckart theorem (cf. [19], (4.120) and (4.175), and [29], (8.46)) we obtain

$$\begin{aligned}
\langle n'L'S'J'm'_J|\, r_q \,|nLSJm_J\rangle &= (-1)^{J'-m'_J}\begin{pmatrix} J' & 1 & J \\ -m'_J & q & m_J\end{pmatrix}\langle n'L'S'J'\|\, r \,\|nLSJ\rangle \\
&= (-1)^{J'-m'_J}\begin{pmatrix} J' & 1 & J \\ -m'_J & q & m_J\end{pmatrix}(-1)^{L'+S'+J+1} \\
&\quad\times\sqrt{(2J+1)(2J'+1)}\begin{Bmatrix} L' & J' & S' \\ J & L & 1\end{Bmatrix}\underbrace{\langle n'L'\|\, r \,\|nL\rangle}_{(-1)^{L'}\sqrt{L'}\mathcal{R}_{n'L',nL}} \\
&= (-1)^{J'+J-m'_J-\frac{1}{2}}\begin{pmatrix} J' & 1 & J \\ -m'_J & q & m_J\end{pmatrix} \\
&\quad\times\sqrt{(2J+1)(2J'+1)(L+1)}\begin{Bmatrix} L+1 & J' & \frac{1}{2} \\ J & L & 1\end{Bmatrix}\mathcal{R}_{n'L+1,nL},
\end{aligned} \tag{S1}$$

where

$$\mathcal{R}_{n'L',nL} \equiv \int_0^\infty R_{n'L'}(r)R_{nL}(r)r^3dr, \tag{S2}$$

is the radial matrix element for the $i \to f$ transition, which has no J or m_J dependence.

In Eq. (S1) the 3-j symbol expresses the relative strength of transitions across the m_J-manifold. Meanwhile, the product in the last line of Eq. (S1) simplifies as follows

With the assumption $L' = L + 1$ there are three possibilities for dipole allowed transitions

p=+1: $J' = J + 1 = L' + 1/2 = L + 3/2$ so that for Eq. (S1)

1. the six-j symbol reads (using Ref. [28] 9.4.2(2) and 9.5.2 (5))
   $\begin{Bmatrix} L+1 & L+\frac{3}{2} & \frac{1}{2} \\ L+\frac{1}{2} & L & 1\end{Bmatrix} = \begin{Bmatrix} L+1 & \frac{1}{2} & L+\frac{3}{2} \\ L+\frac{1}{2} & 1 & L\end{Bmatrix} = \frac{1}{\sqrt{(2L+3)(2L+2)}} = \frac{1}{\sqrt{(2J+2)(2J+1)}}$.
2. $\sqrt{(2J+1)(2J'+1)(L+1)} = \sqrt{(2J+1)(2J+3)(J+\frac{1}{2})} = \sqrt{\frac{1}{2}(2J+1)^2(2J+3)}$.
3. the product of these are $\sqrt{\frac{(2J+1)(2J+3)}{2(2J+2)}} = \sqrt{(2J+3)}\sqrt{\frac{(2J+1)}{2(2J+2)}}$

p=0: $J' = J = L + 1/2$ so that for Eq. (S1)

1. the six-j symbol reads (using Ref. [28] 9.4.2(2) and 9.5.2(4))
   $\begin{Bmatrix} L+1 & L+\frac{1}{2} & \frac{1}{2} \\ L+\frac{1}{2} & L & 1\end{Bmatrix} = \begin{Bmatrix} \frac{1}{2} & L+\frac{1}{2} & L+1 \\ 1 & L & L+\frac{1}{2}\end{Bmatrix} = \sqrt{\frac{2}{(2L+1)(2L+2)^2(2L+3)}} = \sqrt{\frac{1}{J(2J+1)^2(2J+2)}}$
2. $\sqrt{(2J+1)(2J'+1)(L+1)} = \sqrt{(2J+1)^2(J+\frac{1}{2})} = \sqrt{\frac{(2J+1)^3}{2}}$

3. the product of these are $\sqrt{\frac{(2J+1)}{2J(2J+2)}} = \frac{1}{\sqrt{J}}\sqrt{\frac{(2J+1)}{2(2J+2)}}$

p=-1: $J' = J+1 = L'-1/2 = L+1/2$ so that for Eq. (S1)

1. the six-j symbol reads (using Ref. [28] 9.4.2(2) and 9.5.2 (5))
$\begin{Bmatrix} L+1 & L+\frac{1}{2} & \frac{1}{2} \\ L-\frac{1}{2} & L & 1 \end{Bmatrix} = \begin{Bmatrix} \frac{1}{2} & L+\frac{1}{2} & L+1 \\ 1 & L & L-\frac{1}{2} \end{Bmatrix} = \frac{1}{\sqrt{(2L+2)(2L+1)}} = \frac{1}{\sqrt{(2J+3)(2J+2)}}.$
2. $\sqrt{(2J+1)(2J'+1)(L+1)} = \sqrt{(2J+1)(2J+3)(J+\frac{3}{2})} = \sqrt{\frac{(2J+1)(2J+3)^2}{2}}.$
3. the product of these are $\sqrt{\frac{(2J+1)(2J+3)}{2(2J+2)}} = \sqrt{(2J+3)}\sqrt{\frac{(2J+1)}{2(2J+2)}}$

CHAPTER 6

Conclusion & Outlook

This thesis presents a summary of the research carried out during my PhD studies from February 2023 to February 2026 at Aarhus University under the supervision of Prof. Jan Arlt. At the beginning of this PhD project, the previous generation of experiments were still ongoing, but were being concluded. These included the spatial alpha calibration for time-of-flight absorption imaging of ultracold gases [1], characterisation of atom number fluctuations in BEC using a microcanonical ensemble description [2], and time-of-flight expansions of bimodal clouds accounting for interatomic repulsion [3]. Those experiments are thoroughly addressed in earlier PhD theses [33, 48] and are therefore not presented in this thesis.

Initial investigations within my PhD research focused on hybridised light-matter systems in ultracold atomic gases. To pursue this objective, a new experimental platform was constructed, employing EIT to probe light-induced dipole-dipole interactions in the high-density regime. This required substantial extensions of the existing apparatus, including the implementation of a Raman laser system and a single-photon detection system for EIT measurements.

Although the EIT approach ultimately did not succeed in probing the targeted light-induced dipole-dipole interactions, the investigation led to the construction of a more versatile experimental platform capable of supporting a broader research programme. In particular, the narrow frequency scans originally implemented to resolve the EIT transparency window were extended to enable broadband

absorption measurements. Furthermore, the dark-ground imaging configuration was found to enhance the weak signal of thermal atoms even at temperatures well below the critical temperature. This observation initiated systematic studies of dark-ground spectroscopy, culminating in a publication in preparation [4].

Since modelling dark-ground spectra required repeated trap-frequency measurements, a new method was developed to determine trap frequencies from a single atomic cloud. Previously, such measurements relied on absorption imaging, where cloud dynamics were inferred by tracking the centre-of-mass motion across a sequence of images, each requiring preparation of a new atomic sample. In contrast, nondestructive measurements performed on a single cloud significantly improved data acquisition speed. This methodological development enabled a new class of time-resolved measurements and ultimately resulted in a second publication in preparation [5].

Finally, this thesis presents the experimental realisation of a Rydberg-atom-based EIT sensor for microwave (MW) polarimetry, implemented in a room-temperature vapour cell. This work also resulted in a publication in preparation [6]. During the construction of this apparatus, a complementary investigation was undertaken to address a missing experimental result from [14]. Specifically, the AT splitting of highly excited Rydberg states is expected to exhibit a substructure at strong MW fields due to an m_J-dependent interaction strength arising from variations in the Clebsch-Gordan coefficients across the manifold. Although this effect had been theoretically predicted [14], it had not been experimentally observed prior to the realisation of this setup. This work was carried out during a seven-week research stay in the group of Prof. Niels Kjærgaards at Otago University.

The following sections outline the experimental developments and conclude each of the research directions pursued during this research project.

Rebuilding the Experiment

Over the course of this PhD project, all optical systems were redesigned and rebuilt to improve stability, and the experimental sequence was optimised. The master laser system was reconstructed with a minimalistic and compact architecture to ensure stability and low maintenance. This has significantly reduced the previous optical path lengths, and rarely requires adjustment of optical coupling efficiencies. A MOT distribution board was constructed and integrated into the experiment, enhancing stability, simplifying maintenance, and enabling precise balancing of the optical power between each pair of telescopes. These and other improvements

to the MOT stage produced a larger, more efficiently cooled cloud, which now reaches saturation in approximately 10 s. The transfer sequence was optimised to minimise atom loss and heating, while also improving the speed and acceleration of the mechanically moving magnetic coils. These adjustments significantly reduced the experimental cycle time, while maintaining stability to the transfer sequence. As a result of the work on the pre-cooling stage and the transfer sequence, the phase-space density prior to evaporative cooling increased. The entire evaporative cooling sequence was improved thereafter. Most notably, the experimental cycle time was reduced from approximately 90 s [33] to about 30 s per run, enabling faster data acquisition and accelerating experimental progress. In continuous-mode operation, typically used for repeated experiments or parameter scans, the cycle time was further reduced to about 20 s. This improvement was achieved by implementing a MOT pre-loading stage at the end of each run, after the final absorption image and before the next run begins, allowing the experiment to almost fully skip the MOT stage during restart. In addition to faster cycle times, this work resulted in the largest BEC in the group's history, containing approximately 650k atoms.

Minor additions were implemented, including motorised mirrors for controlling the dipole trap beams, allowing overlap and QPT centre offsets to be quickly reset or optimised with improved reversibility and safety. Using the atoms for feedback of the optimisation procedure was also a valuable addition, and scanning positions while evaluating clouds demonstrates the reversibility of the alignment. Three-inch optics were also implemented in one of the detection branches.

The Raman laser system was originally constructed to probe EIT, exploiting its narrow spectroscopic feature to achieve high precision in measuring the weak broadening phenomenon. To this end, the FlexDDS was programmed and configured for both controlling the optical phase-lock loop reference as well as the MW state preparation. Furthermore, a single-photon detector was introduced together with the dark-ground imaging configuration. Although the initial experiments achieved atom number densities between 200 and $300/\lambda^3$, the broadening effects were never observed in the transparency window. The EIT approach was therefore abandoned in favour of alternative spectroscopic methods for three reasons. First, EIT offers no intrinsic metrological advantage for this purpose: the change in linewidth scales relative to the EIT window itself. Consequently, the required *relative* precision remains unchanged, while the experimental complexity increases substantially compared to standard absorption spectroscopy. Second, complete transparency is never achieved due to residual dephasing processes. This is

strongly enhanced by the extreme optical density in-situ for a BEC. The atomic cloud remains optically thick even under EIT conditions, and the contribution to the transparency is dominated by the surrounding thermal component. This is counterproductive for the purpose of probing the high-density regime. Finally, utilising EIT introduces several additional parameters, such as the coupling Rabi frequency, two-photon detuning, and ground-state dephasing, which complicate both the experimental operation and theoretical modelling. Since the relative precision is equivalent to that of standard absorption profiles, the experiments were redirected towards measuring broader absorption spectra. This led to the two main results of this thesis.

Few-Photon Spectroscopy of Bose-Einstein Condensates

Three key developments were employed for this experimental investigation. First, the newly implemented Raman-laser system served as a versatile probe, capable of scanning 9 GHz within approximately 100 ms. Second, the dark-ground imaging configuration enhanced the signal-to-noise ratio and provided sensitivity to dispersive phase shifts. Finally, a single-photon detection system enabled time-resolved measurements at low probe intensities. Together, these developments allowed rapid, nondestructive probing, culminating in the results reported in a publication [6] in preparation.

Light propagation through ultracold clouds was modelled, and the spatial distributions of atoms in thermal, bimodal, and condensed clouds were found to exhibit spectral features that can be fitted to extract cloud parameters such as atom number and temperature. Importantly, this approach does not require high-numerical-aperture optical systems for spatially resolved images. Instead, a single-photon detector module detects the light. While there is no spatial resolution, the signal-to-noise ratio at a given optical power is significantly improved, allowing probe light intensity to be drastically reduced while preserving reliable fitting. Since most of the spectrum is far-detuned, absorption is lower, and the method is correspondingly less destructive than resonant detection techniques. This approach yields a full spectrum from a single atomic cloud, and the nondestructive measurement can be followed by time-of-flight absorption imaging to provide additional data per experimental cycle. For the datasets presented in this thesis, atom loss was kept below 10 %. Introducing a dark-ground obstacle significantly expanded the experimental capabilities, providing sensitivity to both absorption and phase shifts. Theoretical models accurately reproduced the dark-ground spectra. The cloud parameters extracted via the spectral probe

were compared with absorption images, showing good agreement. Interestingly, the complementary detection methods exhibit a unique duality. While standard time-of-flight absorption images display a narrow BEC spike atop a broad thermal distribution, the two components play a reversed role in frequency space, where a narrow thermal peak appears atop a broad BEC distribution. The bimodal cloud profiles observed in time-of-flight imaging arise from the distinct momentum distributions of the two components, whereas the spectral features reflect their optical densities: thermal atoms absorb near resonance, while the BEC remains optically thick at larger detunings. Consequently, each detection method is sensitive to different components. In particular, the spectral probe is highly sensitive to thermal atoms at temperatures well below the critical temperature, where absorption images cannot resolve the weak thermal component hidden in the low-density tail of the bimodal cloud. The clearly separated spectral domains also provide enhanced sensitivity to the dense regions of the cloud with reduced interference from thermal atoms. This can potentially be used to revisit previous investigations on atom number fluctuations between thermal and condensed components, or to investigate density-dependent light-matter interactions, such as the light-induced dipole-dipole broadening.

Dark-Ground Detection of Dynamics in Ultracold Gases

The analysis of the spectroscopic detection of ultracold atomic clouds required repeated measurements of the trap frequency at varying temperatures. Performing these measurements via absorption imaging necessitates the preparation of multiple atomic clouds and the acquisition of a sequence of images along both imaging axes in order to track the centre-of-mass motion in all spatial directions. To reduce this overhead, a new method was developed that utilises the already installed pinhole in the single-photon detector system to introduce indirect spatial resolution to an otherwise single-pixel detector. By placing the pinhole in the intermediate image plane of the atoms, at a position corresponding to the edge of the cloud, and continuously probing the cloud with a weak probe field, the cloud dynamics are encoded as amplitude modulation of the detected signal as the cloud oscillates in and out of the pinhole region. This approach enables real-time measurements on a single atomic cloud. The simplicity and effectiveness of this method motivated further investigations. The dark-ground detection enabled a catalogue of time-resolved experiments which can be categorised into internal- and external dynamics, corresponding to the control of atomic state populations and to measurements of motional behaviour respectively. Accounting

for a typical experimental cycle time of 30 s and repetitions required to improve counting statistics, this approach reduced the data acquisition time for standard calibrations from hours to minutes.

A key outcome of this work is the demonstration of coherent Raman-Rabi oscillations. Direct observation of Rabi oscillations requires the Rabi frequency to exceed the excited-state decay rate. This constraint was overcome by employing a far-detuned two-photon Raman transition between ground-state manifolds. Although the excited state still sets the effective coherence time, its negligible population significantly suppresses decoherence, enabling sustained coherent dynamics. The experimental configuration enabled dual-port detection of both Raman laser fields, which can potentially be used as a robust tool for probing high-density ultracold atomic systems for density-dependent many-body effects.

In addition, a co-linear EIT configuration with dual-port detection was implemented. By combining dark-ground spatial filtering with polarisation-based separation, the need for an etalon to isolate the weak probe from the strong coupling was eliminated, although the two fields have nearly identical wavelengths.

The investigation of time-resolved spectroscopy and real-time detection of both internal and external dynamics in ultracold gases using dark-ground detection led to a publication [4] in preparation.

Rydberg-Atom-Based EIT Sensing

As part of a seven-week long research stay abroad at Otago University under the supervision of Prof. Niels Kjærgaard, a Rydberg-atom-based EIT sensor for external MW fields was constructed using a room-temperature Rb vapour cell. In the first iteration, the experiment employed a homebuilt helical antenna, which proved useful for establishing the system and developing the experimental control architecture. Subsequently, a horn antenna was 3D printed in plastic and copper electroplated to better mimic the yet-to-arrive commercial dual-port horn antenna. With the homebuilt antennas, the experiment performed reliably, enabling the acquisition of substantial datasets while the system was further refined. In addition, control scripts were developed for frequency calibration of both the optical and the MW field, as well as for controlled scans of the MW field strength. The experiments led to two main results: the first was a follow-up investigation of previous work [14], focusing on AT splitting in the strong MW regime and, in particular, resolving substructure in highly excited Rydberg states; and the second concerned measurements of the state of polarisation of MW fields.

The latter is under publication at the time of writing [6].

Furthermore, the experiments motivated the development of a density-matrix simulation framework that proved applicable to both the Aarhus-based and the Dunedin-based experiments. Two experimental regimes are simulated within this framework: first, the steady-state solution of the Lindblad master equation, relevant for EIT spectroscopy, and second, the full time-propagated dynamics, applicable to investigations in the internal dynamics such as the two-photon Raman-Rabi transitions within the D2 line. Together, these two approaches provide a comprehensive framework for modelling all relevant single-atom light-matter interactions considered in this thesis. With the high-density atomic clouds in mind, this framework can also serve as a single-atom reference model, enabling the identification of deviations arising from density-dependent interactions.

Outlook

In conclusion, this thesis has established many of the fundamental building blocks for a novel detection technique that can be performed in-situ for time-resolved spectroscopy and real-time measurements of both internal and external dynamics. The method has been demonstrated through a catalogue of experiments, ranging from dark-ground spectroscopy for extracting atom number and temperature to applications in experimental calibration and studies of time-resolved dynamics.

A natural next step is to resume the investigation of the high-density regime, specifically targeting measurements of light-induced dipole-dipole broadening in the absorption spectrum. Another goal is the implementation of lithium as a new atomic species in the experiment. Significant effort has already been devoted to preparing the laboratory, including reorganising optical tables and electronics to accommodate the necessary equipment. The goal of introducing lithium is to combine a ^{87}Rb BEC with a ^{6}Li Fermi gas, opening up new avenues of experimentation. By employing the tune-out wavelength of ^{87}Rb at approximately 790 nm, a strong dipole trap for ^{6}Li can be achieved, which is invisible to the ^{87}Rb atoms. Hence, the Fermi gas can be modified in the optical trap that remains transparent to the ^{87}Rb atoms. However, introducing ^{6}Li to the experiment necessitates a complete redesign of the vacuum chambers and the reconstruction of the pre-cooling stages, which will form part of the projects to be undertaken by the next generation of PhD students. Combining a two-dimensional MOT for ^{87}Rb with a short-distance Zeeman slower to decelerate a beam of ^{6}Li atoms from a hot oven provides a compact setup [69]. In this setup, an optical push beam

replaces the mechanically controlled magnetic transport coils currently in use for transporting the atomic sample from the MOT chamber to the science chamber. Although the introduction of a new atomic species opens up new avenues of experimentation, it remains a long-term effort compared to the more immediately accessible investigation of the high-density regime.

Another important aspect requiring attention is the experimental control system (ECS). This system is homebuilt [51] and has now been in operation for more than two decades. However, it has proven difficult to configure, and its internal architecture is insufficiently documented. Previous attempts to implement a clock-thief module [33] disrupted the internal timing system. This resulted in a very subtle instability which took two years to realise and was solved at the beginning of this PhD project. Future generations of PhD students would benefit from a modernised control system, and initial steps towards implementing ARTIQ [70] have already been initiated. Such a system would provide substantially greater flexibility and customisation of experimental sequences. For instance, the current ECS does not support scanning more than two parameters simultaneously, and even for two-parameter scans, diagonal or correlated scans are not readily implemented.

Final Remarks

Reflecting on this journey, it has been a privilege to build, refine and explore these experiments, witnessing the evolution from initial ideas to a versatile experimental platform. While the outcomes diverged from the original plan, the methods and tools developed here open exciting avenues for future research. I hope that the techniques, insights and improvements presented in this thesis will continue to inspire experiments, advancing both precision measurements and our understanding of ultracold quantum gases.

Bibliography

[1] T. Vibel, M. B. Christensen, M. A. Kristensen, J. J. Thuesen, L. N. Stokholm, C. A. Weidner, and J. J. Arlt, "Spatial calibration of high-density absorption imaging", Journal of Physics B: Atomic, Molecular and Optical Physics **57**, 145301 (2024).

[2] T. Vibel, M. B. Christensen, R. M. F Andersen, L. N. Stokholm, K. Pawłowski, K. Rzążewski, M. A. Kristensen, and J. J. Arlt, "Atom number fluctuations in Bose gases—statistical analysis of parameter estimation", Journal of Physics B: Atomic, Molecular and Optical Physics **57**, 195301 (2024).

[3] R. M. F Andersen, S. Frederiksen, L. N. Stokholm, I. Zebergs, M. Kristensen, C. Weidner, and J. J. Arlt, "Cloud parameter estimation for interacting BEC after time-of-flight", (2026).

[4] R. M. F Andersen, L. N. Stokholm, I. Zebergs, N. R. Neubert, A. S. Chatterly, and J. J. Arlt, "Few-photon spectroscopy of Bose-Einstein condensates", Manuscript in preparation (expected 2026).

[5] L. N. Stokholm, R. M. F Andersen, I. Zebergs, N. R. Neubert, A. S. Chatterly, and J. J. Arlt, "Observation of dynamics in ultracold gases using dark-ground detection", Manuscript in preparation (expected 2026).

[6] M. Chilcott, L. N. Stokholm, M. Cloutman, J. S. Otto, A. B. Deb, and N. Kjærgaard, "Quantum-enabled complete RF-polarimetry", Manuscript in preparation (expected 2026).

[7] E. P. Wigner, "The glorious days of physics", in *Understanding the fundamental constituents of matter* (1983), pp. 765–774.

[8] A. Einstein, "Quantentheorie des einatomigen idealen Gases", Sitzungsber. Preuß. Akad. Wiss., 261–267 (1924).

[9] A. Einstein, "Quantentheorie des einatomigen idealen Gases. Zweite Abhandlung", Sitzungsber. Preuß. Akad. Wiss., 3–14 (1925).

[10] S. N. Bose, "Plancks Gesetz und Lichtquantenhypothese", Z. Phys. **26**, 178–181 (1924).

[11] M. H. Anderson, J. R. Ensher, M. R. Matthews, C. E. Wieman, and E. A. Cornell, "Observation of Bose-Einstein Condensation in a Dilute Atomic Vapor", Science **269**, 198–201 (1995).

[12] K. B. Davis, M.-O. Mewes, M. A. Joffe, M. R. Andrews, and W. Ketterle, "Evaporative Cooling of Sodium Atoms", Phys. Rev. Lett. **74**, 5202–5205 (1995).

[13] C. C. Bradley, C. A. Sackett, J. J. Tollett, and R. G. Hulet, "Evidence of Bose-Einstein Condensation in an Atomic Gas with Attractive Interactions", Phys. Rev. Lett. **75**, 1687–1690 (1995).

[14] M. Cloutman, M. Chilcott, A. Elliott, J. S. Otto, A. B. Deb, and N. Kjærgaard, "Rydberg atomic polarimetry of radio-frequency fields", `10.48550/arXiv.2503.17997` (2025).

[15] J. J. Sakurai and J. Napolitano, *Modern Quantum Mechanics*, 2nd (2010).

[16] C. J. Foot, *Atomic Physics*, 2nd (2005).

[17] M. Fleischhauer, A. Imamoglu, and J. P. Marangos, "Electromagnetically induced transparency: optics in coherent media", Rev. Mod. Phys. **77**, 633–673 (2005).

[18] R. Finkelstein, S. Bali, O. Firstenberg, and I. Novikova, "A practical guide to electromagnetically induced transparency in atomic vapor", New Journal of Physics **25**, 035001 (2023).

[19] B. H. Bransden and C. J. Joachain, *Physics of Atoms and Molecules*, 2nd (2003).

[20] L. V. Hau, S. E. Harris, Z. Dutton, and C. H. Behroozi, "Light speed reduction to 17 metres per second in an ultracold atomic gas", Nature **397**, 594–598 (1999).

[21] E. Saglamyurek, T. Hrushevskyi, A. Rastogi, K. Heshami, and L. J. LeBlanc, "Coherent storage and manipulation of broadband photons via dynamically controlled autler–townes splitting", Nature Photonics **12**, 774–782 (2018).

[22] A. Rastogi, E. Saglamyurek, T. Hrushevskyi, S. Hubele, and L. J. LeBlanc, "Discerning quantum memories based on electromagnetically-induced-transparency and autler-townes-splitting protocols", Physical Review A **100**, 10.1103/physreva.100.012314 (2019).

[23] E. Saglamyurek, T. Hrushevskyi, L. Cooke, A. Rastogi, and L. J. LeBlanc, "Single-photon-level light storage in cold atoms using the autler-townes splitting protocol", Phys. Rev. Res. **1**, 022004 (2019).

[24] E. Saglamyurek, T. Hrushevskyi, A. Rastogi, L. W. Cooke, B. D. Smith, and L. J. LeBlanc, "Storing short single-photon-level optical pulses in Bose–Einstein condensates for high-performance quantum memory", New Journal of Physics **23**, 043028 (2021).

[25] M. A. Nielsen and I. L. Chuang, *Quantum Computation and Quantum Information*, 10th (2000).

[26] C.-J. Lorenzen and K. Niemax, "Quantum Defects of the $n^2P_{1/2,3/2}$ Levels in ^{39}K I and ^{85}Rb I", Phys. Scripta **27**, 300 (1983).

[27] M. Mack, F. Karlewski, H. Hattermann, S. Höckh, F. Jessen, D. Cano, and J. Fortágh, "Measurement of absolute transition frequencies of ^{87}Rb to nS and nD Rydberg states by means of electromagnetically induced transparency", Phys. Rev. A **83**, 052515 (2011).

[28] M. Marinescu, H. R. Sadeghpour, and A. Dalgarno, "Dispersion coefficients for alkali-metal dimers", Phys. Rev. A **49**, 982–988 (1994).

[29] S. Weber, C. Tresp, H. Menke, A. Urvoy, O. Firstenberg, H. P. Büchler, and S. Hofferberth, "Calculation of Rydberg interaction potentials", Journal of Physics B: Atomic, Molecular and Optical Physics **50**, 133001 (2017).

[30] C. J. Pethick and H. Smith, *Bose-Einstein condensation in dilute gases*, 2nd (2001).

[31] M. Naraschewski and D. M. Stamper-Kurn, "Analytical description of a trapped semi-ideal Bose gas at finite temperature", Physical Review A **58**, 2423–2426 (1998).

[32] Y. Castin and R. Dum, "Bose-Einstein Condensates in Time Dependent Traps", Physical Review Letters **77**, 10.1103/PhysRevLett.77.5315 (1996).

[33] T. Vibel, "Statistical Analysis of Atom Number Fluctuations in Quantum Degenerate Bose Gases", PhD thesis (Aarhus University, 2024).

[34] M. B. Christensen, "Microcanonical Fluctuations in Interacting Bose-Einstein Condensates", PhD thesis (Aarhus University, 2020).

[35] M. A. Kristensen, "Atom Number Fluctuations in Bose-Einstein Condensates", PhD thesis (Aarhus University, 2018).

[36] R. W. Boyd, *Nonlinear Optics*, 4th (2008).

[37] G. Reinaudi, T. Lahaye, Z. Wang, and D. Guéry-Odelin, "Strong saturation absorption imaging of dense clouds of ultracold atoms", Optics Letters **32**, 3143 (2007).

[38] F. Kaminski, N. S. Kampel, M. P. H. Steenstrup, A. Griesmaier, E. S. Polzik, and J. H. Müller, "In-situ dual-port polarization contrast imaging of Faraday rotation in a high optical depth ultracold ^{87}Rb atomic ensemble", The European Physical Journal D **66**, 10.1140/epjd/e2012-30038-0 (2012).

[39] A. Ramanathan, S. R. Muniz, K. C. Wright, R. P. Anderson, W. D. Phillips, K. Helmerson, and G. K. Campbell, "Partial-transfer absorption imaging: a versatile technique for optimal imaging of ultracold gases", Review of Scientific Instruments **83**, 10.1063/1.4747163 (2012).

[40] R. Meppelink, R. A. Rozendaal, S. B. Koller, J. M. Vogels, and P. van der Straten, "Thermodynamics of Bose-Einstein-condensed clouds using phase-contrast imaging", Phys. Rev. A **81**, 10.1103/PhysRevA.81.053632 (2010).

[41] M. R. Andrews, C. G. Townsend, H.-J. Miesner, D. S. Durfee, D. M. Kurn, and W. Ketterle, "Observation of Interference Between Two Bose Condensates", Science **275**, 637–641 (1997).

[42] M. R. Andrews, D. M. Kurn, H.-J. Miesner, D. S. Durfee, C. G. Townsend, S. Inouye, and W. Ketterle, "Propagation of sound in a Bose-Einstein condensate", Phys. Rev. Lett. **79**, 10.1103/PhysRevLett.79.553 (1997).

[43] M. R. Andrews, M.-O. Mewes, N. J. van Druten, D. S. Durfee, D. M. Kurn, and W. Ketterle, "Direct, Nondestructive Observation of a Bose Condensate", Science **273**, 84–87 (1996).

[44] M. Pappa et al., "Ultra-sensitive atom imaging for matter-wave optics", New Journal of Physics **13**, 10.1088/1367-2630/13/11/115012 (2011).

[45] A. Reinhard, J.-F. Riou, L. A. Zundel, and D. S. Weiss, "Dark-ground imaging of high optical thickness atom clouds", Optics Communications **324**, 30–33 (2014).

[46] M. Gajdacz, P. L. Pedersen, T. Mørch, A. J. Hilliard, J. Arlt, and J. F. Sherson, "Non-destructive Faraday imaging of dynamically controlled ultracold atoms", Review of Scientific Instruments **84**, 10.1063/1.4818913 (2013).

[47] W. Ketterle, D. S. Durfee, and D. M. Stamper-Kurn, "Making, probing and understanding Bose-Einstein condensates", 10.3254/978-1-61499-225-7-67 (1999).

[48] R. M. F. Andersen, "Spectrally Probing Ultracold Bosonic Clouds", PhD thesis (Aarhus University, 2025).

[49] E. Hecht, *Optics*, 5th (2017).

[50] D. A. Steck, *Rubidium* 87 *D Line Data*, (2025) http://steck.us/alkalidata (visited on 01/02/2026).

[51] H. K. Andersen, "Bose-Einstein Condensates in Optical Lattices", PhD thesis (Aarhus University, 2008).

[52] J. F. Bertelsen, "Ultracold Atomic Gases Mixtures and Molecules", PhD thesis (Aarhus University, 2007).

[53] S. S. Mai, "Dynamical Control of Matter Waves in Optical Lattices", PhD thesis (Aarhus University, 2010).

[54] P. L. Pedersen, "Multi-Mode Spin Dynamics of a Bose-Einstein Condensate in an Optical Lattice", PhD thesis (Aarhus University, 2014).

[55] M. Gajdacz, "Non-Destructive Imaging and Feedback with Ultracold Gases", PhD thesis (Aarhus University, 2015).

[56] J. Appel, A. MacRae, and A. I. Lvovsky, "A versatile digital GHz phase lock for external cavity diode lasers", Measurement Science and Technology **20**, 055302 (2009).

[57] L. N. Stokholm, "Implementing Two Laser-Based Traps for Cooling to Quantum Degeneracy", Master's thesis (Aarhus University, 2022).

[58] S. Cova, M. Ghioni, A. Lacaita, C. Samori, and F. Zappa, "Avalanche photodiodes and quenching circuits for single-photon detection", Appl. Opt. **35**, 1956–1976 (1996).

[59] Y.-J. Lin, A. R. Perry, R. L. Compton, I. B. Spielman, and J. V. Porto, "Rapid production of ^{87}Rb Bose-Einstein condensates in a combined magnetic and optical potential", Phys. Rev. A **79**, 063631 (2009).

[60] L. Brossard, "Study of Light-Induced Dipolar Interactions in Cold Atoms Assemblies", PhD Thesis (Université Paris-Saclay, 2020).

[61] J. Pellegrino, R. Bourgain, S. Jennewein, Y. R. P. Sortais, A. Browaeys, S. D. Jenkins, and J. Ruostekoski, "Observation of suppression of light scattering induced by dipole-dipole interactions in a cold-atom ensemble", Phys. Rev. Lett. **113**, 133602 (2014).

[62] S. Jennewein et al., "Coherent scattering of near-resonant light by a dense microscopic cold atomic cloud", Phys. Rev. Lett. **116**, 233601 (2016).

[63] A. K. Mohapatra, T. R. Jackson, and C. S. Adams, "Coherent optical detection of highly excited Rydberg states using electromagnetically induced transparency", Phys. Rev. Lett. **98**, 113003 (2007).

[64] H. Kübler, J. Shaffer, T. Baluktsian, R. Löw, and T. Pfau, "Coherent excitation of Rydberg atoms in micrometre-sized atomic vapour cells", Nature Photonics **4**, 112–116 (2010).

[65] J. A. Sedlacek, A. Schwettmann, H. Kübler, R. Löw, T. Pfau, and J. P. Shaffer, "Microwave electrometry with Rydberg atoms in a vapour cell using bright atomic resonances", Nature Physics **8**, 819–824 (2012).

[66] M. Cloutman, M. Chilcott, A. Elliott, J. S. Otto, A. B. Deb, and N. Kjærgaard, "Polarization-insensitive microwave electrometry using Rydberg atoms", Physical Review Applied **21**, 10.1103/PhysRevApplied.21.044025 (2024).

[67] N. Šibalić, J. D. Pritchard, C. S. Adams, and K. J. Weatherill, "ARC: An open-source library for calculating properties of alkali Rydberg atoms", Computer Physics Communications **220**, 319–331 (2017).

[68] W. J. Riley and D. A. Howe, "Handbook of Frequency Stability Analysis", 10.6028/NIST.SP.1065 (2008).

[69] Y.-X. Lu, A.-W. Zhu, C. E. Frank, X.-Y. Huang, and X.-Y. Luo, "High-flux cold lithium-6 and rubidium-87 atoms from compact two-dimensional magneto-optical traps", 10.48550/arXiv.2512.24177 (2026).

[70] S. Bourdeauducq et al., "ARTIQ 2.0: toward a software-defined quantum experiment control system", in Proceedings of the 12th international workshop on reconfigurable communication-centric systems-on-chip (recosoc) (2017).

Acknowledgements

First and foremost, I would like to thank my supervisor, Prof. Jan Arlt, for introducing me to research in experimental atomic physics, for guiding me in the academic world, and for giving me the freedom to try, and sometimes fail, with new ideas. I greatly appreciated your always-open-door, both for encouragement when things worked and for knowing when it was time to move on when they did not. Thank you for trusting me (and the team) to shape the laboratory and steer the direction of experiments.

My experience in the group is that nothing happens in true isolation, and I am grateful to my colleagues for their support throughout this journey. I would like to thank Toke Vibel for dedicating significant time and effort to mentoring me in everyday laboratory life and in navigating the challenges of a PhD. I thank Malthe Andersen for being my lab-mate throughout the years and for the countless troubleshooting sessions, where we often jokingly, albeit half seriously, tried to predict which part of the experiment would fail next based on what we had not yet dealt with. It feels as though we rebuilt the entire experiment from grounds up. While this resulted in fewer publications than initially hoped, it laid the foundation for a robust experiment that will serve the lab for years to come. Thank you Malthe, for being a natural talent and a great friend during these demanding times. Since then, Ilja Zebergs and Nicolai Neubert have joined the team, and I thank you for contributing to both the experiment and its spirit. I am confident that the experiment is in excellent hands for the years to come. I would also like to thank Adam Chatterley for his expertise in lasers and electronics, and for the many "*Now That Is What I Call Music*" competitions that brought much needed levity to the late-evenings in the lab. I am also grateful to our excellent neighbours in the mix laboratory: Andreas Morgen, Søren Balling and Morten Strøe, for helping us whenever needed, and for many stimulating scientific and personal discussions during lunch breaks. More broadly, I thank the group as a

whole for providing an inspiring environment that motivated me to go the extra mile, both in the lab and in the DHL 5k.

During the final year of my PhD, I had the opportunity to visit the Light and Matter group at Otago, led by Prof. Niels Kjærgaard. I am sincerely grateful for the hospitality and for facilitating a change of academic environment that greatly broadened my perspective on experimental physics. Thank you for showing me New Zealand, for the trip to the peninsula to see penguins and albatrosses, and for introducing me to Prof. Blair Blakie, whose company was greatly appreciated during visits to Emmerson's brewery. I am thankful for the freedom and trust I was given in the laboratory. I also wish to thank my colleagues "*down under*", in particular Matthew Chillcot, who warmly welcomed me into the lab and taught me new tricks of the trade. When the delivery of a horn antenna was delayed, you suggested that we design, 3D-print, and copper-electroplate our own, enabling experiments to proceed while performing remarkably well. I also thank Matthew Cloutman and Samyajit Gayen for coffee breaks, walk-and-talks around campus and late-evening burger runs. A special thanks goes to Susi Otto for her kindness and support. She was always there when needed and made many coffee and tea breaks especially pleasant. I am particularly grateful for her reassurance and support when the MOGLabs laser failed. Thank you as well for lending me your mountain bike, which not only extended my lab days beyond the bus schedule but also allowed me to explore the terrain around Dunedin.

I would never have made it this far without the support from my friends and family. I wish to thank the penta-group: Gustav, Mie, Magnus, Anna-Kathrine, Jakob, Maja, Anders and Vania; as well as my fellow physicists Anton Rindom, Frederik Marqversen and Villads Jacobsen, for their encouragement and for reminding me that there is a fulfilling life beyond the laboratory. To my sister, Amalie, and my brother-in-law, Mathias: your perspective and generosity have been a steady source of inspiration making the toughest moments feel lighter and more manageable. To my mother, Helle, for our weekly ballroom dancing. She will never acknowledge that she helped, but that makes the support all the more meaningful. Finally, my deepest thanks to my loving Lisbeth for her unwavering support and patience throughout these years. You stood by me through difficult times, when the laboratory, and the world, seemed in flames. I am profoundly grateful to have you in my life. The conclusion of this thesis marks the beginning of a new journey that we are about to embark on together.

Laurits Nikolaj Stokholm
Aarhus, February 2026